Review of current progress in hole-transporting materials for perovskite solar cells

Prerna Mahajan[1], Bhavya Padha[1], Sonali Verma[1], Vinay Gupta[2], Ram Datt[3], Wing Chung Tsoi[3], Soumitra Satapathi[4], Sandeep Arya[1,*]

[1] Department of Physics, University of Jammu, Jammu, Jammu and Kashmir, 180006, India

[2]Department of Mechanical Engineering, Khalifa University of Science and Technology, Masdar Campus, Abu Dhabi, 54224, United Arab Emirates

[3]SPECIFIC, College of Engineering, Swansea University Bay Campus, Fabian Way, SA1 8EN, Swansea, United Kingdom

[4]Department of Physics, Indian Institute of Technology Roorkee, Uttarakhand 247667, India

[*]Corresponding author email address: snp09arya@gmail.com

Abstract

Recent advancements in perovskites' application as a solar energy harvester have been astonishing. The power conversion efficiency (PCE) of perovskite solar cells (PSCs) is currently reaching parity (>25 percent), an accomplishment attained over past decades. PSCs are seen as perovskites sandwiched between an electron transporting material (ETM) and a hole transporting material (HTM). As a primary component of PSCs, HTM has been shown to have a considerable effect on solar energy harvesting, carrier extraction and transport, crystallization of perovskite, stability, and price. In PSCs, it is still necessary to use a HTM. While perovskites are capable of conducting holes, they are present in trace amounts, necessitating the use of an HTM layer for efficient charge extraction. In this review, we provide an understanding of the significant forms of HTM accessible (inorganic, polymeric and small molecule-based HTMs), to motivate further research and development of such materials. The identification of additional criteria suggests a significant challenge to high stability and affordability in PSC.

Keywords: hole transporting material, perovskite solar cells, power conversion efficiency, stability

1. Introduction

Recently, metal halide hybrid perovskites have emerged as superior photovoltaics material due to their suitable photophysical properties including large absorption coeffeinets, high charge carrier mobility, tunable bandgap, and long carrier diffusion length [1]. Gustav Rose, a German mineralogist, discovered the first naturally occurring perovskite, and named him after his Russian coworker Lev Perovski in 1839. While there are several types of perovskites, those employed in solar cells as well as other fields of optoelectronics are regularly semiconducting hybrid organic-inorganic perovskites.

The chemical formula of perovskite is ABX_3, derived from the first naturally occurring perovskite calcium titanate ($CaTiO_3$). ‘A’ and ‘B’ are cations (‘A’ is larger than ‘B’), while ‘X’ is an anion. An ideal cubic structure, composed of corner-sharing BX_6 octahedra, is ascribed by them. The interstitial space between the eight adjacent octahedra encloses the cation ‘A’ in the

three-dimensional structure (Fig. 1). There is distortion in the crystal structure when the cation size is too large. By changing the ratio of 'A', 'B', and 'X' ions, the behavior of ABX_3 perovskites can be modified [2].

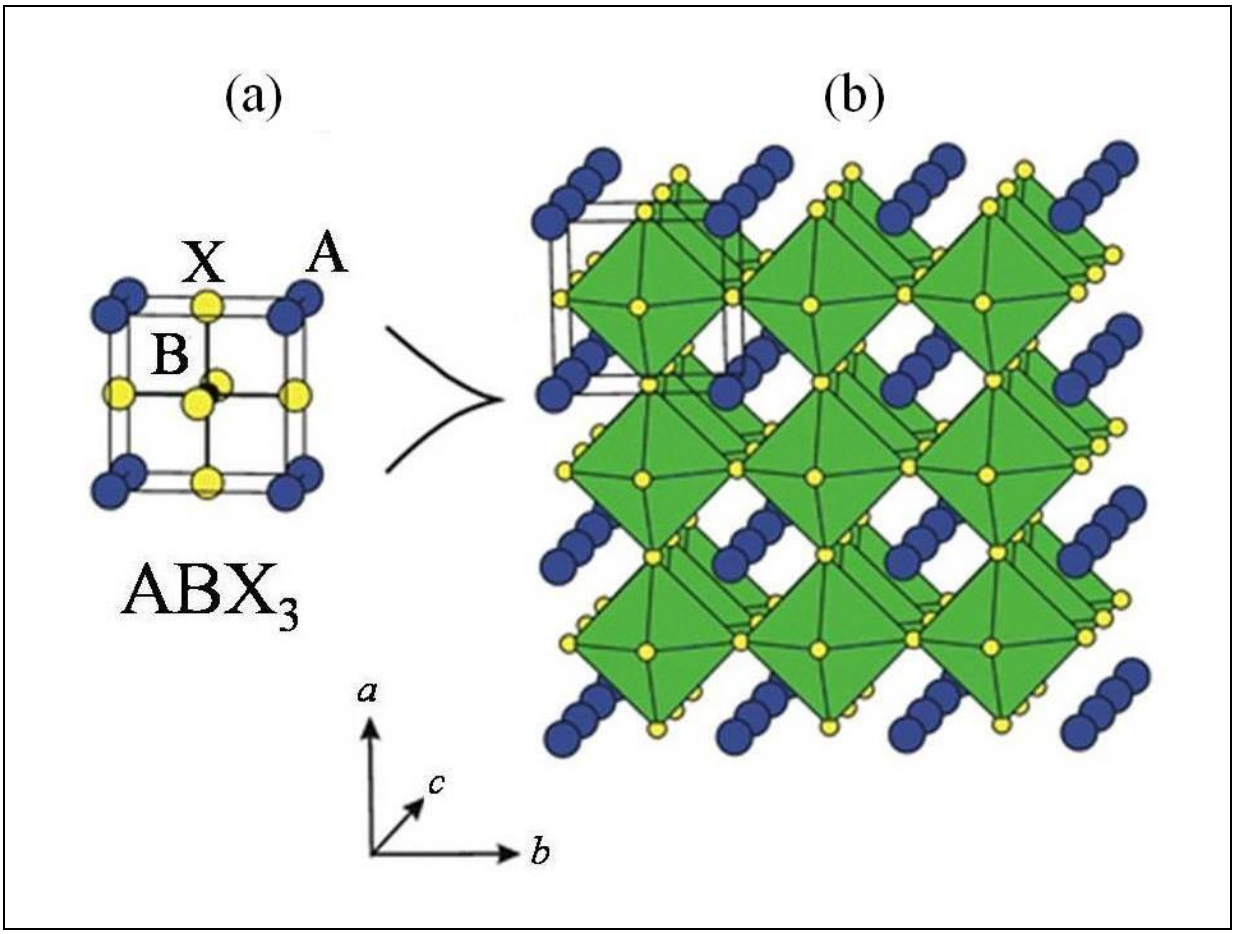

Fig. 1 Crystal structure of ABX_3 perovskite. (a) Ball-stick model of cubic ABX_3 perovskite where A is the cation, B is a divalent metal, and X is a halide (b) 3D extension of the structure (Reproduced from [2] with permission. Copyright 2020, Elsevier)

A is a single monovalent organic cation (usually methylammonium ($CH_3NH_3^+$) or formamidinium $(NH_2)_2CH^+$), Cs^+, or Rb^{2+}. X is a halide ion (Cl^-, Br^-, or I^-). B (Pb^{2+}, Sn^{2+}, Bi^{2+}) is a metallic cation found in organo-metal halide perovskites, frequently utilized in PSCs. The ionic size determines the crystal structure, which may differ from the cubic symmetry [3]. Due to the deformation of the BX_6 octahedra, these perovskites can acquire non-symmetrical geometries, including tetragonal and orthorhombic. Under low temperatures, they experience a phase change but revert to their cubic symmetry at high temperatures. The material that received the greatest

attention is methylammonium lead triiodide ($MAPbI_3$) due to its high efficiency in solar cells [4]. It exhibits exceptional optoelectronic properties, including a broad absorption range up to 800 nm, a high absorption coefficient of 1.5×10^4 cm^{-1} at 550 nm, a high charge carrier mobility (approximately 66 cm^2 V^{-1} s^{-1}), a low exciton binding energy of 10 meV, and a long electron- and hole-diffusion duration (up to 1 mm). Its bandgap can be further modified by adding different organic cations and halide anions [5]. Mixed perovskites comprising organic cations like MA^+ and FA^+, as well as halide anions and metal lead cations have recently exhibited exceptional performance and stability in photovoltaic cells [6].

The desire to adopt eco-friendly energy resources motivated scientists to seek novel ideologies in photovoltaics research area. The use of perovskites in photovoltaic cells began in 2006 using $MAPbBr_3$ in liquid dye-sensitized solar cells (DSSCs), yet only 2.2 % efficiency was achieved [7]. In 2009, the same team recorded an increase in efficiency to 3.8 % and 3.1 %, respectively, using $MAPbI_3$ and $MAPbBr_3$ perovskites as sensitizers and iodine-based liquid electrolytes. The fabricated devices were fragile, lasting for some minutes before dissolving in liquid electrolytes. Im et al. [8] changed the electrolyte solvent, the deposition method, and the TiO_2 surface in the following two years, resulting in a 6.5 % PCE in liquid-based devices using $MAPbI_3$. However, the formed perovskite dissolved in the liquid polar electrolyte every time. The following year, a significant change was observed after substituting a solid-state HTM for liquid electrolytes [9, 10]. Kim et al. [10] used 2,2′,7,7′- tetrakis(N,N-di-p-methoxyphenylamine)-9,9′-spirobifluorene (Spiro-OMeTAD) HTM in PSCs based on $MAPbI_3$ coated over the mesoporous TiO_2 layer, achieving 9.7 % PCE, and 500-hour stability when stored unencapsulated in air at room temperature (RT). Simultaneously, Snaith and colleagues achieved a PCE of greater than 10 % using Al_2O_3. This accomplishment sparked the PSCs research area, which has acquired tremendous momentum since 2012. Many groups focus on the improvements of PSCs by optimizing the perovskite materials, deposition methods, system architecture, and n- and p-type charge-transporters [11-15].

HTMs and electron-transporting materials (ETMs) are critical components of PSCs because they transport charges selectively within the device, control photovoltaic parameters, affect the device's stability, and affect its price [16-19]. The thickness of the HTM is critical for efficient charge extraction and varies according to the processing method and form of HTM [20-22]. Optoelectric devices require an optimal p-type organic semiconductor. To successfully use these

p-type materials in PSCs, the HTM's HOMO must be less energetic than the valence band of perovskite [23-25]. This criterion, however, is only partly applicable. The hole transfer takes place due to the difference in Fermi levels. Additionally, the hole conductor must exhibit sufficient hole mobility ($>10^{-3}$ cm^2 V^{-1} s^{-1}) and be stable under different environmental factors [26,27].

Despite their attractive characteristics, including high hole mobility and cost-effectiveness, the inorganic HTMs used in PSCs, such as CuI, CuO_x, CuSCN, MoO_x and NiO, have drawbacks. The solvent used to deposit them dissolves the perovskite, leading to instability of the system. Polymeric materials have several disadvantages, including a lengthy purification process, complex characterization due to an unknown molecular weight, and a poor infiltration into the nanomaterial, all of which have prompted an increase in the effort to create small organic molecules like HTMs [28-31]. A brief overview of different HTMs used in PSCs in the past few years (2016 to the present) along with their stability issues has been described here. Although every effort was made to include the major works done on the efficient HTMs, we apologize for any omissions made inadvertently.

2. Device configurations

Since the discovery of solid-state PSCs, numerous device configurations have been created. A standard PSC device consists of two electrodes, a perovskite light absorber, an ETM, and an HTM. PSCs could be categorized as n–i–p or p–i–n based devices, depending on whether electrons or holes are collected by the bottom of the conducting substrate, generally, a transparent conducting oxide (TCO) coated glass. The n–i–p structure is often described as a conventional structure, whereas the p-i-n structure is defined as an inverted structure. Fig. 2 illustrates the different device designs. Type (I) architectures are mesoscopic and employ mesoporous nanocrystals on the TCO coated substrate, as shown in Fig. 2(a,b). The perovskite penetrates and fills the mesoporous layer, then capped with HTM or ETM during device fabrication [32,33].

As shown in Fig. 2(c,d) type (II), planar heterojunction, removes the mesoscopic scaffold. This configuration is advantageous owing to its simple fabrication process and economical nature [34]. The concept behind type (III) is to eliminate the carrier transport layer. Fig. 2(e,f) illustrate this ETM- or HTM-free form. In this case, the perovskite acts as both an absorber and a charge

transporter [35–37]. The system performance is not very promising owing to its high charge carrier recombination during illumination. Recently, a selective contact or counter electrode for device configurations like monolithic cells (Fig. 2(g)) and back contact cells (Fig. 2(h)) has also been designed to preserve the perovskite layer and reduce material expense [38-41]. A mesoporous conducting counter electrode should be fabricated on top of a mesoscopic scaffold to create a monolithic cell. Henceforth, perovskite fabrication is the final phase in the production process. This arrangement enables printing or high temperatures to create a template for the entire substrate [41]. Organic HTMs (Spiro-OMeTAD, PTEG, P3HT, PTAA, etc.) are usually present above perovskite in the n–i–p design [42]. In the p–i–n layout, the p-type layer serves as a selective layer and a window in PSCs [43].

Numerous aspects of HTM have indeed been identified within PSCs, including the following:

a) HTM acts as a dielectric among the metal back contact and the perovskite sheet. Thus, prohibiting carrier recombination between electrons of perovskite and holes of metal contact.

b) Due to HTM's high hole mobility, it enhances the hole transport in PSCs.

c) HTM acts as a moisture barrier or metal ion diffusion barrier, metigating PSC degradation. As per literature, HTM covers the perovskite more efficiently than TCO/perovskite/metal [44,45].

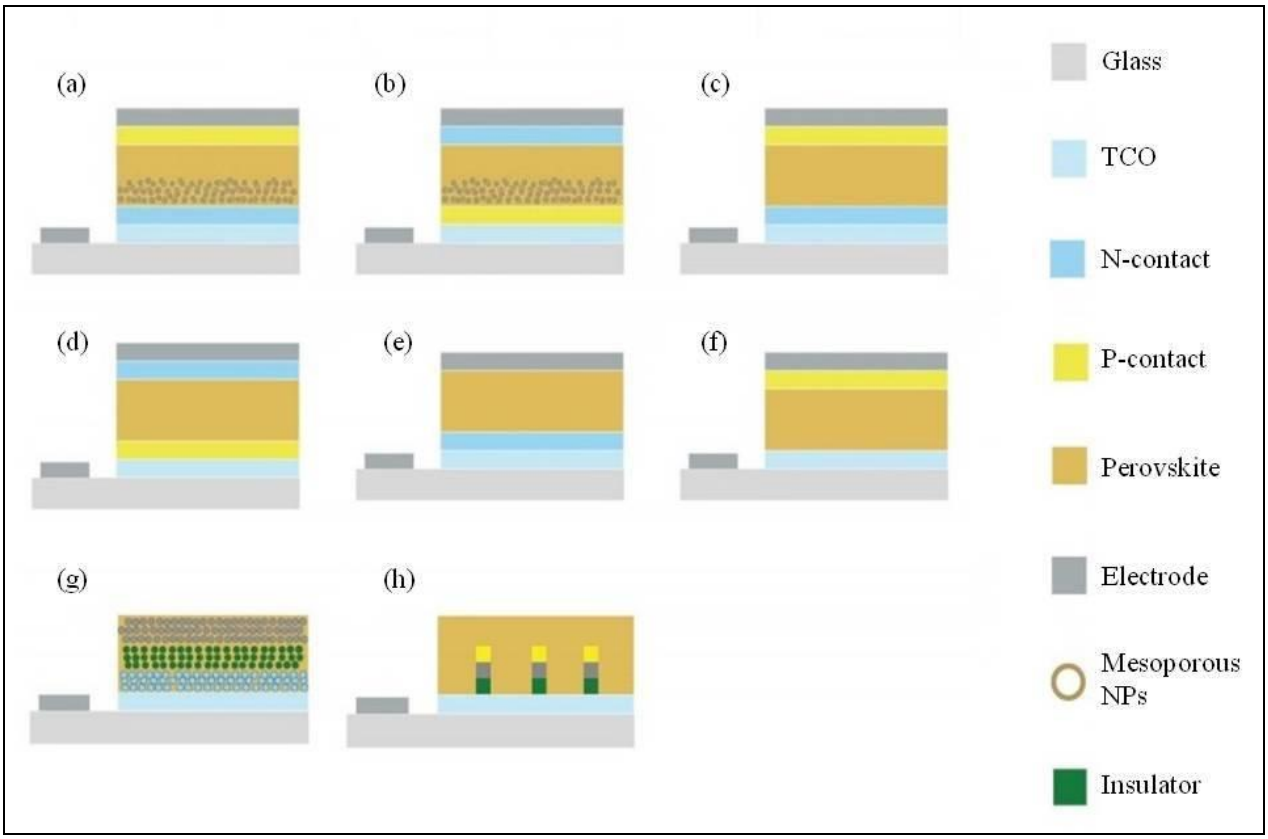

Fig. 2 Various device designs of PSCs (a) mesoscopic n–i–p (b) mesoscopic p–i–n (c) planar n–i–p (d) planar p–i–n (e) HTM-free (f) ETM-free (g) monolithic (h) backcontact architecture (Reproduced from [45] with permission. Copyright 2018, Wiley)

3. Selection criteria for HTMs in PSCs

The photovoltaic processes consist of the following steps: i) absorbing light, ii) separating electron/hole, and iii) charge transport and charge collection. Fast charge carrier transport with a low charge recombination rate is often needed for efficient PSC devices. HTM made significant improvements in the extraction and transportation of hole carriers. In PSCs, recombination resistance, R_{rec}, is inversely proportional to recombination kinetics. R_{rec} is significantly reduced when HTM is used. In other words, HTM increases the efficiency of hole carrier extraction [46]. Another problem related to this is series resistance (R_s) results in decreased fill factor (FF) upon increasing thickness of the HTMs.

During the operation, HTM must promote the energy conversion process as under:

a) Compatibility of the valance band (VB) present in HTM and perovskite. It can minimize the energy barrier encountered during charge (hole) transfer. A broad bandgap or a low electron affinity allows HTM to restrict the movement of electrons and reduce the recombination rate efficiently.
b) A high mobility of carriers, a long diffusion length, and a longtivity. These may help to avoid carrier loss during extraction and transport.
c) Stability under various manufacturing and working conditions and resistance to heat, water, oxygen, and ultraviolet (UV) light.
d) Less expensive materials and economical process.

The conventional n–i–p layout uses HTM in between the perovskite and the metal back contact. If dpinhole exists in HTM, halide ion transfer or metal diffusion occurs, resulting in a metal-halide compound (like AgI) [47]. This leads to the decay of perovskite. By implanting HTM, the perovskite active layer and top metal are well separated, suppressing the carrier shunt path [48]. Graphene oxide (GO) is also an HTM with unique properties such as a good valance band location (-5.2 eV) and high charge mobility (3000- 27,000 cm^2 V^{-1} s^{-1}). Li et al. [49] defined a method for improving the interface among perovskite and HTM (Spiro-OMeTAD) employing GO as a buffer layer. Following buffering, the contact angle reduced from 13.4 to 0 degrees, leading to an increase in the short circuit current density (J_{SC}) from 18.5 to 20.2 mA cm^{-2}. The carrier recombination was reduced by the buffer layer, increasing open-circuit voltage (V_{OC}) and FF. Indeed, V_{OC} increased from 0.93 to 1.04 V, whereas FF increased from 0.64 to 0.73.

The HTM also serves as a window layer for solar cells in the p–i–n structure. It implies that the refractive index along with extinction coefficient of the HTMs must be considered when attempting to reduce photon loss. For instance, if mesoscopic nanocrystals' particle size (or aggregation) is sufficiently large, optical scattering can occur. Due to NiO_x's high hole mobility, broad bandgap, stability and proper energy level, NiO nanocrystals are normally used as the selective layer for p–i–n devices [50–53]. The NiO nanocrystals' size and the pore size created by mesoscopic NiO are related to the penetration of perovskite precursor solution.

4. Recently employed HTMs in PSCs

The usage of HTM for collecting holes from perovskites and transporting them to an electrode is still needed among most PSC structures. The most widely used classical HTM is Spiro-

OMeTAD, which was discovered and authorized by Merck nearly two decades ago [54,55]. Spiro-OMeTAD continues to be the most extensively investigated HTM for solid-state sensitized solar cells. The hole mobility of Spiro-OMeTAD was observed to be less than optimal, and Grätzel and coworkers discovered methods for refining its semiconducting characteristics employing cobalt-based dopants and ionic salt [56]. The cobalt-based dopants acted as single-electron redox shuttles, and their oxidation potential was found to enhance the characteristics of Spiro-OMeTAD. Using an ionic salt for improving carrier mobility, on the other hand, is viewed as a trade-off for stability.

Just a few new nanomaterials are currently investigated for selective electron contacts for PSCs [57-63], with primary focus on developing a practical and ideal HTM. N-type materials like TiO_2 are often used. Various nanomaterials are available in the organic photovoltaics (OPV) group, which are heavily investigated in using p-type materials. The information obtained on p-type organic semiconductors was instrumental in creating and using organic HTMs in PSCs. Lately, several p-type materials, including small organic materials, conducting polymers, inorganic semiconductors and organometallic compounds, are used in PSCs with tremendous success. Still, just some of them are stable enough to compete with classical Spiro-OMeTAD in PSCs.

Inorganic, polymeric, and small molecule HTMs are the three major types of solid-state HTMs used in PSCs as shown in Fig. 3.

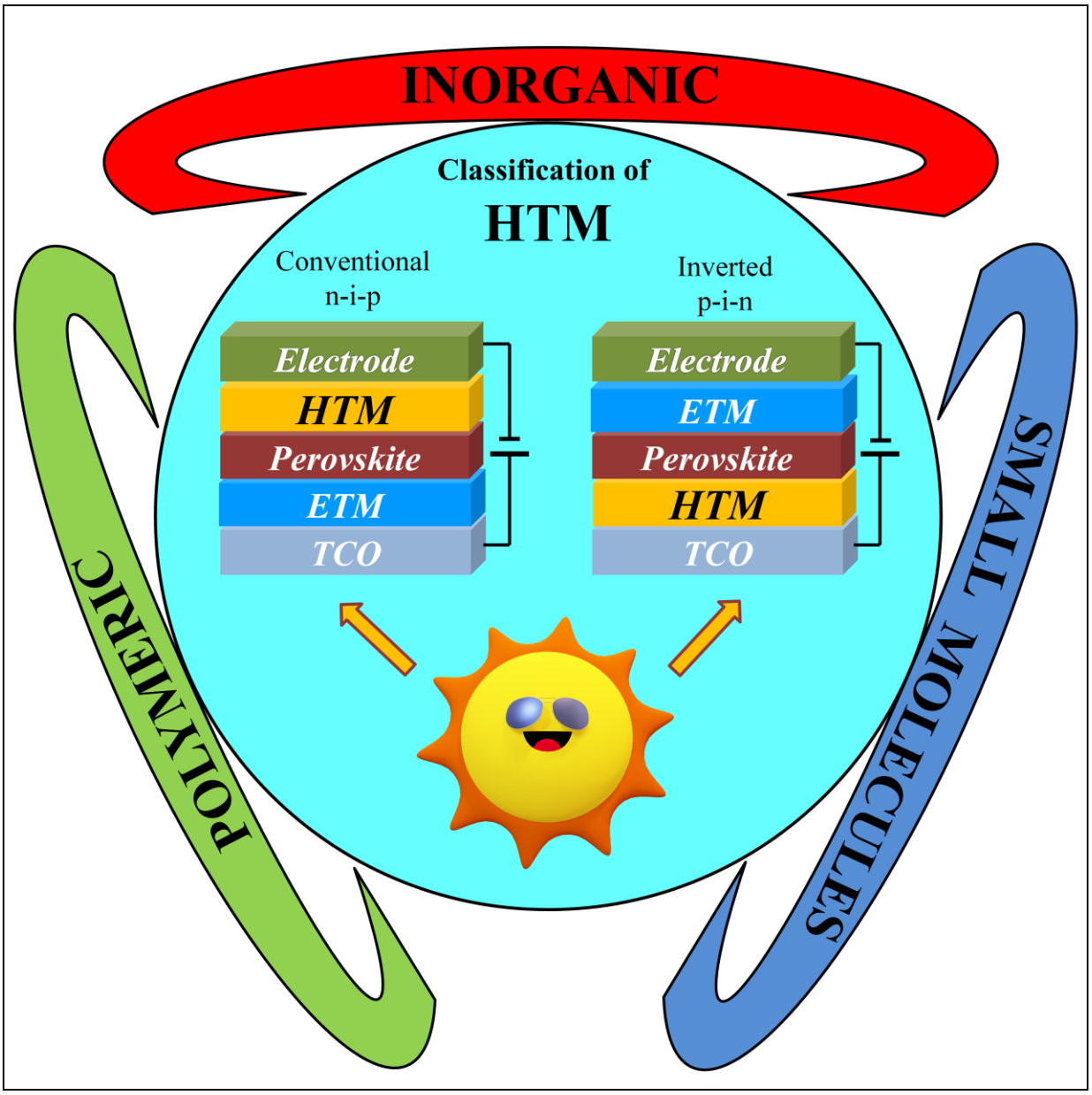

Fig. 3 Classification of available HTMs.

4.1. Inorganic HTM

Inorganic HTMs have emerged as promising candidates to achieve high performance and stability in PSCs. Moreover, a composite of inorganic and organic material is also found to be successful in attaining satisfactory performance. Derivatives of metals such as nickel or copper, transition metal oxides, metal dichalcogenides and organic-inorganic composite materials etc

that effectively play the role of a hole transporting layer are discussed in this section. Table 1 summarizes the photovoltaic parameters of PSCs employing various inorganic HTMs.

4.1.1. Nickel derivatives

By employing the triple cation lead halide perovskite $Cs_{0.08}(MA_{0.17}FA_{0.83})_{0.92}Pb(I_{0.83}Br_{0.17})_3$ as an absorber layer, Weber et al. [64] analyzed various HTMs (solution refined NiO_x, sputtered NiO_x) in planar p-i-n PSCs. Overall, utilizing solution-processed NiO_x as HTM in the devices resulted in reproducible solar cell outputs with PCE up to 12.8 %. In both inverted (p-i-n) planar and normal (n-i-p) mesoscopic organic-inorganic hybrid PSCs, a low-temperature solution-processed nickel NiO_x thin film was used as HTM for the first time by Liu et al. [65]. With an appropriate surface treatment, hole extraction process, perovskite morphology, wetting properties, and absorption in p-i-n PSCs can be dramatically improved, resulting in a significantly increased FF (68.4% to 74.2%) and J_{sc} (from 16.73 to 20.66 mA cm^{-2}). For inverted planar PSCs, a promising PCE of 15.9% with marginal hysteresis was obtained, and 11.8 % for flexible devices was obtained using the NiO_x thin film. Saranin et al. [66] presented a new precursor, tris (ethylene diamine) nickel acetate, for deposition of NiO HTM at a temperature of 280-300 °C. A hybrid investigation involving XRD, Raman, and Auger spectroscopy was used to fully characterize the accumulated NiO film. They discovered a direct correlation between PCE and NiO thickness, with the thinner NiO (10nm) layer achieving the highest efficiency of over 15%. Ayedin et al. [67] created RT sputtered NiO_x and demonstrated inverted PSCs with 17.6% PCE (no hysteresis), which is comparable to the best PSCs made with sputtered and annealed NiO_x without heteroatom doping. Wang et al. [68] presented a basic electrochemical deposition process for producing a mesoporous NiO_x film rapidly and uniformly. The benefits of growing the thickness and lessening the surface roughness of the NiO_x film for light transmission were shown. The ideal condition for preparing NiO_x films was attained by changing the time of deposition at a specific applied current density, that has outstanding optical transmittance and an appropriate thickness and band gap, reducing optical loss and improving hole extraction at the interface between HTM and the perovskite, and thus improving PCE. The optimum thickness of the NiO_x was verified with the finite-difference time-domain simulation. For an active region of 0.25 cm^2, an optimum PCE of 17.77 % was obtained. With a PCE gap of 2% for measuring the various sites from edge to center, the prepared device shows negligible hysteresis and good

reproducibility. Han et al. [69] attained a high PCE of 17.6% (stabilized 17.0%) using a low-temperature solution treated NiO_x film in mixed Pb-Sn low-bandgap PSCs.

Low-temperature ALD has a lot of advantages when it comes to manufacturing uniform, consistent and pinhole-free thin films. Using bis-methylcyclopentadienylnickel abbreviated as $Ni(MeCp)_2$ as a precursor and O_2 plasma as a co-reactant, plasma-assisted ALD of NiO was carried out over a broad temperature range of 50–300 °C. Films deposited at 150 °C with outstanding thickness uniformity on a 4-inch silicon wafer have a growth rate of 0.32 Å per cycle. Post-annealing improves the perovskite layer's wettability and increases the conductivity and mobility of the NiO films, resulting in higher J_{sc} and FF in the fabricated cells. In comparison to the 13.98 % PCE obtained from the pristine NiO-based PSC, the post-annealed NiO-based PSC achieved a superior 17.07 % PCE [70]. The PCE of inverted-type PSCs based on (ALD-NiO)-HTM was 18.78% as shown in Fig. 4(a) [71]. Inverted planar $MAPbI_{3-x}Cl_x$ solar cells based on NiO HTM were investigated by Zhao et al. [72]. Some variables that affect the device's performance were determined. The doping concentration of NiO, the thickness of the NiO layer, the doping concentration of [6,6]-phenyl-C_{61}-butyric acid methyl ester (PCBM), and the thickness of the perovskite layer were all considered. A PCE of 22.0 % was calculated based on the simulation results. Furthermore, based on the experimental condition, a high PCE of 18.08 % was obtained. Liu et al. [73] implemented an efficient colloidal NiO NCs synthetic scheme with ligand-protection to generate high-quality HTMs. The prepared NiO NPs exhibited a pure composition, with no impurities or visible flaws, which is advantageous for their electrical and optical properties. This technique produced NiO nanocrystals that were stable in the reaction phase, well crystalline, and distributed in the chlorobenzene solvent. The concentration of NiO NCs solution affect significantly on the properties of the HTMs and PCE of PSCs. High-quality HTMs were prepared with excellent optical transmittance, decent film-forming performance, little interface traps, and admirable hole transport capability by optimizing the concentration. The PCE of 7.96 % was achieved by PSCs containing HTMs with colloidal NiO NCs. The impact of aged and fresh NiO precursor solution on the development of NiO and perovskite films, as well as their incorporation as HTM in inverted PSC was investigated by Singh et al. [74]. The morphological, structural, and optical (transmittance) properties of both (f-NiO and a-NiO) films were all fine. As opposed to f-NiO/ITO substrate, perovskite films coated on a-NiO/ITO substrate and annealed at 100 °C and 120 °C have improved optical and structural

properties. The Urbach energy equation indicated that at lower annealing temperatures, the $MAPbI_3$ films have less chaos. With a PCE of 7.30 %, the devices with 32 nm NiO film thickness showed the best efficiency. As the NiO film thickness was further increased, the PCE quickly degraded to 3.14 %. Direct current (DC) reactive magnetron sputtering was utilized to make NiO_x thin films by Pan et al. [75]. The properties of NiO_x thin films were studied in-depth, including deposition rate, morphology, electrical and optical properties, grain structure, and chemical composition. During sputtering, the material properties of NiO_x were finely modified while the voltage was monitored. In all-inorganic $CsPbI_2Br$ PSCs, NiO_x thin films were used as HTMs and the resulting devices obtained a maximum performance of 12.6 %.

To improve the film consistency and coverage, phytic acid sodium (PAS) inter-layer was added between the NiO_x HTM and the perovskite absorption layer [76]. A high-quality perovskite film was developed by managing the flow and drying phase of the one-step solution process of perovskite in DMSO and gamma-butyrolactone (GBL) solvent, and the domain size was significantly increased from about 50 µm to 100–200 µm. The system with PAS inter-layer could more easily match energy levels with the perovskite and collect holes due to the lower VB value of 5.3 eV obtained by the PAS modified NiO_x film. Furthermore, PAS improved the interaction between the NiO_x layer and the perovskite layer, leading to an increase in the filling factor (FF) from 52.96 % to 60.82 % by improving the interfacial properties. Finally, in the ambient air, the PCE of the device fabricated by doctor blade coating was increased from 10.07 % to 13.19 %. Pant et al. [77] prepared the perovskite on (radio frequency (RF) sputtered nickel oxide (sp-NiO_x) by a two-step process in which the MAI solution was spin-coated on top of the deposited PbI_2 substrate to examine the dependence of residual PbI_2 on the preparation methods. The existence of a residual PbI_2 layer (20-50 nm) at the perovskite/NiO_x interface was confirmed by a cross-sectional SEM picture of two step method (TSM)-based perovskite. The higher crystallinity of the perovskite film prepared by TSM was verified based on the measurement of the PL peaks and PL lifetimes, despite a higher XRD peak strength of residual PbI_2. The photovoltaic output of PSCs fabricated with TSM is better than that of devices fabricated with one step method (OSM). This paper presented an analysis into the relationship between device efficiency and residual PbI_2 position, which can help to enhance the performance of sp-NiO_x dependent PSCs. For perovskite devices prepared in OSM, the PCE of 8%–10% was obtained while residual PbI_2 was present in bulk and on the perovskite surface. On the other hand, all of

the perovskite (with residual PbI_2 layer at perovskite/NiO_x interface) device parameters greatly improved, with maximum PCE of 13.6 %, respectively. The strong crystallinity of TSM-prepared perovskite, with large grains and uniform morphology resulted in improved performance and high reproducibility of the PSC.

By changing the fuel concentration in the nickel oxide precursor solution, a NiO_x flm with improved conductivity and carrier extraction was obtained by Liu et al. [78]. It was also discovered that greater grain size and lower trap-state densities increased the quality of perovskite film. Consequently, the inverted planar PSCs obtained a maximum power conversion efficiency of 14.37 % by utilizing the 10 ul/ml optimum concentration of acetylacetone in the NiO_x precursor solution. V_{OC} greater than 1 V are difficult to achieve in p-i-n style PSCs using poly(3,4-ethylenedioxythiophene):poly(styrenesulfonate) (PEDOT:PSS) HTMs. However, NiO HTMs have revealed better potential in achieving high V_{oc} values. The hydrothermal approach was used to develop a NiO nanomesh with a Ni^{3+} flaw, resulting in PSCs with V_{oc} constantly exceeding 1.10 V (champion V_{oc} = 1.14 V) [79]. The PCE of the champion system was found to be 17.75 %. To evaluate the power production characteristics under illumination, a planar PSC with a p-i-n inverted configuration is modelled and simulated using SCAPS software [80]. The inverted configuration NiO/$MASnI_3$/PCBM has been utilized, with NiO as the HTM, $MASnI_3$ as the perovskite absorber layer, and PCBM as the ETM. The impact of thickness of the three layers, defect density of the interfaces, the metal work function and the density of states on the PCE were all studied in the simulations. The variation of photovoltaic parameters with HTM thickness is shown in Fig. 4(b). A performance of 22.95 % has been obtained for the optimal parameters of all three layers i.e NiO, $MASnI_3$, and PCBM.

Lee et al. [81] used Zn-doped NiO_x as an HTM in planar heterojunction PSCs since not only does Zn have a comparable atomic size to Ni, but it also forms strongly crystalline oxide materials. In comparison to the un-doped NiO_x equivalent, 5 % Zn doped systems obtained a PCE of up to 13.72 %, with gains in V_{oc} of 4.0 %, J_{sc} of 16.7 %, and FF of 8.9 %. He et al. [82] used RT solution-processing technique to make phase-pure p-type Cu-doped NiO_x NPs having outstanding electronic properties that can be transformed into efficient, uniform and pinhole-free HTMs with large-area homogeinity across a broad range of film thickness. For such a high-quality inorganic HTM, versatile PSCs with an active area >1 cm^2 and a PCE of over 15.01 % can be fabricated without hysteresis. Using software wxAMPS (analysis of microelectronic and

photonic structures)-1D, a composite of NiO and Carbon i.e NiO@Carbon was simulated not only as an HTM but also as a counter electrode in planar heterojunction based PSCs [83]. The impact of band offset between perovskite layer and HTM on PCE was found to be highly dependent on the simulation results. Meanwhile, NiO's valence band offset (E_v) was tuned to be 0.1 to 0.3 eV lower than that of perovskite. A barrier cliff was also discovered at the HTM/absorber interface, which had a major impact on hole extraction. The E_v between the active material and NiO@Carbon-HTM, on the other hand, was calculated to be -0.15 to 0.15 eV, with a higher efficiency of 15 to 16 %. High-performance inverted planar PSCs were demonstrated by Hu et al. [84] using sol-gel treated yttrium (Y)-doped NiO thin films as HTM. A basic sol-gel procedure was used to successfully prepare Y-doped NiO thin films with various Y doping concentrations. The electrical conductivity of NiO thin film was greatly enhanced by Y doping, and the PCE of Y-doped NiO HTM-based PSC devices outperformed that of pristine NiO HTM-based devices. In particular, the PSC with a 5% Y-NiO HTM had the best results, with a V_{oc} of 1.00 V, J_{sc} of 23.82 mA cm^{-2}, FF of 68 %, and PCE of 16.31 %, resulting in a 27.62 % increase in PCE over the NiO system. The improved hole mobility, good quality compact active layer morphology due to the underlying HTM layer, more effective charge extraction from perovskite absorber, and lower charge recombination likelihood may all contribute to the improved efficiency of the Y-doped NiO devices. For the first time, a solution-processed Co-doped NiO_x film was used as the HTM in inverted planar PSCs, and the solar cells have a PCE of 18.6% [85]. It has been discovered that sufficient Co-doping will significantly alter the working mechanism of the NiO_x film and improve its electrical conductivity. Charge accumulation turns out to be more prominent in Co-doped NiO_x based PSC, as shown by capacitance-voltage (C-V) spectra and time-resolved photoluminescence spectra, which inhibits nonradiative recombination at the interface between the Co-doped NiO_x and the active perovskite layers. Furthermore, field-dependent photoluminescence measurements show that Co-doped NiO_x-based devices can effectively inhibit radiative recombination in the perovskite sheet, thus facilitating photocurrent production.

Xiao et al. [86] demonstrated that embedding a small concentration (0.11 At %) of gold NPs (Au-NPs) with a diameter of 2–3 nm into a NiO_x thin film increases the carrier concentration by up to three times. The mechanism of Gold doped NiO_x in the devices is shown in Fig. 4(c). The improvement is attributed to the formation of an Ohmic interaction between Au and NiO_x while

preventing direct interaction with the perovskite. All of the device parameters were altered, and the average PCE was increased from 17.8 % to 20.2 %. Via a simple low-temperature sol-gel process, smooth and dense Sr-doped NiO_x films with various Sr doping concentrations were successfully prepared by Zhang et al. [87]. The 1 atomic % Sr-doped NiO_x HTM-based PSCs demonstrated the best results with a PCE of 20.07 %. The J-V curves of the devices are shown in Fig. 4(d). The outstanding behaviour of Sr-doped NiO_x-based PSCs can be due to improved electrical conductivity, crystallinity of the perovskite film, and energy level matching with the perovskite layer, all of which can significantly increase hole transfer and extraction abilities while reducing carrier recombination, leading to high PCE and good stability. Using a metal-organic framework as a precursor, Cu-Ni bimetallic organic frameworks were synthesized using a simple and stepwise solvothermal process [88]. By calcining the bimetallic organic frameworks at 400 °C in an air atmosphere, core-shell CuO@NiO nanospheres were developed. The Ni-BTC NPs were also calcined in the same conditions to produce NiO nanospheres. This technique was used to make core-shell CuO@NiO and NiO NPs, which were used as HTM in PSCs. As compared to the NiO HTM–based PSC, the PSC with coreshell CuO@NiO HTM had a higher PCE of 10.11 %. The better extraction of charge carriers is due to the favorable energy level alignment between the perovskite and the HTM, enhancement in HTM conductivity, and reduction in defect density in the surface and bulk of HTM is primarily responsible for the better PCE of PSC based on core-shell CuO@NiO HTM. Chandrasekhar et al. [89] provided a systematic analysis of the PCE of PSCs using Fe-doped NiO_x NPs as the HTM. Fe-doped NiO_x NPs were synthesized using a simple solution process, and their corresponding films were deposited by spin coating with Fe-NiO_x inks at RT without any post-treatment. As a result of improved conductivity and work function of the Fe-doped NiO_x films, they improved hole extraction and charge selection while suppressing charge recombination. As a result, Fe-NiO_x based PSC has a substantial increase in PCE (17.57 %) as compared to pristine NiO_x (15.41%). Lee et al. [90] presented a simple method for producing superior-quality NiO_x films annealed by NIR in just 50 seconds. The impact of NIR strength on the film content of sol-gel NiO_x was investigated using a short-wave NIR lamp at 2500 K. PSCs made from NIR-annealed NiO_x (NIR- NiO_x) film have a PCE similar to those made from conventional hot-plate annealed- NiO_x film (HP-NiO_x). In addition, to substitute pristine NIR-NiO_x, NIR annealed cobalt-doped NiO_x (NIR-Co:NiO_x) was synthesized. Due to enhanced hole mobility, decreased interfacial resistance,

and well-matched work function, the PCE of PSCs fabricated from this new NiO_x film was improved from 15.99 % to 17.77 %, resulting from more effective hole extraction, fewer charge accumulation, and reduced V_{oc} loss.

Wang et al. [91] showed that using inverted structures of planar heterojunction PSCs; lithium (Li) and cobalt (Co) codoped in NiO_x that were deposited onto ITO substrates through solution methods at RT, may greatly improve efficiency. Experiments have shown that doping a certain amount of Li and Co into NiO_x films will improve optical transmittance, work function, electrical conductivity, and hole mobility as compared to pristine NiO_x films. As a result, when PSCs is codoped with 10% Li and 5% Co in NiO_x, their PCE improves significantly from 14.1 % to 18.7 %. The J-V curves of the devices are demonstrated in Fig. 4(e). In another study, using the same concentration of dopants Li and Cu, 20.1 % PCE was obtained. Ouyang [93] presented the first RT solution-processed and post-treatment-free Li and Cu codoped NiO_x NP-based HTM. Simultaneously, the Li and Cu codoped NiO_x HTMs demonstrate (1) enhanced electrical conductivity and optical transmittance, (2) good quality film morphology (pin-hole/crack free, lightweight and uniform), (3) favouring larger grain-size perovskite film formation, and (4) thermal stability up to 250 °C. PSCs with Li and Cu codoped NiO_x HTM reached 20.8 % and 18.2 % with rigid and flexible PSCs, respectively.

A radio frequency magnetron sputtering technique was used to deposit NiO layer and NiO/Ag/NiO triple layers as the HTMs of $MAPbI_3$ and $FA_xMA_{1-x}PbI_3$ PSCs on ITO coated glass substrates [94]. The average transmission of the NiO/Ag/NiO (30/7/30 nm) HTM was increased to 70.4 % as compared to the 60-nm-thick NiO HTM, which had an average transmission of 66.8% within the wavelength ranges of 300 to 800 nm. As a result, the NiO/Ag/NiO (30/7/30 nm) HTM increased the efficiency of $MAPbI_3$ PSCs from 11.02 to 11.68 %. Various $FA_xMA_{1-x}PbI_3$ active layers were created by blending various FAI contents with MAI to broaden light absorption. The PCE of $FA_{0.1}MA_{0.9}PbI_3$ PSCs was increased to 12.30 % using 60-nm-thick NiO HTM. The PCE of the PSCs was increased to 12.67 % by combining the optimal $FA_{0.1}MA_{0.9}PbI_3$ active layer with the optimal NiO/Ag/NiO (30/7/30 nm) HTM. The solution-processed low temperature of mixed nickel (acetate/nitrate) is used to create a new phase based on trivalent Ni_2O_3 [95]. In contrast, the novel Ni_2O_3 thin films made from high-temperature solution-processed divalent NiO_x have greater stability and energy compatibility with perovskite thin

films. High-performance PSCs are reliably fabricated using $MA_{0.85}FA_{0.15}PbI_{0.9}Cl_{0.1}$ perovskite, with a PCE of 17.89 % and marginal hysteresis, compared to PCE of 14.37 % for NiO_x. Wang et al. [96] used a simple processing approach on an ultrathin electrochemical mesoporous NiO_x film manipulated by controllable ultraviolet/ozone (UVO) treatment; the length of UVO treatment on the NiO_x film has a substantial impact on the PSCs' photovoltaic properties. The NiO_x film's wettability, electrical conductivity, nonstoichiometry, and valence band energy were improved with differing degrees as the exposure time rises. Furthermore, the device's build-in potential, recombination resistance at the perovskite/NiO_x interface, and perovskite grain size all improve, resulting in higher J_{sc} and V_{oc}. Considering these parameters, the optimum exposure period for UVO treatment on NiO_x film was found to be 5 minutes, resulting in a significantly high PCE of 19.67%. The J-V curves of the devices are shown in Fig. 4(f). Ouyang et al. [97] suggested a novel technique for synthesising ultrasmall ternary oxide NPs, $NiCo_2O_4$, by controlling the deamination of $Co–NH_3$ complexes in a device comprising $Ni(OH)_2$. This method yields ultrasmall (5 nm on average) and well-dispersed $NiCo_2O_4$ NPs free of exotic ligands, allowing for the creation of homogeneous and pin-hole-free films. Big perovskite grains form more easily on the $NiCo_2O_4$ films, which reduces film defects. The findings indicated that when $NiCo_2O_4$ NPs are used as the HTM, the PSCs achieve a high PCE of 18.23% as shown in Fig. 4(g). To the author's awareness, this was the first-time spinel $NiCo_2O_4$ NPs have been effectively used as HTM in PSCs. This research not only shows how ternary oxide $NiCo_2O_4$ can be used as an HTM in hybrid PSCs, but also sheds light on how to design and synthesize ultrasmall and ligand-free NPs HTMs for cost-effective photovoltaic devices. The synthesis and characterization of low-temperature solution-processable monodispersed $NiCo_2O_4$ NPs were demonstrated through a combustion synthesis using tartaric acid as fuel [98]. As opposed to NiO, $NiCo_2O_4$ is a p-type semiconductor that contains environmentally sound, abundant elements and has a higher conductivity. It is demonstrated that the combustion synthesis of spinel $NiCo_2O_4$ with tartaric acid as fuel can be used to monitor NP size and produce flat, smooth, and homogeneous functional HTMs that can be processed by blade coating. The hole extraction performance of PSCs differs with various $NiCo_2O_4$ thicknesses as HTM. As a consequence, PSCs with 15 nm $NiCo_2O_4$ HTM exhibited enhanced hole carrier collection resulting in a PCE of 15.5 % with negligible hysteresis.

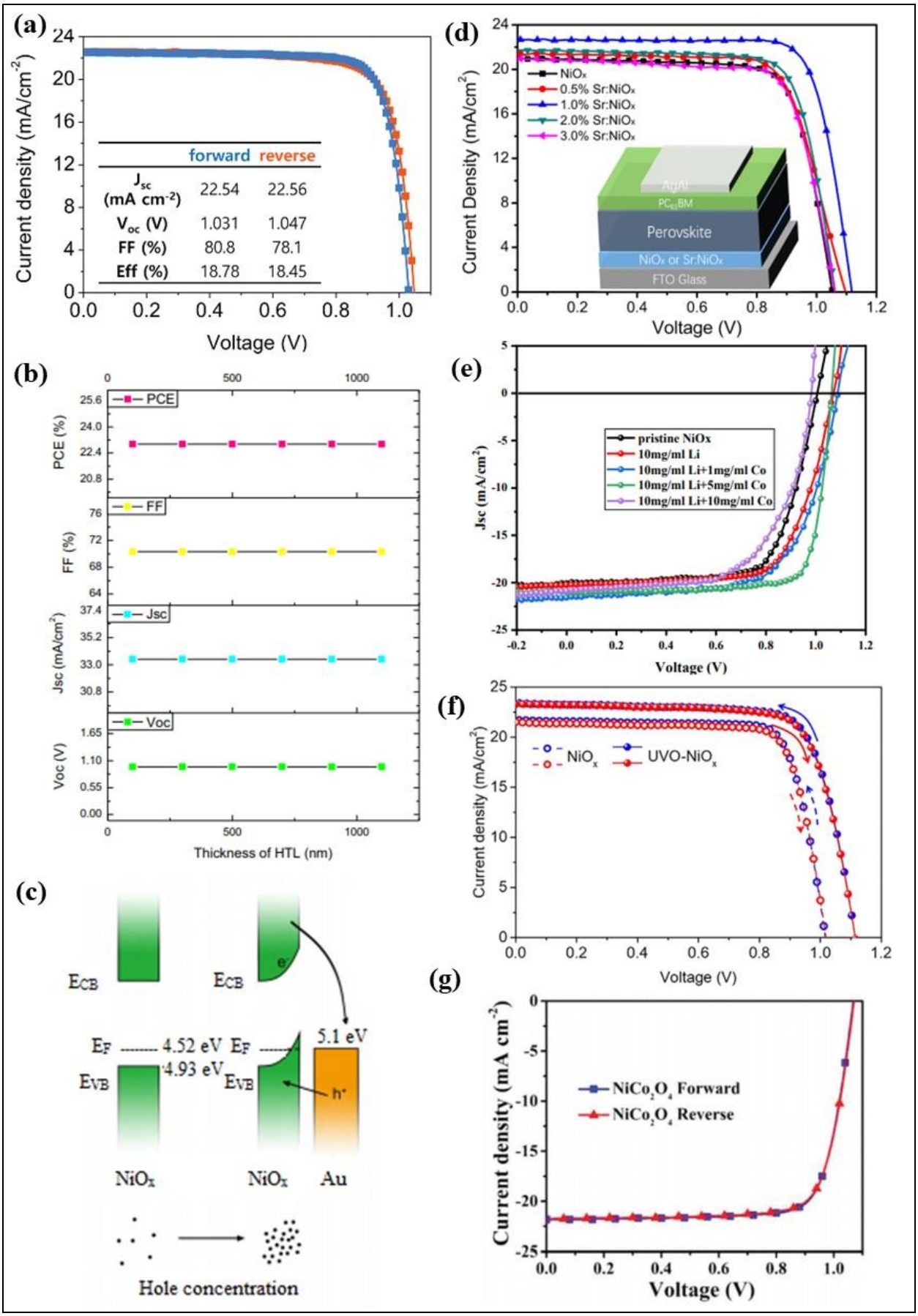
(a)
Current density (mA/cm^{-2})
Voltage (V)
forward reverse
J_{sc} (mA cm^{-2}) 22.54 22.56
V_{oc} (V) 1.031 1.047
FF (%) 80.8 78.1
Eff (%) 18.78 18.45
(b)
PCE (%)
FF (%)
Jsc (mA/cm^2)
Voc (V)
Thickness of HTL (nm)
(c)
E_{CB}
E_F
4.52 eV
4.93 eV
E_{VB}
5.1 eV
NiO_x
Au
Hole concentration
(d)
Current Density (mA/cm^2)
Voltage (V)
NiOx
0.5% Sr:NiOx
1.0% Sr:NiOx
2.0% Sr:NiOx
3.0% Sr:NiOx
Ag/Al
$PC_{61}BM$
Perovskite
NiOx or Sr:NiOx
FTO Glass
(e)
Jsc (mA/cm^2)
Voltage (V)
pristine NiOx
10mg/ml Li
10mg/ml Li+1mg/ml Co
10mg/ml Li+5mg/ml Co
10mg/ml Li+10mg/ml Co
(f)
Current density (mA/cm^2)
Voltage (V)
NiO_x
UVO-NiO_x
(g)
Current density (mA cm^{-2})
Voltage (V)
$NiCo_2O_4$ Forward
$NiCo_2O_4$ Reverse

Fig. 4 (a) J-V curves of NiO based PSC (Reproduced from [71] with permission. Copyright 2018, Wiley), (b) Variation of photovoltaic parameters with HTM thickness (Reproduced from [80] with permission. Copyright 2020, Elsevier) (c) Mechanism of Gold doped NiO_x in the devices (Reproduced from [86] with permission. Copyright 2018, Wiley) (d-g) J-V curves of Sr:NiO_x (Reproduced from [87] with permission. Copyright 2018, Elsevier), Li and Co codoped NiO_x (Reproduced from [91] under Creative Commons Attribution 4.0 License. Copyright 2020, MDPI), UVO treated NiO_x (Reproduced from [96] with permission. Copyright 2019, Wiley) and $NiCo_2O_4$ (Reproduced from [97] with permission. Copyright 2018, Wiley) based PSCs.

4.1.2. Copper derivatives

Gharibzadeh et al. [99] demonstrated the deposition of CuI as a low-cost inorganic HTM using gas–solid phase conversion of Cu to CuI. This technique produced a homogeneous CuI layer with outsized grains and high density, which prevented the contact electrodes from direct connection. CuI-based perovskite solar cells with Au electrodes exhibited an unusually high current density. It resulted from a surprisingly high charge extraction rate in the cells, which is due to the high hole mobility of CuI and various contact points with the perovskite layer. Additionally, this process had no detrimental influence on the perovskite, making it suitable for PSCs. The variation of PCE of fabricated devices with MAI concentration is shown in Fig. 5(a). Sun et al. [100] demonstrated the use of solution processable CuI film as the HTM for inverted PSCs in his work. Consequently, the fabricated device achieved an good PCE of 16.8 %. Additionally, the synthesis of CuI HTM was a straightforward and rapid process requiring no post-treatment that makes it an attractive material for the HTM in inverted PSCs and a possible candidate for flexible tandem photovoltaic cells. Charge transfer and recombination can be further enhanced by monitoring them at the HTM/absorber as well as absorber/ETM interfaces that essentially describe the conduction band offset (CBO) along with valence band offset (VBO). As a result, it is valuable to examine the optimal band offset in order to obtain effective solar cell devices. CuI attained a champion efficiency (PCE=22.69 %) when CBO is set to +0.2 eV and VBO is set to 0 eV. This study suggested that inorganic HTMs based on copper derivative are both effective and stable and can be used to commercialize PSCs [101]. The fabrication of halide PSCs using CuI deposited with ammoniated aqueous solution ink as HTM is described by Khadka et al. [102]. The morphology of the CuI film is found to have an

influence on the growth of the perovskite film and thus on the performance parameters. CuI-treated PSCs demonstrated a PCE of 14.21 % with excellent reproducibility. The capacitance spectrum analysis demonstrates that the perovskite absorber layer induces deep trap states due to the Cu antisites induced in the perovskite layer caused by Cu ions diffusion during device processing. The temperature-dependent V_{oc} results indicate that the perovskite bulk recombination activities are dominant. This study suggests that CuI processed with an aqueous precursor is a viable alternative HTM to PEDOT:PSS for effective and reliable PSCs as well as in tandem devices.

CuO_x HTM was implemented into inverted planar heterojunction PSCs using a simple solution-processed approach [103]. Following device optimization, a champion PCE of 17.1 % was obtained. The ultrathin CuO_x films were deposited using a simple electrochemical deposition process in a mixture of $CuSO_4$ and lactic acid liquids [104]. At pH = 9, CuO_x thin films exhibited superior conduction as well as light transmittance properties. After optimization, the device demonstrated the best PCE of 13.48 %. Fig. 5(b) demonstrates the J-V curves of the devices. Bu et al. [105] described an industrial-scale electrospray deposition method to prepare HTM and active layer in PSCs. The fabricated solar cell using electrosprayed Cu_xO as the HTM outperformed the control PSC constructed with a PEDOT:PSS film. Kumar et al. [106] developed a novel planar perovskite structure using FTO/WS_2/lead-free perovskite/Cu_2O/Au. Owing to the perfect band coordination with perovskites, the cuprous oxide is used as an HTM. Quantitative analysis of the dvice is performed using a solar cell capacitance simulator. The simulations showed that $MASnI_3$ has a high potential for becoming an absorbent layer. The proposed configuration demonstrated an excellent PCE of 23 % when different segment thicknesses were optimized during simulation studies. The impact of neutral defect density as well as defect energy level location relative to the active layer on device performance was quantified. The findings indicate that increasing the total defect density of the interfacial and perovskite layers significantly reduces the values of performance parameters (J_{sc}, FF, V_{oc}, and PCE) of proposed system configurations.

Lee et al. [107] demonstrated a solution-processing approach for the use of spinel $CuCo_2O_4$ as HTM in high-performance PSCs. $CuCo_2O_4$ exhibited a high ability for hole transfer to the perovskite substrate and outstanding optoelectronic properties that were finely tuned by optimizing the annealing temperature, ensuing in planar PSCs with a 14.12 % PCE. Another

notable feature of the $CuCo_2O_4$-based HTM is the device's negligible hysteresis at low scan rates, resulting in extremely stable and consistent photovoltaic efficiency. All of the findings indicate that $CuCo_2O_4$ has a promising future as a novel HTM in PSCs. As a consequence of their small band gap, ease of processing, and favourable energy band position corresponding to the perovskite, delafossite oxides are promising HTM candidates for PSCs. A combination of experimental and computational techniques was employed to explore the properties of $CuCrO_2$ delafossite films [108]. $CuCrO_2$ NPs were first synthesized by hydrothermal approach and then deposited by spin-casting method at RT. Experiments proved that the $CuCrO_2$ films exhibit the required optoelectronic properties for utilization as an HTM, which agrees well with the DFT studies. PSCs fabricated with these films have a PCE of over 14 %, with negligible hysteresis. In comparison to traditional methods for synthesizing $CuCrO_2$ NPs, the recently suggested azeotropic promoted strategy significantly decreases the time of the reaction by 90 % and annealing temperature by one-third, allowing for high throughput output while also lowering power consumption and synthesis costs [109]. Additionally, indium is successfully doped into $CuCrO_2$, a process that is inherently difficult at low temperatures. Doping results in a reduced d–d transition of Cr^{3+}, thus increasing HTM electrical conductivity as well as optical transmittance. Interestingly, these changes to In doped $CuCrO_2$ HTM can be accomplished using a facile ambient-condition approach, allowing PSCs to achieve a PCE of 20.54 %. Fig. 5(c) shows the J-V curves of the devices. Meanwhile, the PSC exhibited a high degree of reproducibility and photostability. As a result, the work contributes to the creation of high-performing PSCs by developing a facile process for realizing pristine as well as doped $CuCrO_2$ based HTM. Behrouznejad et al. [110] demonstrated a doctor blade process for preparing an efficient carbon composite electrode which involves a paste made up of carbon black, graphite flakes, and a hydrophobic polymer. The weight ratios were studied in order to determine how they influenced the sheet resistance as well as the resistivity of the electrode layer. The influence of the composition of the electrode on the charge transport resistance at the interface of perovskite and $CuIn_{0.75}Ga_{0.25}S_2$ HTM was studied by electrochemical impedance spectroscopy (EIS) at various white light intensities and at 530, 660, and 740 nm wavelengths. The champion cell has the best efficiency of 15.9 %. For the first time, Ye et al. [111] showed that a $CuNbO_x$ thin film formed by low-temperature solution processing and comprising of $CuNbO_3$ along with $CuNb_2O_6$ phases could be used as an efficient HTM to fabricate stable PSCs. The $CuNbO_x$-based system achieves

the best efficiency of 16.01 % and negligible hysteresis by optimizing the precursor concentration. The $CuNbO_x$-based device not only outperformed the control device (based on PEDOT:PSS HTM showing PCE of 10%) in terms of photovoltaic efficiency, but it also has much better long-term stability.

The properties of an economical HTM, copper (II) phthalocyanine (CuPc), deposited in PSCs through a solution-process method were investigated by Duong et al. [112]. Over the deposited CuPc thin film, cracks were numerous; resulting in significant shunts and interface recombinations that were found to be substantially reduced by heating treatment at about 85°C. This enhancement was caused by the immigration of Au particles away from the cracks due to heat. Additionally, the heat treatment significantly enhances the doping effect of Au in the CuPc film. After heating treatment, more than 20% PCE was achieved using CuPc. Fig. 5(d) demonstrates the variation of normalized PCE with time for the devices. Flexible PSCs are getting popular owing to their wide variety of possible applications, but finding robust, high conductivity, and energy level appropriate HTMs remains difficult. In this regard, Han et al. [113] incorporated CuPc as HTM in PSCs and showed enhanced efficiency, increased stability, and better reproducibility in comparison to PEDOT:PSS based PSCs. On rigid substrates, PSCs have a champion performance of 15.4 % and on flexible substrates, PCE was 12.8 %. CuPc was used as an HTM in carbon counter electrode based $CsPbBr_3$ inorganic PSCs by Liu et al. [114]. As a reference, HTM-free PSCs were also produced. The CuPc-based device achieved the best efficiency of 6.21 %, which is 63 % higher than the HTM-free device. They conducted systematic characterization and analysis to deduce the underlying mechanism of the improvement caused by the CuPc HTM layer. The findings suggest that putting CuPc inbetween the carbon electrode and perovskite is a simple and effective way to decrease charge recombination and improve charge transfer process in PSCs. More significantly, as compared to HTM-free $CsPbBr_3$ devices and conventional $MAPbI_3$ devices, these devices have excellent durability and promising thermal stability at 100 °C for 1000 hours. CuPC attached with butoxy donor groups (CuPcOBu) was synthesized using a simple two-step synthesis path by Li et al. [115]. 4-tert-butylpyridine (TBP) was used as a dopant in CuPc-OBu for preparing film and then extracted through annealing to produce high-quality HTM film. The PSC using CuPc-OBu as the HTM demonstrated significantly improved efficiency (PCE=19.0%). This research proposes a novel strategy for improving film quality and increasing reliability while keeping costs down.

Yang et al. [116] described a novel CuPc HTM substituted with octamethyl groups ($CuMe_2Pc$). Unlike pristine CuPc, when $CuMe_2Pc$ was deposited through vacuum thermal evaporation, it could enhance the molecular alignment, therefore leading to better hole mobility, extremely compact thin film, and better hydrophobic surface. These characteristics make PSCs more suitable for hole transport applications. Thus, when compared to CuPc, PSCs with $CuMe_2Pc$ had a 25 % higher PCE (PCE= 15.73 %).

Effective surface ligand engineering in semiconductor nanocrystals can enhance the electronic interaction inbetween them, and this feature makes them attractive for inexpensive optoelectronic applications. The utilization of pure Cu_2ZnSnS_4 (CZTS) nanocrystals as the photoactive layer as well as HTM in solar cells was described by Khanzada et al. [117]. Pure CZTS nanocrystals were synthesized through engineering their surface ligands at low-temperature, which were originally encapsulated with the long-chain organic ligand oleylamine. By removal of ligand, CZTS nanocrystals exhibited a significant increase in photoconductivity and mobility, as well as a detectable photoresponse in the fabricated device. CZTS nanocrystals achieved remarkably superior hole transport properties when utilized as an interfacial layer in solar cells, with a PCE of 15.4 % and an outstanding FF of 81%. These results emphasize the critical nature of eliminating unwanted surface ligands and highlight the enormous prospective of CZTS for the fabrication of economical and effective optoelectronic devices. It is highly desirable to incorporate a solution-processable HTM into the low-temperature paintable carbon electrode-based PSCs to further improve their PCE. Simultaneously, this low-cost approach enables roll-to-roll mass production. Cao et al. [118] have demonstrated that CZTS NPs can be used as an HTM in low-temperature paintable carbon electrode-based PSCs. Under optimal conditions, PSCs with a CZTS HTM have an average PCE of 12.53 %, which is 50 % higher than that of PSCs without a CZTS HTM. Simultaneously, PSCs containing CZTS HTM exhibit negligible hysteresis and excellent long-term stability. Nan et al. [119] utilized a novel hole transport composite composed of reduced graphene oxide (RGO) and $Cu_2ZnSn(SSe)_4$ ($CZTS_xSe_{1-x}$) for efficient PSCs through a green sol-gel process. Raman and X-ray based measurements were used to characterize the composition and crystalline structure of $CZTS_xSe_{1-x}$. In comparison to pure RGO HTM, the PSC with RGO/$CZTS_xSe_{1-x}$ composite exhibits superior photovoltaic efficiency and stability. The cell with RGO/$CZTS_{0.5}Se_{0.5}$ composite HTM achieved a maximum PCE of 10.08 % and improved stability. Additionally, the different S/Se ratios of

$CZTS_xSe_{1-x}$ resulted in distinct photovoltaic properties for the PSCs, which is due to a change in energetic structures, which was verified by electrochemical characterizations. Wu et al. [120] used a novel $Cu_2CdZn_{1-x}SnS_4$ (CZTS:Cd) film deposited through thermal evaporation in PSC. Simultaneously, Au nanorods were incorporated in HTM to increase the conversion efficiency of CZTS:Cd. The photoelectric response was found to be extended to 900 nm. Additionally, the suitably matched energy levels of the HTM and active layer allow successful hole extraction from the latter and a reduction in carrier recombination. Consequently, the recording device incorporating both CZTS:Cd and Au simultaneously exhibits a significantly improved PCE (upto 21.11 %). Fig. 5(e) shows the variation of PCE with a doping concentration of Cd. Moreover, the PSC devices exhibit significantly improved long-term reliability. The study indicates that using a perovskite/inorganic-incorporated structure to extend and improve the NIR response of PSCs, is a promising strategy.

Madhavan et al. [121] described stable PSCs with three-dimensional/2-dimensional structured perovskite and copper(I) thiocyanate (CuSCN) HTM were employed. (Phenylethyl)ammonium (PEA) and [(4-fluorophenyl)ethyl]ammonium (FPEA) were chosen as two-dimensional cations, resulting in thin layers of $(PEA)_2PbI_4$ or $(FPEA)_2PbI_4$ over three-dimensional perovskite. The 2D perovskite neutralizes defects on the 3D perovskite absorber surface and protects it from humidity-induced degradation. The fabricated devices using CuSCN HTM demonstrated substantially improved efficiency exceeding 18% and ambient stability. Fig. 5(f) demonstrates the J-V curves of the fabricated devices. Er et al. [122] investigated the application of HTM CuSCN in PSCs where diethylsulfide was used to prepare the precursor solution so as to deposit the HTM without damaging the perovskite. A range of characterization techniques were used to characterize the topography, elemental composition, and electrical properties of spin coated CuSCN layers. Under full sun illumination, a PCE reaching 11.02 % with a V_{oc} of 0.83 V was achieved in the PSCs. The use of a low-temperature solution process as well as a rapid solvent removal strategy resulted in the formation of CuSCN layers that assist in carrier extraction. CuSCN is widely regarded as a very promising inorganic HTM in semitransparent PSCs (ST-PSCs). CuSCN's low electrical conductivity and low work function, on the other hand, result in inadequate hole extraction and significant V_{oc} loss. 2,3,5,6-tetrafluoro-7,7,8,8-tetracyanoquinodimethane (F4TCNQ) was used by Hou et al. [123] for increasing the conductivity of CuSCN and to align the bands at the perovskite and HTM interface. By using the

better-quality transparency of CuSCN, the fabricated bifacial ST-PSCs exhibited the best PCE of 14.8 %. In comparison to spiro-OMeTAD, CuSCN shows better energy level matching with the perovskite resulting in a lower charge injection barrier that facilitates more effective hole extraction, prevented carrier recombination, and decreased ionic capacitance [124]. Wijeyasinghe et al. [125] described the synthesis of CuSCN HTM from a novel solvent, aqueous ammonia by a spin-casting method. The reduced surface roughness of the resultant CuSCN layer aids in the planarization of ITO in solar cells. PSCs derived from aqueous-processed CuSCN HTMs exhibited a maximum PCE of 17.5 %. Notably, cells based on CuSCN that have been aqueously processed consistently outperform devices based on PEDOT:PSS HTMs.

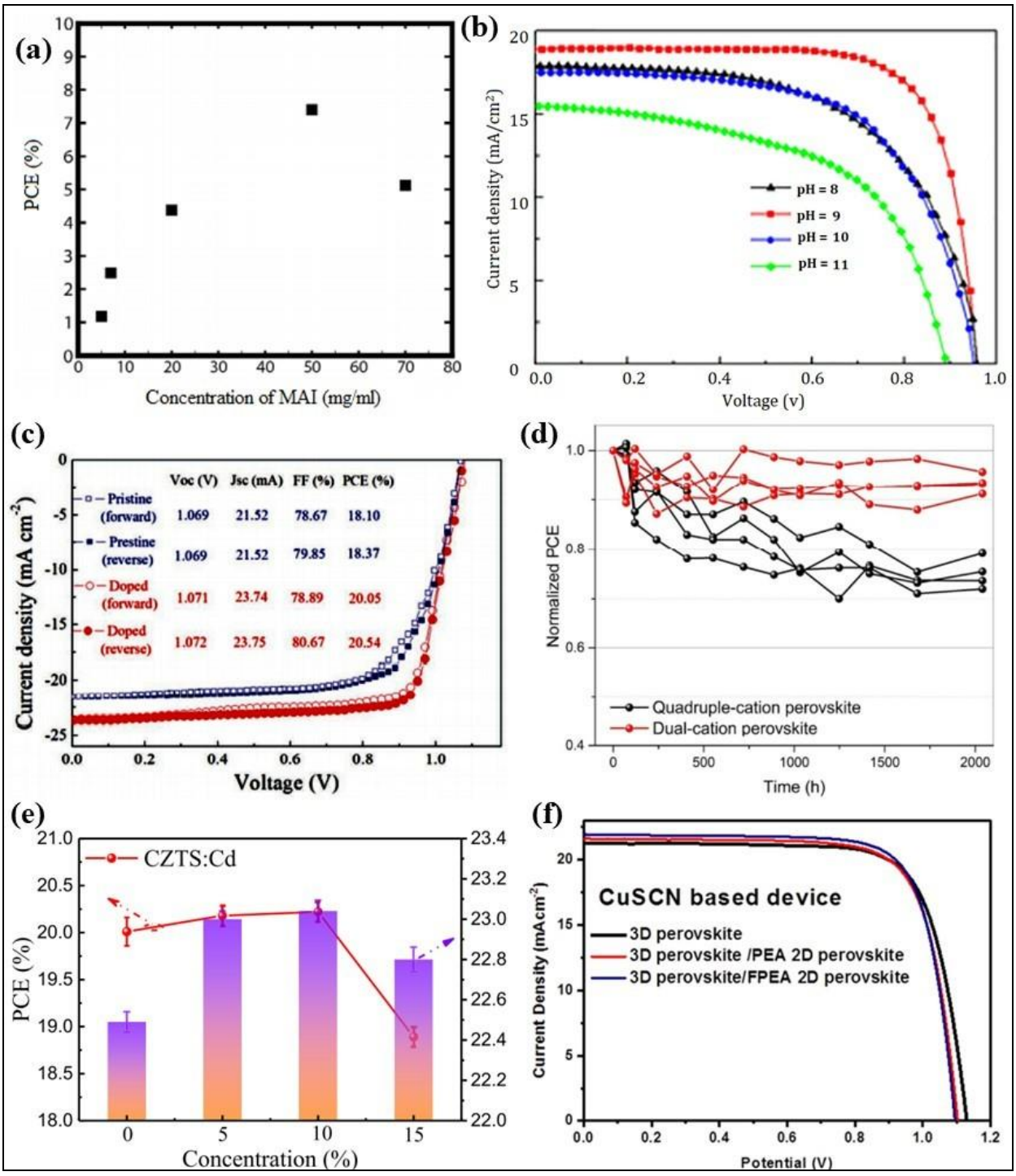

Fig. 5 (a) Variation of PCE of CuI based PSC with MAI concentration (Reproduced from [99] with permission. Copyright 2016, Wiley) (b,c) J-V curves of CuO_x (Reproduced from [104] with permission. Copyright 2019, Elsevier) and $CuCrO_2$ based PSCs (Reproduced from [109] with permission. Copyright 2019, Wiley) (d) Normalized PCE of CuPc based PSC (Reproduced from

[112] with permission. Copyright 2018, American Chemical Society) (e) Variation of PCE with a doping concentration of Cd in CZTS:Cd based PSC (Reproduced from [120] with permission. Copyright 2020, American Chemical Society) (f) J-V curves of CuSCN based PSC (Reproduced from [121] with permission. Copyright 2019, American Chemical Society)

4.1.3. Transition metal oxides (TMOs)

Chu et al. [126] described the utilization of an ultrathin VO_x film, deposited at 50 °C through atomic layer deposition (ALD), as an HTM for PSCs. With a 1 nm VO_x layer, highly proficient PSCs exhibiting a PCE of 11.53 % were attained. UV post-treatment greatly improves the hole transporting capacity of VO_x as compared to pristine ALD VO_x films. For a deep understanding of the hole transport mechanism in VO_x films, photoelectron spectroscopy was used to examine ALD-VO_x films grown on FTO. These findings confirmed that VO_x films with defect states below the Fermi level promote hole extraction and that UV-treated VO_x films have a higher V^{5+} oxidation state ratio. This work demonstrated the potential for versatile and large-area PSCs to be applied by means of VO_x films as the HTMs. While significant progress has been made in PCE for organic-inorganic hybrid PSCs in recent years, the stability of the PSC remains a barrier to commercialization due to the scarcity of effective and stable HTMs. Guo et al. [127] demonstrated a low-temperature processed VO_x HTM for planar heterojunction PSCs. SEM and XRD were used to investigate the morphology and crystallinity of $MAPbI_3$ grown on amorphous VO_x thin film. Since VO_x and $MAPbI_3$ have a suitable energy level match, the holes created in $MAPbI_3$ can efficiently transfer to VO_x HTM. Additionally, the VO_x HTM-based devices revealed a higher PCE of 14.5 % and more excellent stability than the PEDOT: PSS HTM-based PSCs. Ali et al. [128] conducted an analytical simulation to investigate MoO_x as a possible choice for HTM in PSCs. The films were highly transparent and had a smooth surface. MoO_x showed maximum efficiency of 18.25 % in inverted and conventional structures of the PSC, as demonstrated by device simulation. Fig. 6 (a,b) illustrates the variation of photovoltaic parameters with MoO_x thickness in normal and inverted MoO_x based PSCs. Xie et al. [129] confirmed that RGO doping is an easy and efficient method for converting MoO_x into a promising HTM for high-performance PSCs. Conductive MoO_x: RGO HTM can aid in perovskite crystallization and minimize V_{oc} leakage in devices. Thus, a PCE of up to 18.15 % was reached while maintaining a V_{oc} of 1.12 V. More importantly, it establishes the significance

of doping in inorganic buffer interlayers for PSC study. For achieving stable and efficient solar cells, MoO_x can also be modified with F4-TCNQ resulting in 16.26% PCE as shown in Fig. 6 (c,d) [130]. For the first time, an inexpensive and reliable PSC was fabricated via solution-processing technique by employing nanostructured Fe_3O_4 as a promising HTM [131]. The Hall measurements on Fe_3O_4 film indicated the presence of hole carriers with higher mobility. As a result, the Fe_3O_4-based devices exhibited the best 15.42 % PCE indicating that Fe_3O_4 is a potential HTM candidate to fabricate PSCs as a solid and low-cost substitute for the more costly complex materials. Fig. 6(e) demonstrates the J-V curves of the fabricated devices. Zhang et al. [132] investigated p-type conductive oxides based on spinel Co_3O_4 as HTMs in organic and mixed cation PSCs. The structural, electrical, surface chemistry, crystalline, optical and photo-electrochemical properties of spin-coated Co_3O_4 films were explored both with and without lithium dopant. It was observed that lithium doping increases hole mobility as well as optical clarity of the film and results in the formation of a $LiCoO_2$ layer over the Co_3O_4 surface. Consequently, lithium doping enhances the hole transporting properties of Co_3O_4 resulting in a PCE of approximately 14 % and 7 % for the inorganic and mixed cation perovskite halides, respectively. The J-V curves of the fabricated devices are shown in Fig. 6(f). This study demonstrates the potential for cobaltite spinels to be used as working HTMs for a variety of organometallic halide perovskites.

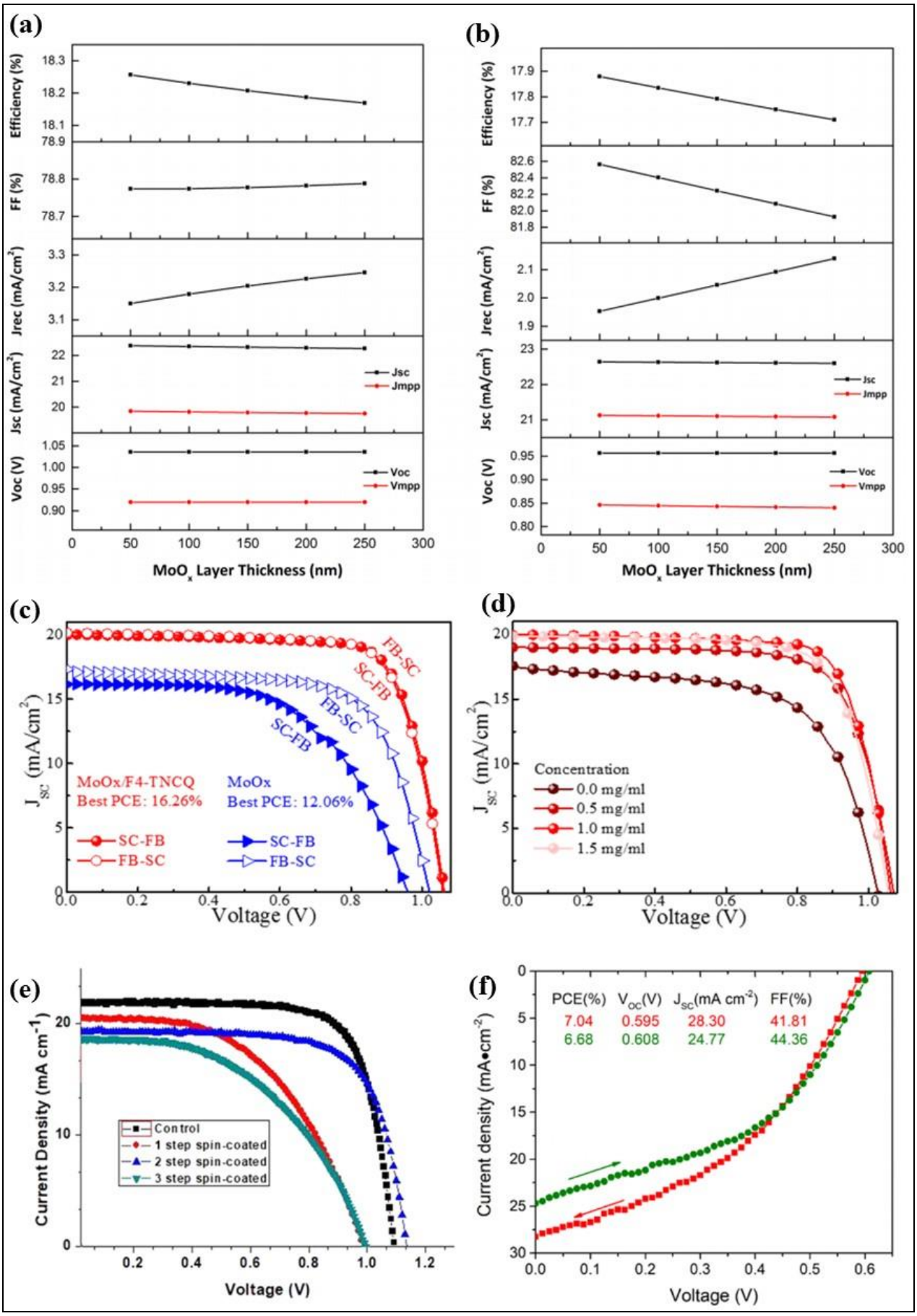
(a)
Efficiency (%)
FF (%)
Jrec (mA/cm²)
Jsc (mA/cm²)
Jsc
Jmpp
Voc (V)
Voc
Vmpp
MoOx Layer Thickness (nm)
(b)
Efficiency (%)
FF (%)
Jrec (mA/cm²)
Jsc (mA/cm²)
Jsc
Jmpp
Voc (V)
Voc
Vmpp
MoOx Layer Thickness (nm)
(c)
FB-SC
SC-FB
FB-SC
SC-FB
MoOx/F4-TNCQ
Best PCE: 16.26%
MoOx
Best PCE: 12.06%
SC-FB
FB-SC
SC-FB
FB-SC
Jsc (mA/cm²)
Voltage (V)
(d)
Concentration
0.0 mg/ml
0.5 mg/ml
1.0 mg/ml
1.5 mg/ml
Jsc (mA/cm²)
Voltage (V)
(e)
Control
1 step spin-coated
2 step spin-coated
3 step spin-coated
Current Density (mA cm⁻¹)
Voltage (V)
(f)
PCE(%) Voc(V) Jsc(mA cm⁻²) FF(%)
7.04 0.595 28.30 41.81
6.68 0.608 24.77 44.36
Current density (mA•cm⁻²)
Voltage (V)

Fig. 6 (a,b) Variation of photovoltaic parameters with MoO_x thickness in regular and inverted MoO_x based PSCs (Reproduced from [128] with permission. Copyright 2017, American Institute of Physics) (c,d) J-V curves of MoO_x/F4-TCNQ (Reproduced from [130] with permission. Copyright 2019, American Chemical Society) (e,f) J-V curves of Fe_3O_4 (Reproduced from [131] with permission. Copyright 2020, American Chemical Society), Li-doped Co_3O_4 based PSCs (Reproduced from [132] with permission. Copyright 2020, American Chemical Society)

4.1.4. Other Inorganic HTMs

Dasgupta et al. [133] have applied the centrifugally casted film preparation approach to single- and few-layered MoS_2 in order to obtain homogeneous and compact thin films. A liquid-based exfoliation procedure was used to obtain the 2H phase of the 2D TMD. MoS_2 thin films that were centrifugally casted were extensively characterised. It was discovered that the hybrid perovskite forms a band configuration of type–II. The TMD layer effectively quenches the perovskite's PL emission, demonstrating a proficient hole transfer process. Thus, the devices fabricated with UVO treatment attained a PCE of 6 % (Fig. 7(a)). The solar cells were further optimized through the variation of different thichnesses of MoS_2. Huang et al. [134] utilized 2D MoS_2 and WS_2 as alternative HTMs in PSCs. They discovered that the 1T phase content in these 2D HTMs is a critical parameter and 1T-rich TMDs (as obtained through exfoliation and without any post-heating) result in significantly improved PCE. More specifically, by substituting 2D TMDs for PEDOT:PSS, the PCE and the stability of PSCs increased appreciably. Fig. 7(b) demonstrates the J-V curves of the fabricated devices. The highest PCE values of 15.00 % and 14.35 % were achieved in PSCs containing WS2 and MoS2, respectively, while the highest PCE value for PSCs containing PEDOT:PSS was only 12.44 %. These are the highest PCEs achieved to date when 2D TMDs are used as HTMs. This work suggested that water-soluble 2D TMDs have significant prospective for use as novel HTMs aimed at producing superior performances and long-lasting PSCs. Shin et al. [135] revealed the utilization of MoS_2 as an HTM in efficient and flexible bifunctional devices with graphene-codoped transparent conducting electrodes. These bifunctional devices can work both as a photodiode and solar cells. Even at 0 V, illumination (1 Sun) increases the current of cells by up to 10^6 times, indicating that it is self-powered. The devices demonstrated a high on/off ratio (maximum 136110 at λ = 700 nm) and high responsivity (maximum 410 mAW^{-1} at λ = 700 nm) in the ultraviolet to the visible light range

when used in photodiode mode and excellent photovoltaic performance when used in solar cell mode (PCE=13.09%). Fig. 7(c,d) illustrates the energy band diagram and J-V curves of photodiode-solar cell bifunctional devices based on MoS_2. These findings indicated that MoS_2 can be lucratively employed as an HTM in rigid as well as flexible optoelectronic devices based on perovskites. Concerns about the environment as well as the high cost of the precursors are the primary impediments to realistic implementation of PSCs. Via vacuum vapor deposition, a new, eco-friendly, and inexpensive MnS film was prepared by Li et al. [136] and used for the first time as an effective inorganic HTM in PSC. Without further interface optimization, a champion 19.86 % PCE was obtained with the device containing inorganic HTM MnS because of its high hole mobility, better optical transparency as well as appropriate band alignment. These findings demonstrated its enormous potential for developing environmentally benign, cost-effective, and reliable photovoltaic devices.

Carbon-based all-inorganic PSCs are gaining considerable interest in the photovoltaic sector due to their economic nature, ease of manufacture, and high thermal stability. The broad energy band-gap between carbon electrodes and $CsPbX_3$, on the other hand, results in reduced hole extraction along with unfavorable charge recombination, lowering the overall performance. In this regard, Zhang et al. [137] prepared tin phthalocyanine (SnPc) film without any dopant to be utilized as an HTM in carbon-based $CsPbI_2Br$ solar cell devices. The fabricated PSCs achieved the best performance of PCE 11.39 % with negligible hysteresis when operated optimally, and it was significantly better than 9.22 % PCE achieved by the control PSC without SnPc HTM (Fig. 7(e)). This result demonstrated that solution-processed SnPc as dopant-free HTM could substantially enhance charge transport and inhibit charge recombination at perovskite and carbon interface. This study described a method for fabricating effective as well as stable carbon-based all-inorganic solar cells at low temperatures and through solution processing. Due to the outstanding electrical and optical properties of carbon-based nanostructures, for instance, graphene, carbon nanotubes, and graphene oxide, they can be used in photovoltaics. A buffer layer composed of single-walled carbon nanotubes (SWNT) and graphene oxide significantly enhances the photovoltaic efficiency of lead halide PSCs. The buffer layer of carbon nanotubes and graphene oxide acts as an effective HTM. As a result of their complementary properties, a PCE of 13.3% was accomplished in the lead halide PSCs [138]. Wang et al. [139] reported a straightforward and common approach for preparing non-corrosive HTM via the treatment of

GO with ammonia or ammonium (i.e., $(NH_4)_2HPO_4$). The fabricated ammonia-treated solar cell achieved enhanced PCE exceeding 14 %, significantly outperforming those based on pristine GO (PCE=12 %). Fig. 7(f) demonstrates the J-V curves of the fabricated devices. The mechanism underlying this improvement was thoroughly investigated, establishing the critical role of ammonia treatment in enhancing efficiency. Significantly, the PSCs based on ammonia-treated HTM were substantially stable than those based on pristine GO.

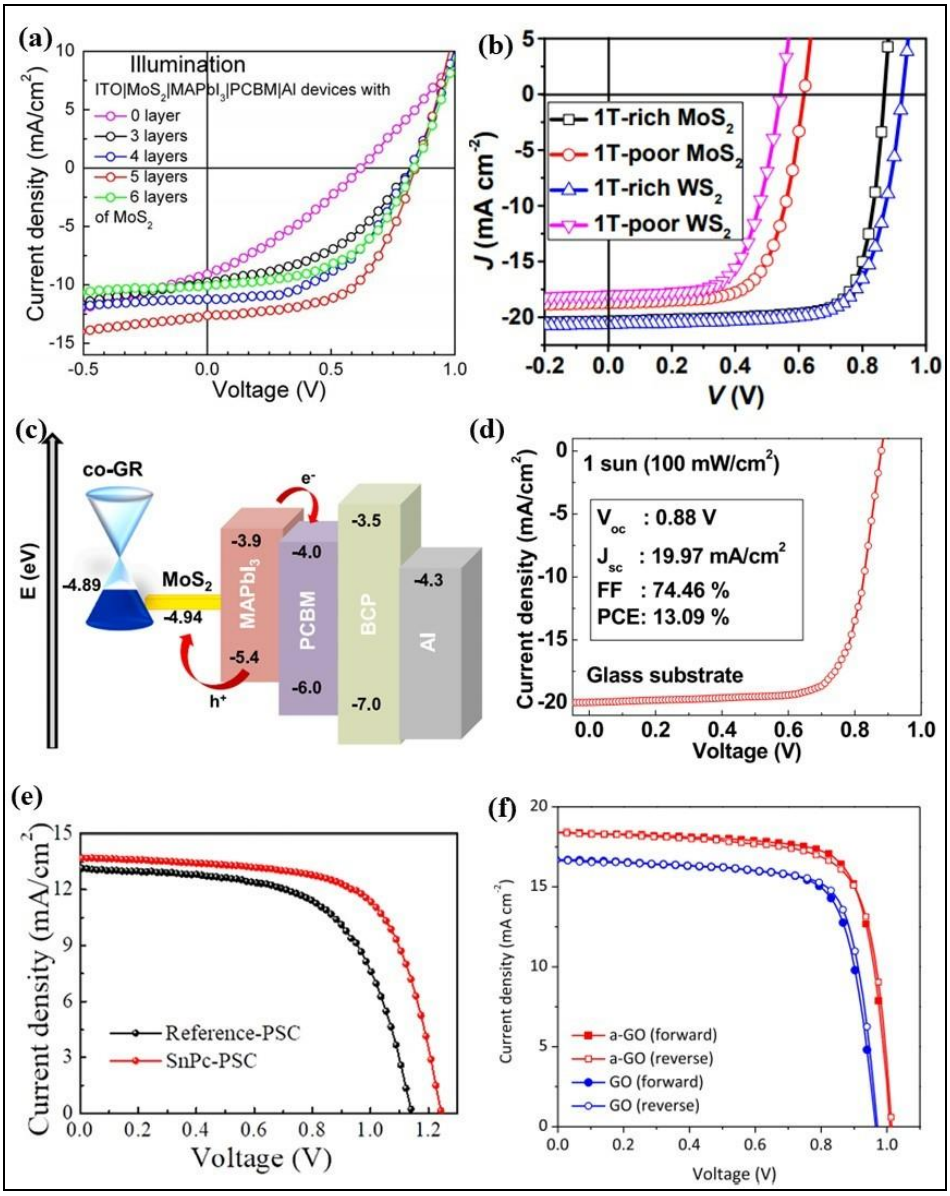

Fig. 7 (a,b) J-V curves of MoS_2 (Reproduced from [133] with permission. Copyright 2017, Elsevier), MoS_2 and WS_2 based PSCs (Reproduced from [134] with permission. Copyright 2017,

American Chemical Society) (c,d) Energy band diagram and J-V curves of photodiodide-solar cell bifunctional devices based on MoS_2 (Reproduced from [135] with permission. Copyright 2020, Elsevier), (e,f) J-V curves of SnPC (Reproduced from [137] with permission. Copyright 2020, American Chemical Society), GO and a-GO based PSCs (Reproduced from [139] with permission. Copyright 2019, Elsevier)

4.1.5. Organic-Inorganic composite HTM

Zhao et al. [140] utilized sol-gel method to dope F4-TCNQ in NiO_x HTM so as to change the band gap and optimize the efficiency of the device. Consequently, the recombination resistance (18804 Ω) is increased when evaluated against the reference device (5349 Ω). And the optimized device with a doped transport layer had a conversion efficiency of 15.7 %, demonstrating superior performance than the device with pristine NiO_x (PCE=13.5%). Hole mobility and charge separation are improved as a result of the perovskite/HTM interface. Ferrocenedicarboxylic acid (FDA) was initially implemented by Zhang et al. [141] to alter p-type NiO_x HTM in PSCs, thereby improving perovskite layer crystallization, hole transporting capabilities, as well as carrier recombination. The devices fabricated with an FDA-tailored NiO_x layer has PCE of 18.20 %. The improved photovoltaic behavior of PSCs was due to the increased crystallization of the thin film perovskite, the passivation impact of FDA, the good interface contact between NiO_x and perovskite, and the increased hole conductivity of FDA-modified NiO_x. According to Lee et al. [142], the PCE of the photovoltaic system was significantly increased from 18.04 % to 20.22 %, following the addition of the organic HTM. Perovskite photovoltaic devices with a p-i-n configuration were fabricated with pristine inorganic NiO HTM as well as a bicomponent HTM (organic-inorganic composite). A small organic molecule with a donor-acceptor-donor (DAD) structure was introduced for preparing bicomponent HTM. The newly designed DAD organic HTM (4′,4‴-(1,3,4-oxadiazole-2,5-diyl)bis(N,N-bis(4-methoxyphenyl)-[1,1′-biphenyl]-4-amine)) has been demonstrated to be a proficient HTM in the absence of a dopant. Methoxy functional units added to the molecules were shown to be helpful in passivating the perovskite defects. Fig. 8(a) shows the J-V curves of composite NiO_x/organic DAD-based PSCs. Additionally, the reduced defect sites and UV-blocking feature of the HTM in p-i-n configuration benefit the stability of the photovoltaic devices. NiO_x/Spiro HTM was developed and applied by Li et al. [143] via integrating the benefits of these two films. The findings indicate that the PSC based on a NiO_x/Spiro HTM has better hole extraction as well as

appropriate energy alignment with the perovskite, resulting in an increase in PCE from 19.8% (of pure spiro based PSC) to 21.66 %. Fig. 8(b) illustrates the comparison of photovoltaic parameters in NiO_x/spiro-OMeTAD and spiro-OMeTAD based PSCs. Wu et al. [144] reported a simple approach for reducing the J-V hysteresis by employing NiO_x/PEDOT:PSS double HTM (DHTM) fabricated p-i-n PSCs. The NiO_x/PEDOT:PSS DHTM-based unit exhibited reduced hysteresis. According to first-principles calculations, Ni of NiO_x forms hydrogen bonds with S and O of PEDOT:PSS, while O of NiO_x forms hydrogen bonds with PSS. As shown by dark current-voltage plots, this pairing creates an interfacial dipole moment heading in the direction of PEDOT: PSS plate. EIS indicates that these dipoles promote charge extraction in a kinetically favorable manner and facilitates the suppression of hysteresis.

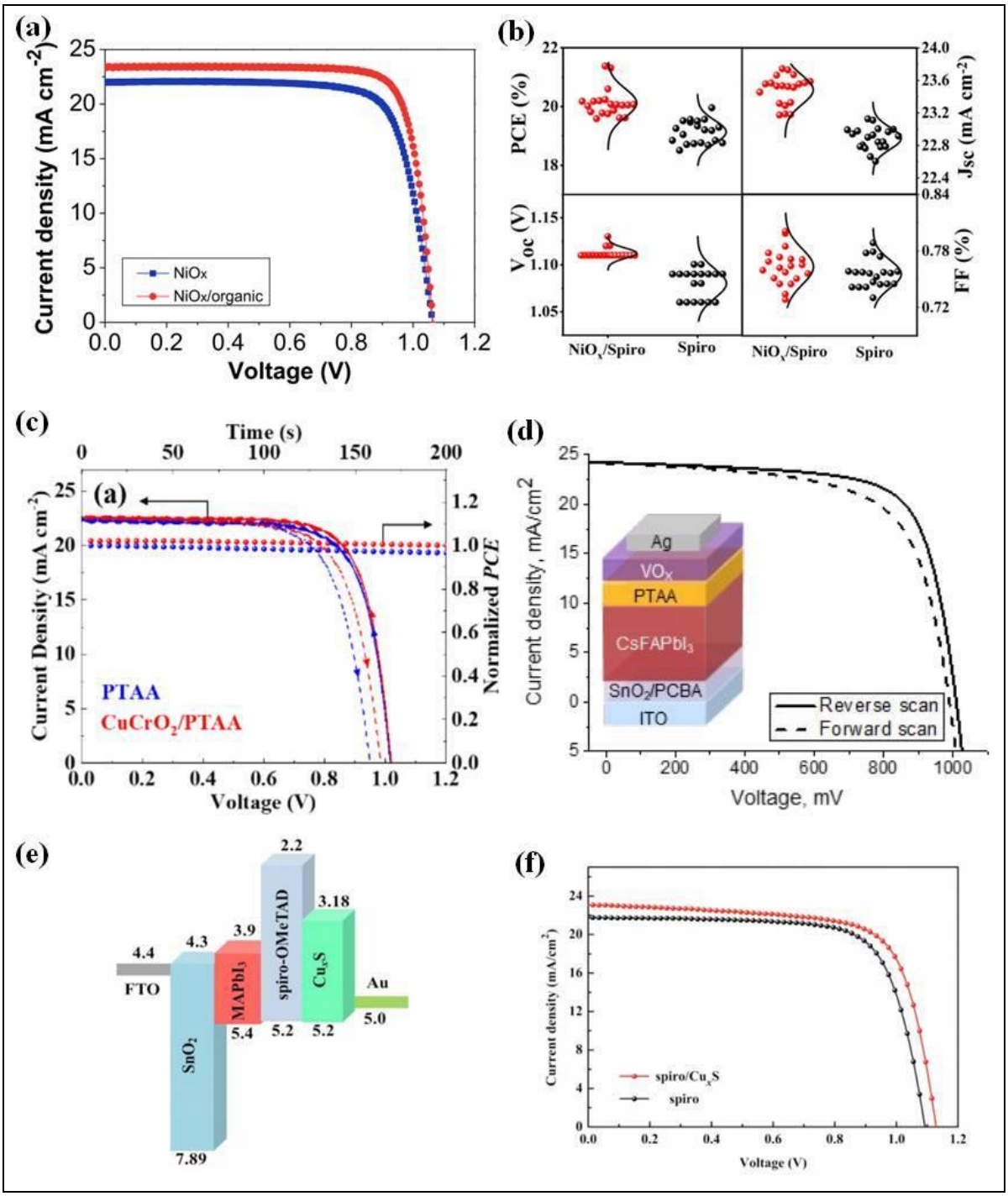

Fig. 8 (a) J-V curves of composite NiO_x/organic DAD based PSCs (Reproduced from [142] with permission. Copyright 2020, American Chemical Society) (b) Comparison of photovoltaic parameters in NiO_x/spiro-OMeTAD based PSCs (Reproduced from [143] with permission. Copyright **2019,** American Chemical Society) (c,d) J-V curves of $CuCrO_2$/PTAA (Reproduced from [150] under Creative Commons Attribution 4.0 License. Copyright 2020, MDPI),

VO_x/PTAA based PSCs (Reproduced from [151] with permission. Copyright 2020, American Chemical Society) (e,f) Energy band diagram and J-V curves of spiro-OMeTAD/Cu_xS composite based PSCs (Reproduced from [152] with permission. Copyright 2017, Wiley)

Wang et al. [145] described a novel interface engineered HTM that incorporates PEDOT:PSS and V_2O_5 bilayer (PVO) for good charge transportation in devices. The systems incorporating bilayer PVO as the HTM have 20 % higher efficiency (PCE=15 %) than traditional PEDOT:PSS devices (PCE=12.52 %). Electrochemical impedance spectroscopy revealed that the devices with PVO bilayer HTM possessed better electronic properties. The bilayer-based devices exhibit a recombination resistance (R_{Rec}) that is 57 % greater than that of reference cells. Along with their high charge selectivity, the novel bilayer-based devices have small interfacial capacitance due to electrode polarization and negligible hysteresis. Additionally, the mechanism underlying better charge transportation in PVO HTM was also evaluated in this study. Two-dimensional (2D) TMDs have attracted considerable research attention in recent years as a result of their superior optoelectronic properties and potential applications in photovoltaics. In this regard, Wang et al. [146] incorporated 2D MoS_2 nanoflakes in PEDOT:PSS to form a hybrid HTM layer. Simultaneously, the modified systems demonstrated major improvements in efficiency and stability. In comparison to the reference PSC, the MoS_2 integrated devices showed increased PCE by approximately 18.5 %. MoS_2 enhanced the charge extraction efficiency across the HTM layer, thereby reducing recombination at the interfaces. This resulted in substantially reduced electrode polarisation and hysteresis as well as improved recombination resistance. Yi et al. [147] confirmed that a PSC containing WO_3 NPs and water-free PEDOT:PSS composite HTM improved the PCE of PSCs. The PSC that used WO_3/PEDOT:PSS as an HTM demonstrated increased device stability and enhanced PCE by approximately 20 %. WO_3 NPs are capable of filling the pinholes in a porous PEDOT:PSS layer, resulting in a homogeneous and uniform HTM surface. The composite layer established significantly increased hole mobility and charge conductivity than the pure PEDOT:PSS. Additionally, the interface between the perovskite and the composite HTM had a lower defect density. Consequently, PCE of 15.1 % was attained due to concurrent enhancement in J_{sc}, V_{oc}, and FF. The $(FASnI_3)_{0.6}(MAPbI_3)_{0.4}$ PSCs with an inverted structure were successfully fabricated by Song et al. [148] using a CuI/PEDOT:PSS

bilayer structure as HTM. CuI/PEDOT:PSS films exhibit a smooth morphology with good interfacial interaction, and the CuI will partially affect the crystallization behaviour of $(FASnI_3)_{0.6}(MAPbI_3)_{0.4}$, which facilitated the growth of high quality perovskite films. Simultaneously, the device's cascading energy alignment and CuI's high hole mobility allowed efficient hole extraction and transport from perovskite to anode. Additionally, as shown by the EIS results, the photovoltaic performance is significantly dependent on the concentration of CuI that defines its thickness. As a result of employing a double-layer CuI/PEDOT:PSS as HTM with a CuI concentration of 10 mg/ml, the fabricated PSCs based on 60% Sn perovskite exhibit an enhanced champion PCE of 15.75 % with negligible J-V hysteresis. Notably, the double HTM of CuI/PEDOT:PSS confers increased stability on the PSCs, which is a crucial trait for their advancement. PSCs with an inverted p-i-n configuration exhibit tremendous potential for use in wearable and versatile devices. The widely employed PEDOT:PSS HTM however requires optimization so as to achieve high efficiency. It was shown that a PEDOT:PSS/Graphene quantum dots (GQDs) composite HTM can be used in place of PEDOT:PSS. The optimized PEDOT:PSS/GQDs based PSC demonstrated a champion PCE of 16.15 % while PEDOT:PSS based device showed less PCE of 12.77% [149].

To boost device efficiency and long-term stability, high-mobility inorganic $CuCrO_2$ NPs were combined with traditional poly(triarylamine) (PTAA) as an HTM for PSCs [150]. Despite the ease with which $CuCrO_2$ NPs can be synthesized through a hydrothermal method, difficulty occurs in preparing a uniform HTM using pristine $CuCrO_2$ because of NP aggregation. $CuCrO_2$ NPs and PTAA were deposited consecutively on perovskite using spin-coating technique, resulting in a uniform HTM with excellent coverage. $CuCrO_2$/PTAA bilayer HTM exhibits superior carrier extraction and transport due to the high mobility of $CuCrO_2$ NPs. Trap-filled limited voltage and capacitance tests often reveal a decrease in trap density. The best performing device produced 17.4 % PCE, while the bare PTAA produced 16.9 % efficiency, and the results are shown in Fig. 8(c). Recent research has demonstrated that charge transporting interlayers with low gas permeability could extend the operating life span of PSCs by acting as a barricade to the immigration of unstable decomposed products from the perovskite active layer. In this regard, a hybrid HTM composed of p-type PTAA and VO_x is a good choicefor PSCs for long-term stability, taking them closer to commercial applications [151]. The J-V curves of the fabricated VO_x/PTAA based PSCs are shown in Fig. 8(d). Lei et al. [152] demonstrated a stable

Cu_xS (x = 1.75) for effective utilization as HTM in planar conventional PSCs. Cu_xS HTM has two primary functions: 1) improving hole transport by forming a physical hydrophobic buffer layer because of its high inherent mobility and proper energy level alignment, leading to improved charge transfer process and reduced recombination; and 2) shielding the spiro layer from damage caused by dampness and Au anode. This straightforward approach results in PSCs with an improved PCE of 18.58 %. The energy band diagram and J-V curves of spiro-OMeTAD/Cu_xS composite-based PSCs are demonstrated in Fig. 8(e,f). This work demonstrated that Cu_xS is a viable HTM for fabricating low-cost, effective, and stable photovoltaic solar cells.

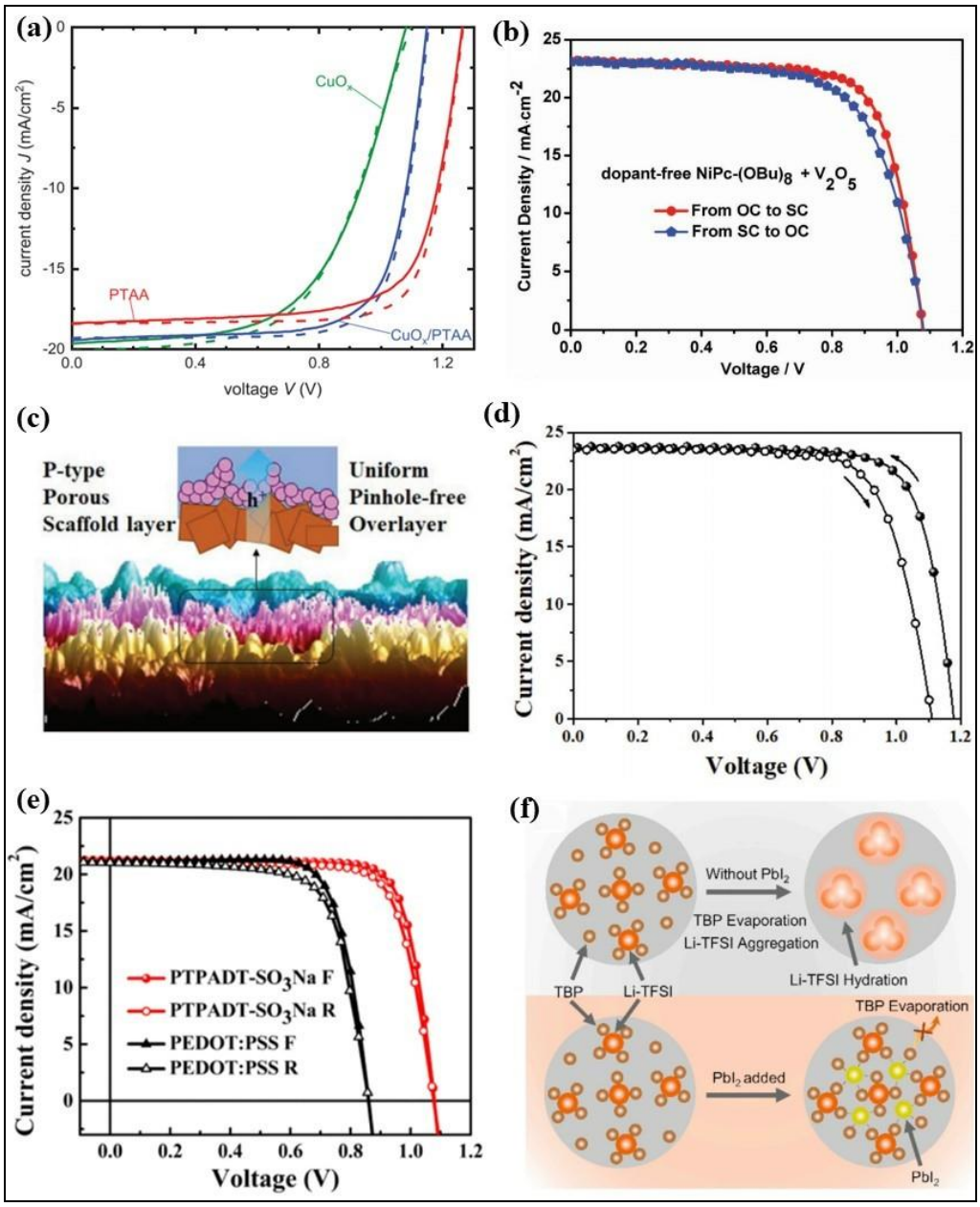

Fig. 9 (a,b) J-V curves of CuO_x/PTAA (Reproduced from [153] under Creative Commons Attribution 4.0 License. Copyright 2020, Wiley), NiPc-$(OBu)_8$/V_2O_5 composite based PSCs (Reproduced from [155] with permission. Copyright 2017, Wiley), (c,d) Representation of probable effects and J-V curves of WO_3/spiro-OMeTAD bilayer based PSC (Reproduced from [156] with permission. Copyright 2018, Wiley) (e) J-V curves of PTPADT-SO_3Na based PSCs (Reproduced from [157] with permission. Copyright 2020, American Chemical Society) (f) Representation of PbI_2 addition in spiro-OMeTAD based PSC (Reproduced from [158] with permission. Copyright 2020, Elsevier)

Haddad et al. [153] examined $MAPbI_3$ PSCs using a variety of different HTMs, including an inorganic HTM, CuO_x (PCE=11.9 %), and a bilayer of CuO_x/PTAA (PCE=16.1 %). Fig. 9(a) demonstrates the J-V curves of the fabricated devices. Although PTAA-based devices exhibit negligible interface recombination losses and V_{oc} >1.2 V; samples with a direct CuO_x/perovskite interface exhibit significant loss which are attributed to the energetic misalignment at the CuO_x/perovskite interface and improved perovskite/PCBM interface recombination velocities. Guo et al. [154] presented an approach for minimizing heterogeneity by the use of an integrated HTM containing inorganic Cu_xO and 5,6-difluorobenzothiadiazole based conjugated polymer (FBT-Th4). The optimized devices exhibited a substantial improvement in performance with PCE reaching 18.85 % with insignificant hysteresis. Mesoscopic PSCs were successfully incorporated with integrated HTMs comprising inorganic V_2O_5 and organic nickel phthalocyanine: Nickel (II) 1, 4, 8, 11, 15, 18, 22, 25-octabutoxy-29H, 31H-phthalocyanine abbreviated as NiPc-$(OBu)_8$. The development of a consistent V_2O_5 film was facilitated by the appearance of a NiPc-$(OBu)_8$ layer on the perovskite surface. Fig. 9(b) reveals that the optimized NiPc-$(OBu)_8$/V_2O_5 integrated HTM exhibited a remarkable PCE of 17.6 % considerably better than that of doped Spiro-OMeTAD/V_2O_5 integrated HTM based devices (PCE=16.7 %) [155]. Kim et al. [156] described the use of composite double-layer HTM comprising of organic spiro-OMeTAD and inorganic WO_3. The fabricated double layer HTM based device yielded a record efficiency of 21.44 %. The double layer's electronic properties are extensively studied using PL, SCLC, and EIS characterizations. WO_3 layer increases V_{oc} significantly by decreasing the quasi-Fermi energy level for holes and minimizing charge recombination, leading to a high V_{oc} of 1.17 V. Additionally, the WO_3 serves as a scaffold for creating a homogeneous and uniform spiro-OMeTAD overlayer in the double layer. Fig. 9(c,d) illustrates the representation of expected

effects and J-V curves of WO_3/spiro-OMeTAD bilayer based PSCs. This study demonstrated a simple method for increasing the PCE and stability of PSCs by forming an organic layer over the top of the inorganic layer.

Li et al. [157] synthesized conjugated polyelectrolyte PTPADT-SO_3Na which exhibiting a self-doping effect and excellent conduction properties. It has a similar valence band to that of perovskites. Consequently, the PTPADT-SO_3Na HTM based device exhibited superior performance, as shown in Fig. 9(e), achieving a maximum efficiency of 18.15 %, which is more than the efficiency of a standard HTM PEDOT:PSS device (PCE=13.86%). By changing HTM with commercially available PbI_2, Liu et al. [158] created a low-cost and simple-to-fabricate technique to significantly reducing undesired voids. The close interaction between PbI_2 and TBP, retards TBP evaporation preventing bis(trifluoromethane)sulfonimide lithium salt (LiTFSI) agglomeration and the formation of voids in the HTM. The effect of PbI_2 addition in spiro-OMeTAD based PSC is demonstrated in Fig. 9(f). As a result, the HTM exhibits significantly improved charge carrier extraction resulting in a faster response to steady-state conditions of less than 1 second for the corresponding photovoltaic cell (where the control device shows more than 26s). By optimizing the amount of PbI_2, a champion PCE of over 20% was obtained. This work presents a straightforward and efficient technique for optimizing the efficiency of HTMs and PSCs. A poly (4-vinylpyridine) (PVP) interlayer is incorporated into perovskite films by a solution-based technique, and the resulting devices by Shardokh et al. [159] exhibited superior performance. A unique way of introducing inorganic HTMs is to apply a quaternary semiconductor Cu_2MSnS_4 (M = Co^{2+}, Ni^{2+}, Zn^{2+}) (CMTS) nanostructure to the perovskite substrate. This modification enhances the long-term stability as well as photovoltaic behavior of the PSCs. Various characterization studies demonstrated that PVP/CMTS interface is capable of significantly reducing the non-radiative recombinations and increasing V_{oc}. The fabricated PSC with PVP interlayer and CZTS HTM yielded an efficiency of 13.57 %. Wang et al. [160] demonstrated the synthesis and use of a novel sequence of metal Schiff base complexes (MMePy, M = Pt, Pd, and Cu) as HTMs in PSCs. It is feasible to adjust the energy levels of the material by altering the central metal, resulting in a more optimal positioning with that of the absorber. The suitably matched energy levels and more crystalline nature of the film, along with low roughness of the surface, resulting in the CuMePy-based devices having the highest PCE of 8.07 % amongst the MMePy-based devices. This work demonstrates the potential utility of this

sequence of metal complexes as hole transporters in solar cells. Zhang et al. [161] described the synthesis of oleylamine (OAm)-capped $CuInSe_2$ (OAm-CISe) quantum dots (QDs) using a new hot injection process. The insulating properties of the long-chain organic ligands linked to QD surface influences charge transfer between the quantum dots. Thus, using a phase transfer technique, the long-chain ligand on the surface of OAm-CISe was substituted by a short-chain ligand of MPA. MPA-capped CISe (MPA-CISe) was also utilized as an HTM and its properties were also studied. PCE for PSCs based on MPA-CISe rose to 8.59 %, up from 7.18 % for PSCs based on OAm-CISe. The experimental findings suggest that the increased PCE ows to the enhanced conduction and transmittance of the MPA-CISe film compared to the OAm-CISe film.

Table 1: Photovoltaic parameters of PSCs employing various inorganic HTMs.

HTM	**Dopants/additive**	**Configuration**	**Perovskite deposition method**	**Device structure**	**V_{oc} (V)**	**J_{sc} (mA/cm^2)**	**FF (%)**	**PCE (%)**	**Year**	**Ref.**
NiO_x	No dopant	ITO/HTM/ $Cs_{0.08}(MA_{0.17}FA_{0.83})_{0.92}Pb(I_{0.83}Br_{0.17})_3$/PCBM/Ag	spin coating	Planar p-i-n	0.94	21.7	62.8	12.8	2018	[64]
NiO_x	UV-O_3 treated, no dopant	ITO/HTM/$MAPbI_3$/PCBM/BCP/Ag	Two-step spin coating	Planar p-i-n	1.03	20.6	74.2	15.9	2017	[65]
NiO_x	UV-O_3 treated, no dopant	PEN/ITO/HTM/$MAPbI_3$/PCBM/ BCP/Ag	Two-step spin coating	Planar p-i-n	1.04	17.7	64.2	11.84	2017	[65]
NiO_x	No dopant	FTO/c-TiO_2/m-TiO_2/ $MAPbI_3$/HTM/Au	Two-step spin coating	Mesoscopic n-i-p	0.88	19.5	53.1	9.11	2017	[65]
NiO	No	FTO/HTM/$MAPbI_3$/C_{60}/	spin coating	Planar p-i-n	-	19.6	74	15.31	201	[66]

	dopant	BCP/Al							8	
NiO_x	No dopant	ITO/HTM/$MAPbI_3$/ PCBM/BCP/Ag	spin coating	Planar p-i-n	1.07	20.6	79	17.6	2018	[67]
NiO_x	No dopant	FTO/HTM/$MAPbI_3$/PCBM/ BCP/Ag	Two-step spin coating	Mesoscopic p-i-n	1.01	21.5	81.3	17.77	2018	[68]
NiO_x	No dopant	ITO/HTM/$MAPbI_{3-x}Cl_x$ /PCBM/AZO/Ag	two-step spin coating	Planar p-i-n	1.04	19.5	65	13.10	2019	[178]
NiO_x	No dopant	ITO/HTM/$Cs_{0.1}MA_{0.2}FA_{0.7}Pb_{0.5}Sn_{0.5}I_3$/$C_{60}$/BCP/Cu	spin coating	Planar p-i-n	-	31	-	17.6	2019	[69]
NiO	No dopant	ITO/HTM/$Cs_{0.05}(MA_{0.17}FA_{0.83})Pb_{1.1}(I_{0.83}Br_{0.17})_3$)/$C_{60}$/BCP /Cu	one-step solution process	Planar p-i-n	1.07	21.7	73.3	17.07	2019	[70]
NiO	No dopant	FTO/HTM/$Cs_{0.05}MA_{0.95}PbI_3$/PCBM/BCP/AZO/Ag	spin coating	Planar p-i-n	1.03	22.5	80.8	18.78	2018	[71]
NiO	No dopant	ITO/HTM/$MAPbI_{3-x}Cl_x$/ PCBM/Ag	spin coating	Planar p-i-n	1.09	22.7	73	18.08	2018	[72]
NiO	Ni^{3+}	FTO/HTM/ $FA_{0.83}MA_{0.17}Pb(I_{0.83}Br_{0.17})_3$/PCBM/ZnO/Al	Two-step spin coating	Planar p-i-n	1.11	22.8	70	17.75	2020	[79]
NiO	No dopant	ITO/HTM/$MASnI_3$/ $PC_{71}BM$/Al	Simulation technique	Planar p-i-n	0.97	33.4	70.3	22.95	2020	[80]
NiO_x	No dopant	ITO/HTM/$MAPbI_3$/$PC_{71}BM$/BCP/Ag	sequential spin coating	Planar p-i-n	1.10	18.9	76	15.87	2017	[82]
NiO_x	No dopant	PEN/ITO/HTM/$MAPbI_3$/$PC_{71}BM$/BCP/Ag	sequential spin coating	Planar p-i-n	1.09	18.9	69	14.27	2017	[82]
NiO_x	Copper	ITO/HTM/$MAPbI_3$/$PC_{71}BM$/BCP/Ag	sequential spin coating	Planar p-i-n	1.11	20.7	81	18.66	2017	[82]

NiO_x	Copper	PEN/ITO/HTM/MAPbI$_3$/PC$_{71}$BM/BCP/Ag	sequential spin coating	Planar p-i-n	1.11	19.8	0.78	17.16	2017	[82]
NiO_x	Zinc	ITO/HTM/MAPbI$_3$/PCBM/ bis-C$_{60}$/Ag	spin coating	Planar p-i-n	1.03	21.8	61	13.72	2018	[81]
NiO	Carbon	FTO/TiO$_2$/MAPbI$_3$/HTM/Au	spin coating	Planar n-i-p	0.85	23.3	78.2	16	2018	[83]
NiO	Yttrium	FTO/HTM/MAPbI$_3$/PCBM/Au	spin coating	Planar p-i-n	1.00	23.8	68	16.31	2018	[84]
NiO_x	Cobalt	ITO/HTM/MAPbI$_3$/PCBM/Ag	Two-step spin coating	Planar p-i-n	1.05	22.3	79	18.6	2018	[85]
NiO_x	Gold	FTO/HTM/MAPbI$_3$/PCBM/PPDIN6/Ag	Two-step spin coating	Planar p-i-n	1.12	22.8	79	20.2	2018	[86]
NiO_x	Strontium	FTO/HTM/ FA$_{0.15}$MA$_{0.85}$Pb(I$_{0.95}$Br$_{0.05}$)$_3$/PCBM/AgAl	consecutive two-step spin-coating process	Planar p-i-n	1.11	22.6	79.1	20.07	2018	[87]
NiO_x	Iron	ITO/HTM/MAPbI$_3$/PCBM/BCP/Ag	two-step spin coating	Planar p-i-n	1.08	19.2	84.8	17.57	2019	[89]
NiO_x	cobalt	FTO/HTM/MAPbI$_3$/PCBM/PEI/Ag	spin coating	Planar p-i-n	1.09	20.4	79.8	17.77	2020	[90]
NiO_x	Lithium and cobalt	ITO/HTM/MAPbI$_{3-x}$Cl$_x$/ PC$_{71}$BM/BCP/Ag	Two-step solution method	Planar p-i-n	1.06	21.7	75	18.7	2020	[91]
NiO_x	Lithium and cobalt	ITO/HTM/MA$_{1-y}$FA$_y$PbI$_{3-x}$Cl$_x$/PCBM/BCP/Ag	two-step spin coating	Planar p-i-n	1.09	23.8	78	20.1	2019	[92]
NiO_x	Lithium and	ITO/HTM/MAPbI$_{3-x}$Cl$_x$/	spin coating	Planar p-i-n	1.11	23.1	81	20.83	2020	[93]

	copper	PCBM:C_{60}/ZrAcac/Ag								
NiO/Ag/Nio	No dopant	ITO/HTM/$FA_xMA_{1-x}PbI_3$/ C_{70}/BCP/Ag	Simple deposition	Planar p-i-n	0.94	20	61.7	11.68	2020	[94]
Ni_2O_3	No dopant	FTO/HTM/$MA_{0.85}FA_{0.15}PbI_{0.9}Cl_{0.1}$/PCBM/BCP/Ag	spin coating	Planar p-i-n	1.1	19.1	83	17.89	2020	[95]
NiO_x	UVO treated	FTO/HTM/$MAPbI_3$/ PCBM/BCP/Ag	spin coating	Planar p-i-n	1.11	23.3	75.5	19.67	2019	[96]
$NiCo_2O_4$	No dopant	ITO/HTM/$MAPbI_{3-x}Cl_x$/ PCBM:C_{60}/ZrAcac/Ag	spin coating	Planar p-i-n	1.07	21.8	78	18.23	2018	[97]
$NiCo_2O_4$	No dopant	ITO/HTM/$MAPbI_3$/PCBM/ Al	spin coating	Planar p-i-n	0.97	19.9	79.9	15.5	2018	[98]
CuI	No dopant	FTO/TiO_2/$MAPbI_3$/HTM/Au	Two-step spin-coating	Planar n-i-p	0.73	32.7	31	7.40	2016	[99]
CuI	No dopant	ITO/HTM/$MAPbI_3$/C_{60}/BCP/Ag	one-step fast deposition-crystallization	Planar p-i-n	0.99	22.6	71.3	16.8	2016	[100]
CuI	No dopant	ITO/HTM/$MAPbI_{3-x}Cl_x$ /PCBM/AZO/Ag	two-step spin coating	Planar p-i-n	0.99	19.2	74	14.06	2019	[178]
CuO_x	No dopant	ITO/HTM/$MAPbI_3$/C_{60}/BCP/Ag	one-step fast deposition-crystallization	Planar p-i-n	1.00	22.2	75.7	16.8	2016	[103]
CuO_x	No dopant	ITO/HTM/$MAPbI_3$/PCBM/Ag	spin coating	Planar p-i-n	0.97	19.0	73	13.48	2019	[104]

Cu_XO	No dopant	ITO/HTM/$MAPbI_3$/C_{60}/BCP/Al	industrial-production-compatible electrospray deposition process	Planar p-i-n	0.70	17.2	48	5.83	2017 [105]
Cu_2O	No dopant	FTO/WS_2/$MASnI_3$/HTM/Au	Simulation technique	Planar n-i-p	0.8	34.8	83.1	23.03	2020 [106]
$CuCo_2O4$	No dopant	ITO/HTM/$MAPbI_3$/PCBM/ Bis-C_{60}/Ag	spin coating	Planar p-i-n	0.99	20.3	70	14.12	2019 [107]
$CuCrO_2$	No dopant	ITO/HTM/$MAPbI_3$/C_{60}/BCP/Ag	-	Planar p-i-n	-	-	-	14.33	2018 [108]
$CuCrO_2$	Indium	ITO/HTM/$Cs_{0.05}(MA_{0.15}FA_{0.85})_{0.95}Pb(I_{0.85}Br_{0.15})_3$/PCBM:C60/ZrAcac/Ag	spin coating	Planar p-i-n	1.07	23.7	80.6	20.54	2019 [109]
$CuNbO_x$	No dopant	ITO/HTM/$MAPbI_3$/PCBM/ PEI	One-step spin coating	Planar p-i-n	0.98	20.3	80.8	16.01	2020 [111]
CuPc	No dopant	ITO/c-TiO_2/m-TiO_2/PCBM/ PMMA/$Cs_{0.07}Rb_{0.03}FA_{0.765}MA_{0.135}PbI_{2.55}Br_{0.45}$/HTM/Au	spin coating	Mesoscopic n-i-p	1.14	23.6	74.2	20.09	2018 [112]
CuPc	No dopant	ITO/HTM/$MAPbI_3$/PCBM/BCP/Ag	spin coating	Planar p-i-n	1.03	19.4	77	15.4	2018 [113]
CuPc	No dopant	FTO/c-TiO_2/m-TiO_2/ $CsPbBr_3$/HTM/C	sequential	Mesoscopic n-i-p	1.26	6.6	74	6.21	2018 [114]

			deposition							
CuPc-OBu	TBP	FTO/c-TiO_2/m-TiO_2/$CsFAMAPb(BrI)_3$/HTM/Au	spin coating	Mesoscopic n-i-p	1.07	23.1	77.1	19.01	2020	[115]
CuPc	No dopant	FTO/SnO_2/PCBM/$MAPbI_3$/ HTM/Au	solvent engineering method	Planar n-i-p	1.03	17.9	57.9	10.73	2016	[116]
$CuMe_2Pc$	No dopant	FTO/SnO_2/PCBM/$MAPbI_3$/ HTM/Au	solvent engineering method	Planar n-i-p	1.08	20.4	65.4	14.34	2016	[116]
CZTS	OAm	ITO/HTM/$MAPbI_3$/PCBM/PrCMA/Ag	Spin coating	Planar p-i-n	0.88	18.1	77	12.2	2016	[117]
CZTS	No dopant	ITO/HTM/$MAPbI_3$/PCBM/PrCMA/Ag	Spin coating	Planar p-i-n	0.92	20.7	81	15.4	2016	[117]
RGO/$CZTS_xSe_{1-x}$	No dopant	FTO/c-TiO_2/m-TiO_2/$MAPbI_3$ /HTM/Au	spin coating	Mesoscopic n-i-p	0.91	17.4	63.0	10.08	2018	[119]
CZTS:Cd	No dopant	ITO/SnO_2/$MAPbI_3$/HTM/Au	Two-step spin-coating	Planar n-i-p	1.14	23.4	77	20.54	2020	[120]
CuSCN	No dopant	FTO/c-TiO_2/m-TiO_2/$(FAPbI_3)_{0.77}(MAPbBr_3)_{0.14}(CsPbI_3)_{0.09}$/HTM/Au	single-step spin coating	Mesoscopic n-i-p	1.13	21.2	75.3	18.09	2019	[121]
CuSCN /NH_3	No dopant	ITO/HTM/$MAPbI_3$/PCBM/Ag	Two-step sequential spin coating	Planar p-i-n	1.1	22.7	71	17.5	2017	[125]
V_2O_5	No dopant	FTO/c-TiO_2/m-TiO_2/$(FAPbI_3)_{0.85}(MAPbBr_3)_{0.15}$/HTM/Au	Two-step spin-coating	mesoscopic n-i-p	0.93	18.3	66.5	11.3	2017	[155]
VO_x	No dopant	FTO/HTM/$MAPbI_3$/PCBM/BCP/Ag	Two-step sequential	Planar p-i-n	0.9	17.9	71.2	11.53	2018	[126]

			deposition							
VO_x	No dopant	FTO/HTM/$MAPbI_3$/PCBM/Al	Two-step spin coating	Planar p-i-n	0.96	20.3	74	14.5	2018	[127]
MoO_x	No dopant	FTO/TiO_2/$MAPbI_3$/HTM/Au	empirical simulation	Planar n-i-p	1.03	22.3	78.7	18.25	2017	[128]
MoO_x	No dopant	FTO/HTM/$MAPbI_3$/PCBM/ Au	empirical simulation	Planar p-i-n	0.97	22.7	82.5	17.88	2017	[128]
MoO_x	RGO	ITO/HTM/$MAPbI_3$/PCBM/BCP/Ag	spin coating	Planar p-i-n	1.12	21.0	77	18.15	2020	[129]
MoO_x	F4-TCNQ	ITO/HTM/$MAPbI_3$/PCBM/BCP/Ag	spin coating	Planar p-i-n	1.06	20.1	76	16.26	2019	[130]
Co_3O_4	Lithium	ITO/HTM/$MAPbI_3$/PCBM/ZnO/Ag	spin-coating	Planar p-i-n	1.03	20.6	65.0	13.96	2020	[132]
MoS_2	No dopant	ITO/HTM/$MAPbI_3$/PCBM/Al	two-step sequential spin-coating	Planar p-i-n	0.84	12.6	57	6.01	2017	[133]
MoS_2	No dopant	ITO/HTM/$MAPbI_{3-x}Cl_x$/C_{60}/ BCP/Al	fast deposition crystallization	Planar p-i-n	0.88	20.9	77.9	14.35	2017	[134]
WS_2	No dopant	ITO/HTM/$MAPbI_{3-x}Cl_x$/C_{60}/ BCP/Al	fast deposition crystallization	Planar p-i-n	0.97	21.2	73	15	2017	[134]
MnS	No dopant	FTO/c-TiO_2/m-TiO_2/ $FA_{0.85}MA_{0.15}Pb(I_{0.85}Br_{0.15})_3$/HTM/Au	anti-solvent method	Mesoscopic n-i-p	1.11	23.4	76.4	19.86	2019	[136]
SnPc	No	ITO/SnO_2/$CsPbI_2Br$/HTM/C	sequential spin-	Planar n-i-p	1.24	13.6	66.9	11.39	202	[137]

	dopant		coating						0	
SWNT	No dopant	FTO/c-TiO_2/m-TiO_2/$MAPbI_3$ /HTM/Au	sequential deposition	mesoscopic n-i-p	0.73	10.5	64	4.9	2016	[138]
SWNT/GO	No dopant	FTO/c-TiO_2/m-TiO_2/$MAPbI_3$ /HTM/Au	sequential deposition	mesoscopic n-i-p	0.89	19.1	57	9.8	2016	[138]
SWNT/GO/PMMA	No dopant	FTO/c-TiO_2/m-TiO_2/$MAPbI_3$ /HTM/Au	sequential deposition	mesoscopic n-i-p	0.97	17.7	60	10.4	2016	[138]
SWNT/GO/PMMA	No dopant	FTO/c-TiO_2/m-TiO_2/$MAPbI_3$ /HTM/Au	One-step deposition	mesoscopic n-i-p	0.95	19.4	72	13.3	2016	[138]
a-GO	No dopant	ITO/HTM/$MAPbI_{3-x}Cl_x$/ PCBM/BCP/Ag	spin coating	Planar p-i-n	1.0	18.4	76.8	14.14	2019	[139]
RGO	No dopant	ITO/HTM/MAPbI3/ PCBM/BCP/Ag	Two-step spin coating	Planar p-i-n	1.07	19.4	74.2	15.4	2017	[176]
NiO_x	FDA	ITO/HTM/$MAPbI_3$/PCBM/AgAl	Two-step spin coating	Planar p-i-n	1.04	22.5	75.8	17.59	2018	[141]
NiO_x and D-A-D typed organic htm	No dopant	ITO/HTM/$Cs_{0.05}(MA_{0.15}FA_{0.85})_{0.95}Pb(I_{0.85}Br_{0.15})_3$/PCBM/BCP/Ag	single-step spin-casting	Planar p-i-n	1.06	23.3	81.6	20.22	2020	[142]
NiO_x/Spiro-OMeTAD	No dopant	FTO/SnO_2/$(FAPbI_3)_x(MAPbBr_3)_{1-x}$/HTM/Au	Two-step spin coating	Planar n-i-p	1.14	23.8	79.8	21.66	2020	[143]
V_2O_5/PEDOT:	No	ITO/HTM/$MAPbI_3$/PCBM/Ag	spin coating	Planar p-i-n	0.88	22.7	74.7	15	201	[145]

PSS	dopant								7	
PEDOT:PSS/MoS_2	No dopant	ITO/HTM/MAPb($I_{0.5}Br_{0.5}$)$_3$/PCBM/BCP/Ag	spin coating	Planar p-i-n	0.95	20.7	72.3	14.7	2018	[146]
PEDOT:PSS/GQDs	No dopant	FTO/HTM/$MAPbI_3$/PCBM/ Ag	spin coating	Planar p-i-n	0.99	21.0	72.6	15.24	2020	[149]
CuCrO$_2$/PTAA	No dopant	ITO/SnO_2/PCBM/$Cs_{0.05}(MA_{0.15}FA_{0.85})_{0.95}Pb(I_{0.85}Br_{0.15})_3$/HTM/Au	spin coating	planar n-i-p	1.02	22.8	75	17.4	2020	[150]
PTAA/VO_x	No dopant	ITO/SnO_2/PCBA/CsFAPbI_3/MAI/HTM/Ag	spin coating	planar n-i-p	1.04	24.6	78	20.1	2020	[151]
Spiro-OMeTAD/Cu_xS	No dopant	FTO/SnO_2/$MAPbI_3$/HTM/Au	spin coating	planar n-i-p	1.12	23.1	71.5	18.58	2017	[152]
CuO_x/PTAA	No dopant	ITO/HTM/$MAPbI_3$/PCBM/ Ag	two-consecutive step program	Planar p-i-n	1.15	19.2	72.9	16.1	2020	[153]
FBT-Th4/Cu_xO	No dopant	FTO/SnO_2/PCBM/$MAPbI_3$/HTM/Au	spin coating	Planar n-i-p	1.12	22.3	75.4	18.85	2018	[154]
NiPc-$(OBu)_8$	No dopant	FTO/c-TiO_2/m-TiO_2/$(FAPbI_3)_{0.85}(MAPbBr_3)_{0.15}$/HTM/Au	Two-step spin-coating	mesoscopic n-i-p	0.89	18.5	63.8	10.6	2017	[155]
NiPc-$(OBu)_8$	LiTFSI, TBP, and FK209	FTO/c-TiO_2/m-TiO_2/$(FAPbI_3)_{0.85}(MAPbBr_3)_{0.15}$/HTM/Au	Two-step spin-coating	mesoscopic n-i-p	1.07	23.0	72.8	17.9	2017	[155]
NiPc-$(OBu)_8$/V_2O_5	No dopant	FTO/c-TiO_2/m-TiO_2/$(FAPbI_3)_{0.85}(MAPbBr_3)_{0.15}$/HTM/Au	Two-step spin-coating	mesoscopic n-i-p	1.08	23.1	73.4	18.3	2017	[155]
WO_3/spiro-OMeT	No dopant	FTO/SnO_2/$Cs_{0.05}(FAPbI_3)_{0.79}(MAPbBr_2)_{0.16}$/HTM/Au	Two-step spin coating	Planar n-i-p	1.17	23.7	77.1	21.44	2018	[156]

AD										
PTPADT-SO_3Na	No dopant	ITO/HTM/$MAPbI_3$/PCBM:C60/BCP/Ag	spin coating with anti-solvent method	Planar p-i-n	1.07	21.2	79.2	18.15	2020	[157]
PbI_2/spiro-OMeTAD	TBP and LiTFSI	FTO/c-TiO_2/m-TiO_2/$FA_xMA_{1-x}Pb(I_yBr_{1-y})_3$/HTM/Au	spin coating	mesoscopic n-i-p	1.12	23.9	75.6	20.3	2020	[158]
CZTS	No dopant	FTO/c-TiO_2/m-TiO_2/$MAPbI_3$/PVP10/HTM/Au	vapor-assisted solution deposition	mesoscopic n-i-p	1.03	18.6	70.6	13.57	2020	[159]
CuMePy	No dopant	FTO/SnO_2/Perovskite/HTM/Au	spin coating	Planar n-i-p	0.94	20.2	42.4	8.07	2020	[160]
MPA-CISe	No dopant	ITO/HTM/$MAPbI_3$/PCBM /BCP/Ag	spin coating	Planar p-i-n	0.89	16.3	5.3	8.59	2020	[161]

4.2. Polymeric HTM

Conducting polymers are one of the most competent HTMs that are employed in PSCs. Unlike other small molecules, the process of charge transportation in polymers is carried out via two pathways i.e., intramolecular and intermolecular charge transportation. In general, the conducting polymers form much longer conjugated systems thereby inducing fast charge transportation. Moreover, intramolecular charge transportation is extremely fast in comparison to intermolecular charge transportation and it greatly depends on the distance between molecules. As a result, these polymers normally assure high charge carrier mobility. Additionally, the comparatively flexible conducting polymers can be deposited in thinner layers in comparison to small and rigid molecules. This in turn facilitates charge transportation in HTM. The recent

studies of important polymeric HTMs are discussed in this section. Table 2 summarizes the photovoltaic parameters of PSCs employing various polymeric HTMs.

4.2.1. PEDOT:PSS

Facilitation of hole transport via the highly conductive PEDOT:PSS HTM was found to trigger the increase in charge carrier lifetimes within the PSCs, resulting in improved photocurrent extraction [162]. Huang et al. [163] showed that the light-harvesting, charge extraction, and photocurrent generation are dramatically enhanced by utilizing DMSO-doped PEDOT:PSS in organo-lead iodide devices. An in-depth look at the X-ray studies of perovskite thin films developed on DMSO-doped PEDOT:PSS showed that perovskite films have larger grains with improved crystallinity. These enhancements resulted in a 16.7% PCE instead of normal p-i-n photovoltaics, where pristine PEDOT:PSS is used. The most essential approach to achieve better and more efficient PSCs is the application of rational HTM materials design [164]. By employing a commonly used p-type dopant, F4-TCNQ, Liu et al. [165] ascertained the influences of F4-TCNQ on the optical and electrical properties of traditional PEDOT:PSS HTM as well as the effects of related PSCs on the photovoltaic efficiency. Modifying the electrical properties of PEDOT:PSS film with F4-TCNQ in a low concentration, lowers the HOMO. The effective carrier transport and favourable energy level alignment of the doped film caused by increased electrical conductivity and the elevated energetic state; enabled perovskite absorbent layers to transfercarriers efficiently from the absorber layer to the HTM. Finally, the PSCs doped with F4-TCNQ showed improved J_{sc}, V_{oc}, and FF. This study demonstrates the benefit of 0.30 wt% F4-TCNQ doping in PEDOT:PSS HTM; the PCE significantly increased from 13.3% to 17.2%, signifying that the film serves as an effective HTM for PSCs.

Luo et al. [166] illustrated the fabrication of a GO-modified PEDOT:PSS HTM by spin-coating a GO solution onto the PEDOT:PSS. As shown in Fig. 10(a), the fabricated PSCs have 15.34% PCE for GO-modified PEDOT:PSS, which is greater than 11.90% of PEDOT:PSS fabricated PSCs. Bruijnaers et al. [167] demonstrated that spin coating of a precursor solution of a metal halide perovskite on top of PEDOT:PSS will chemically minimize the oxidation state of PEDOT:PSS. Consequently, the work function of the PEDOT:PSS was reduced. Thus, the solar cells were less efficient and had a lower V_{oc} and J_{sc}. Thermal annealing of the PEDOT:PSS/perovskite layer stack in the presence of oxygen was able to restore the depleted

PEDOT:PSS. As a result, thermal annealing of the perovskite film in the air increases V_{oc}, improves J_{sc}, which results in solar cells with higher efficiency (up to 14 %). Elbohy et al. [168] stated that the treatment of urea for PEDOT:PSS optimizes the morphology, conductivity, and work function of inverted $MAPbI_3$ PSCs for improving efficiency and stability. The PCE of the $MAPbI_3$ devices were enhanced to 18.8% (Fig. 10(b)) compared to 14.4% for pristine PEDOT:PSS. The urea treatment enhances conductivity of the PEDOT:PSS film from 0.2 S cm^{-1} for pristine PEDOT:PSS to 12.75 S cm^{-1} for 5 wt% urea-treated PEDOT:PSS. A significant benefit of the urea solution is that it improves the atmospheric stability of PEDOT:PSS-based polymer micro-dispersions. Optimizing the urea content in the procedure often reduces the device hysteresis. Using a one-step solution-phase through the use of PEDOT:PSS-NH_2-OH as the HTM, Wang et al. [169] demonstrated highly efficient organic-inorganic hybrid planar heterojunction PSCs. By increasing the performance of devices with PEDOT:PSS-NH_2-OH to 14.16 %, it is possible to improve the reproducibility of devices with PEDOT:PSS to good levels. The HOMO level (5.32 eV) of this newly prepared HTM is similar to the valence band of $MAPbI_3$ absorbers (5.4 eV). These results suggest that the charge extraction capabilities of the $MAPbI_3$ film that was deposited on PEDOT:PSS-NH_2-OH are far more than the film based on PEDOT:PSS. These findings indicate that the photovoltaic devices have an outstanding hole and electron transport as well as large recombination resistance, and even show low series resistance and low contact resistance. Based on the findings, it can be inferred that PEDOT:PSS semiquinone and amine radical changed PEDOT:PSS HTMs can be excellent HTMs. By using an extremely efficient PEDOT:GO (GO-doped PEDOT:PSS) as an HTM, it was shown that the solar cells have excellent optical and electrical properties, such as a higher electrical conductivity, a higher work function, and enhanced crystallinity of the perovskite crystal [170]. These exciting developments for the commercialization of perovskite optoelectronic devices are contributed by high efficiency of 18.09% (Fig. 10(c)) and excellent stability of inverted PSCs.

The sodium citrate-doped PEDOT:PSS (SC- PEDOT:PSS) was employed as an effectual HTM for improving the PCE of PSCs upto 18.39% as shown in Fig. 10(d) [171]. This performance enhancement was the result of the increasing V_{oc} from 1.057 to 1.134 V and the higher work function of the doped PEDOT:PSS film. The hole extraction and transportation of the inverted planar PSCs rely on the efficient use of the PEDOT:PSS HTM. The insulating structure of PSS, however, caused the PEDOT:PSS film to have a lower electrical property, which reduced the

hole transfer from the electrodes and lowered the photocurrent of the PSCs. The PEDOT:PSS thin film was treated with dimethylformamide (DMF), methanol, and their mixture solvents (co-solvent) for improving the film's electrical conductivity [172]. The co-solvents treatment increased the conductivity from 10^{-3} S.cm^{-1} to around 10^{2} S.cm^{-1}. Using the co-solvent treated PEDOT:PSS thin film as the HTM in a PSC, the PCE of the device was improved by 17.5 % as shown in Fig. 10(e). This experiment showed that the post-treatment using a hybrid co-solvent improves the electrical properties of the PEDOT:PSS film and allows PSCs and other thin-film electronic and optoelectronic devices to be fabricated successfully. Reza et al. [173] focused on the successful growth of larger perovskite crystalline domains so as to realize a non-wet conducting HTM surface. The major PSS is removed using ethylene glycol and methanol-based solvent engineering method, resulting in the elimination of the prevailing PSS. The transition resistance was lower in the solvent-engineered PEDOT:PSS-based PSCs due to higher charge carrier lifetime, faster charge transport, and lower transfer impedance. The main advantages of the use of this solvent-engineered treatment in fabricating $MAPbI_3$ PSCs included improved device stability, with a PCE of 18.18%, which was 37% greater than the untreated PEDOT:PSS-based systems. The J-V curves of the fabricated devices are as shown in Fig. 10(f). Wang et al. [174] added an interlayer of PEDOT:PSS with a solvent/solution washing treatment. This shows that when the PEDOT:PSS film was treated with the solvent/solution, the conductivity was greatly enhanced, which improved charge carrier transfer and an increase in J_{sc}. The PCE improved from 14.8% to 16.2%. The PEDOT:PSS surface was modified with hydroquinone (HQ), which lowers the hole transport barrier, and therefore reduces the interfacial resistance. The device with HQ-treated PEDOT:PSS shows substantially reduced leakage current (1.2 mA). The PCE of Pb-Sn hybrid PSCs with the HQ-treated PEDOT:PSS HTM was increased by 5.7% in comparison to PEDOT:PSS HTM-based PSCs [175].

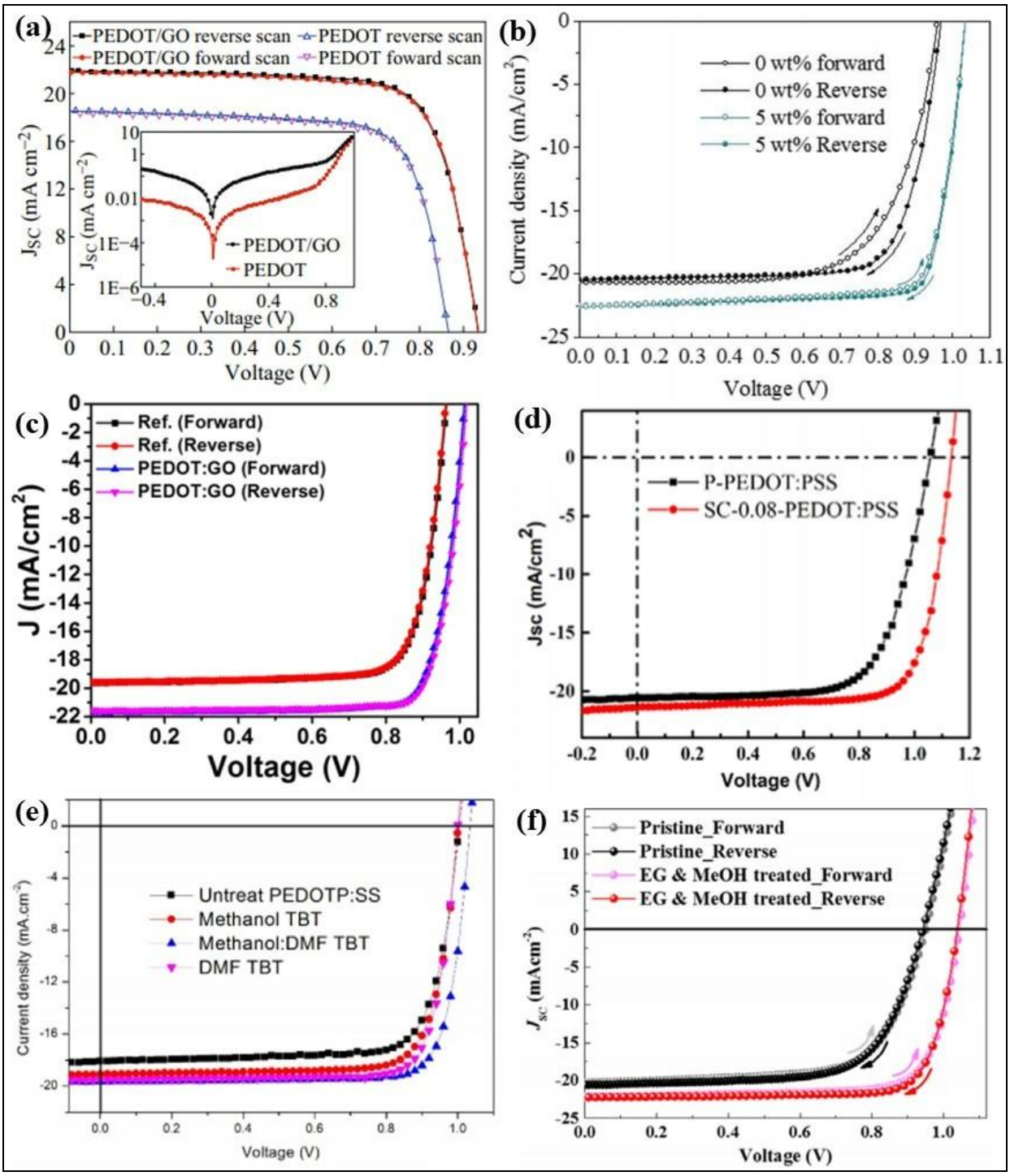

Fig. 10 J-V curves of various PSCs based on (a) GO-modified PEDOT:PSS (Reproduced from [166] under Creative Commons Attribution 4.0 License. Copyright 2017, Springer) (b) Urea treated PEDOT:PSS (Reproduced from [168] with permission. Copyright 2019, Wiley) (c) PEDOT:GO composite (Reproduced from [170] under Creative Commons Attribution 4.0

License. Copyright 2018, Springer) (d) SC-PEDOT:PSS (Reproduced from [171] with permission. Copyright 2019, American Chemical Society) (e) TBT treated PEDOT:PSS (Reproduced from [172] with permission. Copyright 2020, Elsevier) (f) EG & MeOH treated PEDOT:PSS (Reproduced from [173] with permission. Copyright 2020, Elsevier)

4.2.2. PTAA

There are more interest in low-temperature-processed PSCs, which can be fabricated on rigid or flexible substrates, because of their possible widespread applications. To take advantage of the properties of reduced graphene oxide to provide a more stable film and the potential of a PTAA underlayer to boost the quality of overlying perovskite films, Zhou et al. [176] created a bilayer HTM using a low-temperature process. The fabricated bilayer HTM reached a maximum PCE of 17.2 % (as shown in Fig. 11(a)) for the aperture region of 1.02 cm^2. To fabricate inverted PSCs, Xu et al. [177] used PEDOT:PSS (PH 1000) and PTAA as the anode and HTMs, respectively. As a result of ethylene glycol and phosphoric acid treatment, the PEDOT:PSS anode's sheet resistance was decreased to 76 Ω sq^{-1}, which was similar to traditional indium tin oxide. Perovskite crystallization was facilitated due to the hydrophobicity of PTAA, improving the efficiency of the PSCs. For these PSCs fabricated on a rigid glass substrate, a PCE of 14.23% was obtained. The excellent bendability of flexible PSCs on a polyethylene terephthalate substrate was accompanied by a flexible printed circuit board (PCB) that yielded 10 % PCE. Based on these findings, it seems that using PEDOT:PSS and PTAA HTMs for fabricating rigid and flexible PSCs is a feasible and promising process. Khadka et al. [178] assessed the influence of HTMs on the optoelectronic properties of PSCs utilizing PTAA that showed an outstanding PCE of 18.12% as shown in Fig. 11(b).

Sekimoto et al. [179] explored the effect of PTAA on n light-induced degradation (LID) of hybrid PSCs, with a particular focus on the PTAA/OIHP interface. A higher LID was seen in the solar cells that used PTAA as the HTM, compared to the cells that used a spiro HTM. Before and after LID, hard X-ray photoelectron spectroscopy (HAXPES) showed that the chemical bonding condition was drastically changed in the area around the OIHP/HTM and ETM/OIHP interfaces. More iodine was in the OIHP/PTAA interface, after LID, than the OIHP/spiro interface. The impedance of the sample with PTAA as the HTM went negative under light illumination and in the dark after LID, resulting from interfacial degradation. Previous reports show that light-

induced iodide diffusion to the OIHP/HTM interface and the electrochemical reaction to form I_2 diminishes the OIHP solar cell efficiency. An excellent model of LID demonstrates that suppressing the pair reaction and ion migration offers the prospect of enhancing light stability. As a result, the device with PTAA reached 20.58% PCE as shown in Fig. 11(c). Zhao et al. [180] utilized a non-doped planar PTAA in inverted PSCs. The upper perovskite films were studied using contact angle, absorption spectra, X-ray diffraction, fluorescence spectra, and atomic force microscope to calculate the effect of non-doped PTAA. Doped PTAAs had equivalent efficacy to nondoped PTAAs. The non-doped PTAA based inverted planar PSCs showed outstanding performance leading to a PCE of 18.11% as shown in Fig. 11(d) and a very slight hysteresis index of 0.32%. The effects of PTAA HTM combined with a polymericsemiconductor, poly 9,9-dioctyfluorene-co-benzothiazole (F8BT) on the photovoltaic output was studied in PSCs [181]. When the F8BT ratio is modified in the mixed HTM, PCE increases to 14.88% and yields marginal hysteresis. Moreover, an improvement in charge carrier extraction and propagation yields an excellent PCE of 15.41%. This study details a very promising approach for creating highly efficient planar photovoltaic thin-film cells fabricated on a mixed polymer HTM.

Polytriarylamines have gained attraction in the field of organic electronics because of their promising hole transport property. Tepliakova et al. [182] reported a Suzuki polycondensation synthesis of PTAA. To maximise the molecular weight and minimise polydispersity, the Pd-based catalytic device was tailored. To test the synthesised PTAA polymer as an HTM for PSCs with the n-i-p design, experiments on both planar and 3D PSCs were conducted. The systems demonstrated a 17.6% PCE and V_{OC} of 1.06 V, while the reference PTAA devices has a lower efficiency of 16.7% and a V_{oc} of 1.02 V. Since the proposed synthetic solution produces high-quality PTAA with enhanced electrical properties, the approach is an excellent way to produce high-quality PTAA. In a study by Wang et al. [183], polymethyl methacrylate (PMMA) was incorporated into PTAA to produce PSCs. A major improvement in the performance and reliability of PSCs was realized by using PMMA as a dopant when compare to the control system (without PMMA). The champion cell showed an increased PCE of 14.56%, 33% more than the control system (10.92 %). Conductivity enhancement due to the mixed HTM after UVO treatment and the enhanced crystallization properties of perovskite are all contributing factors to the output rise. When this happens, the combination HTM (containing both PMMA and PTAA) is better at keeping moisture out of the perovskite layer than pure PTAA can. While hydroscopic

dopants normally accelerate perovskite degradation, all-inorganic perovskite-based devices are still prone to quicker failure because of hydroscopic dopants. Yang et al. [184] studied a sequence of hydrophilic Spiro-OMeTAD and hydrophobic PTAA that are tuneable in their surface wettability owing to the dominant lateral phase separation. SpiPA-II-based devices produce increased performance up to 12.52% with significantly reduced hysteresis. Tsarev et al. [185] have shown that poly[bis(4-phenyl)(4- methylphenyl)amine] was employed as an HTM, with only one methyl group was assigned to each recurring unit. The polytriarylamine has better band coordination with the perovskite which lead to higher efficiencies in dopant-free PSCs. Polytriarylamine-based HTM was modified with 4-hydroxy-2,2,6,6–tetramethylpiperidine-1-oxyl (TEMPOL) to adjust the physical properties of polytriarylamine-based HTM in a standard n-i-p configuration. TEMPOL catalyzes the oxygen doping of the HTM when the electrode-free stacks are exposed to air, which improves the PCE of the devices. Best 17.5% PCE was achieved for $Cs_{0.12}FA_{0.88}PbI_{2.64}Br_{0.36}$ perovskite absorber using the TEMPOL-induced doped polymeric HTM.

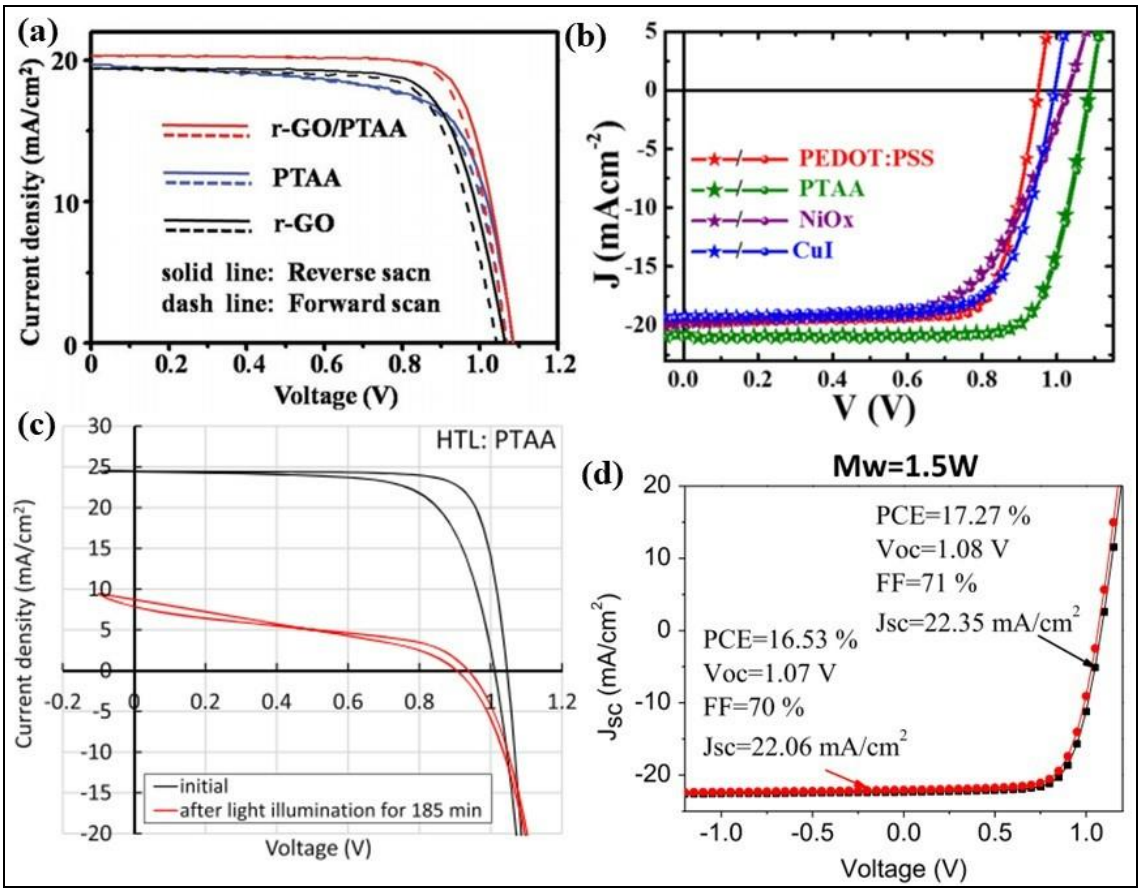

Fig. 11 J-V curves of various PSCs based on (a) RGO/PTAA (Reproduced from [176] with permission. Copyright 2017, Wiley) (b-d) PTAA (Reproduced from [178] with permission. Copyright 2019, American Chemical Society), (Reproduced from [179] with permission. Copyright 2019, American Chemical Society), (Reproduced from [180] with permission. Copyright 2019, Elsevier)

4.2.3. P3HT

Poly(3-hexylthiophene) (P3HT) was utilized as an HTM with negligible photoinduced dipoles [186]. Using spiro-OMeTAD, and P3HT, Kim et al. [187] demonstrated an easy and fast method to enhance the performance and moisture stability of PSCs. The vertical phase separation in the HTM was favored by the blend of spiro-OMeTAD and P3HT. The hydrophobic P3HT was more distributed at the surface (the air) while the hydrophilic spiro-OMeTAD was found to be more distributed near the perovskite layer. By vertically separation, better moisture stability was achieved by effectively blocking moisture in the air. Finally, the optimized composition of spiro-OMeTAD and P3HT allowed for rapid intra-molecular charge transfer, which in turn increased the performance of the solar cells. Further, a proper energy level balance made it easier to conduct charge transfers. Using the HTM blend, the fabricated device exhibited better PCE (18.9%) as shown in Fig. 12(a) and even exhibited good water stability. An alternative doping technique is employed in P3HT to create PSCs that have the mesoscopic structure [188]. Using three dopants TBP, LiTFSI, and Co(III)-TFSI, a PCE of 19.25% is achieved on 0.1 cm^2 (as shown in Fig. 12(b)), 16.29% on 1 cm^2, and 13.3% on a 43 cm^2 module, all of which was realized without the use of any external absorber layer or interlayer at the perovskite/P3HT interface. This demonstrates that cobalt dopant in the form of a salt solution is necessary to get better hole extraction, as well as a reduction in trap-assisted recombination. The crystalline structure of the hole transporting P3HT layer of PSCs was studied by Tran et al. [189]. A strong degree of P3HT agglomeration in polar solvents including chloroform and tetrahydrofuran **(**THF) has been found by UV-visible absorption spectroscopy, resulting in a high level of crystallinity. F4-TCNQ-doped P3HT HTMs have an electrical conductance of nearly twice that of other typical solvents such as 1,2-dichlorobenzene (DCB). For increasing the performance of the P3HT:F4-TCNQ HTM, the usage of THF as the solvent increased PCE of the device to 13.54 % instead of 9.94% by using DCB. THF is an excellent solvent since it allows for the

controlled crystallization of P3HT while also removing residual PbI_2, which boosts the overall performance and stability of the PSC. With its increased stability and more remarkable performance, P3HT becomes an excellent candidate for cheap large-scale PSCs.

4.2.4. P3CT

Li et al. [190] demonstrated that controlling polyelectrolyte aggregation will boost the efficiency of poly[3-(4-carboxybutyl)thiophene-2,5-diyl] (P3CT) based PSCs. P3CT-Na polymer's heavy aggregation can be broken up by counter ions tailoring and solvent optimization. The PCE improves by using P3CT-CH_3NH_2 to substitute P3CT-Na, with an average increase from 16.9 to 18.9 % (highest 19.6 %) as shown in Fig. 12(c). This study demonstrated the significant function of aggregation control in the interlayer of polyelectrolytes and provided new possibilities for its use in PSCs. Li et al. [191] suggested that doping graphdiyne in P3CT-K as HTM was able to increase P3CT-K surface wettability and increased perovskite morphology with homogeneous distribution and decreased grain size. At the same time, it enhanced the mobility of the hole extraction and reduced the charge recombination, and improved device efficiency. The PCE was 19.5% because of high J_{sc} and FF as shown in Fig. 12(d). Moreover, the hysteresis of the J−V curve has also been minimized. To get rid of the undesirable side effects, Zhang et al. [192] employed a polyelectrolyte (P3CT-BN) that is free of dopants. Bare Pb could interact with C=O group of P3CT-BN and allows holes to pass from the perovskite to the HTM at the perovskite/HTM interface. The P3CT-BN layer may minimize interfacial charge recombination and show excellent film-forming properties. This improves the performance of the device from 18.26 to 19.05% when Spiro-OMeTAD is replaced by P3CT-BN. These findings show that P3CT-BN is a viable HTM to achieve a high PCE and long-term PSC stability. Taking into account the affinity of alkaline metal ions Rb^+, Cs^+ with perovskite materials, the HTMs were examined in inverted PSCs utilizing alkaline metal ions (Rb^+, Cs^+) doped P3CT (denoted as P3CT-Rb, P3CT-Cs). The valence band of perovskite fits well with the work function of P3CT-Rb. Using the $MAPbI_{3-x}Cl_x$ perovskite film over the P3CT-Rb film, a thick and uniform morphology was achieved with excellent crystallinity and few pinholes. Because of this, a strong P3CT-Rb HTM-based device performance of 20.52% was obtained, with a V_{oc} of 1.144 V and an FF of 82.78% [193]. As a result of its admirable stability and reasonably high hole mobility, P3CT was noted as a promising HTM for high performance PSCs. Therefore, it's important to

realize that the perovskite film morphology is greatly affected by the substrate materials. The C=O group on P3CT-BN may interact with bare Pb at perovskite surface, which enhance hole transfer at perovskite/HTM interface.

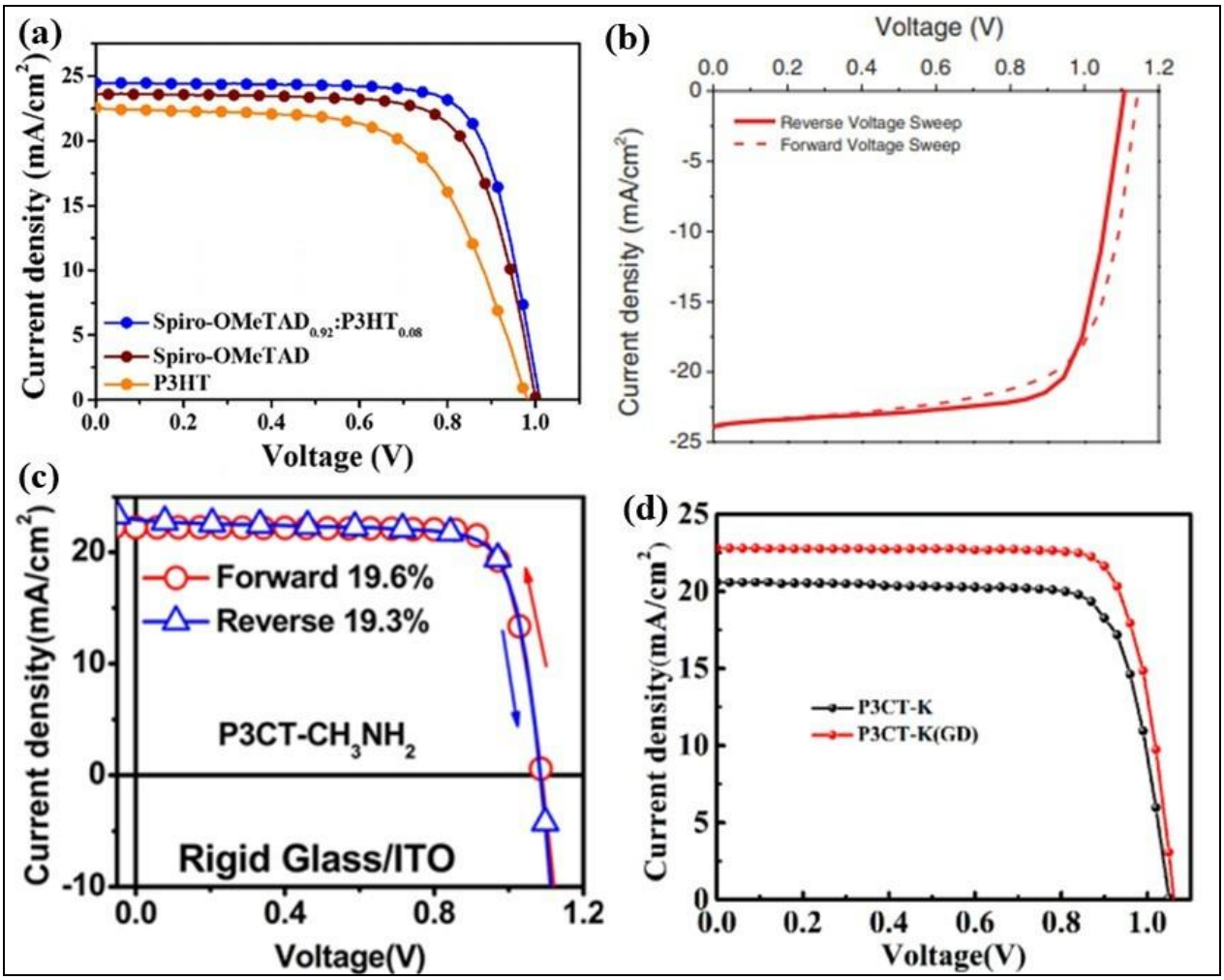

Fig. 12 J-V curves of various PSCs based on (a) SpiroOMeTAD-P3HT composite (Reproduced from [187] with permission. Copyright 2017, American Chemical Society) (b) doped P3HT (Reproduced from [188] with permission. Copyright 2019, Wiley) (c) P3CT-NH_3NH_2 (Reproduced from [190] with permission. Copyright 2017, American Chemical Society) (d) P3CT-K (Reproduced from [191] with permission. Copyright 2018, American Chemical Society)

4.2.5. PTB7

Photoinduced dipoles perform a vital part in HTM charge recombination dynamics and provide a basic understanding of how the HTM polarisation influences its output in PSCs. In this regard, Ahmadi et al. [186] studied the impact of optically generated dipoles in the HTM on the photovoltaic behavior of PSCs. In this particular application, the performance of poly({4,8-bis[(2-ethylhexyl)oxy]benzo[1,2-b:4,5-b′]dithiophene-2,6-diyl}{3-fluoro-2-[(2-ethylhexyl)carbonyl]thieno[3,4-b]thiophenediyl}) (PTB7) was compared to that of P3HT. Under the influence of the device built-in field, it was demonstrated that the photoinduced dipoles were partially present in the amorphous PTB7 layer. The photoinduced dipoles in the PTB7 layer decrease the recombination of photogenerated carriers in the active layer in PSCs. These measurements also show that the photoinduced dipoles in PTB7 can slow down charge accumulation at the electrode interface. The P3HT and PTB7 fabricated devices yielded PCE of 10.8% and 15.9%, respectively as shown in Fig. 13(a). Using a strategy that eliminates the need for dopants, Yuan et al. [194] developed perovskite quantum dot (QD) solar cells with the performance of approximately 12.55 % for PTB7 based device and an incredibly low energy loss of 0.45 eV.

4.2.6. PTEG

PTEG which is a homopolymer comprising tetraethylene glycol (TEG) was synthesized by using a tetraethylene glycol group to regulate the solubility [195]. The planar PSC, which employs PTEG, exhibited an efficiency of 19.8 % without any dopants as shown in Fig. 13(b), which is the maximum performance to date. The research offers a straightforward approach for both the design and synthesis of a wide range of polymeric HTMs. Lee et al. [196] reported a D-A type polymer, alkoxy-PTEG, comprising of benzo[1,2-b:4,5:b′]dithiophene and TEG-substituted 2,1,3-benzothiadiazole. The alkoxy-PTEG is highly soluble even in nonaromatic solvents like 3-methylcyclohexanone (3-MC), which prevents future lead leaching. Finally, alkoxy-PTEG based device without any dopant yielded PCE of 19.9%, whereas the device manufactured with 2-methyl-anisole, which is a commonly used aromatic food additive, achieved PCE of 21.2% as shown in Fig. 13(c). Other properties shown by nuclear magnetic resonance studies indicate that TEG- groups bind lead ions with moderate strength. This lead binding strength is deemed non-destructive to the perovskite lattice since it helps to avoid lead leeching. It is the first paper to investigate the possibility of lead leaching and present solutions to mitigate it.

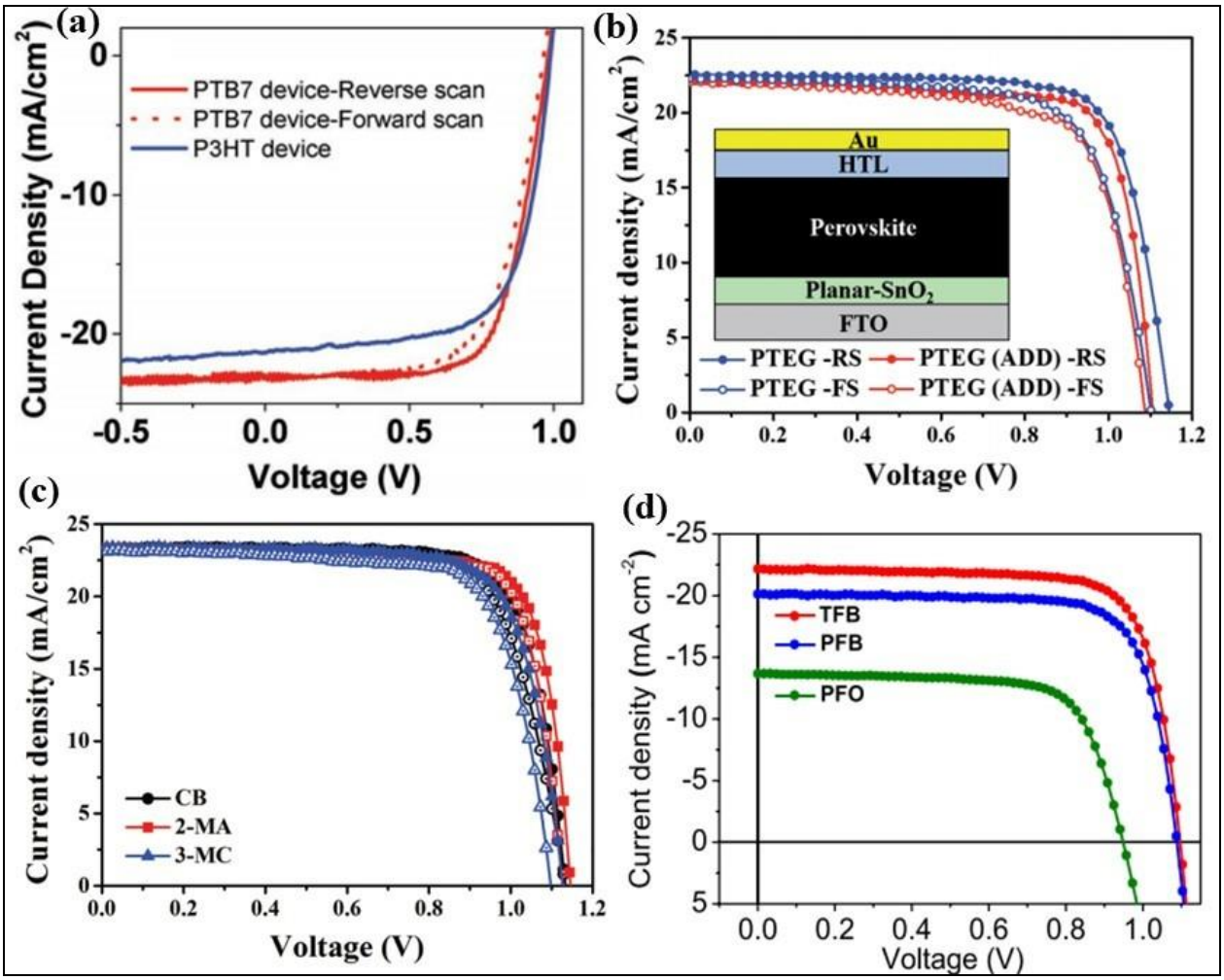

Fig. 13 J-V curves of various PSCs based on (a) PTB7 (Reproduced from [186] with permission. Copyright 2017, Wiley) (b) PTEG (Reproduced from [195] with permission. Copyright 2018, Wiley) (c) Alkoxy-PTEG (Reproduced from [196] with permission. Copyright 2020, Wiley) (d) PFB, TFB, PFO (Reproduced from [198] with permission. Copyright 2020, Wiley)

4.2.7. PFB

Conjugated polymers have long been utilized in preparing mesoscopic PSCs. Perovskite-based solar cells have been fabricated using poly(9,9-dioctylfluorene-co-bis-N,N-(-4-butyl phenyl)-bis-N,N-phenyl-1,4-phenylenediamine) (PFB) as an HTM which is an example of a p-type doped conducting polymer [197]. F4TCNQ was used as a dopant in PFB. The electrical and optical properties of PFB were optimized to maximize the functioning of the solar cell. In the investigation, the maximum PCE observed for F4TCNQ doped mesoscopic PSCs was 14.04%. The obtained efficiency was found to be 57% more than the undoped PFB HTM. This confirms

the presence of oxidation in a p-type doped PFB HTM. The electron transfer from the HOMO of PFB to the LUMO of F4TCNQ was believed to be responsible for this. Using the P-type doped PFB:F4TCNQ composite, the PSC showed superior long-term stability and better efficiency. The polyfluorene copolymer, known as PFB, was studied by Hu et al. [198] for use in constructing an inverted PSC and its performance was compared with TFB and PFO. The electronic properties of the HTM significantly affect the photovoltaic behavior of the device. PFB-based devices have higher interfacial recombination and inferior charge extraction than TFB, resulting in a PCE of 15.91%, and a V_{oc} of up to 1.09 V. This was attributed to the existence of a high energy barrier in the PFO-based devices that causes significant losses in both V_{oc} and photocurrent. On the other hand, TFB exhibited better electronic properties than PFB that led to higher efficiency of 18.48%. The J-V curves of the fabricated devices based on PFB, TFB and PFO are as shown in Fig. 13(d). These findings show that TFB is comparatively better than PFB for inverted PSC HTMs. Finally, it is expected that the designs identified here may influence the molecular design of new HTMs, specifically designed to fabricate highly efficient inverted PSCs.

4.2.8. Other polymeric HTMs

Gaml et al. [199] investigated the HTM 2-ethylhexyl-thienyl group in BDT (PBDTT-FTTE) which can be solution processed. 11.6% PCE was achieved with PBDT-FTTE doped with 3% diiodooctane (DIO), similar to the PCE of 11.6% that was achieved using spiroOMeTAD as the HTM. It was demonstrated that polymer PBDTT-FTTE was processed in an N_2-filled glove box, which is simpler to process while spiroOMeTAD processing was carried out in the ambient air and was doped with additives, causing degradation to the perovskite layer under the film. The surface defects found in perovskite crystals decrease both the overall performance and durability of PSCs. Cai et al. [200] have employed carbazole and benzothiadiazole (BT) based donor-acceptor polymers with various lengths of alkoxy side chains grafted on the BT unit as the dopant-free HTMs. The methoxy group incorporates a beneficial defect passivation effect while also reducing the π−π stacking structural order of these copolymers. In contrast to the Spiro-OMeTAD-based device, the BT unit containing methoxy groups in the copolymer poly[9-(heptadecan-9-yl)-9H-carbazole-2,7-diyl-alt-(5,6- bis(methyloxy)-4,7-di(thiophen-2-yl) benzo[c][1,2,5] thiadiazole-5,5-diyl] (PCDTBT1) showed better PCE and stability, whereas the BT unit containing octyloxy groups in the copolymer poly[9- (heptadecan-9-yl)-9H-carbazole-

2,7-diyl-alt-(5,6-bis-(octyloxy)-4,7-di(thiophen-2-yl)benzo[c] [1,2,5]thiadiazole)-5,5-diyl] (PCDTBT8) resulted in worse efficiency and stability. A superior 19.1% efficiency (as shown in Fig. 14(a)) was obtained using PCDTBT1 as the HTM, owing to the improved charge recombination suppression at the perovskite/PCDTBT1 interface by using methoxy and thiophene groups to enhance the passivation effect. In order to benchmark the effectiveness of PTAA and poly[N,N'-bis(4- butylphenyl)-N,N'-bis(phenyl)benzidine] (PTPD) as alternatives to PEDOT:PSS, Du et al. [201] utilized PEDOT:PSS as the reference and conducted a series of analyses to study main output parameters. The PL intensity difference between short and open circuit conditions is a strong and reasonably simple investigation of surface recombination loss. Through these trials, it was concluded that minimizing p-doping in HTMs would result in improved PCE and higher V_{oc} values, in addition to decreased surface recombination losses. A PCE of 13.49 % was obtained for reference PEDOT:PSS, while an increased PCE of 18.85 % for PTAA, and 19.61 % for PTPD was demonstrated. Lignosulfonic acid-grafted, polyaniline-doped camphorsulfonic acid (LS-PANI-CSA) conducting polymer was investigated as an effective HTM by Dainy et al. [202] for inverted $MAPbI_3$ PSCs prepared by a solution-based low-temperature technique. In this analysis, the morphology and work function of LS-PANI-CSA films were tuned using DMSO as a solvent for further improvement of the effectiveness of the solar cell. It was shown that washing treatment with DMSO improved the LS-PANI-CSA films' electronic properties and increased the hydrophobicity, which was necessary for perovskite formation. The perovskite active layer accumulated on modified LS-PANI-CSA layer has better crystallinity than untreated LS-PANI-CSA and had larger grain size (>5 μm), more consistent and full surface cover and very low pinhole density and residues PbI_2, which lead to higher efficiency and reliability. Using DMSO-treated LS-PANI-CSA as an HTM with 15 nm of film thickness, a maximum 10.8% PCE was obtained. This was a notable improvement over devices using untreated LS-PANI-CSA (5.18%) and PEDOT:PSS-based materials (9.48 %). In addition, the treated LS-PANI-CSA demonstrated higher stability than untreated LS-PANI-CSA and PEDOT:PSS HTM-based units.

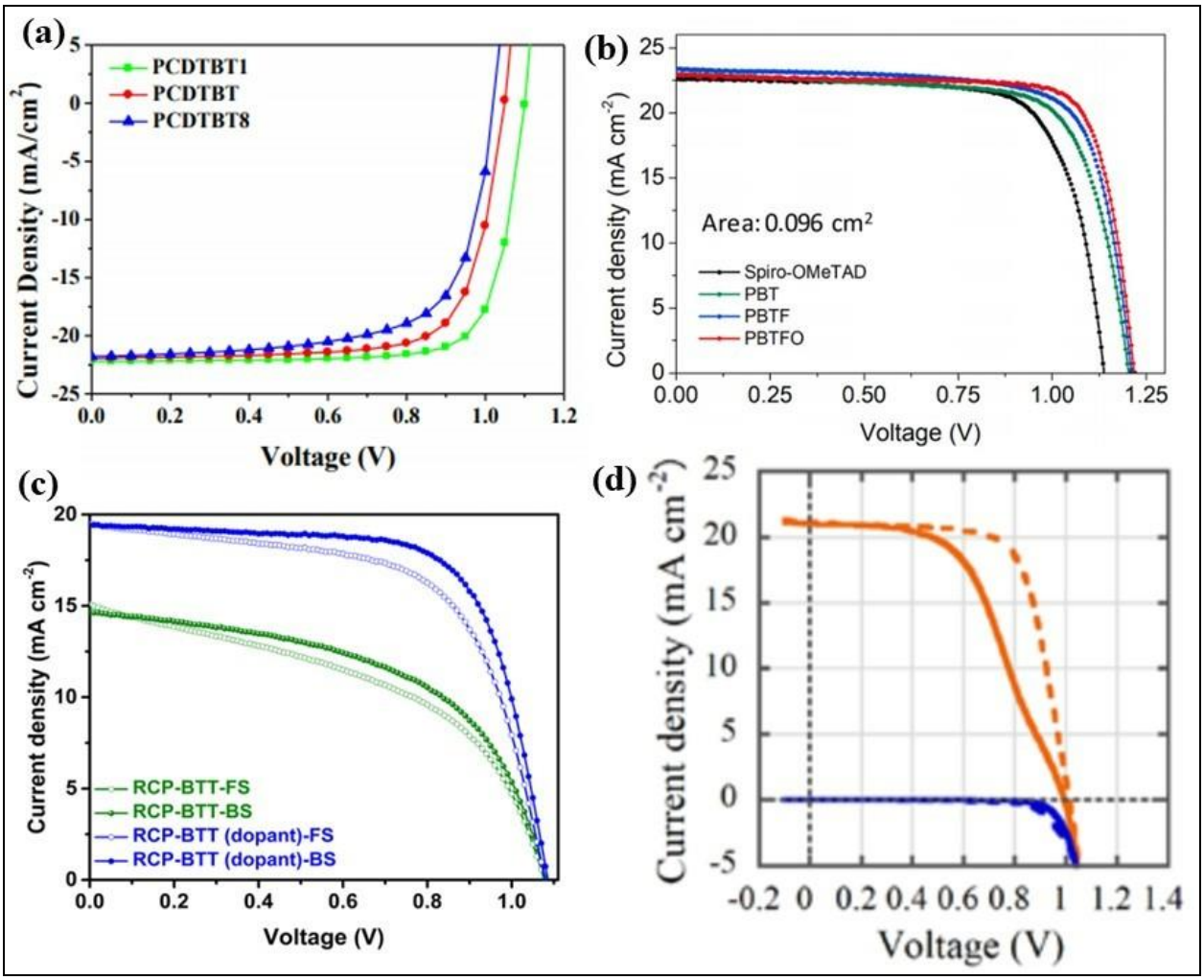

Fig. 14 J-V curves of various PSCs based on (a) PCDTBT (Reproduced from [200] with permission. Copyright 2018, Elsevier) (b) PBTFO, PBT, PBTF (Reproduced from [205] with permission. Copyright 2020, Elsevier) (c) RCP–BTT (Reproduced from [206] with permission. Copyright 2020, Elsevier) (d) PPDT2FBT (Reproduced from [207] under Creative Commons Attribution 4.0 License. Copyright 2020, Chemical Society of Japan)

For developing an HTM based on an ionic liquid polymer, an effective metal-free formulation was formed to overcome reproducibility problems due to the usage of complicated dopant mixtures that use lithium salts and cobalt coordination complexes. 4 orders of magnitude better conductivity was obtained using poly(1-butyl-3- vinylimidazolium bis(trifluoromethylsulfonyl)imide) (PVBI-TFSI) as a dopant, with a value of approximately 1.9×10^{-3} S cm^{-1} [203]. PCE of 20.3% for PVBI-TFSI while 18.4% for the conventional lithium salt-

HTM formulation. PVBI-TFSI appears to serve as a reservoir of protons that accelerates the HTM oxidation. Kulshreshtha et al. [204] showed a new polymer diketopyrene related HTM (poly[[2,5-bis(2- hexyldecyl)-2,3,5,6-tetrahydro-3,6-dioxopyrrolo[3,4-c]pyrrole-1,4-diyl]-alt-[[2,20 -(4,8-bis(4-ethylhexyl-1- phenyl)-benzo[1,2-b:4,5-b0]dithiophene)bis-thieno[3,2-b]thiophen]-5,50 -diyl]])) (PBDTP-DTDPP) for use in PSCs. The material performance was tested in an optimized FTO/SnO_2/perovskite/PBDTP-DTDPP/Au solar cell and 14.78 % PCE was obtained. The time required for non-geminate recombination is far shorter in the polymer HTM than in the spiro-type HTM. The polymeric PBDTP-DTDPP HTM ends reach to the electrode very well and could thus boost the charge collection efficiency of the electrode. A perovskite/polymer graded heterojunction (GHJ) was demonstrated by Li et al. [205] by utilizing a dopant-free polymeric HTM. The intermolecular interactions between perovskite and polymer were maximized which can passive undercoordinated lead cations in perovskite and immobilize its volatile organic cations by forming Lewis-adducts and hydrogen bonds. In order to achieve this objective, new HTMs with functional groups that are defect-healable and cross-linkable were synthesized. It was confirmed that the perovskite crystallinity improves with decreased trap density, thereby increasing the device's built-in ability and reducing carrier recombination, while also improving the overall heat, water, and light stability. The polymer HTM-based devices showed greater reproducibility. The maximum PCE obtainable from PBTFO passivated GHJ devices was 22.1% with a V_{oc} of 1.22 V, J_{sc} of 23.0 mA cm^2, and FF of 78.9%. In the interim, the PBT-based GHJ PSCs achieved a maximum PCE of 20.3%, while PBTF-based GHJ PSCs exhibited the highest PCE of 21.2%. The J-V curves of the fabricated devices are as shown in Fig. 14(b). Murugesan et al. [206] utilized a D-A random copolymer HTM for enhancing the hole extraction and the durability of PSCs. PTB7 has been found to serve as a simple and straight-forward backbone for the formation of highly soluble and mobile D-A dependent, random copolymeric benzodithiophene-thienopyrrole-thienothiophene-thiophene (RCP-BTT) HTMs. Due to its higher compatibility with perovskite, the synthesized RCP-BTT HTM has a deeper HOMO energy level (−5.28 eV) than PTB7 (−5.15 eV). In RCP-BTT PSCs, a gradient band alignment of RCP-BTT lead to better hole extraction, resulting in higher PCE. A RCP-BTT incorporating dopant has a V_{oc} of 1.09 V, which is more than the parent PTB7 (1.06 V), resulting in a higher efficiency of 14.57% than PTB7 (as shown in Fig. 14(c)). Most of the

overall gain in PSC efficiency has been derived from the ability of the polymeric RCP-BTT HTM to have a deeper HOMO energy level, and particularly exceptional hole extraction ability.

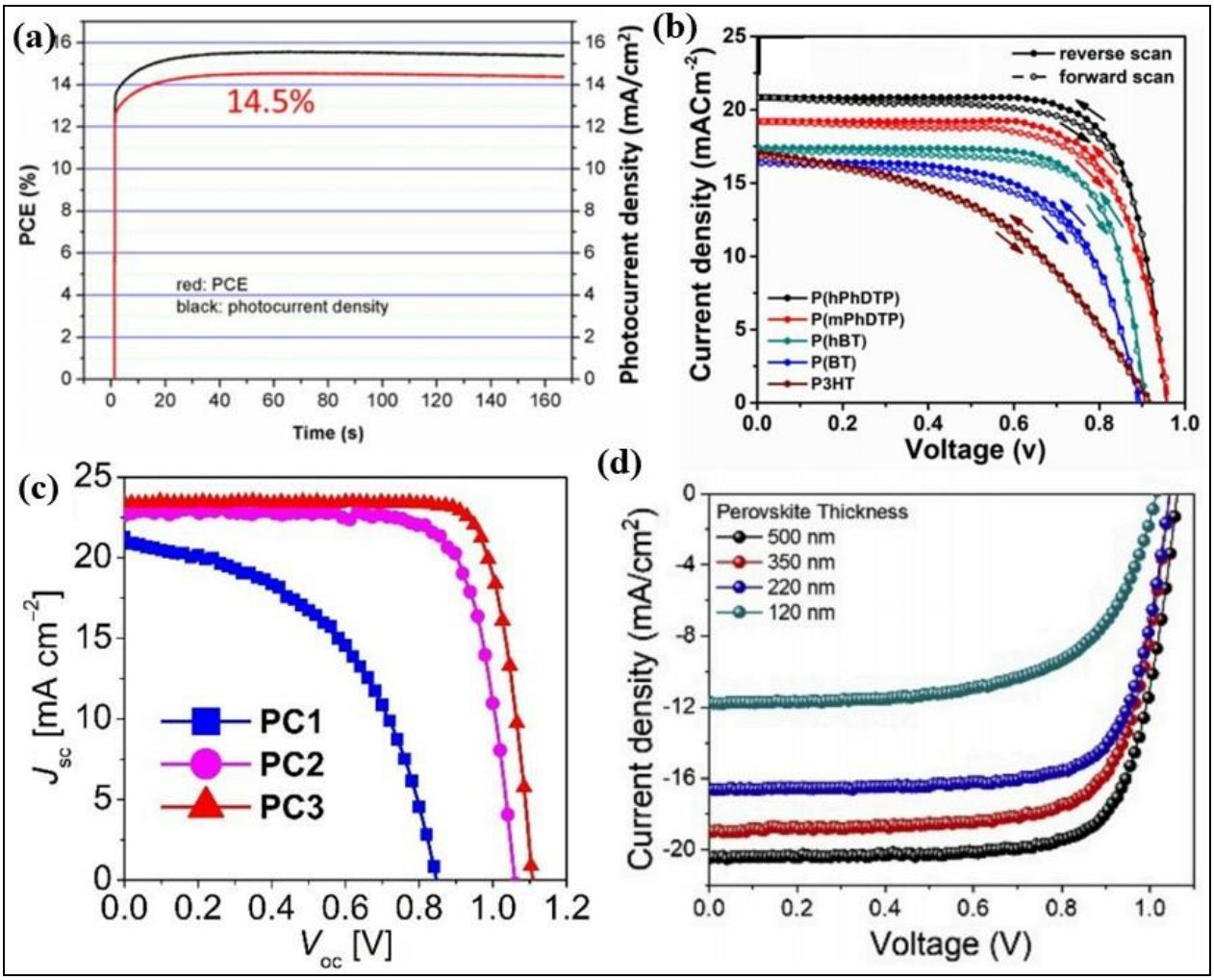

Fig. 15 J-V curves of various PSCs based on (a) poly(DTSTPD-r-BThTPD) (Reproduced from [208] with permission. Copyright 2020, American Chemical Society) (b) P(hPhDTP), P(mPhDTP), P(hBT), P(BT) (Reproduced from [209] with permission. Copyright 2020, Elsevier) (c) PC1, PC2, PC3 (Reproduced from [210] under Creative Commons Attribution 4.0 License. Copyright 2020, American Chemical Society) (d) VNPB (Reproduced from [211] with permission. Copyright 2020, Elsevier)

A donor-acceptor copolymer, poly[(2,5-bis(2- hexyldecyloxy)phenylene)-alt-(5,6-difluoro-4,7-di(thiophen-2-yl)benzo[c][1,2,5]-thiadiazole)] (PPDT2FBT) was used by Nishihara et al. [207] in making mesoporous PSCs. They also implemented a passivation layer between the

perovskite–HTM interface to suppress carrier recombination. It led to an impressive improvement in the FF and consequently, the PCE was increased to 18.4% as shown in Fig. 14(d). Oz et al. [208] reported the formation of $CsPbI_2Br$ α-phase and enhancement of its phase stability in ambient atmosphere via the incorporation of Pb(II) propionate in the $CsPbI_2Br$ precursor. $CsPbI_2Br$ films employing 1 mol% additive and a donor-acceptor polymer poly(DTSTPD-r-BThTPD) as a dopant-free HTM demonstrated PCE of 14.58% as shown in Fig. 15(a). Four new polymers have been examined for effective and stable PSCs as promising processable, dopant-free, polymeric HTM [209]. The HTMs poly(5,5'-dimethyl-2,3'-bithiophene), poly(3-hexyl-5,5'- dimethyl-2,3'-bithiophene), poly(1-(4- methoxyphenyl)-2,5-bis(5-methylthiophen-2-yl)-1H-pyrrole) and poly(1-(4-hexylphenyl)-2,5-bis(5-methylthiophen-2-yl)-1H-pyrrole), abbreviated respectively as p(BT), p(hBT), p(mPhDTP), and p(hPhDTP), were effectively synthesised via a simple synthetic route from reasonably inexpensive raw materials. There is a potential that these polymers will be economical, and the HOMO energy of the perovskite active layer will be favorable with regard to the valence band. The integration of new HTMs into the PSC design showed PCEs of 9.63, 11.10, 14.45, and 16.20 % for p(BT), p(hBT), p(mPhDTP), and p(hPhDTP) respectively, without any dopants and additives as shown in Fig. 15(b). A novel series of polymer-type phenanthrocarbazole (PC) based HTMs (PC1, PC2 and PC3) have been synthesised by the insertion of a PC unit in a polymeric thiophene or selenophen chain to increase the π-π stacking of neighbouring polymer chains and correspondingly for effectively interacting with the perovskite surface via the long and flat conjugated backbone of the PC [210]. The appropriate energy levels, high thermostability and moisture resistivity, along with notable photoelectric properties, were achieved by careful tuning of the elemental composition along with conformation of the polymers. PSCs with PC3 as dopant-free HTM demonstrated 20.8 % stabilized PCE (as shown in Fig. 15(c)) and substantially improved durability, making one of the best PSCs on the basis of dopant-free HTMs. Further theoretical as well as experimental studies showed that the planar shape of the polymers helps to stack the polymer chains orderly and face-to-face. Furthermore, the addition of the “Lewis soft” selenium atom allows the Pb–Se interaction to serve as a passivation layer for perovskite films' surface trap sites, thus facilitating interfacial charge separation. By implementing a thermal cross-linked polymer developed by VNPB polymerization, Yu et al. [211] have successfully demonstrated highly stable semitransparent PSCs as an alternative to Spiro-OMeTAD. It was

noticed that high performance requires the post-annealing of the completed devices featuring poly-VNPB and a dielectric-metal-dielectric MoO_x/Au/MoO_x transparent electrode. The PCE of PSCs was increased from 10.7% to 16.7% with an average visible transmittance of approximately 10%, as shown in Fig. 15(d). This was due to the improved extraction of charges and the suppression of photo-generated charge carriers in the devices, which are possibly due to improved conductivity of PolyVNPB following MoO_x doping.

Table 2: Photovoltaic parameters of PSCs employing various polymeric HTMs.

HTM	**Dopants/additive**	**Configuration**	**Perovskite deposition method**	**Device structure**	**V_{oc} (V)**	**J_{sc} (mA/cm^2)**	**FF (%)**	**PCE (%)**	**Year**	**Ref.**
PEDOT:PSS	No dopant	ITO/HTM/$MAPbI_3$/PCBM/Al	One-step deposition	Planar p-i-n	0.83	16.4	75	10.23	2016	[162]
PEDOT:PSS	No dopant	ITO/HTM/$MAPbI_3$/PCBM/BCP/Ag	Two-step sequential spin coating	Planar p-i-n	0.92	17.2	80	12.7	2017	[163]
PEDOT:PSS	DMSO	ITO/HTM/$MAPbI_3$/PCBM/BCP/Ag	Two-step sequential spin coating	Planar p-i-n	0.92	22.7	80	16.7	2017	[163]
PEDOT:PSS	No dopant	ITO/HTM/$MAPbI_{3-x}Cl_x$/ PCBM/PFN/Al	spin coating	Planar p-i-n	0.83	20.5	65.8	11.33	2017	[164]
PEDOT:PSS	Au	ITO/HTM/$MAPbI_{3-x}Cl_x$/ PCBM/PFN/Al	spin coating	Planar p-i-n	0.83	21.7	67	12.18	2017	[164]
PEDOT:PSS	Ag	ITO/HTM/$MAPbI_{3-x}Cl_x$/ PCBM/PFN/Al	spin coating	Planar p-i-n	0.83	22.3	67.6	12.68	2017	[164]
PEDOT:PSS	Al	ITO/HTM/$MAPbI_{3-x}Cl_x$/ PCBM/PFN/Al	spin coating	Planar p-i-n	0.83	20.9	65.9	11.58	2017	[164]
PEDO	No	ITO/HTM/$MAPbI_{3-}$	spin	Planar p-	0.9	19.	71	13.3	201	[16

T:PSS	dopant	$_xCl_x$/ PCBM/BCP/Ag	coating	i-n	4	9			7	5]
PEDOT:PSS	0.15wt% F4-TCNQ	ITO/HTM/$MAPbI_{3-x}Cl_x$/ PCBM/BCP/Ag	spin coating	Planar p-i-n	0.98	20.6	73	14.76	2017	[165]
PEDOT:PSS	0.30wt% F4-TCNQ	ITO/HTM/$MAPbI_{3-x}Cl_x$/ PCBM/BCP/Ag	spin coating	Planar p-i-n	1.02	21.9	77	17.22	2017	[165]
PEDOT:PSS	0.60wt% F4-TCNQ	ITO/HTM/$MAPbI_{3-x}Cl_x$/ PCBM/BCP/Ag	spin coating	Planar p-i-n	0.99	21.5	76	16.19	2017	[165]
PEDOT:PSS	No dopant	ITO/HTM/$MAPbI_3$/PCBM/Ag	Two-step sequential spin coating	Planar p-i-n	0.87	18.4	74.1	11.90	2017	[166]
PEDOT:PSS/GO-10	No dopant	ITO/HTM/$MAPbI_3$/PCBM/Ag	Two-step sequential spin coating	Planar p-i-n	0.95	18.4	76.4	13.44	2017	[166]
PEDOT:PSS/GO-30	No dopant	ITO/HTM/$MAPbI_3$/PCBM/Ag	Two-step sequential spin coating	Planar p-i-n	0.94	21.9	74.7	15.34	2017	[166]
PEDOT:PSS/GO-50	No dopant	ITO/HTM/$MAPbI_3$/PCBM/Ag	Two-step sequential spin coating	Planar p-i-n	0.92	21.4	74.6	14.82	2017	[166]
PEDOT:PSS	No dopant	ITO/HTM/$MAPbI_3$/PCBM/Ag	spin coating	Planar p-i-n	0.89	18.8	74.0	12.52	2017	[145]
PEDOT:PSS	No dopant	ITO/HTM/$MAPbI_3$/PCBM/Ag	Two-step sequential spin coating	Planar p-i-n	0.9	20.7	73	13.6	2017	[125]
PEDOT:PSS	No dopant	ITO/HTM/$MAPbI_3$/PCBM/Ag	spin coating	Planar p-i-n	0.9	19.3	74.4	12.9	2017	[215]
PEDO	No	ITO/HTM/$MAPbI_3$/PC	Cold	Planar p-	0.9	18.	78	14.2	201	[16

T:PSS	dopant	BM/LiF/Al	casting and spin coating	i-n	6	8			8	7]
PEDOT:PSS	Urea	ITO/HTM/$MAPbI_3$/PCBM/Ag	spin coating	Planar p-i-n	1.03	22.5	81	18.8	2018	[168]
PEDOT:PSS-NH_2-OH	No dopant	ITO/HTM/$MAPbI_3$/PCBM/Al	solvent-induced-fast-crystallization deposition method	Planar p-i-n	0.97	20.2	78.1	15.34	2018	[169]
PEDOT:PSS	GO	ITO/HTM/mixed halide perovskite/PCBM/ZnO/Ag	consecutive 2-step method	Planar p-i-n	1.02	21.5	82.3	18.09	2018	[170]
PEDOT:PSS	sodium citrate	ITO/HTM/$MAPbI_{3-x}Cl_x$ /PCBM/BCP/Ag	spin coating	Planar p-i-n	1.13	21.6	75	18.39	2019	[171]
PEDOT:PSS	Methanol:DMF TBT treatment	ITO/HTM/$MAPbI_3Cl$/PCBM/BCP/Ag	spin coating	Planar p-i-n	1.03	19.7	82.2	16.7	2020	[172]
PEDOT:PSS	ethylene glycol and methanol	ITO/HTM/$MAPbI_3$/PCBM/rhodamine/Ag	spin coating	Planar p-i-n	1.04	22.2	80	18.46	2020	[173]
PEDOT:PSS	DMSO dripping	ITO/HTM/$MAPbX_3$/PCBM/BCP/Ag	two-step spin coating	Planar p-i-n	0.98	22.6	73	16.2	2020	[174]
PEDOT:PSS	hydroquinone	ITO/HTM/$FA_{0.3}MA_{0.7}Pb_{0.7}Sn_{0.3}I_3$/PCBM/BCP/	spin coating	Planar p-i-n	0.7	27.	73.	14.65	202	[17

	(HQ)	Ag			3	0	4		0	5]
PEDOT:PSS	No dopant	ITO/HTM/$MAPbI_{3-x}Cl_x$ /PCBM/AZO/Ag	two-step spin coating	Planar p-i-n	0.95	19.6	78	14.52	2019	[178]
PEDOT:PSS	No dopant	ITO/HTM/$MAPbI_{3-x}Cl_x$/ PCBM/BCP/Ag	spin coating	Planar p-i-n	0.9	20.3	68.8	12.58	2019	[139]
PTAA	No dopant	ITO/HTM/$MAPbI_3$/ PCBM/BCP/Ag	Two-step spin coating	Planar p-i-n	1.09	19.7	69.9	15	2017	[176]
RGO/ PTAA	No dopant	ITO/HTM/$MAPbI_3$/ PCBM/BCP/Ag	Two-step spin coating	Planar p-i-n	1.09	20.3	77.7	17.2	2017	[176]
PTAA	No dopant	ITO/HTM/$MAPbI_3$/PCBM/BCP/Ag	spin coating	Planar p-i-n	1.05	20.1	74.1	15.67	2018	[177]
PTAA	No dopant	ITO/HTM/$MAPbI_3$/PCBM/LiF/Ag	spin coating	Planar p-i-n	1.07	22.1	79.2	18.85	2019	[201]
PTAA	No dopant	ITO/HTM/$MAPbI_{3-x}Cl_x$ /PCBM/AZO/Ag	two-step spin coating	Planar p-i-n	1.1	20.8	79	18.12	2019	[178]
PTAA	No dopant	ITO/ATO/c-TiO_2/m-TiO_2/perovskite/HTM/ Au	two-step spin coating	Mesoscopic n-i-p	1.04	24.4	80.4	20.58	2019	[179]
PTAA	No dopant	ITO/HTM/$MAPbI_3$/PCBM/BCP/Ag	spin coating	Planar p-i-n	1.1	22.4	71	18.11	2019	[180]
PTAA	F8BT	ITO/HTM/$MAPbI_3$/PCBM/Bphen/Ag	spin coating	Planar p-i-n	0.01	21.2	71.7	14.88	2020	[181]
PTAA	No dopant	ITO/SnO_2/PCBA/$MAPbI_3$/HTM/MoO_x/Ag	spin coating	Planar n-i-p	1.06	22.1	75	17.6	2020	[182]
PTAA	PMMA	ITO/HTM/$MAPbI_3$/PCBM/Bphen/Ag	one-step spin coating	Planar p-i-n	0.96	22.9	62.2	14.56	2020	[183]
SpiPA-II	No	ITO/HTM/$CsPbI_2Br$/ZnO:C60/Ag	two-step thermal	Planar p-i-n	1.1	14.	76.	12.52	202	[18

(spiro-OMeTAD/PTAA)	dopant		annealing		4	3	4		0	4]
PTAA	TEMPOL	ITO/SnO_2/PCBA/$Cs_{0.12}FA_{0.88}PbI_{2.64}Br_{0.36}$/HTM/$MoO_3$/Ag	spin coating	Planar n-i-p	1.07	22.6	69.5	17.5	2020	[185]
P3HT	No dopant	ITO/TiO_x/$MAPbI_{3-x}Cl_x$/HTM /Au	One-step deposition	Planar n-i-p	0.94	20.5	56	10.8	2016	[186]
spiro-$OMeTAD_{0.92}$/$P3HT_{0.08}$	No dopant	FTO/SnO_2/$(FAPbI_3)_{0.85}(MAPbBr_3)_{0.15}$/HTM/Ag	Two-step spin coating	Planar n-i-p	1.01	24.5	76.2	18.9	2017	[187]
P3HT	No dopant	FTO/SnO_2/$(FAPbI_3)_{0.85}(MAPbBr_3)_{0.15}$/HTM/Ag	Two-step spin coating	Planar n-i-p	0.97	22.8	63.5	13.9	2017	[187]
P3HT	Li-TFSI, TBP, and FK209 Co(III)-TFSI	FTO/c-TiO_2/m-TiO_2/$(FA_{1-x-y}MA_xCs_y)Pb(I_{1-x}Br_x)_3$/HTM/Au	two-step spin coating	Mesoscopic n-i-p	1.09	23.8	73.7	19.25	2019	[188]
P3HT	F4-TCNQ	FTO/SnO_2/$(FAPbI_3)_{0.875}(CsPbBr_3)_{0.125}$ /HTM/Au	spin coating	Planar n-i-p	0.92	22.2	66.2	13.54	2020	[189]
P3CT-Na	No dopant	ITO/HTM/$MAPbI_3$/PCBM/C_{60}/BCP/Ag	spin coating	Planar p-i-n	1.05	21.3	75	18.3	2017	[190]
P3CT-Na	No dopant	PET/ITO/HTM/$MAPbI_3$/PCBM/C_{60}/BCP/Ag	spin coating	Planar p-i-n	1.05	20.8	58	12.6	2017	[190]
P3CT-CH_3NH_2	No dopant	ITO/HTM/$MAPbI_3$/PCBM/C_{60}/BCP/Ag	spin coating	Planar p-i-n	1.09	22.6	77	19.6	2017	[190]

P3CT-CH_3NH_2	No dopant	PET/ITO/HTM/$MAPbI_3$/PCBM/C_{60}/BCP/Ag	spin coating	Planar p-i-n	1.09	22.1	75	18.2	2017	[190]
P3CT-K	graphdiyne	ITO/HTM/$MAPbI_3$/PCBM/ZnO/Al	spin coating	Planar p-i-n	1.06	22.8	80.8	19.5	2018	[191]
P3CT-BN	No dopant	ITO/SnO_2/CPTA/$MAPbI_3$/HTM/Au	spin coating	Planar n-i-p	1.1	23.1	74.8	19.05	2019	[192]
P3CT	Rubidium	ITO/HTM/$MAPbI_{3-x}Cl_x$/ C_{60}/BCP/Ag	spin coating	Planar p-i-n	0.11	21.6	82.7	20.52	2020	[193]
PTB7	No dopant	ITO/TiO_x/$MAPbI_{3-x}Cl_x$/HTM /Au	One-step deposition	Planar n-i-p	0.98	22.9	70	15.9	2016	[186]
PTB7	No dopant	FTO/TiO_2/$CsPbI_3$/HTM/ MoO_3/Ag	consecutive 2-step method	Planar n-i-p	1.27	12.3	80	12.55	2018	[194]
PTEG	No dopant	FTO/c-TiO_2/m-TiO_2/Cs-perovskite/HTM/Au	Two-step spin coating	mesoscopic n-i-p	1.09	22.7	75.4	18.6	2017	[195]
PTEG	TBP and LiTFSI	FTO/c-TiO_2/m-TiO_2/Cs-perovskite/HTM/Au	Two-step spin coating	mesoscopic n-i-p	1.11	22.2	77.3	19.1	2017	[195]
PTEG	No dopant	FTO/SnO_2/Cs-perovskite/HTM/Au	Two-step spin coating	Planar n-i-p	1.14	22.5	77	19.8	2017	[195]
PTEG	TBP and LiTFSI	FTO/SnO_2/Cs-perovskite/HTM/Au	Two-step spin coating	Planar n-i-p	1.1	22.1	78.1	19	2017	[195]
Alkoxy-PTEG	No dopant	FTO/SnO_2/$Cs_{0.06}FA_{0.78}MA_{0.16}Pb_{0.94}I_{2.4}Br_{0.48}$/HTM/Au	spin coating	Planar n-i-p	1.14	23.2	79.8	21.2	2020	[196]
PFB	F4TCNQ	FTO/c-TiO_2/m-TiO_2/$(FAPbI_3)_{0.85}(MAPbBr_3)_{0.15}$/HTM/Au	Two-step spin coating	Mesoscopic n-i-p	1.02	23	67	15.81	2018	[197]
PFB	No dopant	ITO/HTM/Al_2O_3/$Cs_{0.05}(FA_{0.82}MA_{0.14})_{0.95}Pb(I_{0.8}$	spin coating	Planar p-i-n	1.09	19.7	74.3	15.91	202	[198]

		$_5Br_{0.15})_3$/PCBM/BCP/Ag							0	
TFB	No dopant	ITO/HTM/Al_2O_3/$Cs_{0.05}$($FA_{0.82}MA_{0.14})_{0.95}Pb(I_{0.85}Br_{0.15})_3$/PCBM/BCP/Ag	spin coating	Planar p-i-n	1.10	22.1	75.9	18.48	2020	[198]
PBDTT-FTTE	No dopant	FTO/c-TiO_2/m-TiO_2/$MAPbI_3$/HTM/Ag	Two-step sequential dip coating	mesoscopic n-i-p	1	16.6	61.8	10.3	2017	[199]
PBDTT-FTTE	3% DIO	FTO/c-TiO_2/m-TiO_2/$MAPbI_3$/HTM/Ag	Two-step sequential dip coating	mesoscopic n-i-p	0.93	20.6	61	11.6	2017	[199]
PCDTBT	No dopant	ITO/TiO_2/PCBM/$MAPbI_3$/HTM/MoO_3/Au	spin coating	Planar n-i-p	1.05	21.6	72.3	17.1	2018	[200]
PCDTBT1	No dopant	ITO/TiO_2/PCBM/$MAPbI_3$/HTM/MoO_3/Au	spin coating	Planar n-i-p	1.1	21.7	77.6	19.1	2018	[200]
PCDTBT8	No dopant	ITO/TiO_2/PCBM/$MAPbI_3$/HTM/MoO_3/Au	spin coating	Planar n-i-p	1.02	21.2	67.3	15.4	2018	[200]
PTPD	No dopant	ITO/HTM/$MAPbI_3$/PCBM/LiF/Ag	spin coating	Planar p-i-n	1.09	22.3	79.8	19.61	2019	[201]
T-LS-PANI-CSA	No dopant	ITO/HTM/$MAPbI_3$/PCBM/BCP/Ag	One-step method	Planar p-i-n	0.81	19.5	68	10.82	2020	[202]
PBDTP-DTDPP	No dopant	FTO/SnO_2/$Cs_{0.05}(MA_{0.17}FA_{0.83})_{0.95}Pb(I_{0.83}Br_{0.17})_3$/HTM/Au	spin coating	Planar n-i-p	1.08	19.4	68.9	14.73	2020	[204]
PBDTP-DTDPP	TBP and Li-TFSI	FTO/SnO_2/$Cs_{0.05}(MA_{0.17}FA_{0.83})_{0.95}Pb(I_{0.83}Br_{0.17})_3$/HTM/Au	spin coating	Planar n-i-p	1.01	19.2	72.8	14	2020	[204]
PBTFO	No	ITO/SnO_2/Perovskite/	spin	Planar n-	1.2	23	78.	22.1	202	[20

	dopant	HTM/Au	coating	i-p	2		9		0	5]
PBT	No dopant	ITO/SnO_2/Perovskite/ HTM/Au	spin coating	Planar n-i-p	1.2	23	73.5	20.3	2020	[205]
PBTF	No dopant	ITO/SnO_2/Perovskite/ HTM/Au	spin coating	Planar n-i-p	1.21	23.3	75.1	21.2	2020	[205]
RCP–BTT	TBP and LiTFSI	FTO/c-TiO_2/m-TiO_2/$Cs_{0.05}(FA_{0.85}MA_{0.15})_{0.95}Pb(I_{0.85}Br_{0.15})_3$/HTM/Au	Spin coating	mesoscopic n-i-p	1.09	19.4	69	14.57	2020	[206]
PPDT2FBT	No dopant	FTO/c-TiO_2/m-TiO_2/ $FAPbBr_{3-x}I_x$/HTM/Au	Spin coating	mesoscopic n-i-p	1.01	21.1	70	14.9	2020	[207]
poly(DTSTPD-r-BThTPD)	Pb(II) Propionate	FTO/c-TiO_2/m-TiO_2/ $CsPbI_2Br$/HTM/Au	Spin coating	mesoscopic n-i-p	1.15	15.6	81	14.58	2020	[208]
P(hPhDTP)	No dopant	FTO/c-TiO_2/m-TiO_2/ $MAPbI_3$/HTM/Ag	Spin coating	mesoscopic n-i-p	0.97	20.8	80	17.95	2020	[209]
P(mPhDTP)	No dopant	FTO/c-TiO_2/m-TiO_2/ $MAPbI_3$/HTM/Ag	Spin coating	mesoscopic n-i-p	0.96	19.2	78	16.17	2020	[209]
P(hBT)	No dopant	FTO/c-TiO_2/m-TiO_2/ $MAPbI_3$/HTM/Ag	Spin coating	mesoscopic n-i-p	0.92	17.4	68	15.35	2020	[209]
P(BT)	No dopant	FTO/c-TiO_2/m-TiO_2/ $MAPbI_3$/HTM/Ag	Spin coating	mesoscopic n-i-p	0.91	16.4	64	14.47	2020	[209]
PC1	No dopant	FTO/c-TiO_2/m-SnO_2/ $MAPbI_3$/HTM/Au	Spin coating	mesoscopic n-i-p	0.85	21.3	49.1	8.8	2020	[210]
PC2	No dopant	FTO/c-TiO_2/m-SnO_2/ $MAPbI_3$/HTM/Au	Spin coating	mesoscopic n-i-p	1.06	22.7	76.2	18.3	2020	[210]
PC3	No dopant	FTO/c-TiO_2/m-SnO_2/ $MAPbI_3$/HTM/Au	Spin coating	mesoscopic n-i-p	1.11	23.5	80	20.8	2020	[210]

VNPB	No dopant	FTO/SnO_2/C60-SAM/Perovskite/HTM/MoO_x/Au/MoO_x	Two-step spin coating	Planar n-i-p	1.08	20.3	75.8	16.72	2020	[211]

4.3. Small molecule based HTMs

Recently, small molecules have been highlighted as an alternativeHTM candidates. They are comparatively easy to synthesize and have well-defined molecular weights without batch-to-batch variation. Additionally, their strong intermolecular stacking can lead to high charge mobility. Numerous small molecules have been efficaciously exploited as undoped and doped HTMs in PSCs. This section deals with the recently employed small molecules as HTM in PSCs. Table 3 summarizes the photovoltaic parameters of PSCs employing various small molecule-based HTMs.

Among the numerous compositions explored, the cubic α-phase of formamidinium lead triiodide has arisen as the most auspicious semiconductor for highly competent and stable PSCs, and optimising this material's performance in such devices is critical for the perovskite research community. Recently, Jeong et al. [212] pioneered the concept of anion engineering, which employs the pseudo-halide anion formate ($HCOO^-$) to suppress anion-vacancy defects at grain boundaries and on the surface of perovskite films, as well as to enhance the films' crystallinity. The resulting PSC attained a record-breaking PCE of 25.6%, exhibited lasting operational stability (450 hours), and showed intense electroluminescence with external quantum efficiency more than 10%. These findings demonstrate a straightforward method for eliminating the most prevalent and detrimental lattice defects in metal halide perovskites, allowing for easy access to solution-processable films with enhanced optoelectronic performance. Tavakoli et al. [213] reported an effective strategy for boosting the performance of spiro-OMeTAD based PSCs utilizing adamantylammonium halides (ADAHX, X = Cl, Br, I). The solid-state NMR spectroscopy results revealed that ADAHI strongly interacts with the perovskite surface and inturn decreases the non-radiative recombination when incorporated into spiro-OMeTAD. Consequently, ADAHI-modified spiro based HTM increased the performance of the device leading to a high PCE approaching 22%. Fig. 16(a) shows the J–V characteristics of champion PSCs based on ADAHI-containing HTMs. Wang et al. [214] confirmed that altering the

symmetry of spiro-core to a lower level is helpful for designing HTMs. A new spirobisindane-based HTM, Spiro-I was synthesized with a low molecular symmetry and twisted V-shaped structure. Homogeneous pinhole-free films were formed which act as an effective barrier for the perovskite to moisture resulting in high device stability. As a result, PSCs based on Spiro-I as the HTM showed superior performance (PCE=18.57%). Zhang et al. [215] synthesized three copper-based complexes $Cu^{(I/II)}(dpm)_2(PF_6)_2$, $Cu^{(I/II)}(dpe)_2(PF_6)_2$ and $Cu^{(I/II)}(dmbp)_2(PF_6)_2$ abbreviated respectively as JQ1, JQ2 and JQ3 and used them as dopants in spiro-OMeTAD HTM. The redox potential of these complexes notably influenced the doping level and thus, the conductivity of spiro-OMeTAD also increased significantly. The optimized devices with dopants JQ1, JQ2 and JQ3 has PCE of 19.1%, 15.7%, and 17.4%, respectively. In another study by Hu et al. [216], spiro-OMeTAD was used as HTM but with no additive or dopant. Here, the solvent pentachloroethane was utilized instead of chlorobenzene. The fabricated device resulted in 16.4% PCE with improved stability. Although, the device with chlorobenzene solvent and the dopants showed a PCE of 18.4%, the observed stability was low. An outstanding PCE of 21.38% is reported by Sathiyan et al. [217] in spiro-OMeTAD HTM based device where PFPPY was used as dopant. On the other hand, the reference device based on dopants TBP and tris[2-(1H-pyrazol-1-yl)-4-*tert*-butylpyridine)cobalt(III)-tris(bis(trifluoromethylsulfonyl)imide)] (FK209), showed less PCE of 19.69%. Fig. 16(b,c) demonstrates the J-V curve and IPCE spectra of PFPPY based PSC. It was suggested that PFPPY could effectively take the place of TBP and FK209 at the same time. Mirzaei et al. [218] synthesized a new spiro-based HTM, Spiro-Omethoxyimidazole (Spiro-OMeIm 2) which consisted of a cyclic spiro-backbone attached with four diphenylimidazole substituents. In comparison with traditional spiro HTM, the incorporation of the imidazole into this molecule reduced the first oxidation potential from 0.6 V to 0.53 V. This reduced potential approaches the HOMO level of the active layer perovskite. As a result, Spiro-OMeIm 2 based PSC attained PCE as high as 17.1%. Moreover, the cost of the precursors utilized for synthesizing Spiro-OMeIm 2 is nearly 80% less than those used to prepare other spiro-OMeTAD derivatives. Wang et al. [219] synthesized spiro-TTB as an HTM in one-step solution-processed $MAPbI_3$ PSCs. An orthogonal solvent was selected that helped in the deposition of uniform and pinhole-free perovskite films. A favorable energy-level alignment was achieved with spiro-TTB along with high hole mobility. Consequently, the fabricated solar cell device yielded 18.38% PCE. Liu et al. [220] fabricated undoped and doped spiro-OMeTAD-

based solar cells. The undoped spiro-OMeTAD based device exhibited very low PCE and an S-shaped J−V characteristic curve that was attributed to the strong accrual of charges at spiro-OMeTAD and perovskite boundary. The HTM doped with LiTFSI attained a PCE of 19.1%. Conversely, when Lewis acid tris- (pentafluorophenyl)borane (TPFB) (12% content) was doped into spiro-OMeTAD, the resulting device exhibited maximum 20.1% PCE. The improved performance was the result of drastically enhanced charge transportation as well as low recombination loss.

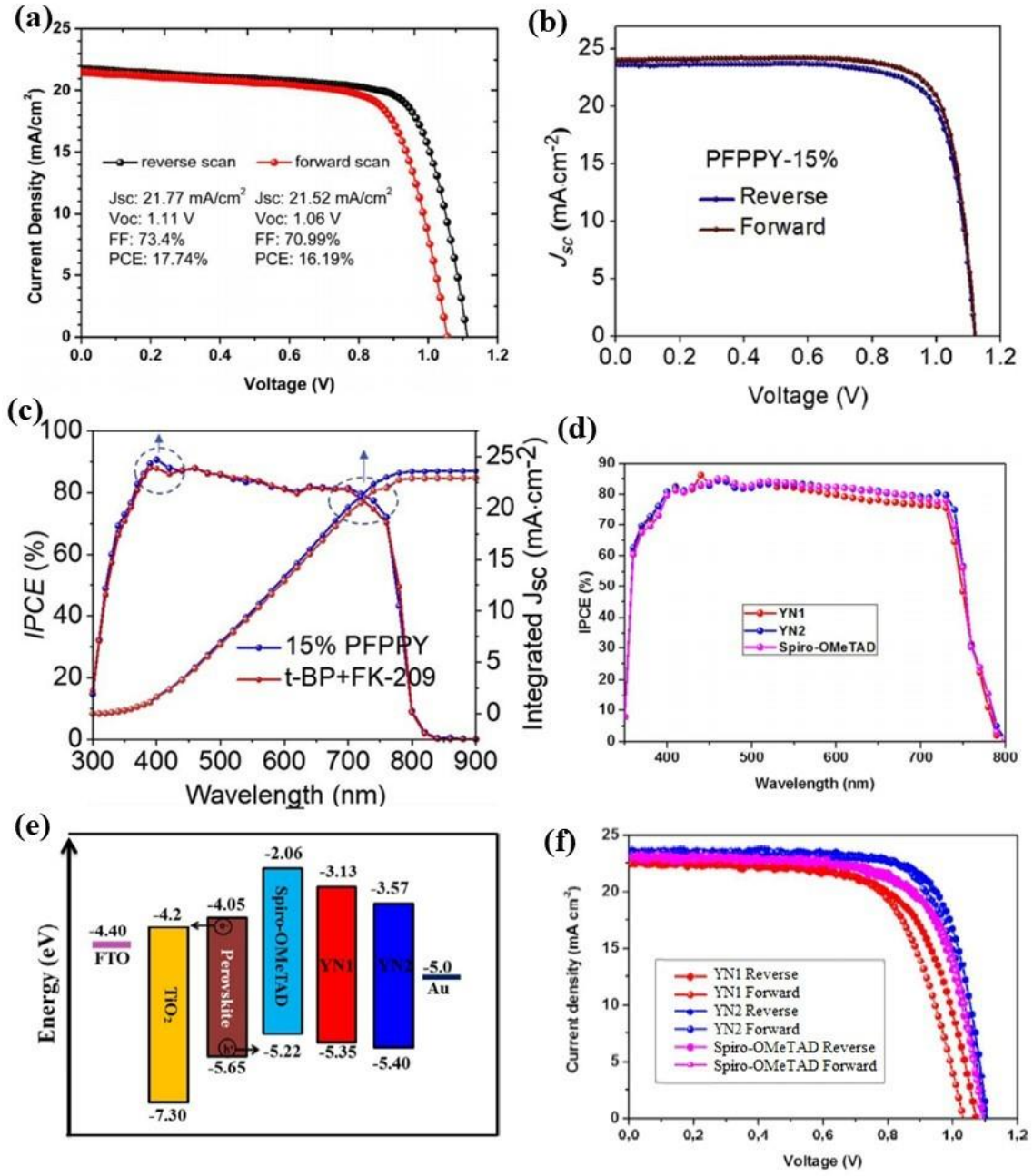

Fig. 16 (a) J–V characteristics of champion PSCs based on ADAHI-containing HTMs (Reproduced from [213] with permission. Copyright 2018, The Royal Society of Chemistry) (b,c) J-V curve and IPCE spectra of PFPPY based PSC (Reproduced from [217] with permission. Copyright 2020, Elsevier) (d-f) J-V curves and energy band diagram of YN1 and YN2 based PSCs (Reproduced from [231] with permission. Copyright 2018, American Chemical Society)

Azmi et al. [221] designed three dopant-free HTMs mDPA-DBTP, pTPA-DBTP and pDPA-DBTP for PSCs. These small molecule HTMs contain di(1-benzothieno)[3,2-b:2′,3′-d]pyrrole (DBTP) as a core unit. Higher hole mobilities and interfacial charge transfer rates were obtained for these HTMs than the well-known undoped and doped spiro-OMeTAD. The best device has 18.09% PCE with mDPA-DBTP HTM and has insignificant hysteresis. Liu et al. [222] designed two unique D–A-conjugated HTMs, DORDTS–DFBT and DERDTS–TBDT. Both these HTMs were dopant-free and had tunable energy levels. The photovoltaic device fabricated using DERDTS–TBDT has a champion PCE of 16.2%, but the performance of the device fabricated using DORDTS–DFBT was, however, low (PCE=6.2%). The high performance of DERDTS–TBDT HTM-based PSCs was ascribed to their high hole mobility and matched energy levels. Moreover, DERDTS–TBDT utilizes an electron-donating benzo[1,2-b:4,5-b′]dithiophene (TBDT) core unit and therefore, the extraction and transportation of hole carriers by this HTM is more efficient than DORDTS–DFBT, that utilizes an electron-withdrawing 5,6-difluoro-2,1,3-benzothiadiazole (DFBT) core unit. Dao et al. [223] reported a non-peripherally substituted octapentyl phthalocyanine ($C5PcH_2$) HTM and showed that its performance could be enhanced by thermal annealing. The results revealed that EQE enhances from 78 to 84 %, the FF and J_{sc} also improved significantly after thermal annealing. A maximum PCE of 12.2 % was obtained at a temperature of 130 ºC when annealed for 10 min. The improved performance was attributed to the enhanced hole extraction and transportation from the perovskite layer to the Au anode as a result of an increase in charge carrier mobility in $C5PcH_2$. Yang et al. [224] synthesized highly efficient and stable PSC consisting of small molecule HTM 4,4′-cyclohexylidenebis[N,N-bis(4-methylphenyl) benzenamine] (TAPC). This π-conjugated hydrophobic HTM was deposited by solution casting without utilizing any dopant. The hole conductivity and charge transportation were improved by thermal annealing due to the enhancement in TAPC crystallinity. Further, a higher charge recombination resistance was obtained, and the champion device showed

maximum PCE of 18.80%. A one-step synthesis strategy was employed by Yin et al. [225] to prepare 50 nm thick carbazole-based HTM 4,4′,4″,4‴-(9-octylcarbazole-1,3,6,8-tetrayl) tetrakis(N,Nbis(4-methoxyphenyl)aniline (CZ-TA). The fabricated PSCs with CZ-TA HTM demonstrated high FF (>81%) and champion PCE of 18.32 % while spiro-OMeTAD based PSC showed PCE of 18.28%. The higher performance was obtained as a result of better hole extraction, transportation as well as reduced recombination. Zhang et al. [226] demonstrated a novel approach for the designing of quaternary ammonium-based molecule X44. Here, the dopant-free HTM was modified by including charged moieties that were escorted by counter ions. The results suggest that no additional doping is required in HTM X44. The homogeneity and the hole conductivity of X44 thin film were considerably affected by the incorporated counter ions and as a result, the fabricated PSC showed 16.2% PCE.

Liu et al. [227] designed simple carbazole-based HTM having triphenylamine moieties that achieved a maximum PCE of 17.18% when used in PSC. This promising PCE was obtained from a carbazole-based material with triphenylamine moieties (LD22) doped with Li-TFSI, TBP, and FK209. On the other hand, the pristine LD22 based device exhibited 13.04% PCE. The efficient performance of the device was attributed to the proper HOMO level (-5.27 eV), high hole mobility (1.65×10^{-5} cm^2V^{-1} s^{-1}), and quite high T_g (132 ºC) of LD22. Further, the device showed excellent reproducibility and the concentration of LD22 had slight to no consequence on the device performance apart from the presence of dopants. In a study by Liu et al. [228], the significance of an appropriate regulation of the precursors' ratio in a one-step solution approach was revealed. A proper adjustment is crucial due to the possibility of the difference in the affinities of the precursors with the different underlying transport layers. This was confirmed by synthesizing a starburst amine molecule 4,4′,4″-tris(3-methylphenylphenylamino)triphenylamine (m-MTDATA) with no dopant as an efficient HTM in PSC. The unreacted PbI_2 in the perovskite was observed to have small resistance loss. Consequently, 17.73% PCE and 79.6% FF was achieved with m-MTDATA based PSC. Mabrouk et al. [229] reported a facile synthesis approach to crosslink 4-(4-methoxyphenyl)-4H-dithieno[3,2-b:2',3'-d]pyrrole (MPDTP) and N-(4-(4H-dithieno[3,2-b:2',3'-d]pyrrol-4-yl)phenyl)-4-methoxy-N-(4-methoxyphenyl)aniline (TPDTP) units with triarylamine-based donor groups that resulted in two new HTMs, H16 and H18, respectively. MPDTP and TPDTP have better π-conjugation across the fused thiophene rings. A higher conductivity, hole mobility as well as superior film quality was achieved with

H16 leading to a higher PCE of 18.16% in H16 based PSC. The PSC based on H18 however displayed a PCE of 15.29%. Using a lucrative precursor ANT dye, Pham et al. [230] reported two highly proficient dopant-free HTMs, 4,10-bis(1,2-dihydroacenaphthylen-5-yl)-6,12-bis(octyloxy)-6,12-dihydronaphtho[7,8,1,2,3-nopqr]tetraphene (ACE-ANT-ACE) and 4,4′-(6,12-bis(octyloxy)-6,12-dihydronaphtho[7,8,1,2,3-nopqr]tetraphene-4,10-diyl)bis(N,N-bis(4-methoxyphenyl)aniline) (TPA-ANT-TPA). The corresponding HTMs based PSCs achieved high PCEs of 17.5% and 13.1% respectively. These new HTMs formed entirely homogeneous and consistent films on the active layer surface that acted as protective coatings for the underlying perovskite films. Moreover, the devices fabricated using non-doped TPA-ANT-TPA showed humidity-resistance and increased stability. Xu et al. [231] synthesized two D-A-D structured HTMs (YN1 and YN2) and employed them in PSCs. These HTMs have low HOMO levels and remarkable hole mobility. YN2 based PSC demonstrated better performance (PCE=19.27%) than YN1 based PSC (PCE=16.03%). J-V curves and energy band diagrams of fabricated PSCs are shown in Fig. 16(d-f). The superior performance of the former PSC was attributed to the utilization of a stronger electronwithdrawing group in YN2.

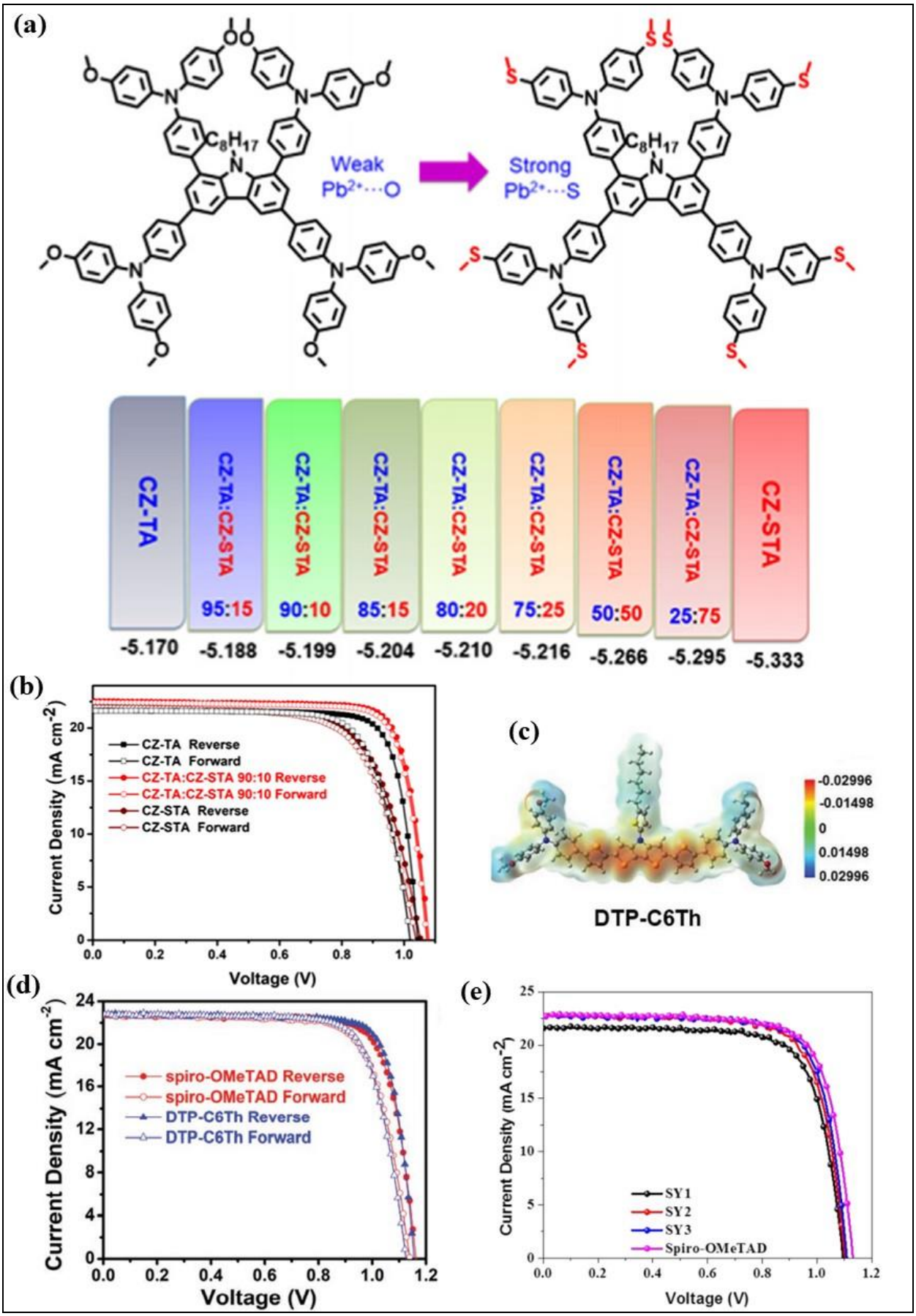
(a)
Weak
Pb2+···O
Strong
Pb2+···S
C8H17
CZ-TA
CZ-TA:CZ-STA
95:15
90:10
85:15
80:20
75:25
50:50
25:75
CZ-STA
-5.170
-5.188
-5.199
-5.204
-5.210
-5.216
-5.266
-5.295
-5.333
(b)
Current Density (mA cm-2)
Voltage (V)
CZ-TA Reverse
CZ-TA Forward
CZ-TA:CZ-STA 90:10 Reverse
CZ-TA:CZ-STA 90:10 Forward
CZ-STA Reverse
CZ-STA Forward
(c)
-0.02996
-0.01498
0
0.01498
0.02996
DTP-C6Th
(d)
Current Density (mA cm-2)
Voltage (V)
spiro-OMeTAD Reverse
spiro-OMeTAD Forward
DTP-C6Th Reverse
DTP-C6Th Forward
(e)
Current Density (mA cm-2)
Voltage (V)
SY1
SY2
SY3
Spiro-OMeTAD

Fig. 17 (a) Chemical structures and HOMO values of CZ-TA and CZ-STA in different weight ratios (b) J-V curves of fabricated devices based on CZ-TA and CZ-STA HTMs (Reproduced from [232] with permission. Copyright 2018, Elsevier) (c) Computed electrostatic surface potential of DTP-C6Th. (d) J-V curves of DTP-C6Th based PSC (Reproduced from [235] with permission. Copyright 2019, Wiley) (e) J-V curves of SY1, SY2, SY3 based PSCs (Reproduced from [244] with permission. Copyright 2020, The Royal Society of Chemistry)

The performance of PSCs is enhanced by the development of new HTM materials. As such, it is highly desired to precisely tune their energy levels especially the HOMO. In this regard, Yin et al. [232] for the first time proposed a binary strategy to synthesize binary HTM composed of CZ-TA and 4,4',4",4"'-(9-octylcarbazole-1,3,6,8-tetrayl)tetrakis(N,N-bis(4-methylthiophenyl)aniline (CZ-STA). An ideal HOMO level was acquired by optimizing the composition of CZ-TA and CZ-STA which have HOMO of -5.170 eV and -5.333 eV, respectively. Chemical structures and HOMO values of CZ-TA and CZ-STA in different weight ratios are depicted in Fig. 17(a). On the addition of 10 wt% CZ-TA, the binary HTM based PSC realized a PCE of 18.32%. On the other hand, for 10 wt% CZ-STA, 19.85% PCE was obtained. J-V curves of fabricated devices based on CZ-TA and CZ-STA HTMs are shown in Fig. 17(b). The better performance of CZ-STA based device was due to the presence of S atom in CZ-STA that downshifted the HOMO level and formed stronger Pb-S interaction with the perovskite than Pb-O in CZ-TA. Schloemer et al. [233] designed and synthesized triarylamine-based HTM doped with its oxidized salt analog (EH44/EH44-ox). The fabricated devices showed high stability in ambient conditions. It was suggested that a minimum of two para-electron-donating groups must be contained by the triarylamine-based dopants in order to achieve stabilized radical cation that prevents the formation of impurity. The PSC that was fabricated by utilizing EHCz-3EtCz/EHCz-3EtCz-ox HTM showed comparable performance to that of Li+ doped spiro-OMeTAD. The PSCs fabricated with EHCz-3EtCz/EHCz-3EtCz-ox demonstrated a little increased performance (PCE=16.33%) in comparison to the PSCs fabricated with EH44/EH44-ox (PCE=16.29%) due to increased V_{oc}. On the contrary, the PSCs fabricated using EHCz-2EtCz/EHCz-2EtCz-ox and EHCz-MeFl/EHCz-MeFl-ox as the HTM showed very low performance. An economical and novel dopant-free fluorinated N',N',N",N"-tetrakis(4-methoxyphenyl)spiro[fluorene-9,9'-xanthene]-2,7-diamine (2mF-X59) organic small molecule was synthesized by Yang et al. [234]. Moreover, 2mF-X59 was modified by F4-TCNQ and its utilization as HTM in $CsPbI_2Br$ PSC

resulted in a PCE of 14.42% due to an impressive V_{oc} of 1.23 V. Yin et al. [235] demonstrated a simple dithieno[3,2-b:2′,3′-d]pyrrol-cored small molecule, DTP-C6Th as an efficient HTM. An ultrathin PMMA passivation layer was added, and the perovskite composition was suitably tuned. Consequently, the DTP-C6Th based device exhibited an outstanding PCE of 21.04%. Fig. 17(c,d) shows the computed electrostatic surface potential of DTP-C6Th and J-V curves of the fabricated devices. Guan et al. [236] utilized benzoic acid as a dopant in spiro-OMeTAD to improve its conductivity and accelerate the oxidation process. Lithium benzoate was formed that helped in the production of a uniform spiro-OMeTAD film by the reduction of voids. In the interim, by the optimization of the dopant concentration, the hysteresis of the fabricated PSC also reduced efficiently attaining high PCE approaching 16.26%. Zhang et al. [237] synthesized D-A-D structured dopant-free YN3 and employed it as HTM in hybrid as well as completely inorganic PSCs. This cyclopenta[hi]aceanthrylene-based HTM exhibited PCEs of 12.05% and 18.84% in $CsPbI_2Br$ and $(FAPbI_3)_{0.85}(MAPbBr_3)_{0.15}$ devices, respectively. An aggregation-induced emission (AIE) molecule, 2-(2,7-bis(4- (bis(4-methoxyphenyl)amino)phenyl)-9H-fluoren-9-ylidene)malononitrile (TFM) was utilized as HTM by Cao et al. [238] that showed better performance than PEDOT:PSS HTM. The PSC employing TFM showed PCE of 16.03%, whereas for the device based on PEDOT:PSS, PCE was 14.95%. XPS measurements showed that there was efficient passivation of unreacted Pb on the perovskite surface by the cyanide groups of TFM that led to suppressed nonradiative recombination at the HTM/perovskite interface.

Most recently, HTMs with a D-A type molecular framework was syntheisized by Chen et al. [239] via a new dendritic engineering approach. In this technique, the dendrons were constructed by using the building block carbazole or diphenylamine or both. It was suggested that the photovoltaic parameters of fabricated PSCs could be finely tuned by variation of the dendron structure. The HTMs used were MPA-PA-BTI, MPA-Cz-BTI, MCz-PA-BTI, and MCz-Cz-BTI that showed exceptional PCEs of 17.41%, 20.81%, 20.09% and 21.35%, respectively. Duan et al. [240] designed three dopant-free HTMs D104, D105, and D106, constructed with a 2,4,6-triarylpyridine building block. Different Y-shapes were formed by varying the periphery 4-methoxyphenyl and bis(4-methoxyphenyl)- amine groups. As a result, the PSCs fabricated using D104, D105, and D106 exhibited excellent PCEs of 16.28%, 17.40%, and 18.24%, respectively. Gao et al. [241] studied the impact of the exchange of dopants in the triarylamine-based HTMs.

Their analogous radical triarylamine cationic salt dopants were exchanged between different HTMs. When EH44-ox was utilized as a dopant, the PCE of all the studied HTMs increased. Further, the hydrophobicity also improved appreciably due to the increase in the ethylhexyl chains per molecule. Moreover, these chains were positioned at the periphery instead of the core. It was also observed that the device performance depends highly on the total ratio of EH44-ox and the concentrations of TBP and precursor solutions. The champion PSC employing HTM EtCz-3EHCz with dopant EH44-ox exhibited 17.75% PCE. An effective and novel immersing method (I-method) was described by Liu et al. [242] for the preparation of organic monomolecular layers (MLs). In this study, MLs of PTPD were prepared as HTMs by a simple immersing and washing strategy. The MLs enhanced the wettability of perovskite precursors that led to the development of dense and homogeneous perovskite films. Additionally, there is an improved energy-level alignment between the perovskite and the MLs. As a result, a high PCE of 18.81% was achieved with ML-PTPD based PSCs. On the other hand, pristine PTPD based PSCs showed 17.21% PCE.

For the first time, a novel and environmental-friendly HTM was employed in PSC by Lu et al. [243]. Two new HTMs F22 and F23 were designed and synthesized that attained 15.31% and 17.6% PCE, respectively in the fabricated devices. These HTMs were processed with nonhalogenated green solvent THF. Higher PCE was achieved with F23 due to the uniform and smooth morphology of the film. Moreover, F23 exhibited outstanding hole transport properties. In a report by Ou et al. [244], a one-pot reaction was used to prepare three inexpensive D-π-D HTMs employing three different π-bridges. Biphenyl, phenanthrene and pyrene were incorporated as π-bridges to prepare SY1, SY2 and SY3, respectively. Among these three, HTM SY3 exhibited higher hole mobility, enhanced hole transportation and better film formation than SY1 and SY2. As a result, the devices with SY3 HTM showed superior performances leading to 13.41% PCE in completely inorganic perovskite and 19.08% in hybrid perovskite-based PSCs. Fig. 17(e) shows the J-V curves of the fabricated devices. An efficient small molecule HTM is reported by Pashaei et al. [245] that is suggested as a good substitute to the expensive spiro-OMeTAD. In this study, a simple CuI-catalyzed reaction was used to prepare triphenylamine-N-phenyl-4-(phenyldiazenyl)aniline (TPA-AZO). It was observed that the HOMO level of TPA-AZO matches with the conduction band of the perovskite active layer and is deeper than spiro-OMeTAD. The PSC fabricated by this HTM TPA-AZO exhibited 17.86% PCE. An HTM

Dibenzo{[f,f′]-4,4′,7,7′-tetraphenyl}diindeno[1,2,3-cd :1′,2′,3′-lm]perylene (DBP) was used in a solar cell with a mixed perovskite as absorber. This device showed a PCE of 9.02% [246]. Pham et al. [247] designed and synthesized a novel HTM 2,3-bis(4′-(bis(4-methoxyphenyl) amino)-[1,1′-biphenyl]-4-yl)fumaronitrile (TPA-BPFN-TPA) which is of the type D-A-D i.e. donor-acceptor-donor. Here, biphenyl fumaronitrile (BPFN) was used as acceptor and triphenylamine (TPA) was taken as a donar, and the conjugated system was employed as the building block for the synthesis of TPA-BPFN-TPA. The prepared HTM was observed to have low-lying HOMO and it was used without any dopant in mesoporous PSCs. The fabricated devices achieved PCE as high as 18.4%. Pineda et al. [248] synthesized two unique stars shaped HTMs STR0 and STR1 that are based on triarylamine. In STR0, partially oxygen-bridged triphenylamine was utilized as core while in STR1, the core was triphenylamine and for side arms, para-substituted triphenylamine was employed. STR0 HTM based solar cell showed a higher PCE of 13.3% than STR1 for which PCE was 11.5% only. The better performance of STR0 was attributed to its more planar configuration, extra stable amorphous glassy state, higher T_g and red-shifted absorption as compared to STR1.

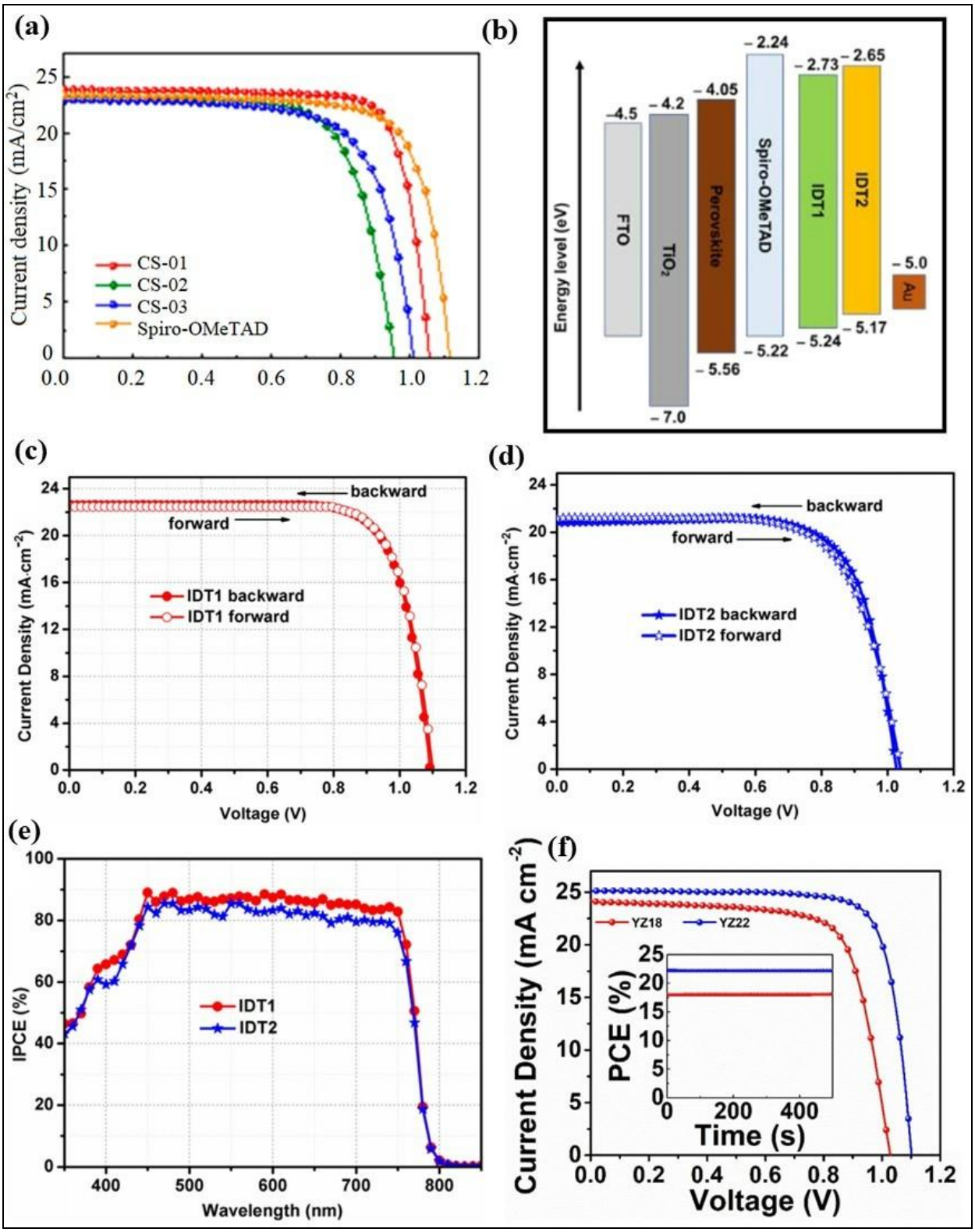

Fig. 18 (a) J-V curves of CS-01, CS-02, CS-03 based PSCS (Reproduced from [249] with permission. Copyright 2020, American Chemical Society) (b-e) Energy band diagram, J-V

curves and IPCE spectra of IDT1 and IDT2 based PSCs (Reproduced from [253] with permission. Copyright 2020, Elsevier) (f) J-V curves of YZ18, YZ22 based PSCs (Reproduced from [256] with permission. Copyright 2020, The Royal Society of Chemistry)

Three dopant-free molecules CS-01, CS-02, and CS-03 that are based on sulfonyldibenzene were synthesized by Qin et al. [249] and employed as HTMs in PSCs. These molecules were inspired by sulfonyldibenzene-based organic thermally activated delayed fluorescence (TADF) materials that have distorted structures and excellentcharge transport properties. These CS series HTMs offered excellent solubility, relatively good thermal stability, as well as appropriate energy levels matched with the perovskite material. Fig. 18(a) shows the J-V curves of the fabricated CS based devices. The highest PCE of 19.94% was achieved with CS-01 HTM based PSC and the fabricated device showed excellent thermal stability. A novel synthesis approach was reported by Tepliakova et al. [250] to utilize thermally evaporated films of four pyrene derivatives Y1, Y2, Y3 and Y4 as dopant-free HTMs in PSCs. These compounds comprise of large aromatic moieties that were able to interact within the film at an intermolecular level. This strategy increased the conductivity of the film and a high PCE of 17.9% was obtained in Y2 HTM based device. Tian et al. [251] presented a new D-A-D structured molecule with 4,4′-dimethoxy triphenylamine as the donor, thiophene as a bridge, and fluorine substituted benzothiadiazole as acceptor, forming tpa-t-FBTD. This molecule was synthesized by using commercial precursors in two steps. Various characterizations revealed that tpa-t-FBTD possessed a planar molecular configuration, high hole mobility, appropriate energy level, and exceptional thermal stability. As a result, dopant-free HTM tpa-t-FBTD yielded 18.9% PCE in planar PSC. Another efficient dopant-free HTM BTPA-8 was reported by Wu et al. [252] that was prepared by the incorporation of anthracene-based central bridge and four dimethoxytriphenylamine leaflets. It was showed that BTPA-8 has high thermal stability and hole mobility. Moreover, it also has matchable band alignment with $MAPbI_3$ and $FA_{0.85}MA_{0.15}PbI_3$ and obtained the best PCE of 12.31% and 17.99% respectively. Wu et al. [253] synthesized two promising HTMs IDT1 and IDT2 that were based on indaceno[1,2-b:5,6-b’]dithiophene (IDT) as core building blocks. The modification of morphology and stacking behaviour of these HTMs was achieved by the introduction of side alkyl chains. Further, for the enhancement of hole transport and the control of energy levels, peripheral triarylamine arms were incorporated. Fig. 18(b-e) shows the energy band diagram, J-V curves and IPCE spectra of IDT1 and IDT2 based PSCs. The J-V

characterictics revealed superior behavior of IDT1 (PCE=19.55%) in comparison to IDT2 (PCE=15.77%) based PSC. Zhang et al. [254] presented facile and inexpensive dopant-free HTMs TBC-1, TBC-2 and TBC-3 that were basically the derivatives of phosphorous tetrabenzotriazacorrole (TBC). A promising PCE of nearly 16.2% was achieved in the device based on α-substituted TBC-1 while β-substituted TBC-2 (PCE=11.4%) and unsubstituted TBC-3 (PCE=6.81%) showed considerablylower PCE. Three D-A-D structured HTMs B1, B2 and B3 were designed and synthesized with benzothiadiazole acceptor unit via the introduction of electron-withdrawing group fluorine atoms and electron-donating group alkoxy as side groups. 12.1% PCE was achieved with B3 based devices that were remarkably higher than those based on B1 and B2. The higher performance of B3 was attributed to its higher hole mobility than the other two HTMs [255]. Recently, a high efficiency of 22.4% was stated by Zhao et al. [256] in PSCs that are based on functionalized HTMs. Two HTMs YZ-18 and YZ-22 were synthesized by a facile strategy where phenanthrene and 1,10-phenanthroline were employed as conjugated cores, respectively, and dianisylphenylamine as side groups. Both YZ18 and YZ22 have similar chemical structures and appropriate HOMO levels and hole mobilities for effective utilization as HTMs in PSCs. The HTMs passivated the perovskite surface defects efficiently and enabled the active layers with lesser surface trap densities. Moreover, the HTMs facilitated proficient charge transfer processes. Consequently, all these features lead to outstanding PCEs to the fabricated solar cell devices i.e. 18.1% for HTM YZ18 and 22.4% for HTM YZ22 based PSC (Fig. 18(f)). YZ22 exhibited the highest reported PCE to date using small molecular dopant-free HTMs. This study encourages further research in the field of PSCs using these functionalized small molecule HTMs.

Table 3: Photovoltaic parameters of PSCs employing various small molecule based HTMs.

HTM	**Dopants/additive**	**Configuration**	**Perovskite deposition method**	**Device structure**	**V_{oc} (V)**	**J_{sc} (mA/cm^2)**	**FF (%)**	**PCE (%)**	**Year**	**Ref.**
Spiro-OMeTAD	No dopant	FTO/SnO_2/$MAPbI_3$/HTM/Au	spin coating	planar n-i-p	1.09	21.7	72.7	17.34	2017	[152]

Spiro-OMeTAD/Cu_xS	No dopant	FTO/SnO_2/$MAPbI_3$/HTM/Au	spin coating	planar n-i-p	1.12	23.1	71.5	18.58	2017	[152]
Spiro-OMeTAD	LiTFSI, TBP, and FK209	FTO/c-TiO_2/m-TiO_2/$(FAPbI_3)_{0.85}(MAPbBr_3)_{0.15}$/HTM/Au	Two-step spin-coating	mesoscopic n-i-p	1.1	23.5	74.8	19.4	2017	[155]
Spiro-OMeTAD	No dopant	ITO/ATO/c-TiO_2/m-TiO_2/perovskite/HTM/Au	two-step spin coating	Mesoscopic n-i-p	1.07	23.7	81.2	20.72	2019	[179]
Spiro-OMeTAD	No dopant	FTO/SnO_2/$(FAPbI_3)_{0.85}(MAPbBr_3)_{0.15}$/HTM/Ag	Two-step spin coating	Planar n-i-p	1	23.4	72.1	16.9	2017	[187]
Spiro-OMeTAD	TBP and LiTFSI	FTO/c-TiO_2/m-TiO_2/$MAPbI_3$/HTM/Ag	Two-step sequential dip coating	mesoscopic n-i-p	0.9	22.6	57	11.6	2017	[199]
Spiro-OMeTAD	Li-TFSI and TBP	ITO/TiO_2/PCBM/$MAPbI_3$/HTM/MoO_3/Au	spin coating	Planar n-i-p	1.09	22.2	78.9	19.4	2018	[200]
spiro-OMeTAD	PVBI-TFSI	FTO/c-TiO_2/m-TiO_2/$K_{0.05}(MA_{0.15}FA_{0.85})_{0.95}PbI_{2.55}Br_{0.45}$/HTM/Au	spin coating	mesoscopic n-i-p	1.16	22.9	76	20.33	2020	[203]
Spiro-OMeTAD	No dopant	FTO/c-TiO_2/m-TiO_2/$FAPbI_3$/ octylammonium iodide/HTM/Au	spin coating	mesoscopic n-i-p	1.18	26.3	81.7	25.6	2021	[212]
spiro-OMeTAD	ADAHX, TBP and LiTFSI	FTO/c-TiO_2/m-TiO_2/triple-cation (FAMACs) perovskite /HTM/Au	Two-step spin coating	Mesoscopic n-i-p	1.16	24.3	77.3	21.9	2018	[213]
Spiro-I	No dopant	FTO/TiO_2/perovskite/ HTM/Au	spin coating	Planar n-i-p	1.06	24.6	71	18.57	2018	[214]

spiro-OMeTAD	JQ1	FTO/c-TiO_2/m-TiO_2/$Rb_{0.05}Cs_{0.05}FA_{0.8}MA_{0.1}Pb(I_{0.85}Br_{0.15})_3$/HTM/Au	spin coating	Mesoscopic n-i-p	0.11	22.8	75	19.1	2018	[215]
spiro-OMeTAD	JQ2	FTO/c-TiO_2/m-TiO_2/$Rb_{0.05}Cs_{0.05}FA_{0.8}MA_{0.1}Pb(I_{0.85}Br_{0.15})_3$/HTM/Au	spin coating	Mesoscopic n-i-p	0.10	22.5	65	15.7	2018	[215]
spiro-OMeTAD	JQ3	FTO/c-TiO_2/m-TiO_2/$Rb_{0.05}Cs_{0.05}FA_{0.8}MA_{0.1}Pb(I_{0.85}Br_{0.15})_3$/HTM/Au	spin coating	Mesoscopic n-i-p	0.10	22.2	72	17.4	2018	[215]
Spiro-OMeTAD	Benzoic acid	FTO/SnO_x/$MAPbI_3$/HTM/Ag	two-step spin coating	Planar n-i-p	1.05	20	77	16.26	2020	[216]
Spiro-OMeTAD in CB solvent	LiTFSI, TBP, and $Co^{III}(pztbpy)_3$	FTO/c-TiO_2/m-TiO_2/$Cs_{0.05}FA_{0.79}MA_{0.16}PbBr_{0.51}I_{2.49}$/HTM/Au	two-step spin coating	Mesoscopic n-i-p	1.10	23.1	72	18.4	2020	[216]
Spiro-OMeTAD in pentachloroethane solvent	No dopant	FTO/c-TiO_2/m-TiO_2/$Cs_{0.05}FA_{0.79}MA_{0.16}PbBr_{0.51}I_{2.49}$/HTM/Au	two-step spin coating	Mesoscopic n-i-p	1.07	23.1	67	16.4	2020	[216]
Spiro-OMeTAD	PFPPY	FTO/c-TiO_2/m-TiO_2/perovskite/HTM/Au	spin coating	Mesoscopic n-i-p	1.12	23.9	79.6	21.38	2020	[217]
Spiro-OMeTAD	TBP, FK209	FTO/c-TiO_2/m-TiO_2/perovskite/HTM/Au	spin coating	Mesoscopic n-i-p	1.08	23.3	78	19.69	2020	[217]
Spiro-OMeIm 2	No dopant	FTO/c-TiO_2/m-TiO_2/$(FAPbI_3)_{0.85}(MAPbBr_3)_{0.15}$/HTM/Au	two-step spin coating	Mesoscopic n-i-p	1.1	20.4	76	17.10	2020	[218]

Spiro-TTB	No dopant	ITO/HTM/$MAPbI_3$/PCBM/BCP/Ag	vacuum assisted blade-coating method	Planar p-i-n	1.07	22.0	78	18.38	2020	[219]
Spiro-OMeTAD	LiTFSI	ITO/SnO_2/$Cs_{0.05}FA_{0.80}MA_{0.15}PbI_{2.55}Br_{0.45}$/HTM/$MoO_3$/Ag	spin coating	Planar n-i-p	1.13	23.1	72.7	19.1	2020	[220]
Spiro-OMeTAD	TPFB	ITO/SnO_2/$Cs_{0.05}FA_{0.80}MA_{0.15}PbI_{2.55}Br_{0.45}$/HTM/$MoO_3$/Ag	spin coating	Planar n-i-p	1.14	23.4	75	20.1	2020	[220]
Spiro-OMeTAD	No dopant	ITO/ZnO/$MAPbI_3$/HTM/Au	sequential deposition	Planar n-i-p	0.9	15.4	49	6.75	2018	[221]
Spiro-OMeTAD	Li-TFSI and TBP	ITO/ZnO/$MAPbI_3$/HTM/Au	sequential deposition	Planar n-i-p	1.12	20.8	75	17.82	2018	[221]
mDPA-DBTP	No dopant	ITO/ZnO/$MAPbI_3$/HTM/Au	sequential deposition	Planar n-i-p	1.12	21.1	76	18.09	2018	[221]
pTPA-DBTP	No dopant	ITO/ZnO/$MAPbI_3$/HTM/Au	sequential deposition	Planar n-i-p	1.09	20.1	72	15.63	2018	[221]
pDPA-DBTP	No dopant	ITO/ZnO/$MAPbI_3$/HTM/Au	sequential deposition	Planar n-i-p	1.06	19.4	68	14.10	2018	[221]
DORDTS – DFBT	No dopant	ITO/TiO_2/$MAPbI_{3-x}Cl_x$/HTM / MoO_3/Ag	Spin coating	Planar n-i-p	0.98	17.1	37.2	6.2	2016	[222]

DERDTS–TBDT	No dopant	ITO/TiO_2/$MAPbI_{3-x}Cl_x$/HTM / MoO_3/Ag	Spin coating	Planar n-i-p	1.05	21.2	72.8	16.2	2016	[222]
C5PcH$_2$	No dopant	FTO/c-TiO_2/m-TiO_2/$MAPbI_3$/HTM/MoO_x/Au	One-step deposition	mesoscopic n-i-p	0.99	18.8	55	11.5	2017	[223]
TAPC	No dopant	ITO/HTM/$MAPbI_3$/PCBM/Ag	spin coating	Planar p-i-n	1.04	22.3	81.1	18.8	2017	[224]
CZ-TA	No dopant	FTO/SnO_2/C_{60}-SAM/$MA_{0.7}FA_{0.3}PbI_3$/HTM/Au	spin coating	Planar n-i-p	1.04	21.6	81	18.32	2017	[225]
X44	No dopant	FTO/c-TiO_2/m-TiO_2/$FA_{0.85}MA_{0.15}Pb(I_{0.85}Br_{0.15})_3$ /HTM/Au	spin coating	Mesoscopic n-i-p	1.08	21.0	67	15.2	2017	[226]
LD22	No dopant	FTO/c-TiO_2/m-TiO_2/$(FAPbI_3)_{0.85}(MAPbBr_3)_{0.15}$/HTM/Au	Two-step spin coating	Mesoscopic n-i-p	1.03	19.6	65	13.04	2018	[227]
LD22	Li-TFSI, TBP and FK209	FTO/c-TiO_2/m-TiO_2/$(FAPbI_3)_{0.85}(MAPbBr_3)_{0.15}$/HTM/Au	Two-step spin coating	Mesoscopic n-i-p	1.06	21.1	77	17.18	2018	[227]
m-MTDATA	No dopant	ITO/HTM/$MAPbI_3$/C_{60}/BCP/Ag	one-step solution approach	Planar p-i-n	1.03	21.5	79.6	17.73	2018	[228]
H16	No dopant	FTO/c-TiO_2/m-TiO_2/mixed perovskite/HTM/Au	Two-step spin coating	Mesoscopic n-i-p	1.10	23.2	70.4	18.16	2018	[229]
H18	No dopant	FTO/c-TiO_2/m-TiO_2/mixed perovskite/HTM/Au	Two-step spin coating	Mesoscopic n-i-p	1.08	22.3	62.8	15.29	2018	[229]
TPA-ANT-TPA	No dopant	FTO/c-TiO_2/m-TiO_2/$MAPbI_3$/HTM/Ag	solvent engineering	Mesoscopic n-i-p	1.03	21.0	79.6	17.5	2018	[230]
ACE-ANT-	No	FTO/c-TiO_2/m-TiO_2/$MAPbI_3$/HTM/A	solvent engineeri	Mesoscopic n-i-p	1.03	18.7	67.1	13.1	201	[230]

ACE	dopant	g	ng						8	
YN1	No dopant	FTO/c-TiO_2/m-TiO_2/$(FAPbI_3)_{0.85}(MAPbBr_3)_{0.15}$/HTM/Au	Two-step spin coating	Mesoscopic n-i-p	1.07	22.3	67	16.03	2018	[231]
YN2	No dopant	FTO/c-TiO_2/m-TiO_2/$(FAPbI_3)_{0.85}(MAPbBr_3)_{0.15}$/HTM/Au	Two-step spin coating	Mesoscopic n-i-p	1.11	23.1	75	19.27	2018	[231]
CZ-TA:CZ-STA	No dopant	FTO/SnO_2/C_{60}-SAM/$MA_{0.7}FA_{0.3}PbI_3$/HTM/Au	spin coating	Planar n-i-p	1.08	22.5	81.5	19.85	2018	[232]
EH44	EH44-ox	ITO/SnO_2/perovskite/HTM/MoO_x/Al	spin coating	Planar n-i-p	1.07	21.8	69	16.29	2019	[233]
EHCz-3EtCz	EHCz-3EtCz-ox	ITO/SnO_2/perovskite/HTM/MoO_x/Al	spin coating	Planar n-i-p	1.09	21.5	69	16.33	2019	[233]
2mF-X59 + F4-TCNQ	No dopant	FTO/TiO_2/$CsPbI_2Br$/HTM/Au	two-step spin coating	Planar n-i-p	1.23	15.2	77.1	14.42	2019	[234]
DTP-C6Th	No dopant	FTO/SnO_2/C60-SAM/$MA_{0.7}FA_{0.3}Pb(I_{0.925}Br_{0.075})_3$/HTM/Au	two-step spin coating	Planar n-i-p	1.15	22.7	79.9	21.04	2019	[235]
YN3	No dopant	FTO/c-TiO_2/m-TiO_2/$(FAPbI_3)_{0.85}(MAPbBr_3)_{0.15}$/HTM/Au	spin coating	Mesoscopic n-i-p	1.12	22.4	75	18.84	2019	[237]
YN3	No dopant	FTO/c-TiO_2/m-TiO_2/$CsPbI_2Br$/HTM/Au	spin coating	Mesoscopic n-i-p	1.12	14.9	72	12.05	2019	[237]
TFM	No dopant	ITO/HTM/CsFAMA-mixed perovskite/C60/BCP/Ag	one-step anti-solvent method	Planar p-i-n	0.97	22.6	72.9	16.03	2020	[238]
MPA-PA-BTI	No dopant	ITO/HTM/CsFAMA-mixed perovskite/C60/BCP/Ag	one-step antisolvent method	Planar p-i-n	0.99	22.1	79.4	17.41	2021	[239]

MPA-Cz-BTI	No dopant	ITO/HTM/CsFAMA-mixed perovskite/C60/BCP/Ag	one-step antisolvent method	Planar p-i-n	1.07	22.8	85.2	20.81	2020	[239]
MCz-PA-BTI	No dopant	ITO/HTM/CsFAMA-mixed perovskite/C60/BCP/Ag	one-step antisolvent method	Planar p-i-n	1.08	22.6	82.1	20.09	2020	[239]
MCz-Cz-BTI	No dopant	ITO/HTM/CsFAMA-mixed perovskite/C60/BCP/Ag	one-step antisolvent method	Planar p-i-n	1.10	23.2	83.5	21.35	2020	[239]
D104	No dopant	ITO/HTM/$MAPbI_3$/PCBM/Ag	spin coating	Planar p-i-n	1.05	21.2	73.4	16.28	2020	[240]
D105	No dopant	ITO/HTM/$MAPbI_3$/PCBM/Ag	spin coating	Planar p-i-n	1.04	21.9	76.1	17.40	2020	[240]
D106	No dopant	ITO/HTM/$MAPbI_3$/PCBM/Ag	spin coating	Planar p-i-n	1.05	22.3	77.8	18.24	2020	[240]
EtCz-3EHCz + EH44-ox	No dopant	FTO/c-TiO_2/m-TiO_2/ $Cs_{0.05}(MA_{0.13}FA_{0.87})_{0.95}Pb(I_{0.83}Br_{0.17})_3$/HTM/Au	spin coating	Mesoscopic n-i-p	1.08	22.1	74.1	17.75	2020	[241]
P_{UV}-PTPD	No dopant	ITO/HTM/$MAPbI_{3-x}Cl_x$/ C60/BCP/Ag	spin coating	Planar p-i-n	1.06	20.7	78.1	17.21	2020	[242]
ML-PTPD	No dopant	ITO/HTM/$MAPbI_{3-x}Cl_x$/ C60/BCP/Ag	spin coating	Planar p-i-n	1.07	21.1	83.2	18.81	2020	[242]
F22	No dopant	ITO/C60/$MAPbI_{3-x}Cl_x$/HTM /MoO_3/Ag	spin coating	Planar n-i-p	1.0	21.1	72.0	15.31	2020	[243]
F23	No dopant	ITO/C60/$MAPbI_{3-x}Cl_x$/HTM /MoO_3/Ag	spin coating	Planar n-i-p	1.0	21.6	76.0	17.60	2020	[243]
SY1	No	ITO/SnO_2/ZnO_2/$CsPbI_2Br$/HTM/MoO_3/Ag	spin coating	Planar n-i-p	1.0	21.	73.	17.46	202	[24

	dopant				9	6	5		0	4]
SY2	No dopant	ITO/SnO_2/ZnO_2/$CsPbI_2Br$/HTM/MoO_3/Ag	spin coating	Planar n-i-p	1.09	22.5	74.6	18.49	2020	[244]
SY3	No dopant	ITO/SnO_2/ZnO_2/$CsPbI_2Br$/HTM/MoO_3/Ag	spin coating	Planar n-i-p	1.11	22.6	75.7	19.08	2020	[244]
TPA-AZO	No dopant	FTO/c-TiO_2/m-TiO_2/$(FAPbI_3)_{0.85}(MAPbBr_3)_{0.15}$/HTM/Au	two-step spin coating	Mesoscopic n-i-p	1.12	20.7	77	17.86	2020	[245]
DBP	No dopant	FTO/c-TiO_2/m-TiO_2/$(FAPbI_3)_{0.85}(MAPbBr_3)_{0.15}$/HTM/Au	two-step spin coating	Mesoscopic n-i-p	0.88	18.7	55.1	9.10	2020	[246]
TPA-BPFN-TPA	No dopant	FTO/c-TiO_2/m-TiO_2/$MAPbI_3$/HTM/Ag	spin coating	Mesoscopic n-i-p	1.04	22.7	78	18.4	2020	[247]
STR0	No dopant	FTO/c-TiO_2/m-TiO_2/$MAPbI_3$/HTM/Au	spin coating	Mesoscopic n-i-p	1.02	16.3	78	13.3	2020	[248]
STR1	No dopant	FTO/c-TiO_2/m-TiO_2/$MAPbI_3$/HTM/Au	spin coating	Mesoscopic n-i-p	0.95	17.3	67	11.5	2020	[248]
CS-01	No dopant	FTO/c-TiO_2/m-TiO_2/$(FAPbI_3)_{0.875}(MAPbBr_3)_{0.075}(CsPbI_3)_{0.05}(PbI_3)_{0.03}$/HTM/Au	spin coating	Mesoscopic n-i-p	1.06	23.8	79	19.94	2020	[249]
CS-02	No dopant	FTO/c-TiO_2/m-TiO_2/$(FAPbI_3)_{0.875}(MAPbBr_3)_{0.075}(CsPbI_3)_{0.05}(PbI_3)_{0.03}$/HTM/Au	spin coating	Mesoscopic n-i-p	0.95	23.1	71	15.62	2020	[249]
CS-03	No dopant	FTO/c-TiO_2/m-TiO_2/$(FAPbI_3)_{0.875}(MAPbBr_3)_{0.075}(CsPbI_3)_{0.05}(PbI_3)_{0.03}$/HTM/Au	spin coating	Mesoscopic n-i-p	1.01	22.9	70	16.17	2020	[249]
Y1	No dopant	ITO/SnO_2:PCBA/$MAPbI_3$/HTM/MoO_x/Ag	spin coating	Planar n-i-p	1.07	22.2	61	14.2	2021	[250]
Y2	No	ITO/SnO_2:PCBA/MAP	spin	Planar n-	1.1	21.	78	17.9	202	[25

	dopant	bI_3/HTM/MoO_x/Ag	coating	i-p	0	2			1	0]
Y3	No dopant	ITO/SnO_2:PCBA/MAP bI_3/HTM/MoO_x/Ag	spin coating	Planar n-i-p	1.06	22	70	16.1	2021	[250]
Y4	No dopant	ITO/SnO_2:PCBA/MAP bI_3/HTM/MoO_x/Ag	spin coating	Planar n-i-p	1.06	21.3	64	14.5	2021	[250]
tpa-t-FBTD	No dopant	FTO/SnO_2/perovskite/ HTM/Au	spin coating	Planar n-i-p	1.08	22.4	78.1	18.9	2021	[251]
BTPA-8	No dopant	FTO/c-TiO_2/m-TiO_2/ $FA_{0.85}MA_{0.15}PbI_3$/HTM /Au	two-step spin coating	Mesoscopic n-i-p	1.04	24.2	71	17.99	2020	[252]
IDT-1	No dopant	FTO/c-TiO_2/m-TiO_2/ $(FAPbI_3)_{0.85}(MAPbBr_3)_{0.15}$/HTM/Au	spin coating	Mesoscopic n-i-p	1.10	22.6	78.6	19.55	2020	[253]
IDT-2	No dopant	FTO/c-TiO_2/m-TiO_2/ $(FAPbI_3)_{0.85}(MAPbBr_3)_{0.15}$/HTM/Au	spin coating	Mesoscopic n-i-p	1.03	20.8	73.4	15.77	2020	[253]
TBC-1	No dopant	FTO/c-TiO_2/m-TiO_2/ $MAPbI_3$/HTM/Ag	two-step spin coating	Mesoscopic n-i-p	1.00	22.2	61.5	16.2	2020	[254]
TBC-2	No dopant	FTO/c-TiO_2/m-TiO_2/ $MAPbI_3$/HTM/Ag	two-step spin coating	Mesoscopic n-i-p	0.87	20.8	53.2	11.4	2020	[254]
B1	No dopant	FTO/c-TiO_2/m-TiO_2/ $MAPbI_3$/HTM/Au	spin coating	Mesoscopic n-i-p	0.90	16.9	44	6.95	2020	[255]
B2	No dopant	FTO/c-TiO_2/m-TiO_2/ $MAPbI_3$/HTM/Au	spin coating	Mesoscopic n-i-p	0.92	18.5	60	10.3	2020	[255]
B3	No dopant	FTO/c-TiO_2/m-TiO_2/ $MAPbI_3$/HTM/Au	spin coating	Mesoscopic n-i-p	0.91	20.9	64	12.1	2020	[255]
YZ-18	No dopant	FTO/c-TiO_2/m-TiO_2/ $Cs_{0.1}FA_{0.9}PbI_3$/HTM/Au	spin coating	Mesoscopic n-i-p	1.03	24.1	73	18.1	2020	[256]
YZ-22	No	FTO/c-TiO_2/m-TiO_2/ $Cs_{0.1}FA_{0.9}PbI_3$/HTM/A	spin coating	Mesoscopic n-i-p	1.1	25.	81	22.4	202	[25

	dopant	u				1			0	6]

5. Challenges related to stability

Many kinds of photovoltaic devices and architectures have demonstrated superb performance in nearly all their design categories with inorganic, polymeric and small molecule HTMs, but degradation is known to occur due to a variety of factors (Fig. 19) viz. internal factors as well as when exposed to external circumstances such as light, temperature, humidity, electric field, air and water. Perovskite crystal structures are intrinsically unstable due to the instability of the crystal's chemical components. Due to the stability issues of PSCs, we have done a literature review on different types of HTMs and compiled a list of their device structure and their photovoltaic parameters (V_{OC}, J_{SC}, FF, and efficiency, η), which have more stable efficiency after aging and can reliably serve as a reference for future HTMs for PSCs.

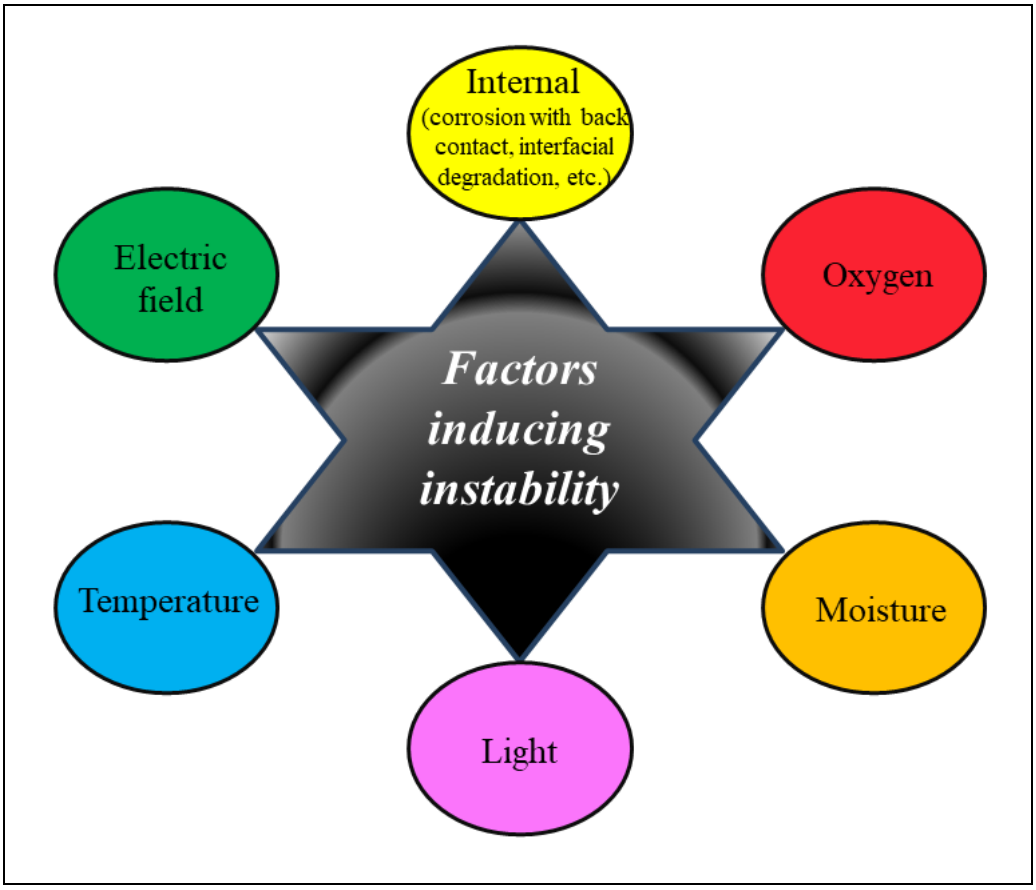

Fig. 19 Factors affecting the stability of PSCs: External and Internal.

A list of tables about the stability are provided below for each classification of the reviewed HTMs. Based on these tables, it can be inferred that the perovskite device's stability will be affected by the HTMs use. To obtain a more stable device, we must first know the source of the instability, which means having a good grasp of the device's structural and morphological features. Additionally, PSCs may have environmental and economic concerns. However, their architecture may be optimized in the future. By following the tables below, researchers may be able to enhance the efficiency and stability of PSCs by optimization of the HTM.

In the following subsections, we have discussed the stability test results of some of the efficient inorganic, polymeric and small molecule HTMs based PSCs.

5.1. Stability of inorganic HTMs

When strontium-doped NiO_x HTM was employed in a solar cell, the device exhibited an outstanding PCE of 20.07%. This device was stored under ambient air at a humidity of 18% for nearly 100 days and as a result, more than 60% of its initial PCE was maintained as shown in Fig. 20(a). In contrast, the device with pristine NiO_x showed relatively poor stability [87]. Fig. 20(b) depicts the long-term stability of the device, which consists of CZTS:Cd/spiro-OMeTAD which was kept at 25 °C [120]. After being stored under ambient air for 2000 hours, the PCE of the control device (based on spiro-OMeTAD) has dropped to only 10% of its initial PCE. However, 90% of the initial PCE remains after the CZTS:Cd device has aged for 3000 hours. The device's humidity stability was also tested. 87% of the initial PCEs are retained for the device with CZTS:Cd after 500 hours of operation at 85% relative humidity, which is much better than the Spiro-OMeTAD-based device. Monitoring the device degradation in an ambient atmosphere and tested in a N_2-filled glovebox under continuous AM 1.5G illumination were used to study the stability of MoO_x/F4-TCNQ based device [130]. Fig. 20(c) shows that the MoO_x based reference device demonstrated poor stability, losing over 50% of its initial efficiency after 150 hours in an ambient atmosphere. Approximately 95% and 70% of the PCE was maintained after 150 and 300 hours, respectively for MoO_x/F4-TCNQ. 95% of initial efficiency was maintained after 40 hours of continuous AM 1.5G irradiation in the glovebox without any UV-filter. But after only one hour, the reference device had degraded to 73% of its initial PCE. These results show that MoO_x HTM-based PSCs are more stable when modified with F4-TCNQ. PSCs employing NiO_x HTM, with and without the organic HTM, were tested

for 500 hours under an inert environment (N_2) [142]. Fig. 20(d) shows that the PSC without the organic HTM maintained approximately 30% of its initial PCE, whereas PSC with the organic HTM maintained nearly 95% of its original PCE, during the same storage time. In order to prevent water and oxygen permeation into the perovskite layer, the improved crystallinity of the perovskite layer along with the refined interfacial contact, is essential. The stability tests of PTAA/VO_x and PTAA/MoO_x based PSCs were performed using an aging chamber integrated into the nitrogen-filled glovebox [151]. A metal halide lamp (37±3 mW/cm^2) was used to illuminate the samples at a temperature of 45±1 °C for 3200 hours. Following that, the treatment with light continued for 1000 hours using high-power LEDs, which emitted light with intensity of 100±3 mW/cm^2 at 50±1 °C. The UV filters were not used throughout the entire aging experiment, which was conducted under open-circuit conditions. The PCE were recorded during the illumination of the device as shown in Fig. 20(e). Reference cells with PTAA/MoO_x as HTM exhibited excellent stability retention (a PCE drop of 24% after 3,200 hours at 30 mW/cm^2 and a drop of 25% after 1,300 hours at 100 mW/cm^2). Higher light intensity and temperature in the second stage triggered the observed accelerated ageing. The PTAA/VO_x HTM shows no decrease in efficiency after the light illumination for 3,200 hours, and there is only a 10% loss in performance after exposed to light for 1300 hours at 100 mW/cm^2. Thus, the findings show that VO_x helps boost PSC operational stability far better than that of MoO_x. Either the films exhibit different phase behavior or the lead halide perovskites react in a chemically different manner. MoO_x is speculated to accelerate the decomposition of $MAPbI_3$, and it could also have an antagonistic effect on other complex lead halides.

The stability of WO_3/spiro-OMeTAD and spiro-OMeTAD-based devices were initially examined under ambient circumstances at room temperature and relative humidity of approximately 20% [156]. Both devices maintained their initial efficiency for about 5 days, as shown in Fig. 20(f); however, after 30 days, the spiro-OMeTAD device's performance deteriorated. Dopants generated pores in the spiro-OMeTAD layer, and these dopants offered a degrading pathway for devices. Alkyl amine radicals or ions can pass through these holes and react with organic chemicals or metal electrodes in the spiro-OMeTAD layer. The WO_3/spiro-OMeTAD layer, on the other hand, avoid such flaws, presumably resulting in better stability. Thermal and moisture stabilities were measured for further investigation. Volatile hydrogen halide and alkyl amine gases are emitted when the perovskite is thermally destroyed; this process

can be thermodynamically enhanced by holes in the spiro-OMeTAD layer. Furthermore, when heated, the spiro-OMeTAD layer undergoes morphological deterioration and collapses. Such issues can be solved using the WO_3 scaffold layer. The thermal stability of the devices was tested at 100 °C. Under both inert and air conditions, the WO_3/spiro-OMeTAD device showed better thermal stability. The WO_3/spiro-OMeTAD device maintained 90% of its initial efficiency under inert conditions over 300 hours, but the spiro-OMeTAD device only maintained 70 % of its initial efficiency due to the lower FF. Both devices showed a rapid drop in efficiency within 100 hours when exposed to air, while the WO_3/spiro-OMeTAD device was marginally more stable. The performance of these devices could not be maintained since the deterioration process is influenced by a variety of external influences, excluding heat. The devices turn yellow as hydrogen halide and alkyl amine gases are emitted, indicating lead iodide deterioration. However, because the WO_3/spiro-OMeTAD layer did not have holes generated by the dopants, these events were not observed. Also noteworthy was the remarkable moisture stability demonstrated by WO_3/spiro-OMeTAD devices. At an exceptionally high humidity of approximately 80%, the moisture stability was studied. WO_3/spiro-OMeTAD's efficiency declined marginally, however the device was still operating at 60% of its initial efficiency after 160 hours. In contrast, the efficiency of the spiro-OMeTAD device suddenly dropped. It was ascribed to the homogenous and compact spiro-OMeTAD layer, which improved the overall stability. A second blocking layer is formed on the perovskite layer via the water-insoluble WO_3 layer on top of it. But while the HTM still contained dopants such as LiTFSI, the absolute moisture stability was not good. It may be possible to further increase the moisture stability if a dopant-free small molecule (that can infiltrate and fill WO_3 pores) is utilized. Table 4 summarizes the stability of PSCs employing various inorganic HTMs.

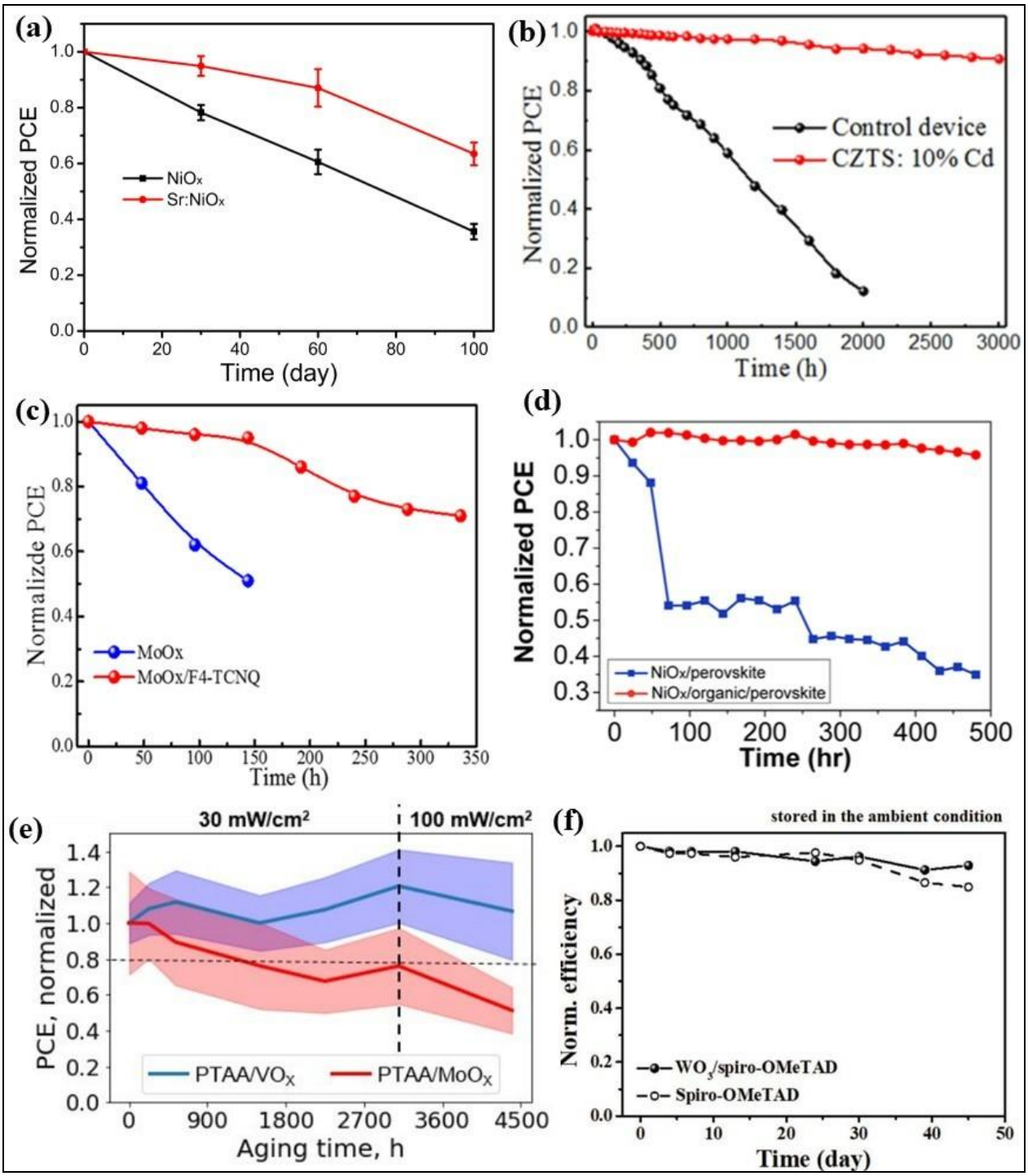

Fig. 20 Stability test results of some of the efficient PSCs based on inorganic HTMs (a) Sr:NiO_x (Reproduced from [87] with permission. Copyright 2018, Elsevier), (b) CZTS:Cd/spiro-OMeTAD (Reproduced from [120] with permission. Copyright 2020, American Chemical Society), (c) MoO_x/F4-TCNQ (Reproduced from [130] with permission. Copyright 2019**,** American Chemical Society), (d) NiO_x with and without organic layer (Reproduced from [142]

with permission. Copyright 2020, American Chemical Society), (e) PTAA/VO_x, PTAA/MoO_x (Reproduced from [151] with permission. Copyright 2020, American Chemical Society), (f) WO_3/spiro-OMeTAD (Reproduced from [156] with permission. Copyright 2018, Wiley)

Table 4: Stability of PSCs employing various inorganic HTMs.

HTM	**Technique used**	**Stability**	**Testing environment**	**Test duration**	**Year**	**Ref.**
NiO_x	Electrochemical deposition	80.5% of its initial PCE was maintained	At RT and RH: 60%	40 days	2018	[68]
NiO_x	Low-temperature solution processing	95% of its initial PCE was retained	under dark storage in a N_2-filled glovebox	102 days	2019	[69]
NiO	interface-engineering	86.7% of its initial PCE was retained	Ambient air conditions under continuous 1 Sun illumination(T: 85˚C)	500 hours	2018	[71]
NiO_x	chemical coprecipitation method	75% of its initial PCE was retained	ambient environment (RH: 40%, T: 25˚C)	1 month	2017	[82]
Cu:NiO_x	chemical coprecipitation method	86% of its initial PCE was retained	ambient environment (RH: 40%, T: 25˚C)	1 month	2017	[82]
NiO_x	Embedding an ultra-low concentration of Au NPs	High stability	RH: 20-30%	30 days	2018	[86]
NiO_x:Sr	low temperature	>60% of its initial PCE was	Under	100	201	[87]

	sol-gel method	maintained	ambient air (RH: 18%)	days	8	
NiO_x:Co	fabrication by NIR process	PCE reduces to 80% of the initial value	ambient condition (RH: 40-60%, T: 25˚C)	250 hours	2020	[90]
Li:Co co-doped NiO_x	Co-doping strategy	94% of its initial PCE was retained	Ambient conditions (RH: 30-40%)	30 days	2019	[92]
Li:Cu co-doped NiO_x	Co-doping strategy	95% of its initial PCE was retained	Inert conditions: in a nitrogen-filled glovebox	60 days	2020	[93]
NiO_x	Ultraviolet/ozone (UVO) treatment	84% of its initial PCE was maintained	inert environment (H_2O<1ppm, O_2<0.1 ppm) at RT	40 days	2019	[96]
$NiCo_2O_4$	By synthesizing ultrasmall ternary oxide NPs	90% of its initial PCE was maintained	illumination at AM 1.5G (100 mW cm^{-2})	500 hours	2018	[97]
CuI	low-temperature solution-processing technique	> 93% of its initial PCE was maintained	Air	288 hours	2016	[100]
CuO_x	facile solution-processed method	~90% of its initial PCE was maintained	Air	200 hours	2016	[103]
CuO_x	Room-temperature electrochemical deposition	>75% of its initial PCE was retained	ambient environment	500 hours	2019	[104]

$CuCo_2O_4$	Solution-processing technique	71% of its initial PCE was retained	Ambient conditions (RH: ~70%)	96 hours	2019	[107]
In:$CuCrO_2$	azeotropic promoted approach	90% of its initial PCE was maintained	N_2 filled glovebox	800 hours illumination at AM 1.5G (100 mW cm^{-2})	2019	[109]
$CuNbO_x$	Low-temperature solution processing technique	~80% of its initial PCE was maintained	(RH: 0-20%, T: 25˚C)	1000 hours	2020	[111]
CuPc	solution-process method	<80% of its initial PCE was retained	85 ˚C in the dark and N_2 environment	2000 hours	2018	[112]
CuPc	thermal evaporation process	~80% of its initial PCE was retained	ambient air condition (RH: 40-50%, T: 20-25˚C)	7 days	2018	[113]
CuPc	Vacuum evaporation	Excellent stability	Under dark environment (RH: 30-40%)	2000 hours	2018	[114]
CuPc-OBu	TBP assisted low-cost method	85% of its initial PCE was sustained	(RH: 45%, T: 85˚C)	1000 hours	2020	[115]
CuPc	Molecularly engineered technique	76% of its initial PCE was retained	ambient environment (RH: 50%, T: 25˚C)	2000 hours	2016	[116]

$CuMe_2Pc$	Molecularly engineered technique	95% of its initial PCE was retained	ambient environment (RH: 50%, T: 25˚C)	2000 hours	2016	[116]
$RGO/CZTS_xSe_{1-x}$	Green sol-gel method	PCE reduced by 14%	ambient air condition at RT	500 hours	2018	[119]
CZTS:Cd	thermal evaporation method	87% of its initial PCE was retained	Air (RH: 85%)	500 hours	2020	[120]
CuSCN	Employing 3D/2D Perovskite	>90% of its initial PCE was retained	ambient laboratory atmosphere (RH: 40-70%)	400 days	2019	[121]
$CuSCN/NH_3$	aqueous-based synthetic route	91.1% of its initial PCE was retained	Nitrogen environment at RT	2 hours	2017	[125]
VO_x	low-temperature solution-processing technique	65.7% of its initial PCE was retained	Under dark and ambient atmosphere (RH: ~25%)	500 hours	2018	[127]
$RGO:MoO_x$	Doping of RGO	17% of its initial PCE was retained	Air (RH: 30±2%)	30 days	2020	[129]
MoO_x/F4-TCNQ	F4-TCNQ modification	>95% of its initial PCE was retained	Ambient conditions (RH: ~45%)	150 hours	2019	[130]
MoS_2	exfoliation of corresponding bulk materials with lithium-intercalation reaction	78% of its initial PCE was retained	Nitrogen atmosphere	56 days	2017	[134]
WS_2	exfoliation of corresponding	72% of its initial PCE was retained	Nitrogen	56 days	201	[134]

	bulk materials with lithium-intercalation reaction		atmosphere		7	
MnS	employing an eco-friendly and low-cost HTM	>90% of its initial PCE was retained	Under ambient air (RH: 80%)	1000 hours	2019	[136]
SWNT/GO/PMMA	Introduction of all-carbon buffer layer	Excellent stability with ~5% PCE decay	moist air mass conditions (RH: 70-80%, T: 298 K)	10 days	2016	[138]
a-GO	Ammonia treatment	PCE decreased by < 10% of the initial value	dry N_2 atmosphere	30 days	2019	[139]
NiO_x/Spiro-OMeTAD	A mitigation strategy for reducing V_{OC} deficit	90% of its initial PCE was maintained	ambient air condition (RH: ≤30%)	1200 hours	2020	[143]
V_2O_5/PEDOT:PSS	Using interface engineered bilayer	95% of its initial PCE was retained	Ambient conditions	18 days	2017	[145]
WO_3/PEDOT:PSS	Solution processing technique	~80% of its initial PCE was retained	in a nitrogen gas purged desiccator	1 week	2019	[147]
$CuCrO_2$/PTAA	Incorporaton of $CuCrO_2$ nanoparticles	>90% of its initial PCE was retained	ambient air condition (RH: 85%, T: 85˚C)	900 hours	2020	[150]
PTAA/ VO_x	Incorporating hybrid HTM	No loss in PCE	Light soaking at 37±3 mW/cm^2, T: 45±1 °C	3200 hours	2020	[151]
Spiro-	RT-vapor	>90% of its initial PCE was	ambient air	1000	201	[15

OMeTAD/Cu_xS	deposition	retained	(RH: 40%, T: 25˚C)	hours	7	2]
FBT-Th4/Cu_xO	Incorporating solution-processable conjugated polymer	90% of its initial PCE was retained	ambient conditions (RH: 70-80%)	500 hours	2018	[154]
NiPc-$(OBu)_8/V_2O_5$	solution-processed technique	75% of its initial PCE was retained	Dark ambient conditions (RH: 40-45%, T: 20-25˚C)	30 days	2017	[155]
WO_3/spiro-OMeTAD	Incorporating solution-processable inorganic–organic double layer	90% of its initial PCE was maintained	T: 100˚C	300 hours	2018	[156]
PTPADT-SO_3Na	Utilizing a self-doping polyelectrolyte	81% of its initial PCE was maintained	ambient air condition (RH: 50%, T: 85˚C)	500 hours	2020	[157]

5.2. Stability of polymeric HTMs

Fig. 21(a) depicts the ambient stability of PSCs fabricated with PEDOT:PSS films which was treated with urea (0–10 wt%) [168]. All devices was kept in ambient air in dark with a relative humidity of around 35%. For the PSCs using pristine PEDOT:PSS, the PCE decreased from 14.6% to 9.9% (reduced by ≈32%.) after 10 days. Additionally, the unstable PSCs are caused by acidic PEDOT:PSS that accelerates perovskite layer degradation and ITO corrosion. After the treatments, the PCE losses in the PSCs with 2, 5, 8, and 10 wt% urea-treated PEDOT:PSS were 14%, 9%, 4%, and 3%, respectively. The improvement in device stability is due to the decline in the acidity behavior of PEDOT:PSS with an increased urea concentration. In the case of J_{SC} and

FF, the same stability tendency was found. However, the V_{OC} values remain stable in all circumstances. The findings on the acidity reduction via urea treatment reveal that PEDOT:PSS for PSC formation can be improved by lowering the acidity. In an experiment, the long-term stability of RGO/PTAA based PSC irradiated with 100 mW cm^{-2} was studied, and the rate of decline in photovoltaic parameters was determined [176]. As illumination time increased, a gradual decline in J_{SC} was observed, which could be due to perovskite decomposition because of ions movement. Small V_{OC} increases were noticed on the first few days, maybe due to a decrease in the number of charge traps present in the perovskite film after it was illuminated. At first, there is minor reduction in FF, and eventually it stopped fluctuating significantly. A weak binding force between RGO and ITO could explain this result. dand these in turn, affect device performance. Even after 500 hours of continuous illumination, the device with the hole-transport bilayer preserved about 90% of its original PCE. Additionally, the long-term stability of the PSC with RGO as the HTM was also carried out using the same illumination regime as that used on the device with RGO/PTAA, and the RGO based device demonstrated good long-term stability similar to that of the RGO/PTAA-based device after 500 hours of continuous illumination as shown in Fig. 21(b). Additionally, the device's overall stability was tested by measuring it with RGO, PTAA, and RGO/PTAA under continuous one sun irradiation. Both RGO/PTAA and RGO based PSCs exhibited similar efficiency as 96% of original PCE for nearly 10 hours. However, after 100 hours of continuous illumination, the RGO-based device showed decreased stability, as it only retained approximately 67% of the original PCE.

Shelf-life analysis, thermal stress, and constant 1-sun light-soaking accelerated test (encapsulated devices) have been used to evaluate the lifetime of P3HT-based PSCs (large area device structures with 1.0 cm^2 active area) that contain (Li+TBP+Co) or (Li+TBP) dopant combinations [188]. Unencapsulated PSCs kept in ambient condition at a temperature of 25 °C with relative humidity of 60% were evaluated for atmospheric shelf-life span analysis. Based on the results, which are presented in Fig. 21(c), the Co-based devices retain about 80% of their initial PCEs after 1500 hours. Additionally, to test thermal stability, encapsulated PSCs are heated to 85 °C in an oven, out of the glove box. After 500 hours of thermal stress, 80% of the initial PCE is retained in Co-doped devices. Light soaking has been done on the same encapsulated large area devices to study their stability. Following 100 hours of continuous irradiation, Co-based PSC could preserve around 90% of the initial efficienc. Intrinsic features of P3HT such as oxygen

impermeability and hydrophobicity, and improved interfacial contact between perovskite and the HTM have contributed to P3HT's increased shelf life and heat and light stability. The Co-complex located at the perovskite/HTM interface can help inhibit trap states, resulting in better interfacial polarity compatibility. Additional dopants in P3HT, such as F4TCNQ and single-walled carbon nanotubes, show less stabilities than those observed with Li+TBP+Co doping. Stability was assessed at ambient circumstances (40–50% relative humidity and room temperature) for alkoxy-PTEG-based devices [196]. The devices were stored in a dark environment, and they were unencapsulated. Twenty devices were tested which showed varying photovoltaic parameters, with the resulting figures (Fig. 21(d)) graphed with average values and error bars. During the 30 days period, they normally maintained 88% of initial PCE. The degradation of LiTFSI and TBP-free alkoxy-PTEG polymers were worse despite the lack of dopants (LiTFSI and TBP). Hydrophilic TEG groups in the alkoxy-PTEG could be responsible for this effect. The stability results look good when high humidity conditions and other undoped HTMs are considered. It was also evaluated at the same ambient settings with the enclosed encapsulated alkoxy-PTEG device. There was no decrease in efficiency. The temperature was further increased to 100 °C to study the thermal stability. 94% of its original efficiency was retained throughout 4 days. However, after 4 weeks, the device's thermal stability was intrinsically low and showed 29% of its initial PCE. This issue must be dealt with because it is perovskite's own thermal stability that needs to be found. Polymer HTM PBTFO was investigated in regards to the perovskite's ability to keep air, UV, and heat stability by performing various stress tests, including stress tests at 25 °C/65% RH in a dark environment, stress tests at 25 °C/N_2 chamber under UV illumination (365 nm, 8 W from the perovskite-side), and stress tests in a 150 °C/N_2 chamber in the dark [205]. Under these conditions the bare perovskite film's absorbance decreased below 80% while that of the PBTFO-cast perovskite film has absorbance retention of over 95%. Additionally, the perovskite films and the PBTFO-cast perovskite were exposed to a considerably harsher condition, 65 °C/70% RH and the PBTFO-cast perovskite again showed superior stability. Fig. 21(e) illustrates that PCE loss on a PBTFO-based GHJ device is just 5% after 500 hours under ambient conditions (25 °C/20–60% RH). However, after 300 hours, the PCE of the Spiro-OMeTAD-based planar heterojunction (PHJ) device is only at 60% of its initial value. PBTFO-based GHJ device has greater light stability when it is exposed to additional light illumination (under AM 1.5 G 100 mW/cm^{-2}) in ambient

air (25 °C/20–60% RH), maintaining over 92% of its initial PCE after 500 h while the PCE of Spiro-OMeTAD-based PHJ device significantly decreases to 22% of its original PCE after 50 h. In addition, nearly 95% of the PCE in the PBTFO-based GHJ device was preserved after exposure to UV-illumination (365 nm and 8 W) in ambient air for 24 hours. This GHJ gadget, PBTFO-based, is also stable at higher temperatures (65 °C) for 500 hours. Table 5 summarizes the stability of PSCs employing various polymeric HTMs.

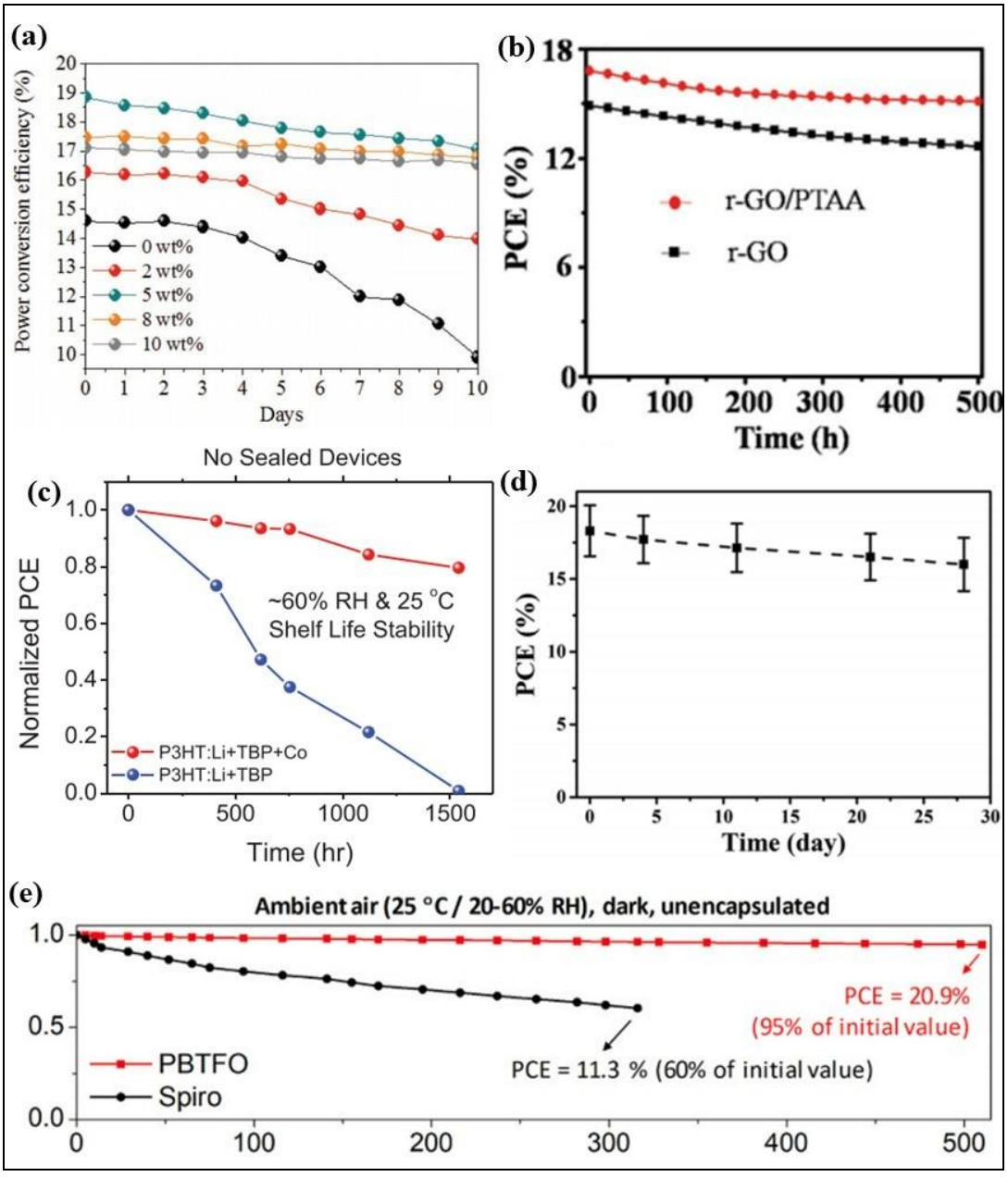

Fig. 21 Stability test results of some of the efficient PSCs based on polymeric HTMs (a) Urea treated PEDOT:PSS (Reproduced from [168] with permission. Copyright 2019, Wiley), (b) RGO/PTAA (Reproduced from [176] with permission. Copyright 2017, Wiley), (c) P3HT (Reproduced from [188] with permission. Copyright 2019, Wiley), (d) Alkoxy-PTEG (Reproduced from [196] with permission. Copyright 2020, Wiley), (e) PBTFO (Reproduced from [205] with permission. Copyright 2020, Elsevier)

Table 5: Stability of PSCs employing various polymeric HTMs.

HTM	**Technique used**	**Stability**	**Testing environment**	**Test duration**	**Year**	**Ref.**
PEDOT:PSS	-	91% of its initial PCE was retained	Nitrogen environment at RT	3 hours	2017	[125]
PEDOT:PSS	-	65% of its initial PCE was retained	Ambient conditions	18 days	2017	[145]
PEDOT:PSS	MoS_2 incorporation	>95% of its initial PCE was retained	Glovebox	4 weeks	2018	[146]
DMSO doped PEDOT:PSS	DMSO treatment	~83% of its initial PCE was retained	Nitrogen atmosphere	590 hours	2017	[163]
PEDOT:PSS	-	60% of its initial PCE was retained	ambient atmosphere (RH: 15%, drying cabinet)	39 days	2017	[166]
PEDOT:PSS/GO	Spin coating of GO solution	83.5% of its initial PCE was retained	ambient atmosphere (RH: 15%, drying cabinet)	39 days	2017	[166]
PEDOT:PSS	Urea treatment	~9% loss in PCE	Under dark and ambient atmosphere	10 days	2018	[168]

			(RH: ~35%)			
PEDOT:GO	Incorporating GO	80% of its initial PCE was maintained	ambient air conditions	25 days	2018	[170]
SC-PEDOT:PSS	Sodium citrate doping	97.9% of its initial PCE was maintained	Glovebox	23 days	2019	[171]
PEDOT:PSS	ethylene glycol and methanol treatment	65% of its initial PCE was maintained	RH: 45%, RT	350 hours	2020	[173]
PEDOT:PSS	-	PCE reduced to 0%	ambient conditions (RH: 50-85%, T: 20-30˚C)	17 days	2017	[215]
RGO/PTAA	Using low-temperature processed bilayer	90% of its initial PCE was retained	continuously illuminated at 100 mW cm^{-2}	500 hours	2017	[176]
PTAA	Metal oxide-free HTM	Good stability	Ambient conditions (RH: 20-30%, T: 25˚C)	150 hours	2018	[177]
P3HT	doping strategy	>80% of its initial PCE was maintained	atmospheric conditions (RH: ≈ 60%, RT)	1500 hours	2019	[188]
P3CT-BN	Employing dopant-free polyelectrolyte	80% of its initial PCE was maintained	dark condition (RT, RH: 30%-40%)	1800 hours	2019	[192]
Alkoxy-PTEG	Nonaromatic Green-Solvent-Processing technique	88% of its initial PCE was maintained	ambient conditions (RH: 40-50%, RT)	30 days	2020	[196]

PFB:F4TCNQ	Enhancement of bulk conductivity of the material	PCE increased unusually by 97.15 %	Under dark and ambient atmosphere (RH: ±40%)	960 hours	2018	[197]
TFB	Incorporating polyfluorene copolymer	81.3% of its initial PCE was retained	Ambient air (RH: 50%±10%)	1 month	2020	[198]
PFB	Incorporating polyfluorene copolymer	74.8% of its initial PCE was retained	Ambient air (RH: 50%±10%)	1 month	2020	[198]
PFO	Incorporating polyfluorene copolymer	71.5% of its initial PCE was retained	Ambient air (RH: 50%±10%)	1 month	2020	[198]
PCDTBT	molecular engineering of conjugated polymers	90% of its initial PCE was maintained	ambient conditions (RH: 40-70%, T: 25-35˚C)	30 days	2018	[200]
PCDTBT1	molecular engineering of conjugated polymers	90% of its initial PCE was maintained	ambient conditions (RH: 40-70%, T: 25-35˚C)	30 days	2018	[200]
PBTFO	Graded heterojunction of perovskite/HTM	95% of its initial PCE was retained	Ambient air under dark conditions (RH: 20-60%, T: 25˚C)	500 hours	2020	[205]
P(mPhDTP)	Solution processing technique	PCE reduced by 0%	ambient air environment (RH: 55%, RT)	100 hours	2020	[209]
P(hBT)	Solution processing technique	PCE reduced by 9%	ambient air environment (RH: 55%,	100 hours	2020	[209]

			RT)			
P(BT)	Solution processing technique	PCE reduced by 12%	ambient air environment (RH: 55%, RT)	100 hours	2020	[209]
PC3	Conformational and compositional tuning	Approximately no change in PCE	Ambient environment and irradiated with indoor light	1000 hours	2020	[210]
VNPB	Solution-processable cross-linking technique	60% of its initial PCE was maintained	humid conditions (RH: 60%, T: 25˚C)	30 days	2020	[211]

5.3. Stability of small molecule-based HTMs

Under ambient environment with 40–50% relative humidity, the long-term stability of the PFPPY doped spiro-OMeTAD device was compared to the control device i.e spiro-OMeTAD doped with TBP and FK-209 [217]. Both devices were unencapsulated. Fig. 22(a) shows the normalized PCE as a function of time. It is shown that PFPPY dopant-based devices retain up to 90% of their initial PCE after 600 hours of operation, whereas the reference device retained only 54% of the initial PCE. Furthermore, to quantify the influence of PFPPY dopant on the perovskite stability, 600-hour storage under ambient conditions before and after subjecting the samples to 40–50% RH conditions for the same time period was conducted. After 600 h of storage, the absorption spectra of the control film show a noticeable drop when compared to PFPPY dopant-based one. This is attributed to the degradation of perovskite, which is found in the control film. Fewer pinholes in the HTM layer reduce the penetration of moisture into the perovskite in PFPPY dopant-based PSC devices. In addition, a one sun irradiation from white LEDs at maximum power point (MPP) was also performed. With a 15% PFPPY-based device, around 83% of initial PCE remained following a light soaking test for 120 h, while just 49% of

initial PCE remained in the control device. It appears the newly created additive is beneficial for maintaining light stability as well. The stability of PSCs with YN1, YN2, and Spiro-OMeTAD as an HTM without encapsulation was investigated in the air (temperature: 25 °C, humidity: 40-45%) as shown in Fig. 22(b) [231]. The PCEs of YN1 and YN2-based solar cells are operational with 91.3 % and 61.6 % performance retention after 1000 hours, respectively. Under the similar working conditions, the device based on Spiro-OMeTAD retains only 42.2 % of its initial PCE. It should be highlighted that the YN2-based device was more stable due to its smoothness which acts as an excellent moisture barrier. In order to evaluate the stability of binary HTMs such as those made of a blend of 90:10 CZ-TA:CZ-STA, the device performance was compared to the doped spiro-OMeTAD [232]. The environmental stability of the PSCs, which uses CZ-STA:CZ-TA (90:10) blend and spiro-OMeTAD as HTMs, respectively, was then tested in ambient air under a relative humidity of ~50 %. Fig. 22(c) depicts the PCE decay curves for both devices, and it shows the CZ-STA:CZ-TA (90:10) HTM based device maintaining 82% of its initial PCE after 60 days. On the other hand, the device employing the spiro-OMeTAD lost approximately 90% of its PCE in the same time span. The higher PCE and better device stability obtained by using the binary CZ-TA:CZ-STA (90:10) HTM shows that this binary HTM could be promising for PSCs.

To assess the long-term stability of DTP-C6Th and spiro-OMeTAD-based PSCs, unencapsulated devices were kept in a glovebox or ambient air with a relative humidity of 35% over two months [235]. As shown in Fig. 22(d), by storing the PSCs in a glovebox for 60 days, there is no significant change in PCE with DTP-C6Th even though only 63% of the initial PCEs retained in spiro-OMeTAD devices. Diffusion of dopants and ions is probably the main factor to the PCE loss for spiro-OMeTAD-based PSCs. There was impressive retention of device parameters (80% of initial PCEs) with DTP-C6Th devices placed in the air after 60 days. However, PCE loss (67%) in spiro-OMeTAD-based devices occurred most likely due to the hydrophilic nature of dopants. In other words, the DTP-C6Th HTM produces a greater PCE (21%) as well as higher long-term stability, making it ideal for the future commercialization of PSCs. Aging tests were done in a chamber under one-sun illumination, with 30% relative humidity, to determine the stability of the HTMs SY1, SY2, and SY3 in the without encapsulation [244]. In Fig. 22(e), it shows that the PSCs based on SY3 has the best stability, declining to 87% of its initial efficiency only after 480 hours, whereas the efficiency of other two PSCs, those based on SY2 and SY1,

fell to 82% and 76% respectively. After constant 400-hour one-sun illumination, the overall efficiency drops by 30%, 25%, and 19% for SY1, SY2, and SY3-based devices, respectively. For the long-term stability of PSCs, the hydrophobicity of SY3 is essential. This further serves to protect the perovskite from deterioration under humid conditions. In Fig. 22(f), the results of the aging tests for the IDT1, IDT2, and Spiro-OMeTAD-based PSCs are shown when the conditions are set to be 45% relative humidity at room temperature [253]. When the process started, all the devices saw an improvement in PCE. Although the gains can partly be attributable to the passivation of perovskite surface imperfections by TBP in HTM, improvements are also possible due to better processing. By contrast, for IDT1 and IDT2, the sulfur atoms on IDT ring were shown to act as passivation agents for the defects on the perovskite surface. Achieving a higher PCE from the initial stage takes some time as a result of the passivation effect of TBP and sulfur atoms. However, a potentially negative side effect, which is perovskite degradation, may also be due to the additive LiTFSI, resulting in a reduced PCE after a long period of time. 85% of the initial efficiency was retained by IDT1-based devices. Homogeneity and minor hydrophobicity are the key reasons for IDT1 film being preferred. Table 6 summarizes the stability of PSCs employing various small molecule-based HTMs.

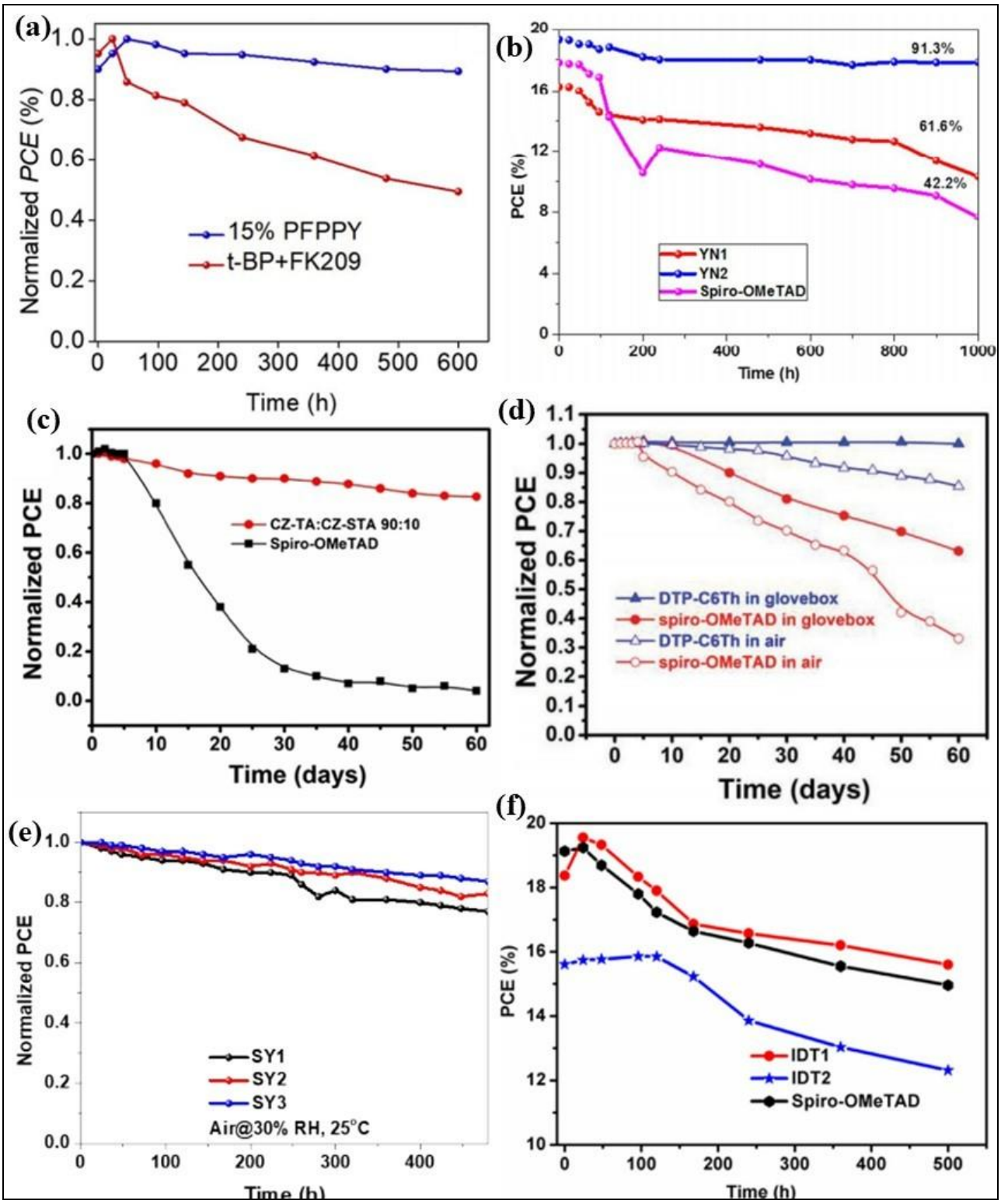

Fig. 22 Stability test results of some of the efficient PSCs based on small molecule HTMs (a) PFPPY doped Spiro-OMeTAD (Reproduced from [217] with permission. Copyright 2020, Elsevier), (b) YN1, YN2 (Reproduced from [231] with permission. Copyright 2018, American

Chemical Society), (c) CZTA:CZSTA (Reproduced from [232] with permission. Copyright 2018, Elsevier), (d) DTP-C6Th (Reproduced from [235] with permission. Copyright 2019, Wiley), (e) SY1, SY2, SY3 (Reproduced from [244] with permission. Copyright 2020, The Royal Society of Chemistry), (f) IDT1, IDT2 (Reproduced from [253] with permission. Copyright 2020, Elsevier)

Table 6: Stability of PSCs employing various small molecule-based HTMs.

HTM	**Technique used**	**Stability**	**Testing environment**	**Test duration**	**Year**	**Ref.**
Spiro-OMeTAD	Pseudo-halide anion engineering	Only 10% degradation	Under dark (RH: 20%, T: 25˚C)	1000 hours	2021	[212]
spiro-OMeTAD	Modification with ADAHI	a negligibly small performance loss	at room temperature under nitrogen atmosphere	500 hours	2018	[213]
Spiro-I	By lowering the molecular symmetry of spiro core	80% of its initial PCE was retained	Ambient air conditions (RH: 50-60%)	2400 hours	2018	[214]
spiro-OMeTAD	Doping with copper-based complexes	Good stability	Under dark and ambient atmosphere (RH: 50%, T: 25˚C)	1 week	2018	[215]
Spiro-OMeTAD in pentachloroethane solvent	Solvent engineering	>70% of its initial PCE was retained	Under dark (RH: 15%, T: 80˚C)	500 hours	2020	[216]
spiro-OMeTAD	PFPPY doping	>90% of its initial PCE was maintained	ambient conditions (RH: 40-	600 hours	2020	[217]

			50%)			
Spiro-OMeTAD	Lewis-Acid Doping	85% of its initial PCE was retained	ambient atmosphere (RH: 20-35%, RT)	1000 hours	2020	[220]
mDPA-DBTP	Using DBTP as a core unit in conjugated small-molecule	81% of its initial PCE was retained	ambient air condition (RH: 40±5%, T: 25±3˚C)	33 days	2018	[221]
TAPC	solution casting	PCE reduced to ~6%	ambient conditions (RH: 50-85%, T: 20-30˚C)	30 days	2017	[224]
X44	introduced counter ions $TFSI^-$	increase in PCE from the initial 15.2% to 16.2%	Nitrogen atmosphere in dark (RH: <20%, T: RT)	15 days	2017	[226]
LD22	Incorporating a simple carbazole-triphenylamine compound	Good stability	In dark drying oven (RH: 15%)	100 hours	2018	[227]
m-MTDATA	Using nonstoichiometric precursors	~89% of its initial PCE was retained	ambient environment (RH: ≈30%)	30 days	2018	[228]
H16	by cross linking triarylamine-based donor groups with the MPDTP unit	90% of its initial PCE was retained	ambient air condition (RH: 20%)	2 months	2018	[229]
H18	by cross linking triarylamine-based donor	78% of its initial PCE was retained	ambient air condition (RH: 20%)	2 months	2018	[229]

	groups with TPDTP unit					
TPA-ANT-TPA	Molecular engineering using ANT dye	PCE reduced to 14%	Dark condition (RH: ≥58%, T: 22˚C)	50 hours	2018	[230]
YN1	D-A-D structured	91.3% of its initial PCE was retained	Air conditions (RH: 40-45%, T: 25˚C)	1000 hours	2018	[231]
YN2	D-A-D structured	61.6% of its initial PCE was retained	Air conditions (RH: 40-45%, T: 25˚C)	1000 hours	2018	[231]
CZ-TA:CZ-STA	Binary strategy	>82% of its initial PCE was maintained	Air conditions (RH: 50%)	60 days	2018	[232]
2mF-X59	F4-TCNQ modification	94% of its initial PCE was retained	Ambient atmosphere at RT, RH: ~30%	30 days	2019	[234]
DTP-C6Th	effective device engineering strategy	85% of its initial PCE was retained	ambient air (RH: ≈35%)	60 days	2019	[235]
YN3	Employing dopant-free D-A-D typed HTMs	92% (for hybrid PSC) and 97% (for all-inorganic PSC) of its initial PCE was retained	RH: 40-45%, T: 25˚C	300 hours	2019	[237]
TFM	aggregation-induced emission	~24% of its initial PCE was retained	Ambient environment (RH: 55-65%, T: 26˚C)	100 hours	2020	[238]
MCz-Cz-BTI	Engineering of dendritic	80% of its initial PCE was retained	RH: 55-60%	900 hours	202	[23

	molecules				0	9]
D104	pyridine core	33% of its initial PCE was retained	Ambient environment under dark (RH: 30%, T: 20˚C)	275 hours	2020	[240]
D105	pyridine core	70% of its initial PCE was retained	Ambient environment under dark (RH: 30%, T: 20˚C)	275 hours	2020	[240]
D106	pyridine core	75% of its initial PCE was retained	Ambient environment under dark (RH: 30%, T: 20˚C)	275 hours	2020	[240]
EtCz-3EHCz + EH44-ox	Exchanging dopants	50% of its initial PCE was retained	Illumination (RH: 10-20%, T: 50˚C)	500 hours	2020	[241]
P_{UV}-polyTPD	organic monomolecular approach	20% drop in PCE	ambient air (RH: 35%)	120 hours	2020	[242]
F23	green-solvent-processing	80% of its initial PCE was maintained	Ambient air (RH: 25-30%, T: 20˚C)	200 hours	2020	[243]
SY1	one-pot reaction	76% of its initial PCE was maintained	Illumination (RH: 30%)	480 hours	2020	[244]
SY2	one-pot reaction	82% of its initial PCE was maintained	Illumination (RH: 30%)	480 hours	2020	[244]
SY3	one-pot reaction	87% of its initial PCE was maintained	Illumination (RH: 30%)	480 hours	2020	[244]
TPA-BPFN-TPA	D-A-D	43.5% of its initial PCE was	RH: 70%, T:	100	202	[24

	structured	maintained	22˚C	hours	0	7]
CS-01	sulfonyldibenzene-based molecule	91% of its initial PCE was retained	-	30 days	2020	[249]
CS-02	sulfonyldibenzene-based molecule	79% of its initial PCE was retained	-	30 days	2020	[249]
CS-03	sulfonyldibenzene-based molecule	83% of its initial PCE was retained	-	30 days	2020	[249]
tpa-t-FBTD	D-A-D structured	87% of its initial PCE was maintained	ambient conditions (RH: 45%, RT)	480 hours	2020	[251]
BTPA-8	Lucky clover synthesis	PCE reduced by 7%	air (RH: 30%)	10 days	2020	[252]
TBC-1	Solution processing technique	84% of its initial PCE was retained	ambient conditions	30 days	2020	[254]
YZ18	Facile approach for functionalizing HTM	65% of its initial PCE was retained	Ambient air (RH: 35%, T: 30˚C)	1000 hours	2020	[256]
YZ22	Facile approach for functionalizing HTM	>80% of its initial PCE was retained	Ambient air (RH: 35%, T: 30˚C)	1000 hours	2020	[256]

6. Discussion

In this article, we discuss some of the perovskite solar cell HTMs that have been developed. Because they are one of the main layers that in the perovskite solar cell, HTMs have a noteworthy impact on the efficiency and stability. From the literature, there are many different types of materials which are currently being investigated as HTMs. However, since the costly

Spiro-OMeTAD is still a very popular choice, it appears that additional investigation is still required to confidently identify and/or develop some HTMs. To accomplish this, they must guarantee a high efficiency, high stability, low cost, and good film formation over large areas by scalable methods. The HTM should possess sufficient levels of energy so that holes created in the perovskite layer are easily transmitted into the HTM. Moreover, it should also contain discriminating factors, such as blocking recombination of electrons at this contact (thus low electron affinities are sought). In order to have high fill factor, HTMs also require large hole mobilities (and small thicknesses) and high transparency, all of which is necessary in order to enable light passage (either from the bottom TCO electrode or reflected from the top metal electrode). From tables 1-3, it is shown that many HTMs can be used in PSCs with outstanding efficiencies of more than 20%. Maximum efficiency of 25.6 % was reported with spiro-OMeTAD while Cu_2O, NiO, YZ22, PBTFO, MCz-Cz-BTI, spiro-OMeTAD based composites and DTP6Th were other superior HTMs. Fig. 23 presents a diagram of “efficiency tree” that displays the best efficiency levels (>21 %) of the HTMs applied to PSCs.

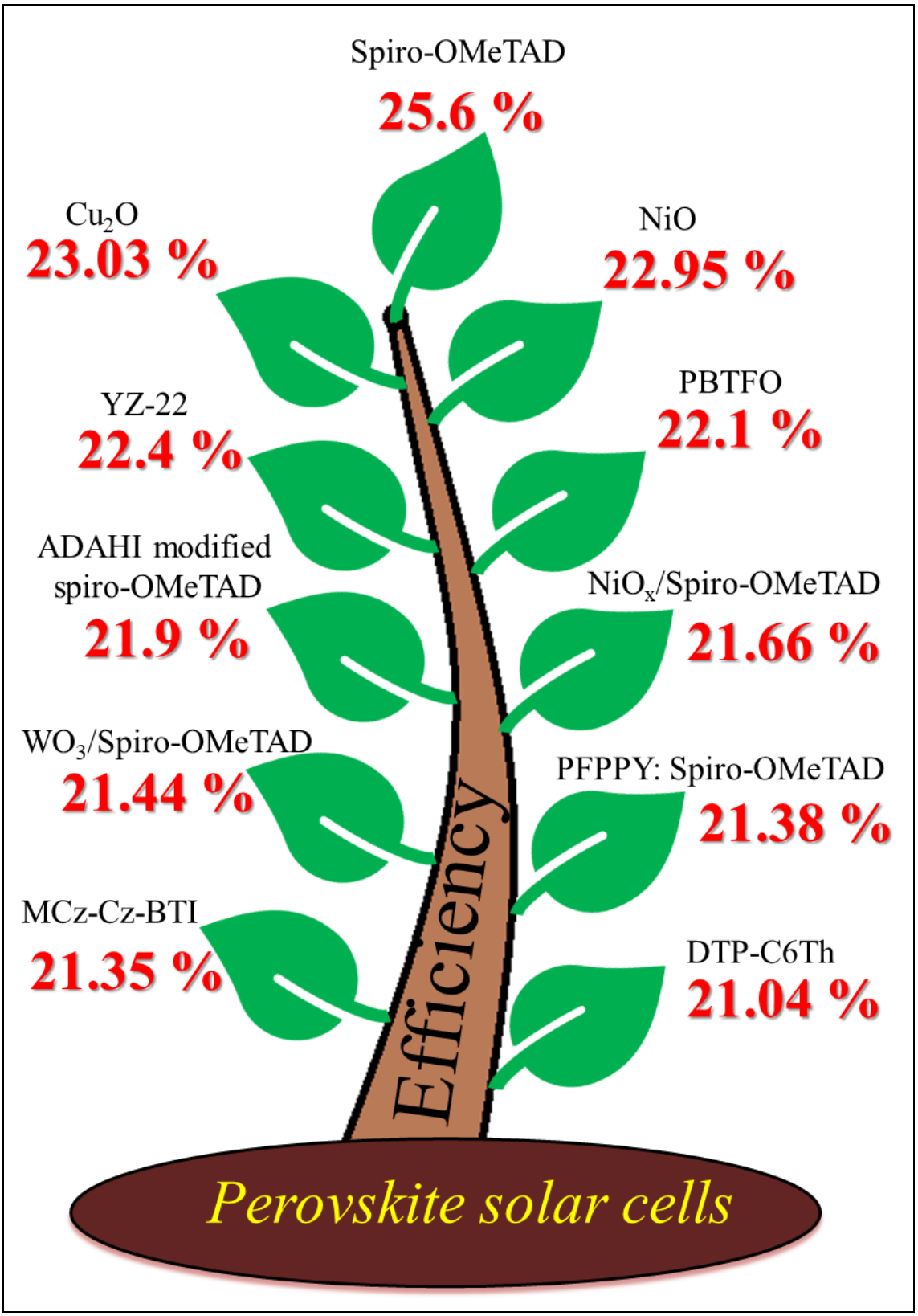

Fig. 23 Efficiency tree.

While the original intention was to boost the stability of solar cells, the use of spiro-OMeTAD as a common HTM with several additives is commonly employed as a means to enhance performance. A striking feature of PCEs reached with this material is the wide range of considerations in terms of costs and stability, and as a result, there are many alternatives that have been developed and incorporated. Inorganic materials such as CuI, CuSCN, NiO, Cu_2O, MoO_3, and GO as well as semiconducting and conducting polymers like P3HT, CNT composites, PTAA, PEDOT:PSS, are common HTMs used in different PSCs. While typically exhibiting greater efficiency, the use of doped organic transport layers is more susceptible to deterioration over time as opposed to their original counterparts. Another approach is that inorganic HTMs could help to improve stability particularly when substituting a material such as PEDOT:PSS, which is affected by humidity because of its hygroscopic nature and thus requires replacement. It's also possible to make similar comparisons, such as the growth of the organic light-emitting diode (OLED) and solar cell industries, where the use of inorganic hole transporting layers has grown due to their increased stability. Similar to other photovoltaic technologies, we expect perovskite solar cells to experience the same trends. It is also noteworthy to mention that the importance of the transport layer properties differs depending on the level of illumination and and the device architecture. The ETMs have delivered significant performance under 1 sun as well as under artificial indoor lightening, however, the roles of HTMs under these conditions remain to be determined. Besides, how the inorganic HTMs are deposited and perform on the large-area module scale instead of just on the small cell level, are issues that need to be investigated. Even though, initially, the best option is to choose the solution that works best for each layer, however, in the long-term throughputs, it is uncertain what the influence of vacuum-based vs solution-based deposition is for the cost of the photovoltaic technology (which is a decisive parameter for entering the market). Thus, we call for future studies that include more details on this subject. A good film-forming property is essential in order to produce an even coating. Additionally, the HTMs are located beneath the top electrode and come into contact with humidity and oxygen as well as interfacing with the perovskite prior to other materials in the common n-i-p architecture. In other words, it must be resistant to chemical degradation and provide a stable electronic interface. Examples of stabilization strategies include stabilizing electronic properties and materials over a wide range of temperatures and water vapor permeation. In this way, there are better results using HTMs

made of composite materials/layers, as well as HTMs which are deposited from different techniques, which results in improved performance and stability. These strategies might be viewed as effective in decoupling the different effect of HTMs (such as interfacial and permeation barriers versus bulk mobility, blocking and film coverage) and additional studies in this area will advance our understanding of different properties and effects of HTMs on overall device efficiency and stability.

7. Future perspectives and outlook

After analyzing various HTMs, the following characteristics of a good HTM must be present.

a) Doping is required to increase the efficiency of PSCs but can also reduce the structural stability of PSC. If the HTM in its pristine form can provide sufficient hole mobility and a suitable HOMO level, it can result in improved performance. Hole mobilities in the range of 10^{-3}–10^{-4} cm^2 V^{-1} s^{-1} can be adequate for efficient hole extraction in PSCs [257].

b) It is frequently stated that HTM's HOMO should be lower (in absolute numbers) than the perovskite valence band for capturing holes. However, this criterion is oversimplified since it confuses energy and free energy. Moreover, since various HTMs having well-aligned HOMO levels exhibit a range of different V_{OC} values. Therefore, the charge carrier recombination rate must not be increased by the transfer of holes from perovskite to HTM in order to maintain a high V_{oc}. The position of surface dipoles and reactions at the HTM-perovskites interface is critical for minimizing recombination losses and ensuring the necessary driving force for hole extraction.

c) The structural stability is ensured by increasing T_g of the HTM above 120˚C, preventing structural changes caused by exposure to sunlight.

d) Although optical transparency in the visible region is desirable, it is not compulsory; a low bandgap HTM can also enhance light absorption in the red region of the electromagnetic spectrum, wherein perovskites exhibit low absorption coefficient. However, tandem cells must use a hole conductor that is transparent to visible and near-infrared light.

e) A pinhole-free layer of HTM is needed so that the perovskite is not in contact with the electrode. To solve this, the thickness of the HTM sheet is increased; however, this increases the resistance as well. Hence, a thick HTM layer must be used, having sufficient conductivity to decrease resistance; otherwise, the FF will be reduced.

As mentioned in this article, there is relatively less available inorganic p-type semiconductors, like CuI, CuSCN, and NiO. Despite their high conductivity and stability, their deposition technique must be improved by the choice of solvent that doesnot affect the perovskite. On the contrary, polymeric HTMs, like PTAA, demonstrated the best efficiency among the polymers used. Still, their possible disadvantages like polydispersity, batch-to-batch variation, purity, and stability under low vacuum conditions must be tackled before their usage in technical applications. Small molecules have shown the highest efficiency and can be tailored to meet the perovskite's requirements.

Nevertheless, additional research is required to ensure the stability of PSCs concerning high temperature and low pressure. Small molecules are monodispersed, having different molecular weights and well-defined molecular structure. They have infinite chemical structures, and their electrical conductivity can be adjusted by molecular engineering of their optoelectronic properties, like bandgap, HOMO–LUMO levels, and charge mobility.

Spiro-OMeTAD continues to rule as the standard HTM in solid-state pigmented solar cells twenty years after its introduction. In Recent years, cost-effective options like triazatruxene and others based on the dithiophene core (FDT) were investigated and exhibited exceptional photovoltaic efficiency. As is the case with Spiro-OMeTAD, the primary disadvantage of FDT is the need for external doping with an ionic salt and additives. The conductivity could be increased, and the Fermi level is moved toward the HOMO level if HTMs are p doped. While doping enhances their success, it also impairs their stability. So, the existence of hygroscopic lithium salts could destabilize the perovskite and cause more hysteresis. This issue could be resolved by a hydrophobic dopant or engineering the molecules to improve the π–π^* stacking and thus the charge mobility/conductivity. V_{OC} relates to the conductivity of the HTM, with a low V_{OC} indicating a slower hole transport rate and more recombination of photogenerated electron-hole pairs. If a FF of 80 % or greater can be achieved with novel molecules, the PCE

could go upto 24 %. Presently, up to 81.7 % FF has been achieved with Spiro-OMeTAD. In recent years, we have seen significant advancements in HTMs and overall performance improvements in PSCs with the help of the practical design of new HTMs and the judicious choice of perovskite absorbers for improving the reliability and performance of photovoltaic systems. Additional band synchronization of interfaces, optimized doping, improved processing conditions, and reduction of recombination losses are all potential avenues.

8. Conclusions and summary

PSCs have sparked exciting advances in the field of novel HTMs and their incorporation into device fabrication. Although most HTMs studied in PSCs were focused on small molecules, other HTMS including conducting polymers, organometallic complexes, and inorganic p-type semiconductors have also been studied. We have highlighted recent advances in designing and synthezising various types of HTM for mesoscopic and planar heterojunction PSCs in this review. Although the traditional small-molecule-based HTM, Spiro-OMeTAD, remains the apparent option, other alternatives have been identified recently that can compete with its use. The lengthy synthetic processes, enhanced purity, UV sensitivity, low hole mobility, and risk of crystallization upon heating all contribute to the difficulty of widespread application. New HTMs are being created, but it isn't easy imagining a novel molecule as an HTM meeting all the aspirations for efficiency and good stability at the same time. Nonetheless, by molecular engineering HTMs for sufficient hole extraction, a balance of properties can be achieved.

In summary, this article was about the modifications and critical challenges that arise when synthesizing various HTM, as well as important issues to consider for improving the efficiency and stability of PSC devices.

Conflict of Interest

The authors declare that there is no conflict of interest.

Data Availability Statement

The raw/processed data required to reproduce these findings cannot be shared at this time due to technical limitations.

References

[1] Kazim, S., Nazeeruddin, M.K., Grätzel, M. and Ahmad, S., 2014. Perovskite as light harvester: a game changer in photovoltaics. *Angewandte Chemie International Edition*, *53*(11), pp.2812-2824.

[2] Arya, S., Mahajan, P., Gupta, R., Srivastava, R., Kumar Tailor, N., Satapathi, S., Radhakrishnan, S., Datt, R. and Gupta, V., 2020. A comprehensive review on synthesis and applications of single crystal perovskite halides. *Progress in Solid State Chemistry*, p.100286.

[3] Kour, R., Arya, S., Verma, S., Gupta, J., Bandhoria, P., Bharti, V., Datt, R. and Gupta, V., 2019. Potential substitutes for replacement of lead in perovskite solar cells: a review. *Global Challenges*, *3*(11), p.1900050.

[4] Savenije, T.J., Ponseca Jr, C.S., Kunneman, L., Abdellah, M., Zheng, K., Tian, Y., Zhu, Q., Canton, S.E., Scheblykin, I.G., Pullerits, T. and Yartsev, A., 2014. Thermally activated exciton dissociation and recombination control the carrier dynamics in organometal halide perovskite. *The journal of physical chemistry letters*, *5*(13), pp.2189-2194.

[5] Dong, Q., Fang, Y., Shao, Y., Mulligan, P., Qiu, J., Cao, L. and Huang, J., 2015. Electron-hole diffusion lengths> 175 μm in solution-grown $CH_3NH_3PbI_3$ single crystals. *Science*, *347*(6225), pp.967-970.

[6] Mahajan, P., Datt, R., Tsoi, W.C., Gupta, V., Tomar, A. and Arya, S., 2020. Recent progress, fabrication challenges and stability issues of lead-free tin-based perovskite thin films in the field of photovoltaics. *Coordination Chemistry Reviews*, p.213633.

[7] Kojima, A., Teshima, K., Shirai, Y. and Miyasaka, T., 2009. Organometal halide perovskites as visible-light sensitizers for photovoltaic cells. *Journal of the American Chemical Society*, *131*(17), pp.6050-6051.

[8] Im, J.H., Lee, C.R., Lee, J.W., Park, S.W. and Park, N.G., 2011. 6.5% efficient perovskite quantum-dot-sensitized solar cell. *Nanoscale*, *3*(10), pp.4088-4093.

[9] Lee, M.M., Teuscher, J., Miyasaka, T., Murakami, T.N. and Snaith, H.J., 2012. Efficient hybrid solar cells based on meso-superstructured organometal halide perovskites. *Science*, *338*(6107), pp.643-647.

[10] Kim, H.S., Lee, C.R., Im, J.H., Lee, K.B., Moehl, T., Marchioro, A., Moon, S.J., Humphry-Baker, R., Yum, J.H., Moser, J.E. and Grätzel, M., 2012. Lead iodide perovskite sensitized all-solid-state submicron thin film mesoscopic solar cell with efficiency exceeding 9%. *Scientific reports*, *2*(1), pp.1-7.

[11] Jung, H.S. and Park, N.G., 2015. Perovskite solar cells: from materials to devices. *Small*, *11*(1), pp.10-25.

[12] Eperon, G.E., Stranks, S.D., Menelaou, C., Johnston, M.B., Herz, L.M. and Snaith, H.J., 2014. Formamidinium lead trihalide: a broadly tunable perovskite for efficient planar heterojunction solar cells. *Energy & Environmental Science*, *7*(3), pp.982-988.

[13] Pang, S., Hu, H., Zhang, J., Lv, S., Yu, Y., Wei, F., Qin, T., Xu, H., Liu, Z., and Cui, G., 2014. $NH_2CH{=}NH_2PbI_3$: an alternative organolead iodide perovskite sensitizer for mesoscopic solar cells. *Chemistry of Materials*, *26*(3), pp.1485-1491.

[14] Koh, T.M., Fu, K., Fang, Y., Chen, S., Sum, T.C., Mathews, N., Mhaisalkar, S.G., Boix, P.P. and Baikie, T., 2014. Formamidinium-containing metal-halide: an alternative material for near-IR absorption perovskite solar cells. *The Journal of Physical Chemistry C*, *118*(30), pp.16458-16462.

[15] Smith, I.C., Hoke, E.T., Solis-Ibarra, D., McGehee, M.D. and Karunadasa, H.I., 2014. A layered hybrid perovskite solar-cell absorber with enhanced moisture stability. *Angewandte Chemie*, *126*(42), pp.11414-11417.

[16] Hao, F., Stoumpos, C.C., Cao, D.H., Chang, R.P. and Kanatzidis, M.G., 2014. Lead-free solid-state organic–inorganic halide perovskite solar cells. *Nature Photonics*, *8*(6), pp.489-494.

[17] Kumar, M.H., Dharani, S., Leong, W.L., Boix, P.P., Prabhakar, R.R., Baikie, T., Shi, C., Ding, H., Ramesh, R., Asta, M. and Graetzel, M., 2014. Lead-free halide perovskite solar cells with high photocurrents realized through vacancy modulation. *Advanced Materials*, *26*(41), pp.7122-7127.

[18] Hao, F., Stoumpos, C.C., Chang, R.P. and Kanatzidis, M.G., 2014. Anomalous band gap behavior in mixed Sn and Pb perovskites enables broadening of absorption spectrum in solar cells. *Journal of the American Chemical Society*, *136*(22), pp.8094-8099.

[19] Noh, J.H., Im, S.H., Heo, J.H., Mandal, T.N. and Seok, S.I., 2013. Chemical management for colorful, efficient, and stable inorganic–organic hybrid nanostructured solar cells. *Nano Letters*, *13*(4), pp.1764-1769.

[20] Jeon, N.J., Noh, J.H., Kim, Y.C., Yang, W.S., Ryu, S. and Seok, S.I., 2014. Solvent engineering for high-performance inorganic–organic hybrid perovskite solar cells. *Nature Materials*, *13*(9), pp.897-903.

[21] Jeon, N.J., Noh, J.H., Yang, W.S., Kim, Y.C., Ryu, S., Seo, J. and Seok, S.I., 2015. Compositional engineering of perovskite materials for high-performance solar cells. *Nature*, *517*(7535), pp.476-480.

[22] Burschka, J., Pellet, N., Moon, S.J., Humphry-Baker, R., Gao, P., Nazeeruddin, M.K. and Grätzel, M., 2013. Sequential deposition as a route to high-performance perovskite-sensitized solar cells. *Nature*, *499*(7458), pp.316-319.

[23] Liu, M., Johnston, M.B. and Snaith, H.J., 2013. Efficient planar heterojunction perovskite solar cells by vapour deposition. *Nature*, *501*(7467), pp.395-398.

[24] Chen, Q., Zhou, H., Hong, Z., Luo, S., Duan, H.S., Wang, H.H., Liu, Y., Li, G. and Yang, Y., 2014. Planar heterojunction perovskite solar cells via vapor-assisted solution process. *Journal of the American Chemical Society*, *136*(2), pp.622-625.

[25] Xiao, M., Huang, F., Huang, W., Dkhissi, Y., Zhu, Y., Etheridge, J., Gray-Weale, A., Bach, U., Cheng, Y.B. and Spiccia, L., 2014. A fast deposition-crystallization procedure for highly efficient lead iodide perovskite thin-film solar cells. *Angewandte Chemie International Edition*, *53*(37), pp.9898-9903.

[26] Huang, F., Dkhissi, Y., Huang, W., Xiao, M., Benesperi, I., Rubanov, S., Zhu, Y., Lin, X., Jiang, L., Zhou, Y. and Gray-Weale, A., 2014. Gas-assisted preparation of lead iodide perovskite films consisting of a monolayer of single crystalline grains for high-efficiency planar solar cells. *Nano Energy*, *10*, pp.10-18.

[27] Chen, C.W., Kang, H.W., Hsiao, S.Y., Yang, P.F., Chiang, K.M. and Lin, H.W., 2014. Efficient and uniform planar-type perovskite solar cells by simple sequential vacuum deposition. *Advanced Materials*, *26*(38), pp.6647-6652.

[28] Habisreutinger, S.N., Leijtens, T., Eperon, G.E., Stranks, S.D., Nicholas, R.J. and Snaith, H.J., 2014. Enhanced hole extraction in perovskite solar cells through carbon nanotubes. *The Journal of Physical Chemistry Letters*, *5*(23), pp.4207-4212.

[29] Eperon, G.E., Burlakov, V.M., Docampo, P., Goriely, A. and Snaith, H.J., 2014. Morphological control for high performance, solution-processed planar heterojunction perovskite solar cells. *Advanced Functional Materials*, *24*(1), pp.151-157.

[30] Zhang, F., Yang, X., Wang, H., Cheng, M., Zhao, J. and Sun, L., 2014. Structure engineering of hole–conductor free perovskite-based solar cells with low-temperature-processed commercial carbon paste as cathode. *ACS Applied Materials & Interfaces*, *6*(18), pp.16140-16146.

[31] Mei, A., Li, X., Liu, L., Ku, Z., Liu, T., Rong, Y., Xu, M., Hu, M., Chen, J., Yang, Y. and Grätzel, M., 2014. A hole-conductor–free, fully printable mesoscopic perovskite solar cell with high stability. *Science*, *345*(6194), pp.295-298.

[32] Lee, M.M., Teuscher, J., Miyasaka, T., Murakami, T.N. and Snaith, H.J., 2012. Efficient hybrid solar cells based on meso-superstructured organometal halide perovskites. *Science*, *338*(6107), pp.643-647.

[33] Li, M.H., Shen, P.S., Wang, K.C., Guo, T.F. and Chen, P., 2015. Inorganic p-type contact materials for perovskite-based solar cells. *Journal of Materials Chemistry A*, *3*(17), pp.9011-9019.

[34] Liu, M., Johnston, M.B. and Snaith, H.J., 2013. Efficient planar heterojunction perovskite solar cells by vapour deposition. *Nature*, *501*(7467), pp.395-398.

[35] Liu, D., Yang, J. and Kelly, T.L., 2014. Compact layer free perovskite solar cells with 13.5% efficiency. *Journal of the American Chemical Society*, *136*(49), pp.17116-17122.

[36] Yu, H., Ryu, J., Lee, J.W., Roh, J., Lee, K., Yun, J., Lee, J., Kim, Y.K., Hwang, D., Kang, J. and Kim, S.K., 2017. Large grain-based hole-blocking layer-free planar-type perovskite solar cell with best efficiency of 18.20%. *ACS Applied Materials & Interfaces*, *9*(9), pp.8113-8120.

[37] Cohen, B.E., Aharon, S., Dymshits, A. and Etgar, L., 2016. Impact of antisolvent treatment on carrier density in efficient hole-conductor-free perovskite-based solar cells. *The Journal of Physical Chemistry C*, *120*(1), pp.142-147.

[38] Werner, J., Weng, C.H., Walter, A., Fesquet, L., Seif, J.P., De Wolf, S., Niesen, B. and Ballif, C., 2016. Efficient monolithic perovskite/silicon tandem solar cell with cell area> 1 cm^2. *The Journal of Physical Chemistry Letters*, *7*(1), pp.161-166.

[39] Li, M.H., Yang, Y.S., Wang, K.C., Chiang, Y.H., Shen, P.S., Lai, W.C., Guo, T.F. and Chen, P., 2017. Robust and recyclable substrate template with an ultrathin nanoporous counter electrode for organic-hole-conductor-free monolithic perovskite solar cells. *ACS Applied Materials & Interfaces*, *9*(48), pp.41845-41854.

[40] Lin, X., Jumabekov, A.N., Lal, N.N., Pascoe, A.R., Gómez, D.E., Duffy, N.W., Chesman, A.S., Sears, K., Fournier, M., Zhang, Y. and Bao, Q., 2017. Dipole-field-assisted charge extraction in metal-perovskite-metal back-contact solar cells. *Nature Communications*, *8*(1), pp.1-8.

[41] Mei, A., Li, X., Liu, L., Ku, Z., Liu, T., Rong, Y., Xu, M., Hu, M., Chen, J., Yang, Y. and Grätzel, M., 2014. A hole-conductor–free, fully printable mesoscopic perovskite solar cell with high stability. *Science*, *345*(6194), pp.295-298.

[42] Zhao, X. and Wang, M., 2018. Organic hole-transporting materials for efficient perovskite solar cells. *Materials Today Energy*, *7*, pp.208-220.

[43] Kim, J.H., Liang, P.W., Williams, S.T., Cho, N., Chueh, C.C., Glaz, M.S., Ginger, D.S. and Jen, A.K.Y., 2015. High-performance and environmentally stable planar heterojunction perovskite solar cells based on a solution-processed copper-doped nickel oxide hole-transporting layer. *Advanced Materials*, *27*(4), pp.695-701.

[44] Domanski, K., Correa-Baena, J.P., Mine, N., Nazeeruddin, M.K., Abate, A., Saliba, M., Tress, W., Hagfeldt, A. and Grätzel, M., 2016. Not all that glitters is gold: metal-migration-induced degradation in perovskite solar cells. *ACS Nano*, *10*(6), pp.6306-6314.

[45] Kung, P.K., Li, M.H., Lin, P.Y., Chiang, Y.H., Chan, C.R., Guo, T.F. and Chen, P., 2018. A review of inorganic hole transport materials for perovskite solar cells. *Advanced Materials Interfaces*, *5*(22), p.1800882.

[46] Guerrero, A., Garcia-Belmonte, G., Mora-Sero, I., Bisquert, J., Kang, Y.S., Jacobsson, T.J., Correa-Baena, J.P. and Hagfeldt, A., 2016. Properties of contact and bulk impedances in hybrid lead halide perovskite solar cells including inductive loop elements. *The Journal of Physical Chemistry C*, *120*(15), pp.8023-8032.

[47] Kato, Y., Ono, L.K., Lee, M.V., Wang, S., Raga, S.R. and Qi, Y., 2015. Silver iodide formation in methyl ammonium lead iodide perovskite solar cells with silver top electrodes. *Advanced Materials Interfaces*, *2*(13), p.1500195.

[48] Zhang, Y., Liu, W., Tan, F. and Gu, Y., 2015. The essential role of the poly (3-hexylthiophene) hole transport layer in perovskite solar cells. *Journal of Power Sources*, *274*, pp.1224-1230.

[49] Li, W., Dong, H., Guo, X., Li, N., Li, J., Niu, G. and Wang, L., 2014. Graphene oxide as dual functional interface modifier for improving wettability and retarding recombination in hybrid perovskite solar cells. *Journal of Materials Chemistry A*, *2*(47), pp.20105-20111.

[50] Burschka, J., Pellet, N., Moon, S.J., Humphry-Baker, R., Gao, P., Nazeeruddin, M.K. and Grätzel, M., 2013. Sequential deposition as a route to high-performance perovskite-sensitized solar cells. *Nature*, *499*(7458), pp.316-319.

[51] Liu, Z., Zhang, M., Xu, X., Cai, F., Yuan, H., Bu, L., Li, W., Zhu, A., Zhao, Z., Wang, M. and Cheng, Y.B., 2015. NiO nanosheets as efficient top hole transporters for carbon counter electrode based perovskite solar cells. *Journal of Materials Chemistry A*, *3*(47), pp.24121-24127.

[52] Tian, H., Xu, B., Chen, H., Johansson, E.M. and Boschloo, G., 2014. Solid-state perovskite-sensitized p-type mesoporous nickel oxide solar cells. *ChemSusChem*, *7*(8), pp.2150-2153.

[53] Jeng, J.Y., Chen, K.C., Chiang, T.Y., Lin, P.Y., Tsai, T.D., Chang, Y.C., Guo, T.F., Chen, P., Wen, T.C. and Hsu, Y.J., 2014. Nickel oxide electrode interlayer in $CH_3NH_3PbI_3$ perovskite/PCBM planar-heterojunction hybrid solar cells. *Advanced Materials*, *26*(24), pp.4107-4113.

[54] Bach, U., Lupo, D., Comte, P., Moser, J.E., Weissörtel, F., Salbeck, J., Spreitzer, H. and Grätzel, M., 1998. Solid-state dye-sensitized mesoporous TiO_2 solar cells with high photon-to-electron conversion efficiencies. *Nature*, *395*(6702), pp.583-585.

[55] Krüger, J., Plass, R., Cevey, L., Piccirelli, M., Grätzel, M. and Bach, U., 2001. High efficiency solid-state photovoltaic device due to inhibition of interface charge recombination. *Applied Physics Letters*, *79*(13), pp.2085-2087.

[56] Burschka, J., Dualeh, A., Kessler, F., Baranoff, E., Cevey-Ha, N.L., Yi, C., Nazeeruddin, M.K. and Grätzel, M., 2011. Tris (2-(1 H-pyrazol-1-yl) pyridine) cobalt (III) as p-type dopant for organic semiconductors and its application in highly efficient solid-state dye-

sensitized solar cells. *Journal of the American Chemical Society*, *133*(45), pp.18042-18045.

[57] Qiu, J., Qiu, Y., Yan, K., Zhong, M., Mu, C., Yan, H. and Yang, S., 2013. All-solid-state hybrid solar cells based on a new organometal halide perovskite sensitizer and one-dimensional TiO_2 nanowire arrays. *Nanoscale*, *5*(8), pp.3245-3248.

[58] Kim, H.S., Lee, J.W., Yantara, N., Boix, P.P., Kulkarni, S.A., Mhaisalkar, S., Grätzel, M. and Park, N.G., 2013. High efficiency solid-state sensitized solar cell-based on submicrometer rutile TiO_2 nanorod and $CH_3NH_3PbI_3$ perovskite sensitizer. *Nano Letters*, *13*(6), pp.2412-2417.

[59] Dar, M.I., Ramos, F.J., Xue, Z., Liu, B., Ahmad, S., Shivashankar, S.A., Nazeeruddin, M.K. and Grätzel, M., 2014. Photoanode based on (001)-oriented anatase nanoplatelets for organic–inorganic lead iodide perovskite solar cell. *Chemistry of Materials*, *26*(16), pp.4675-4678.

[60] Yella, A., Heiniger, L.P., Gao, P., Nazeeruddin, M.K. and Grätzel, M., 2014. Nanocrystalline rutile electron extraction layer enables low-temperature solution processed perovskite photovoltaics with 13.7% efficiency. *Nano Letters*, *14*(5), pp.2591-2596.

[61] Gao, X., Li, J., Baker, J., Hou, Y., Guan, D., Chen, J. and Yuan, C., 2014. Enhanced photovoltaic performance of perovskite $CH_3NH_3PbI_3$ solar cells with freestanding TiO_2 nanotube array films. *Chemical Communications*, *50*(48), pp.6368-6371.

[62] Bi, D., Boschloo, G., Schwarzmüller, S., Yang, L., Johansson, E.M. and Hagfeldt, A., 2013. Efficient and stable $CH_3NH_3PbI_3$-sensitized ZnO nanorod array solid-state solar cells. *Nanoscale*, *5*(23), pp.11686-11691.

[63] Son, D.Y., Im, J.H., Kim, H.S. and Park, N.G., 2014. 11% efficient perovskite solar cell based on ZnO nanorods: an effective charge collection system. *The Journal of Physical Chemistry C*, *118*(30), pp.16567-16573.

[64] Weber, S., Rath, T., Mangalam, J., Kunert, B., Coclite, A.M., Bauch, M., Dimopoulos, T. and Trimmel, G., 2018. Investigation of NiO_x-hole transport layers in triple cation perovskite solar cells. *Journal of Materials Science: Materials in Electronics*, *29*(3), pp.1847-1855.

[65] Liu, Z., Zhu, A., Cai, F., Tao, L., Zhou, Y., Zhao, Z., Chen, Q., Cheng, Y.B. and Zhou, H., 2017. Nickel oxide nanoparticles for efficient hole transport in pin and nip perovskite solar cells. *Journal of Materials Chemistry A*, *5*(14), pp.6597-6605.

[66] Saranin, D.S., Mazov, V.N., Luchnikov, L.O., Lypenko, D.A., Gostishev, P.A., Muratov, D.S., Podgorny, D.A., Migunov, D.M., Didenko, S.I., Orlova, M.N. and Kuznetsov, D.V., 2018. Tris (ethylene diamine) nickel acetate as a promising precursor for hole transport layer in planar structured perovskite solar cells. *Journal of Materials Chemistry C*, *6*(23), pp.6179-6186.

[67] Schwingenschlögl, U., De Wolf, S., Laquai, F., Aydin, E., Troughton, J., Neophytou, M., Baran, D., De Bastiani, M., Ugur, E., Sajjad, M. and Alzahrani, A., 2018. Room-Temperature-Sputtered Nanocrystalline Nickel Oxide as Hole Transport Layer for pin Perovskite Solar Cells. *ACS Applied Energy Materials*.

[68] Wang, T., Ding, D., Wang, X., Zeng, R., Liu, H. and Shen, W., 2018. High-Performance Inverted Perovskite Solar Cells with Mesoporous NiO_x Hole Transport Layer by Electrochemical Deposition. *ACS Omega*, *3*(12), pp.18434-18443.

[69] Han, Q., Wei, Y., Lin, R., Fang, Z., Xiao, K., Luo, X., Gu, S., Zhu, J., Ding, L. and Tan, H., 2019. Low-temperature processed inorganic hole transport layer for efficient and stable mixed Pb-Sn low-bandgap perovskite solar cells. *Science Bulletin*, *64*(19), p.1399.

[70] Koushik, D., Jošt, M., Dučinskas, A., Burgess, C., Zardetto, V., Weijtens, C., Verheijen, M.A., Kessels, W.M., Albrecht, S. and Creatore, M., 2019. Plasma-assisted atomic layer deposition of nickel oxide as hole transport layer for hybrid perovskite solar cells. *Journal of Materials Chemistry C*, *7*(40), pp.12532-12543.

[71] Seo, S., Jeong, S., Bae, C., Park, N.G. and Shin, H., 2018. Perovskite Solar Cells with Inorganic Electron-and Hole-Transport Layers Exhibiting Long-Term (≈ 500 h) Stability at 85° C under Continuous 1 Sun Illumination in Ambient Air. *Advanced Materials*, *30*(29), p.1801010.

[72] Zhao, P., Liu, Z., Lin, Z., Chen, D., Su, J., Zhang, C., Zhang, J., Chang, J. and Hao, Y., 2018. Device simulation of inverted $CH_3NH_3PbI_3- xCl_x$ perovskite solar cells based on PCBM electron transport layer and NiO hole transport layer. *Solar Energy*, *169*, pp.11-18.

[73] Liu, H., Song, J., Qin, Y., Mou, J., Qiu, Q., Zhao, Y., Zhu, L. and Qiang, Y., 2020. Inverted planar perovskite solar cells featuring ligand-protecting colloidal NiO nanocrystals hole transport layer. *Vacuum*, *172*, p.109077.

[74] Singh, A., Ranjan, R., Ranjan, S., Singh, A., Garg, A. and Gupta, R.K., 2020. Effect of NiO Precursor Solution Ageing on the Perovskite Film Formation and Their Integration as Hole Transport Material for Perovskite Solar Cells. *Journal of Nanoscience and Nanotechnology*, *20*(6), pp.3710-3717.

[75] Pan, L., Liu, C., Zhu, H., Wan, M., Li, Y. and Mai, Y., 2020. Fine modification of reactively sputtered NiO_x hole transport layer for application in all-inorganic $CsPbI_2Br$ perovskite solar cells. *Solar Energy*, *196*, pp.521-529.

[76] Wu, C., Huang, Y., Wang, S., Miao, X., Ma, R. and Wang, C., 2020. Phytate modifies the hole transport layer and assists in blade coating to prepare efficient perovskite solar cells. *Solar Energy*, *203*, pp.25-31.

[77] Pant, N., Kulkarni, A., Yanagida, M., Shirai, Y., Miyasaka, T. and Miyano, K., 2020. Residual PbI_2 Beneficial in the Bulk or at the interface? An investigation study in sputtered NiO_x hole-transport-layer-based Perovskite solar cells. *ACS Applied Energy Materials*, *3*(7), pp.6215-6221.

[78] Liu, Y., Cai, H., Su, J., Ye, X., Yang, J., Liang, X., Guan, J., Zhou, X., Yin, J., Ni, J. and Li, J., 2020. Solution-combustion-based nickel oxide hole transport layers via fuel regulation in inverted planar perovskite solar cells. *Journal of Materials Science: Materials in Electronics*, pp.1-8.

[79] Thakur, U.K., Kumar, P., Gusarov, S., Kobryn, A.E., Riddell, S., Goswami, A., Alam, K.M., Savela, S., Kar, P., Thundat, T. and Meldrum, A., 2020. Consistently High V_{oc} Values in pin Type Perovskite Solar Cells Using Ni^{3+}-Doped NiO Nanomesh as the Hole Transporting Layer. *ACS Applied Materials & Interfaces*, *12*(10), pp.11467-11478.

[80] Shamna, M.S., Nithya, K.S. and Sudheer, K.S., 2020. Simulation and optimization of $CH_3NH_3SnI_3$ based inverted perovskite solar cell with NiO as Hole transport material. *Materials Today: Proceedings*, *33*, pp.1246-1251.

[81] Lee, J.H., Noh, Y.W., Jin, I.S. and Jung, J.W., 2018. Efficient planar heterojunction perovskite solar cells employing a solution-processed Zn-doped NiO_X hole transport layer. *Electrochimica Acta*, *284*, pp.253-259.

[82] He, Q., Yao, K., Wang, X., Xia, X., Leng, S. and Li, F., 2017. Room-temperature and solution-processable Cu-doped nickel oxide nanoparticles for efficient hole-transport layers of flexible large-area perovskite solar cells. *ACS Applied Materials & Interfaces*, *9*(48), pp.41887-41897.

[83] Elseman, A.M., Ji, J., Dou, S., Huang, H., Cui, P., Wei, D. and Li, M., 2018. Novel hole transport layer of nickel oxide composite with carbon for high-performance perovskite solar cells. *Chinese Physics B*, *27*(1), p.017305.

[84] Hu, Z., Chen, D., Yang, P., Yang, L., Qin, L., Huang, Y. and Zhao, X., 2018. Sol-gel-processed yttrium-doped NiO as hole transport layer in inverted perovskite solar cells for enhanced performance. *Applied Surface Science*, *441*, pp.258-264.

[85] Xie, Y., Lu, K., Duan, J., Jiang, Y., Hu, L., Liu, T., Zhou, Y. and Hu, B., 2018. Enhancing photovoltaic performance of inverted planar perovskite solar cells by cobalt-doped nickel oxide hole transport layer. *ACS Applied Materials & Interfaces*, *10*(16), pp.14153-14159.

[86] Xiao, S., Xu, F., Bai, Y., Xiao, J., Zhang, T., Hu, C., Meng, X., Tan, H., Ho, H.P. and Yang, S., 2019. An Ultra-low Concentration of Gold Nanoparticles Embedded in the NiO Hole Transport Layer Boosts the Performance of p-i-n Perovskite Solar Cells. *Solar RRL*, *3*(2), p.1800278.

[87] Zhang, J., Mao, W., Hou, X., Duan, J., Zhou, J., Huang, S., Ou-Yang, W., Zhang, X., Sun, Z. and Chen, X., 2018. Solution-processed Sr-doped NiO_x as hole transport layer for efficient and stable perovskite solar cells. *Solar Energy*, *174*, pp.1133-1141.

[88] Hazeghi, F., Mozaffari, S. and Ghorashi, S.M.B., 2020. Metal organic framework–derived core-shell CuO@ NiO nanosphares as hole transport material in perovskite solar cell. *Journal of Solid State Electrochemistry*, *24*, pp.1427-1438.

[89] Chandrasekhar, P.S., Seo, Y.H., Noh, Y.J. and Na, S.I., 2019. Room temperature solution-processed Fe doped NiO_x as a novel hole transport layer for high efficient perovskite solar cells. *Applied Surface Science*, *481*, pp.588-596.

[90] Lee, P.H., Li, B.T., Lee, C.F., Huang, Z.H., Huang, Y.C. and Su, W.F., 2020. High-efficiency perovskite solar cell using cobalt doped nickel oxide hole transport layer fabricated by NIR process. *Solar Energy Materials and Solar Cells*, *208*, p.110352.

[91] Wang, S., Guan, H., Yin, Y., Chang, J. and Zhang, C., 2020. The Performance Improvement of Using Hole Transport Layer with Lithium and Cobalt for Inverted Planar Perovskite Solar Cell. *Coatings*, *10*(4), p.354.

[92] Wang, S., Zhang, B., Feng, D., Lin, Z., Zhang, J., Hao, Y., Fan, X. and Chang, J., 2019. Achieving high performance and stable inverted planar perovskite solar cells using lithium and cobalt co-doped nickel oxide as hole transport layers. *Journal of Materials Chemistry C*, *7*(30), pp.9270-9277.

[93] Ouyang, D., Zheng, J., Huang, Z., Zhu, L. and Choy, W.C., 2021. An efficacious multifunction codoping strategy on a room-temperature solution-processed hole transport layer for realizing high-performance perovskite solar cells. *Journal of Materials Chemistry A*, *9*(1), pp.371-379.

[94] Chang, K.C., Yeh, T.H., Lee, H.Y. and Lee, C.T., 2020. High performance perovskite solar cells using multiple hole transport layer and modulated $FA_xMA_{1-x}PbI_3$ active layer. *Journal of Materials Science: Materials in Electronics*, *31*(5), pp.4135-4141.

[95] Elseman, A.M., Luo, L. and Song, Q.L., 2020. Self-doping synthesis of trivalent Ni_2O_3 as a hole transport layer for high fill factor and efficient inverted perovskite solar cells. *Dalton Transactions*, *49*(40), pp.14243-14250.

[96] Wang, T., Ding, D., Zheng, H., Wang, X., Wang, J., Liu, H. and Shen, W., 2019. Efficient inverted planar perovskite solar cells using ultraviolet/ozone-treated NiO_x as the hole transport layer. *Solar RRL*, *3*(6), p.1900045.

[97] Ouyang, D., Xiao, J., Ye, F., Huang, Z., Zhang, H., Zhu, L., Cheng, J. and Choy, W.C., 2018. Strategic synthesis of ultrasmall $NiCo_2O_4$ NPs as hole transport layer for highly efficient perovskite solar cells. *Advanced Energy Materials*, *8*(16), p.1702722.

[98] Papadas, I.T., Ioakeimidis, A., Armatas, G.S. and Choulis, S.A., 2018. Low-temperature combustion synthesis of a spinel $NiCo_2O_4$ hole transport layer for perovskite photovoltaics. *Advanced Science*, *5*(5), p.1701029.

[99] Gharibzadeh, S., Nejand, B.A., Moshaii, A., Mohammadian, N., Alizadeh, A.H., Mohammadpour, R., Ahmadi, V. and Alizadeh, A., 2016. Two-step physical deposition of a compact CuI Hole-Transport layer and the formation of an interfacial species in perovskite solar cells. *ChemSusChem*, *9*(15), pp.1929-1937.

[100] Sun, W., Ye, S., Rao, H., Li, Y., Liu, Z., Xiao, L., Chen, Z., Bian, Z. and Huang, C., 2016. Room-temperature and solution-processed copper iodide as the hole transport layer for inverted planar perovskite solar cells. *Nanoscale*, *8*(35), pp.15954-15960.

[101] Haider, S.Z., Anwar, H., Jamil, Y. and Shahid, M., 2020. A comparative study of interface engineering with different hole transport materials for high-performance perovskite solar cells. *Journal of Physics and Chemistry of Solids*, *136*, p.109147.

[102] Khadka, D.B., Shirai, Y., Yanagida, M. and Miyano, K., 2020. Ammoniated aqueous precursor ink processed copper iodide as hole transport layer for inverted planar perovskite solar cells. *Solar Energy Materials and Solar Cells*, *210*, p.110486.

[103] Sun, W., Li, Y., Ye, S., Rao, H., Yan, W., Peng, H., Li, Y., Liu, Z., Wang, S., Chen, Z. and Xiao, L., 2016. High-performance inverted planar heterojunction perovskite solar cells based on a solution-processed CuO_x hole transport layer. *Nanoscale*, *8*(20), pp.10806-10813.

[104] Miao, X., Wang, S., Sun, W., Zhu, Y., Du, C., Ma, R. and Wang, C., 2019. Room-temperature electrochemical deposition of ultrathin CuO_x film as hole transport layer for perovskite solar cells. *Scripta Materialia*, *165*, pp.134-139.

[105] Bu, I.Y., Fu, Y.S., Li, J.F. and Guo, T.F., 2017. Large-area electrospray-deposited nanocrystalline Cu_XO hole transport layer for perovskite solar cells. *RSC Advances*, *7*(74), pp.46651-46656.

[106] Kumar, A. and Singh, S., 2020. Numerical modeling of planar lead free perovskite solar cell using tungsten disulfide (WS_2) as an electron transport layer and Cu_2O as a hole transport layer. *Modern Physics Letters B*, *34*(24), p.2050258.

[107] Lee, J.H., Jin, I.S., Noh, Y.W., Park, S.H. and Jung, J.W., 2019. A Solution-Processed Spinel CuCo2O4 as an Effective Hole Transport Layer for Efficient Perovskite Solar Cells with Negligible Hysteresis. *ACS Sustainable Chemistry & Engineering*, *7*(21), pp.17661-17670.

[108] Dunlap-Shohl, W.A., Daunis, T.B., Wang, X., Wang, J., Zhang, B., Barrera, D., Yan, Y., Hsu, J.W. and Mitzi, D.B., 2018. Room-temperature fabrication of a delafossite $CuCrO_2$ hole transport layer for perovskite solar cells. *Journal of Materials Chemistry A*, *6*(2), pp.469-477.

[109] Yang, B., Ouyang, D., Huang, Z., Ren, X., Zhang, H. and Choy, W.C., 2019. Multifunctional Synthesis Approach of In: $CuCrO_2$ Nanoparticles for Hole Transport Layer in High-Performance Perovskite Solar Cells. *Advanced Functional Materials*, *29*(34), p.1902600.

[110] Behrouznejad, F., Forouzandeh, M., Khosroshahi, R., Meraji, K., Badrabadi, M.N., Dehghani, M., Li, X., Zhan, Y., Liao, Y., Ning, Z. and Taghavinia, N., 2020. Effective Carbon Composite Electrode for Low-Cost Perovskite Solar Cell with Inorganic $CuIn_{0.75}Ga_{0.25}S_2$ Hole Transport Material. *Solar RRL*, *4*(5), p.1900564.

[111] Ye, X., Wen, Z., Zhang, R., Ling, H., Xia, J. and Lu, X., 2021. High-performance and stable inverted perovskite solar cells using low-temperature solution-processed $CuNbO_x$ hole transport layer. *Journal of Power Sources*, *483*, p.229194.

[112] Duong, T., Peng, J., Walter, D., Xiang, J., Shen, H., Chugh, D., Lockrey, M., Zhong, D., Li, J., Weber, K. and White, T.P., 2018. Perovskite solar cells employing copper phthalocyanine hole-transport material with an efficiency over 20% and excellent thermal stability. *ACS Energy Letters*, *3*(10), pp.2441-2448.

[113] Han, J., Tu, Y., Liu, Z., Liu, X., Ye, H., Tang, Z., Shi, T. and Liao, G., 2018. Efficient and stable inverted planar perovskite solar cells using dopant-free CuPc as hole transport layer. *Electrochimica Acta*, *273*, pp.273-281.

[114] Liu, Z., Sun, B., Liu, X., Han, J., Ye, H., Shi, T., Tang, Z. and Liao, G., 2018. Efficient carbon-based $CsPbBr_3$ inorganic perovskite solar cells by using Cu-phthalocyanine as hole transport material. *Nano-Micro Letters*, *10*(2), pp.1-13.

[115] Li, C., He, R., Liang, Q., Cao, J., Yin, J. and Tang, Y., 2020. 4-Tert-butylpyridine-assisted low-cost and soluble copper phthalocyanine as dopant-free hole transport layer for efficient Pb-and Sn-based perovskite solar cells. *Science China Chemistry*, *63*(8), pp.1053-1058.

[116] Yang, G., Wang, Y.L., Xu, J.J., Lei, H.W., Chen, C., Shan, H.Q., Liu, X.Y., Xu, Z.X. and Fang, G.J., 2017. A facile molecularly engineered copper (II) phthalocyanine as hole transport material for planar perovskite solar cells with enhanced performance and stability. *Nano Energy*, *31*, pp.322-330.

[117] Khanzada, L.S., Levchuk, I., Hou, Y., Azimi, H., Osvet, A., Ahmad, R., Brandl, M., Herre, P., Distaso, M., Hock, R. and Peukert, W., 2016. Effective ligand engineering of

the Cu_2ZnSnS_4 nanocrystal surface for increasing hole transport efficiency in perovskite solar cells. *Advanced Functional Materials*, *26*(45), pp.8300-8306.

[118] Cao, Y., Wu, H., Li, W., Zhao, Z., Xiao, Z., Zi, W., Cheng, N., Liu, J. and Tu, Y., 2020. Cu_2ZnSnS_4 as an efficient hole transporting material for low temperature paintable carbon electrode based perovskite solar cells. *Organic Electronics*, *76*, p.105455.

[119] Nan, H., Han, J., Yin, X., Zhou, Y., Yao, Z., Li, X. and Lin, H., 2019. Reduced Graphene Oxide/$CZTS_xSe_{1-x}$ Composites as a Novel Hole-Transport Functional Layer in Perovskite Solar Cells. *ChemElectroChem*, *6*(5), pp.1500-1507.

[120] Wu, Y., Bi, W., Shi, Z., Zhuang, X., Song, Z., Liu, S., Chen, C., Xu, L., Dai, Q. and Song, H., 2020. Unraveling the Dual-Functional Mechanism of Light Absorption and Hole Transport of $Cu_2Cd_xZn_{1-x}SnS_4$ for Achieving Efficient and Stable Perovskite Solar Cells. *ACS Applied Materials & Interfaces*, *12*(15), pp.17509-17518.

[121] Madhavan, V.E., Zimmermann, I., Baloch, A.A., Manekkathodi, A., Belaidi, A., Tabet, N. and Nazeeruddin, M.K., 2019. CuSCN as hole transport material with 3D/2D perovskite solar cells. *ACS Applied Energy Materials*, *3*(1), pp.114-121.

[122] Er, U., Icli, K.C. and Ozenbas, M., 2020. Spin-coated copper (I) thiocyanate as a hole transport layer for perovskite solar cells. *Journal of Solid State Electrochemistry*, *24*(2), pp.293-304.

[123] Hou, S., Shi, B., Wang, P., Li, Y., Zhang, J., Chen, P., Chen, B., Hou, F., Huang, Q., Ding, Y. and Li, Y., 2020. Highly efficient bifacial semitransparent perovskite solar cells based on molecular doping of CuSCN hole transport layer. *Chinese Physics B*, *29*(7), p.078801.

[124] Yang, Y., Hoang, M.T., Yao, D., Pham, N.D., Tiong, V.T., Wang, X. and Wang, H., 2020. Spiro-OMeTAD or CuSCN as a preferable hole transport material for carbon-based planar perovskite solar cells. *Journal of Materials Chemistry A*, *8*(25), pp.12723-12734.

[125] Wijeyasinghe, N., Regoutz, A., Eisner, F., Du, T., Tsetseris, L., Lin, Y.H., Faber, H., Pattanasattayavong, P., Li, J., Yan, F. and McLachlan, M.A., 2017. Copper (I) thiocyanate (CuSCN) hole-transport layers processed from aqueous precursor solutions and their application in thin-film transistors and highly efficient organic and organometal halide perovskite solar cells. *Advanced Functional Materials*, *27*(35), p.1701818.

[126] Chu, S., Zhao, R., Liu, R., Gao, Y., Wang, X., Liu, C., Chen, J. and Zhou, H., 2018. Atomic-layer-deposited ultra-thin VO_x film as a hole transport layer for perovskite solar cells. *Semiconductor Science and Technology*, *33*(11), p.115016.

[127] Guo, Q., Wang, C., Li, J., Bai, Y., Wang, F., Liu, L., Zhang, B., Hayat, T., Alsaedi, A. and Tan, Z.A., 2018. Low-temperature solution-processed vanadium oxide as hole transport layer for efficient and stable perovskite solar cells. *Physical Chemistry Chemical Physics*, *20*(33), pp.21746-21754.

[128] Ali, F., Khoshsirat, N., Duffin, J.L., Wang, H., Ostrikov, K., Bell, J.M. and Tesfamichael, T., 2017. Prospects of e-beam evaporated molybdenum oxide as a hole transport layer for perovskite solar cells. *Journal of Applied Physics*, *122*(12), p.123105.

[129] Xie, B., Zhang, Y., Li, Y., Chen, W., Hu, X. and Zhang, S., 2020. Solution preparation of molybdenum oxide on graphene: a hole transport layer for efficient perovskite solar cells with a 1.12 V high open-circuit voltage. *Journal of Materials Science: Materials in Electronics*, pp.1-7.

[130] Chen, L., Xie, Q., Wan, L., Zhang, W., Fu, S., Zhang, H., Ling, X., Yuan, J., Miao, L., Shen, C. and Li, X., 2019. Solution-Processed MoO_x Hole-Transport Layer with F4-TCNQ Modification for Efficient and Stable Inverted Perovskite Solar Cells. *ACS Applied Energy Materials*, *2*(8), pp.5862-5870.

[131] Ansari, F., Salavati-Niasari, M., Amiri, O., Mir, N., Abdollahi Nejand, B. and Ahmadi, V., 2020. Magnetite as inorganic hole transport material for lead halide perovskite-based solar cells with enhanced stability. *Industrial & Engineering Chemistry Research*, *59*(2), pp.743-750.

[132] Zhang, Y., Ge, J., Mahmoudi, B., Förster, S., Syrowatka, F., Maijenburg, A.W. and Scheer, R., 2020. Synthesis and Characterization of Spinel Cobaltite (Co_3O_4) Thin Films for Function as Hole Transport Materials in Organometallic Halide Perovskite Solar Cells. *ACS Applied Energy Materials*, *3*(4), pp.3755-3769.

[133] Dasgupta, U., Chatterjee, S. and Pal, A.J., 2017. Thin-film formation of 2D MoS_2 and its application as a hole-transport layer in planar perovskite solar cells. *Solar Energy Materials and Solar Cells*, *172*, pp.353-360.

[134] Huang, P., Wang, Z., Liu, Y., Zhang, K., Yuan, L., Zhou, Y., Song, B. and Li, Y., 2017. Water-soluble 2D transition metal dichalcogenides as the hole-transport layer for highly

efficient and stable p–i–n perovskite solar cells. *ACS Applied Materials & Interfaces*, *9*(30), pp.25323-25331.

[135] Shin, D.H., Shin, S.H. and Choi, S.H., 2020. Self-powered and flexible perovskite photodiode/solar cell bifunctional devices with MoS_2 hole transport layer. *Applied Surface Science*, *514*, p.145880.

[136] Li, X., Yang, J., Jiang, Q., Lai, H., Li, S., Tan, Y., Chen, Y. and Li, S., 2019. Perovskite solar cells employing an eco-friendly and low-cost inorganic hole transport layer for enhanced photovoltaic performance and operational stability. *Journal of Materials Chemistry A*, *7*(12), pp.7065-7073.

[137] Zhang, X., Gao, N., Li, Y., Xie, L., Yu, X., Lu, X., Gao, X., Gao, J., Shui, L., Wu, S. and Liu, J.M., 2020. A solution-processed dopant-free tin phthalocyanine (SnPc) hole transport layer for efficient and stable carbon-based $CsPbI_2Br$ planar perovskite solar cells prepared by a low-temperature process. *ACS Applied Energy Materials*, *3*(8), pp.7832-7843.

[138] Wang, F., Endo, M., Mouri, S., Miyauchi, Y., Ohno, Y., Wakamiya, A., Murata, Y. and Matsuda, K., 2016. Highly stable perovskite solar cells with an all-carbon hole transport layer. *Nanoscale*, *8*(23), pp.11882-11888.

[139] Wang, Y., Hu, Y., Han, D., Yuan, Q., Cao, T., Chen, N., Zhou, D., Cong, H. and Feng, L., 2019. Ammonia-treated graphene oxide and PEDOT: PSS as hole transport layer for high-performance perovskite solar cells with enhanced stability. *Organic Electronics*, *70*, pp.63-70.

[140] Zhao, S., Zhuang, J., Liu, X., Zhang, H., Zheng, R., Peng, X., Gong, X., Guo, H., Wang, H. and Li, H., 2021. F4-TCNQ doped strategy of nickel oxide as high-efficient hole transporting materials for invert perovskite solar cell. *Materials Science in Semiconductor Processing*, *121*, p.105458.

[141] Zhang, J., Luo, H., Xie, W., Lin, X., Hou, X., Zhou, J., Huang, S., Ou-Yang, W., Sun, Z. and Chen, X., 2018. Efficient and ultraviolet durable planar perovskite solar cells via a ferrocenecarboxylic acid modified nickel oxide hole transport layer. *Nanoscale*, *10*(12), pp.5617-5625.

[142] Lee, S., Lee, J., Park, H., Choi, J., Baac, H.W., Park, S. and Park, H.J., 2020. Defect-Passivating Organic/Inorganic Bicomponent Hole-Transport Layer for High Efficiency

Metal-Halide Perovskite Device. *ACS Applied Materials & Interfaces*, *12*(36), pp.40310-40317.

[143] Li, R., Wang, P., Chen, B., Cui, X., Ding, Y., Li, Y., Zhang, D., Zhao, Y. and Zhang, X., 2019. NiO_x/Spiro Hole Transport Bilayers for Stable Perovskite Solar Cells with Efficiency Exceeding 21%. *ACS Energy Letters*, *5*(1), pp.79-86.

[144] Wu, F., Pathak, R., Chen, C., Tong, Y., Xu, H., Zhang, T., Jian, R., Li, X. and Qiao, Q., 2020. Reduced hysteresis in perovskite solar cells using metal oxide/organic hybrid hole transport layer with generated interfacial dipoles. *Electrochimica Acta*, *354*, p.136660.

[145] Wang, D., Elumalai, N.K., Mahmud, M.A., Wright, M., Upama, M.B., Chan, K.H., Xu, C., Haque, F., Conibeer, G. and Uddin, A., 2018. V_2O_5-PEDOT: PSS bilayer as hole transport layer for highly efficient and stable perovskite solar cells. *Organic Electronics*, *53*, pp.66-73.

[146] Wang, D., Elumalai, N.K., Mahmud, M.A., Yi, H., Upama, M.B., Chin, R.A.L., Conibeer, G., Xu, C., Haque, F., Duan, L. and Uddin, A., 2018. MoS_2 incorporated hybrid hole transport layer for high performance and stable perovskite solar cells. *Synthetic Metals*, *246*, pp.195-203.

[147] Yi, H., Wang, D., Duan, L., Haque, F., Xu, C., Zhang, Y., Conibeer, G. and Uddin, A., 2019. Solution-processed WO_3 and water-free PEDOT: PSS composite for hole transport layer in conventional perovskite solar cell. *Electrochimica Acta*, *319*, pp.349-358.

[148] Song, J., Hu, W., Li, Z., Wang, X.F. and Tian, W., 2020. A double hole-transport layer strategy toward efficient mixed tin-lead iodide perovskite solar cell. *Solar Energy Materials and Solar Cells*, *207*, p.110351.

[149] Li, W., Cheng, N., Cao, Y., Zhao, Z., Xiao, Z., Zi, W. and Sun, Z., 2020. Boost the performance of inverted perovskite solar cells with PEDOT: PSS/Graphene quantum dots composite hole transporting layer. *Organic Electronics*, *78*, p.105575.

[150] Gil, B., Kim, J., Yun, A.J., Park, K., Cho, J., Park, M. and Park, B., 2020. $CuCrO_2$ Nanoparticles Incorporated into PTAA as a Hole Transport Layer for 85° C and Light Stabilities in Perovskite Solar Cells. *Nanomaterials*, *10*(9), p.1669.

[151] Tepliakova, M.M., Mikheeva, A.N., Frolova, L.A., Boldyreva, A.G., Elakshar, A., Novikov, A.V., Tsarev, S.A., Ustinova, M.I., Yamilova, O.R., Nasibulin, A.G. and Aldoshin, S.M., 2020. Incorporation of Vanadium (V) Oxide in Hybrid Hole Transport

Layer Enables Long-term Operational Stability of Perovskite Solar Cells. *The Journal of Physical Chemistry Letters*, *11*(14), pp.5563-5568.

[152] Lei, H., Yang, G., Zheng, X., Zhang, Z.G., Chen, C., Ma, J., Guo, Y., Chen, Z., Qin, P., Li, Y. and Fang, G., 2017. Incorporation of high-mobility and room-temperature-deposited Cu_xS as a hole transport layer for efficient and stable organo-lead halide perovskite solar cells. *Solar RRL*, *1*(6), p.1700038.

[153] Haddad, J., Krogmeier, B., Klingebiel, B., Krückemeier, L., Melhem, S., Liu, Z., Hüpkes, J., Mathur, S. and Kirchartz, T., 2020. Analyzing Interface Recombination in Lead-Halide Perovskite Solar Cells with Organic and Inorganic Hole-Transport Layers. *Advanced Materials Interfaces*, *7*(16), p.2000366.

[154] Guo, Y., Lei, H., Xiong, L., Li, B. and Fang, G., 2018. An integrated organic–inorganic hole transport layer for efficient and stable perovskite solar cells. *Journal of Materials Chemistry A*, *6*(5), pp.2157-2165.

[155] Cheng, M., Li, Y., Safdari, M., Chen, C., Liu, P., Kloo, L. and Sun, L., 2017. Efficient perovskite solar cells based on a solution processable nickel (II) phthalocyanine and vanadium oxide integrated hole transport layer. *Advanced Energy Materials*, *7*(14), p.1602556.

[156] Kim, G.W., Kang, G., Choi, K., Choi, H. and Park, T., 2018. Solution Processable Inorganic–Organic Double-Layered Hole Transport Layer for Highly Stable Planar Perovskite Solar Cells. *Advanced Energy Materials*, *8*(26), p.1801386.

[157] Li, S., Wan, L., Chen, L., Deng, C., Tao, L., Lu, Z., Zhang, W., Fang, J. and Song, W., 2020. Self-Doping a Hole-Transporting Layer Based on a Conjugated Polyelectrolyte Enables Efficient and Stable Inverted Perovskite Solar Cells. *ACS Applied Energy Materials*.

[158] Liu, Y., Hu, Y., Zhang, X., Zeng, P., Li, F., Wang, B., Yang, Q. and Liu, M., 2020. Inhibited aggregation of lithium salt in spiro-OMeTAD toward highly efficient perovskite solar cells. *Nano Energy*, *70*, p.104483.

[159] Shadrokh, Z., Sousani, S., Gholipour, S. and Abdi, Y., 2020. Enhanced stability and performance of poly (4-vinylpyridine) modified perovskite solar cell with quaternary semiconductor Cu_2MSnS_4 (M= Co^{2+}, Ni^{2+}, Zn^{2+}) as hole transport materials. *Solar Energy Materials and Solar Cells*, *211*, p.110538.

[160] Wang, Y., Ye, W., Yang, X., Rezaee, E., Shan, H., Yang, S., Cai, S., Pan, J.H., Xu, J. and Xu, Z.X., 2020. Hole transport layers based on metal Schiff base complexes in perovskite solar cells. *Synthetic Metals*, *259*, p.116248.

[161] Zhang, Y., Zhang, Z., Liu, Y., Gao, H. and Mao, Y., 2020. Short-chain ligands capped $CuInSe_2$ quantum dots as hole transport material for inverted perovskite solar cells. *Materials Science in Semiconductor Processing*, *120*, p.105267.

[162] Sin, D.H., Ko, H., Jo, S.B., Kim, M., Bae, G.Y. and Cho, K., 2016. Decoupling charge transfer and transport at polymeric hole transport layer in perovskite solar cells. *ACS Applied Materials & Interfaces*, *8*(10), pp.6546-6553.

[163] Huang, D., Goh, T., Kong, J., Zheng, Y., Zhao, S., Xu, Z. and Taylor, A.D., 2017. Perovskite solar cells with a DMSO-treated PEDOT: PSS hole transport layer exhibit higher photovoltaic performance and enhanced durability. *Nanoscale*, *9*(12), pp.4236-4243.

[164] Kakavelakis, G., Alexaki, K., Stratakis, E. and Kymakis, E., 2017. Efficiency and stability enhancement of inverted perovskite solar cells via the addition of metal nanoparticles in the hole transport layer. *RSC Advances*, *7*(21), pp.12998-13002.

[165] Liu, D., Li, Y., Yuan, J., Hong, Q., Shi, G., Yuan, D., Wei, J., Huang, C., Tang, J. and Fung, M.K., 2017. Improved performance of inverted planar perovskite solar cells with F4-TCNQ doped PEDOT: PSS hole transport layers. *Journal of Materials Chemistry A*, *5*(12), pp.5701-5708.

[166] Luo, H., Lin, X., Hou, X., Pan, L., Huang, S. and Chen, X., 2017. Efficient and air-stable planar perovskite solar cells formed on graphene-oxide-modified PEDOT: PSS hole transport layer. *Nano-Micro Letters*, *9*(4), p.39.

[167] Bruijnaers, B.J., Schiepers, E., Weijtens, C.H., Meskers, S.C., Wienk, M.M. and Janssen, R.A., 2018. The effect of oxygen on the efficiency of planar p–i–n metal halide perovskite solar cells with a PEDOT: PSS hole transport layer. *Journal of Materials Chemistry A*, *6*(16), pp.6882-6890.

[168] Elbohy, H., Bahrami, B., Mabrouk, S., Reza, K.M., Gurung, A., Pathak, R., Liang, M., Qiao, Q. and Zhu, K., 2019. Tuning hole transport layer using urea for high-performance perovskite solar cells. *Advanced Functional Materials*, *29*(47), p.1806740.

[169] Wang, C., Li, Y., Zhang, C., Shi, L., Tong, S., Guo, B., Zhang, J., He, J., Gao, Y., Su, C. and Yang, J., 2018. Enhancing the performance of planar heterojunction perovskite solar cells using stable semiquinone and amine radical modified hole transport layer. *Journal of Power Sources*, *390*, pp.134-141.

[170] Yu, J.C., Hong, J.A., Jung, E.D., Kim, D.B., Baek, S.M., Lee, S., Cho, S., Park, S.S., Choi, K.J. and Song, M.H., 2018. Highly efficient and stable inverted perovskite solar cell employing PEDOT: GO composite layer as a hole transport layer. *Scientific reports*, *8*(1), pp.1-9.

[171] Hu, W., Xu, C.Y., Niu, L.B., Elseman, A.M., Wang, G., Liu, D.B., Yao, Y.Q., Liao, L.P., Zhou, G.D. and Song, Q.L., 2019. High open-circuit voltage of 1.134 V for inverted planar perovskite solar cells with sodium citrate-doped PEDOT: PSS as a hole transport layer. *ACS Applied Materials & Interfaces*, *11*(24), pp.22021-22027.

[172] Li, P., Mohamed, M.I.O., Xu, C., Wang, X. and Tang, X., 2020. Electrical property modified hole transport layer (PEDOT: PSS) enhance the efficiency of perovskite solar cells: Hybrid co-solvent post-treatment. *Organic Electronics*, *78*, p.105582.

[173] Reza, K.M., Gurung, A., Bahrami, B., Mabrouk, S., Elbohy, H., Pathak, R., Chen, K., Chowdhury, A.H., Rahman, M.T., Letourneau, S. and Yang, H.C., 2020. Tailored PEDOT: PSS hole transport layer for higher performance in perovskite solar cells: enhancement of electrical and optical properties with improved morphology. *Journal of Energy Chemistry*, *44*, pp.41-50.

[174] Wang, X., Lu, G., Zhang, M., Gao, Y., Liu, Y., Zhou, L. and Lin, Z., 2020. High performance planar structure perovskite solar cells using a solvent dripping treatment on hole transporting layer. *Coatings*, *10*(2), p.127.

[175] Zhang, M., Chi, D., Wang, J., Wu, F. and Huang, S., 2020. Improved performance of lead-tin mixed perovskite solar cells with PEDOT: PSS treated by hydroquinone. *Solar Energy*, *201*, pp.589-595.

[176] Zhou, Z., Li, X., Cai, M., Xie, F., Wu, Y., Lan, Z., Yang, X., Qiang, Y., Islam, A. and Han, L., 2017. Stable inverted planar perovskite solar cells with low-temperature-processed hole-transport bilayer. *Advanced Energy Materials*, *7*(22), p.1700763.

[177] Xu, C., Liu, Z. and Lee, E.C., 2018. High-performance metal oxide-free inverted perovskite solar cells using poly (bis (4-phenyl)(2, 4, 6-trimethylphenyl) amine) as the hole transport layer. *Journal of Materials Chemistry C*, *6*(26), pp.6975-6981.

[178] Khadka, D.B., Shirai, Y., Yanagida, M. and Miyano, K., 2019. Unraveling the impacts induced by organic and inorganic hole transport layers in inverted halide perovskite solar cells. *ACS applied materials & interfaces*, *11*(7), pp.7055-7065.

[179] Sekimoto, T., Matsui, T., Nishihara, T., Uchida, R., Sekiguchi, T. and Negami, T., 2019. Influence of a hole-transport layer on light-induced degradation of mixed organic–inorganic halide perovskite solar cells. *ACS Applied Energy Materials*, *2*(7), pp.5039-5049.

[180] Zhao, Q., Wu, R., Zhang, Z., Xiong, J., He, Z., Fan, B., Dai, Z., Yang, B., Xue, X., Cai, P. and Zhan, S., 2019. Achieving efficient inverted planar perovskite solar cells with nondoped PTAA as a hole transport layer. *Organic Electronics*, *71*, pp.106-112.

[181] Oo, A.M., Fan, P., Zhang, X. and Yu, J., 2020. Efficiency Improvement of Planar Inverted Perovskite Solar Cells by Introducing Poly 9, 9-Dioctyfluorene-co-benzothiazole into Polytriarylamine as Mixed Hole-Transport Layer. *Energy Technology*, *8*(3), p.1901042.

[182] Tepliakova, M.M., Akkuratov, A.V., Tsarev, S.A. and Troshin, P.A., 2020. Suzuki polycondensation for the synthesis of polytriarylamines: A method to improve hole-transport material performance in perovskite solar cells. *Tetrahedron Letters*, *61*(38), p.152317.

[183] Wang, Z., Fan, P., Zhang, D., Yang, G. and Yu, J., 2020. Enhanced efficiency and stability of pin perovskite solar cells using PMMA doped PTAA as hole transport layers. *Synthetic Metals*, *265*, p.116428.

[184] Yang, Y., Yuan, Q., Li, H., Niu, Y., Han, D., Yang, Q., Yang, Y., Yi, S., Zhou, D.Y. and Feng, L., 2020. Dopant free mixture of Spiro-OMeTAD and PTAA with tunable wettability as hole transport layer enhancing performance of inverted CsPbI2Br perovskite solar cells. *Organic Electronics*, *86*, p.105873.

[185] Tsarev, S., Kraevaya, O.A., Luchkin, S.Y., Stevenson, K.J. and Troshin, P.A., 2020. TEMPOL-promoted oxygen doping of a polytriarylamine hole-transport layer for

efficient and stable lead halide perovskite solar cells. *Journal of Materials Chemistry C*, *8*(7), pp.2419-2424.

[186] Ahmadi, M., Hsiao, Y.C., Wu, T., Liu, Q., Qin, W. and Hu, B., 2017. Effect of Photogenerated Dipoles in the Hole Transport Layer on Photovoltaic Performance of Organic–Inorganic Perovskite Solar Cells. *Advanced Energy Materials*, *7*(4), p.1601575.

[187] Kim, G.W., Kang, G., Malekshahi Byranvand, M., Lee, G.Y. and Park, T., 2017. Gradated mixed hole transport layer in a perovskite solar cell: improving moisture stability and efficiency. *ACS Applied Materials & Interfaces*, *9*(33), pp.27720-27726.

[188] Yaghoobi Nia, N., Lamanna, E., Zendehdel, M., Palma, A.L., Zurlo, F., Castriotta, L.A. and Di Carlo, A., 2019. Doping strategy for efficient and stable triple cation hybrid perovskite solar cells and module based on poly (3-hexylthiophene) hole transport layer. *Small*, *15*(49), p.1904399.

[189] Tran, H.C.V., Jiang, W., Lyu, M. and Chae, H., 2020. Tetrahydrofuran as Solvent for P3HT/F4-TCNQ Hole-Transporting Layer to Increase the Efficiency and Stability of FAPbI3-Based Perovskite Solar Cell. *The Journal of Physical Chemistry C*, *124*(26), pp.14099-14104.

[190] Li, X., Wang, Y.C., Zhu, L., Zhang, W., Wang, H.Q. and Fang, J., 2017. Improving efficiency and reproducibility of perovskite solar cells through aggregation control in polyelectrolytes hole transport layer. *ACS Applied Materials & Interfaces*, *9*(37), pp.31357-31361.

[191] Li, J., Zhao, M., Zhao, C., Jian, H., Wang, N., Yao, L., Huang, C., Zhao, Y. and Jiu, T., 2018. Graphdiyne-doped P3CT-K as an efficient hole-transport layer for $MAPbI_3$ perovskite solar cells. *ACS Applied Materials & Interfaces*, *11*(3), pp.2626-2631.

[192] Zhang, W., Wan, L., Li, X., Wu, Y., Fu, S. and Fang, J., 2019. A dopant-free polyelectrolyte hole-transport layer for high efficiency and stable planar perovskite solar cells. *Journal of Materials Chemistry A*, *7*(32), pp.18898-18905.

[193] Li, S., He, B., Xu, J., Lu, H., Jiang, J., Zhu, J., Kan, Z., Zhu, L. and Wu, F., 2020. Highly efficient inverted perovskite solar cells incorporating P3CT-Rb as a hole transport layer to achieve a large open circuit voltage of 1.144 V. *Nanoscale*, *12*(6), pp.3686-3691.

[194] Yuan, J., Ling, X., Yang, D., Li, F., Zhou, S., Shi, J., Qian, Y., Hu, J., Sun, Y., Yang, Y. and Gao, X., 2018. Band-aligned polymeric hole transport materials for extremely low energy loss α-$CsPbI_3$ perovskite nanocrystal solar cells. *Joule*, *2*(11), pp.2450-2463.

[195] Kim, G.W., Lee, J., Kang, G., Kim, T. and Park, T., 2018. Donor–Acceptor Type Dopant-Free, Polymeric Hole Transport Material for Planar Perovskite Solar Cells (19.8%). *Advanced Energy Materials*, *8*(4), p.1701935.

[196] Lee, J., Kim, G.W., Kim, M., Park, S.A. and Park, T., 2020. Nonaromatic Green-Solvent-Processable, Dopant-Free, and Lead-Capturable Hole Transport Polymers in Perovskite Solar Cells with High Efficiency. *Advanced Energy Materials*, *10*(8), p.1902662.

[197] Elawad, M., Sun, L., Mola, G.T., Yu, Z. and Arbab, E.A.A., 2019. Enhanced performance of perovskite solar cells using p-type doped PFB: F4TCNQ composite as hole transport layer. *Journal of Alloys and Compounds*, *771*, pp.25-32.

[198] Hu, J., You, J., Peng, C., Qiu, S., He, W., Li, C., Liu, X., Mai, Y. and Guo, F., 2020. Polyfluorene Copolymers as High-Performance Hole-Transport Materials for Inverted Perovskite Solar Cells. *Solar RRL*, *4*(3), p.1900384.

[199] Gaml, E.A., Dubey, A., Reza, K.M., Hasan, M.N., Adhikari, N., Elbohy, H., Bahrami, B., Zeyada, H., Yang, S. and Qiao, Q., 2017. Alternative benzodithiophene (BDT) based polymeric hole transport layer for efficient perovskite solar cells. *Solar Energy Materials and Solar Cells*, *168*, pp.8-13.

[200] Cai, F., Cai, J., Yang, L., Li, W., Gurney, R.S., Yi, H., Iraqi, A., Liu, D. and Wang, T., 2018. Molecular engineering of conjugated polymers for efficient hole transport and defect passivation in perovskite solar cells. *Nano Energy*, *45*, pp.28-36.

[201] Du, T., Xu, W., Daboczi, M., Kim, J., Xu, S., Lin, C.T., Kang, H., Lee, K., Heeney, M.J., Kim, J.S. and Durrant, J.R., 2019. p-Doping of organic hole transport layers in p–i–n perovskite solar cells: correlating open-circuit voltage and photoluminescence quenching. *Journal of Materials Chemistry A*, *7*(32), pp.18971-18979.

[202] Al-Dainy, G.A., Watanabe, F., Kannarpady, G.K., Ghosh, A., Berry, B., Biris, A.S. and Bourdo, S.E., 2020. Optimizing Lignosulfonic Acid-Grafted Polyaniline as a Hole-Transport Layer for Inverted $CH_3NH_3PbI_3$ Perovskite Solar Cells. *ACS Omega*, *5*(4), pp.1887-1901.

[203] Geffroy, C., Grana, E., Bessho, T., Almosni, S., Tang, Z., Sharma, A., Kinoshita, T., Awai, F., Cloutet, E., Toupance, T. and Segawa, H., 2020. p-Doping of a Hole Transport Material via a Poly (ionic liquid) for over 20% Efficiency and Hysteresis-Free Perovskite Solar Cells. *ACS Applied Energy Materials*, *3*(2), pp.1393-1401.

[204] Kulshreshtha, C., Clement, A., Pascher, T., Sundström, V. and Matyba, P., 2020. Investigating ultrafast carrier dynamics in perovskite solar cells with an extended π-conjugated polymeric diketopyrrolopyrrole layer for hole transportation. *RSC Advances*, *10*(11), pp.6618-6624.

[205] Li, Z., Park, J., Park, H., Lee, J., Kang, Y., Ahn, T.K., Kim, B.G. and Park, H.J., 2020. Graded heterojunction of perovskite/dopant-free polymeric hole-transport layer for efficient and stable metal halide perovskite devices. *Nano Energy*, *78*, p.105159.

[206] Murugesan, V.S., Michael, R.R., Jena, A.K., Kang, J.W., Kim, N.H., Segawa, H., Miyasaka, T. and Lee, J.H., 2020. Benzodithiophene-thienopyrroledione-thienothiophene-based random copolymeric hole transporting material for perovskite solar cell. *Chemical Engineering Journal*, *382*, p.122830.

[207] Nishihara, Y., Onozawa-Komatsuzaki, N., Zou, X., Marumoto, K., Chikamatsu, M. and Yoshida, Y., 2020. Effect of Passivation on the Interface between Perovskite and Donor–Acceptor Copolymer-based Hole-transport Layer in Perovskite Solar Cells. *Chemistry Letters*, *49*(11), pp.1341-1344.

[208] Oz, S., Jena, A.K., Kulkarni, A., Mouri, K., Yokoyama, T., Takei, I., Ünlü, F., Mathur, S. and Miyasaka, T., 2020. Lead (II) propionate additive and a dopant-free polymer hole transport material for $CsPbI_2Br$ perovskite solar cells. *ACS Energy Letters*, *5*(4), pp.1292-1299.

[209] Shalan, A.E., Sharmoukh, W., Elshazly, A.N., Elnagar, M.M., Al Kiey, S.A., Rashad, M.M. and Allam, N.K., 2020. Dopant-free hole-transporting polymers for efficient, stable, and hysteresis-less perovskite solar cells. *Sustainable Materials and Technologies*, *26*, p.e00226.

[210] Yao, Z., Zhang, F., Guo, Y., Wu, H., He, L., Liu, Z., Cai, B., Guo, Y., Brett, C.J., Li, Y. and Srambickal, C.V., 2020. Conformational and Compositional Tuning of Phenanthrocarbazole-Based Dopant-Free Hole-Transport Polymers Boosting the

Performance of Perovskite Solar Cells. *Journal of the American Chemical Society*, *142*(41), pp.17681-17692.

[211] Yu, J.C., Sun, J., Chandrasekaran, N., Dunn, C.J., Chesman, A.S. and Jasieniak, J.J., 2020. Semi-transparent perovskite solar cells with a cross-linked hole transport layer. *Nano Energy*, *71*, p.104635.

[212] Jeong, J., Kim, M., Seo, J., Lu, H., Ahlawat, P., Mishra, A., Yang, Y., Hope, M.A., Eickemeyer, F.T., Kim, M. and Yoon, Y.J., 2021. Pseudo-halide anion engineering for α-FAPbI 3 perovskite solar cells. *Nature*, *592*(7854), pp.381-385.

[213] Tavakoli, M.M., Tress, W., Milić, J.V., Kubicki, D., Emsley, L. and Grätzel, M., 2018. Addition of adamantylammonium iodide to hole transport layers enables highly efficient and electroluminescent perovskite solar cells. *Energy & Environmental Science*, *11*(11), pp.3310-3320.

[214] Wang, X., Zhang, J., Yu, S., Yu, W., Fu, P., Liu, X., Tu, D., Guo, X. and Li, C., 2018. Lowering Molecular Symmetry To Improve the Morphological Properties of the Hole-Transport Layer for Stable Perovskite Solar Cells. *Angewandte Chemie International Edition*, *57*(38), pp.12529-12533.

[215] Zhang, J., Daniel, Q., Zhang, T., Wen, X., Xu, B., Sun, L., Bach, U. and Cheng, Y.B., 2018. Chemical dopant engineering in hole transport layers for efficient perovskite solar cells: insight into the interfacial recombination. *ACS Nano*, *12*(10), pp.10452-10462.

[216] Hu, M., Wu, X., Tan, W.L., Tan, B., Scully, A.D., Ding, L., Zhou, C., Xiong, Y., Huang, F., Simonov, A.N. and Bach, U., 2020. Solvent Engineering of a Dopant-Free Spiro-OMeTAD Hole-Transport Layer for Centimeter-Scale Perovskite Solar Cells with High Efficiency and Thermal Stability. *ACS Applied Materials & Interfaces*, *12*(7), pp.8260-8270.

[217] Sathiyan, G., Syed, A.A., Chen, C., Wu, C., Tao, L., Ding, X., Miao, Y., Li, G., Cheng, M. and Ding, L., 2020. Dual effective dopant based hole transport layer for stable and efficient perovskite solar cells. *Nano Energy*, *72*, p.104673.

[218] Hajikhanmirzaei, L., Shahroosvand, H., Pashaei, B., Delle Monache, G., Nazeeruddin, M.K. and Pilkington, M., 2020. A cost-device efficiency balanced spiro based hole transport material for perovskite solar cells. *Journal of Materials Chemistry C*, *8*(18), pp.6221-6227.

[219] Wang, C., Hu, J., Li, C., Qiu, S., Liu, X., Zeng, L., Liu, C., Mai, Y. and Guo, F., 2020. Spiro-Linked Molecular Hole-Transport Materials for Highly Efficient Inverted Perovskite Solar Cells. *Solar RRL*, *4*(3), p.1900389.

[220] Liu, J., Liu, W., Aydin, E., Harrison, G.T., Isikgor, F.H., Yang, X., Subbiah, A.S. and De Wolf, S., 2020. Lewis-Acid Doping of Triphenylamine-Based Hole Transport Materials Improves the Performance and Stability of Perovskite Solar Cells. *ACS Applied Materials & Interfaces*, *12*(21), pp.23874-23884.

[221] Azmi, R., Nam, S.Y., Sinaga, S., Akbar, Z.A., Lee, C.L., Yoon, S.C., Jung, I.H. and Jang, S.Y., 2018. High-performance dopant-free conjugated small molecule-based hole-transport materials for perovskite solar cells. *Nano Energy*, *44*, pp.191-198.

[222] Liu, Y., Hong, Z., Chen, Q., Chen, H., Chang, W.H., Yang, Y., Song, T.B. and Yang, Y., 2016. Perovskite solar cells employing dopant-free organic hole transport materials with tunable energy levels. *Advanced Materials*, *28*(3), pp.440-446.

[223] Dao, Q.D., Fujii, A., Tsuji, R., Takeoka, Y. and Ozaki, M., 2017. Efficiency enhancement in perovskite solar cell utilizing solution-processable phthalocyanine hole transport layer with thermal annealing. *Organic Electronics*, 43, pp. 156-161.

[224] Yang, L., Cai, F., Yan, Y., Li, J., Liu, D., Pearson, A.J. and Wang, T., 2017. Conjugated small molecule for efficient hole transport in high-performance p-i-n type perovskite solar cells. *Advanced Functional Materials*, *27*(31), p.1702613.

[225] Yin, X., Guan, L., Yu, J., Zhao, D., Wang, C., Shrestha, N., Han, Y., An, Q., Zhou, J., Zhou, B. and Yu, Y., 2017. One-step facile synthesis of a simple carbazole-cored hole transport material for high-performance perovskite solar cells. *Nano Energy*, *40*, pp.163-169.

[226] Zhang, J., Xu, B., Yang, L., Mingorance, A., Ruan, C., Hua, Y., Wang, L., Vlachopoulos, N., Lira-Cantú, M., Boschloo, G. and Hagfeldt, A., 2017. Incorporation of Counter Ions in Organic Molecules: New Strategy in Developing Dopant-Free Hole Transport Materials for Efficient Mixed-Ion Perovskite Solar Cells. *Advanced Energy Materials*, *7*(14), p.1602736.

[227] Liu, X., Shi, X., Liu, C., Ren, Y., Wu, Y., Yang, W., Alsaedi, A., Hayat, T., Kong, F., Liu, X. and Ding, Y., 2018. A simple carbazole-triphenylamine hole transport material

for perovskite solar cells. *The Journal of Physical Chemistry C*, *122*(46), pp.26337-26343.

[228] Liu, C., Zhang, D., Li, Z., Zhang, X., Shen, L. and Guo, W., 2018. Efficient 4, 4′, 4 ″-tris (3-methylphenylphenylamino) triphenylamine (m-MTDATA) Hole Transport Layer in Perovskite Solar Cells Enabled by Using the Nonstoichiometric Precursors. *Advanced Functional Materials*, *28*(36), p.1803126.

[229] Mabrouk, S., Zhang, M., Wang, Z., Liang, M., Bahrami, B., Wu, Y., Wu, J., Qiao, Q. and Yang, S., 2018. Dithieno [3, 2-b: 2′, 3′-d] pyrrole-based hole transport materials for perovskite solar cells with efficiencies over 18%. *Journal of Materials Chemistry A*, *6*(17), pp.7950-7958.

[230] Pham, H.D., Do, T.T., Kim, J., Charbonneau, C., Manzhos, S., Feron, K., Tsoi, W.C., Durrant, J.R., Jain, S.M. and Sonar, P., 2018. Molecular engineering using an anthanthrone dye for low-cost hole transport materials: a strategy for dopant-free, high-efficiency, and stable perovskite solar cells. *Advanced Energy Materials*, *8*(16), p.1703007.

[231] Xu, P., Liu, P., Li, Y., Xu, B., Kloo, L., Sun, L. and Hua, Y., 2018. D–A–D-typed hole transport materials for efficient perovskite solar cells: tuning photovoltaic properties via the acceptor group. *ACS Applied Materials & Interfaces*, *10*(23), pp.19697-19703.

[232] Yin, X., Wang, C., Zhao, D., Shrestha, N., Grice, C.R., Guan, L., Song, Z., Chen, C., Li, C., Chi, G. and Zhou, B., 2018. Binary hole transport materials blending to linearly tune HOMO level for high efficiency and stable perovskite solar cells. *Nano Energy*, *51*, pp.680-687.

[233] Schloemer, T.H., Gehan, T.S., Christians, J.A., Mitchell, D.G., Dixon, A., Li, Z., Zhu, K., Berry, J.J., Luther, J.M. and Sellinger, A., 2019. Thermally stable perovskite solar cells by systematic molecular design of the hole-transport layer. *ACS Energy Letters*, *4*(2), pp.473-482.

[234] Yang, S., Zhao, H., Wu, M., Yuan, S., Han, Y., Liu, Z., Guo, K., Liu, S.F., Yang, S., Zhao, H. and Yuan, S., 2019. Highly efficient and stable planar $CsPbI_2Br$ perovskite solar cell with a new sensitive-dopant-free hole transport layer obtained via an effective surface passivation. *Solar Energy Materials and Solar Cells*, *201*, p.110052.

[235] Yin, X., Zhou, J., Song, Z., Dong, Z., Bao, Q., Shrestha, N., Bista, S.S., Ellingson, R.J., Yan, Y. and Tang, W., 2019. Dithieno [3, 2-b: 2′, 3′-d] pyrrol-Cored Hole Transport Material Enabling Over 21% Efficiency Dopant-Free Perovskite Solar Cells. *Advanced Functional Materials*, *29*(38), p.1904300.

[236] Guan, L., Zheng, Z. and Guo, Y., 2020. Enhanced hole transport in benzoic acid doped spiro-OMeTAD composite layer with intergrowing benzoate phase for perovskite solar cells. *Journal of Alloys and Compounds*, *832*, p.154991.

[237] Zhang, D., Xu, P., Wu, T., Ou, Y., Yang, X., Sun, A., Cui, B., Sun, H. and Hua, Y., 2019. Cyclopenta [hi] aceanthrylene-based dopant-free hole-transport material for organic–inorganic hybrid and all-inorganic perovskite solar cells. *Journal of Materials Chemistry A*, *7*(10), pp.5221-5226.

[238] Cao, Y., Chen, W., Sun, H., Wang, D., Chen, P., Djurišić, A.B., Zhu, Y., Tu, B., Guo, X., Tang, B.Z. and He, Z., 2020. Efficient Perovskite Solar Cells with a Novel Aggregation-Induced Emission Molecule as Hole-Transport Material. *Solar RRL*, *4*(2), p.1900189.

[239] Chen, W., Wang, Y., Liu, B., Gao, Y., Wu, Z., Shi, Y., Tang, Y., Yang, K., Zhang, Y., Sun, W. and Feng, X., 2021. Engineering of dendritic dopant-free hole transport molecules: enabling ultrahigh fill factor in perovskite solar cells with optimized dendron construction. *Science China Chemistry*, *64*(1), pp.41-51.

[240] Duan, L., Chen, Y., Jia, J., Zong, X., Sun, Z., Wu, Q. and Xue, S., 2020. Dopant-free hole-transport materials based on 2, 4, 6-triarylpyridine for inverted planar perovskite solar cells. *ACS Applied Energy Materials*, *3*(2), pp.1672-1683.

[241] Gao, L., Schloemer, T.H., Zhang, F., Chen, X., Xiao, C., Zhu, K. and Sellinger, A., 2020. Carbazole-Based Hole-Transport Materials for High-Efficiency and Stable Perovskite Solar Cells. *ACS Applied Energy Materials*, *3*(5), pp.4492-4498.

[242] Liu, H., Liu, C., Li, W., Kong, W., Chen, H., Zhang, H., Zhang, X., Wang, W. and Cheng, C., 2020. Approaching the Most Economic Preparation of Hole Transport Layer by Organic Monomolecular Strategy for Efficient Inverted Perovskite Solar Cells. *Solar RRL*, *4*(6), p.2000011.

[243] Lu, H., He, B., Ji, Y., Shan, Y., Zhong, C., Xu, J., LiuYang, J., Wu, F. and Zhu, L., 2020. Dopant-free hole transport materials processed with green solvent for efficient perovskite solar cells. *Chemical Engineering Journal*, *385*, p.123976.

[244] Ou, Y., Sun, A., Li, H., Wu, T., Zhang, D., Xu, P., Zhao, R., Zhu, L., Wang, R., Xu, B. and Hua, Y., 2021. Developing D–π–D hole-transport materials for perovskite solar cells: the effect of the π-bridge on device performance. *Materials Chemistry Frontiers*, *5*(2), pp.876-884.

[245] Pashaei, B., Bellani, S., Shahroosvand, H. and Bonaccorso, F., 2020. Molecularly engineered hole-transport material for low-cost perovskite solar cells. *Chemical Science*, *11*(9), pp.2429-2439.

[246] Pegu, M., Caliò, L., Ahmadpour, M., Rubahn, H.G., Kazim, S., Madsen, M. and Ahmad, S., 2020. Dibenzo-tetraphenyl diindeno perylene as hole transport layer for high-bandgap perovskite solar cells. *Emergent Materials*, *3*, pp.109-116.

[247] Pham, H.D., Jain, S.M., Li, M., Wang, Z.K., Manzhos, S., Feron, K., Pitchaimuthu, S., Liu, Z., Motta, N., Durrant, J.R. and Sonar, P., 2020. All-Rounder Low-Cost Dopant-Free D-A-D Hole-Transporting Materials for Efficient Indoor and Outdoor Performance of Perovskite Solar Cells. *Advanced Electronic Materials*, *6*(4), p.1900884.

[248] Pineda, R.F., Zems, Y., Troughton, J., Niazi, M.R., Perepichka, D.F., Watson, T. and Robertson, N., 2020. Star-shaped triarylamine-based hole-transport materials in perovskite solar cells. *Sustainable Energy & Fuels*, *4*(2), pp.779-787.

[249] Qin, T., Wu, F., Ma, D., Mu, Y., Chen, X., Yang, Z., Zhu, L., Zhang, Y., Zhao, J. and Chi, Z., 2020. Asymmetric Sulfonyldibenzene-Based Hole-Transporting Materials for Efficient Perovskite Solar Cells: Inspiration from Organic Thermally-Activated Delayed Fluorescence Molecules. *ACS Materials Letters*, *2*(9), pp.1093-1100.

[250] Tepliakova, M., Yakushenko, I.K., Romadina, E.I., Novikov, A.V., Kuznetsov, P.M., Stevenson, K.J. and Troshin, P.A., 2021. Strength of attraction: pyrene-based hole-transport materials with effective π–π stacking for dopant-free perovskite solar cells. *Sustainable Energy & Fuels*, *5*(1), pp.283-288.

[251] Tian, Y., Tao, L., Chen, C., Lu, H., Li, H., Yang, X. and Cheng, M., 2021. Facile synthesized fluorine substituted benzothiadiazole based dopant-free hole transport material for high efficiency perovskite solar cell. *Dyes and Pigments*, *184*, p.108786.

[252] Wu, G., Zhang, Y., Kaneko, R., Kojima, Y., Islam, A., Sugawa, K., Otsuki, J. and Liu, S., 2020. Facile synthesis of “lucky clover” hole-transport material for efficient and stable large-area perovskite solar cells. *Journal of Power Sources*, *454*, p.227938.

[253] Wu, C., Chen, C., Tao, L., Ding, X., Zheng, M., Li, H., Li, G., Lu, H. and Cheng, M., 2020. Highly efficient perovskite solar cells based on symmetric hole transport material constructed with indaceno [1, 2-b: 5, 6-b'] dithiophene core building block. *Journal of Energy Chemistry*, *43*, pp.98-103.

[254] Zhang, X.F., Liu, C., Wu, J. and Xu, B., 2020. Tetrabenzotriazacorrole and its derivatives as undoped hole transporting materials for perovskite solar cells: synthesis, device fabrication, and device performance. *Journal of Energy Chemistry*, *43*, pp.139-147.

[255] Zhou, X., Kong, F., Sun, Y., Huang, Y., Zhang, X. and Ghadari, R., 2020. Dopant-free benzothiadiazole bridged hole transport materials for highly stable and efficient perovskite solar cells. *Dyes and Pigments*, *173*, p.107954.

[256] Zhao, X., Yao, C., Gu, K., Liu, T., Xia, Y. and Loo, Y.L., 2020. A hole-transport material that also passivates perovskite surface defects for solar cells with improved efficiency and stability. *Energy & Environmental Science*, *13*(11), pp.4334-4343.

[257] Calió, L., Kazim, S., Grätzel, M. and Ahmad, S., 2016. Hole-transport materials for perovskite solar cells. *Angewandte Chemie International Edition*, *55*(47), pp.14522-14545.s